



POP Pincer Complexes of Ruthenium and Manganese for Small Molecule Transformations

Nikol, Alexander Tobias

Publication date:
2023

Document Version
Publisher's PDF, also known as Version of record

[Link back to DTU Orbit](#)

Citation (APA):
Nikol, A. T. (2023). *POP Pincer Complexes of Ruthenium and Manganese for Small Molecule Transformations*. DTU Chemistry.

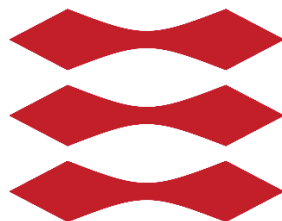
General rights

Copyright and moral rights for the publications made accessible in the public portal are retained by the authors and/or other copyright owners and it is a condition of accessing publications that users recognise and abide by the legal requirements associated with these rights.

- Users may download and print one copy of any publication from the public portal for the purpose of private study or research.
- You may not further distribute the material or use it for any profit-making activity or commercial gain
- You may freely distribute the URL identifying the publication in the public portal

If you believe that this document breaches copyright please contact us providing details, and we will remove access to the work immediately and investigate your claim.

DTU



POP Pincer Complexes of Ruthenium and Manganese for Small Molecule Transformations

PhD thesis

ALEXANDER TOBIAS NIKOL

Supervisor:

MARTIN NIELSEN

Co-supervisor:

ANDERS RIISAGER

Department of Chemistry, Technical University of Denmark (DTU),

2800 Kongens Lyngby, Denmark

August 2023

“Da steh‘ ich nun, ich armer Tor!
Und bin so klug als wie zuvor.“

„And here, poor fool! with all my lore
I stand, no wiser than before.”

Taken from

“Faust. Eine Tragödie”, by JOHANN WOLFGANG VON GOETHE

Preface

This dissertation describes my research work carried out during the period from May 2020 to August 2023 at the Department of Chemistry, Center for Catalysis and Sustainable Chemistry of the Technical University of Denmark (DTU) under the direction and supervision of Associate Professor MARTIN NIELSEN and co-supervision of Professor ANDERS RIISAGER.

Included in the PhD program were multiple courses with a total point count of 30.5 ECTS, as well as 420 hours of departmental work such as the teaching of Bachelor students in first and third semester lab courses for qualitative analytical and synthetic chemistry. Additionally, the project included 500 hours of scientific dissemination work, attendance of multiple conferences, as well as seminars.

An external research stay at the Leibniz Institute for Catalysis (LIKAT) in Rostock/Germany was attended in the time between March and June 2022. Results of this external stay are added to this work as a separate chapter.

I hereby declare that I have written this PhD thesis on my own using only the cited references.



ALEXANDER TOBIAS NIKOL

Kongens Lyngby, 2023-08-14

This work is dedicated to:

KURT NIKOL
(1929-1997)

IRENE KÄTHCHEN NIKOL (née BOHL)
(1932-2018)

JOHANNES WILHELM FIGGEN
(*1935)

MARIA ANNA FIGGEN (née KREVET)
(*1933)

Acknowledgements

As a PhD thesis is a large project, support from coworkers and superiors is required for a successful completion. I would therefore first and foremost like to express my gratitude to Associate Professor MARTIN NIELSEN and Professor ANDERS RIISAGER, my two research supervisors, for their guidance, encouragement and useful critiques during the planning, development, and execution of this work.

Special thanks also go to all my colleagues in the NIELSEN workgroup, the workshop staff, as well as the administration of DTU Kemi. Among all these great colleagues, a few people deserve special recognition:

- MIKE STEFFEN BERNHARD JØRGENSEN for valuable advice regarding synthesis techniques, for introducing me to the practical aspects of single-crystal X-ray crystallography, and for helping in the translation of this thesis's abstract and for valuable proofreading.
- MATHIAS THOR NIELSEN for always offering solutions to synthetic problems when encountered, and for being a delightful colleague whose "humour" kept me in a good mood during most of the time in the laboratory.
- ROSA MARIA PADILLA PAZ for introducing me to the workgroup's workflow, new synthetic and analytic techniques that my prior education did not yet provide and for lending a helping hand whenever needed.
- JOSÉ TIAGO MENEZES CORREIA for having valuable discussions about the organic chemistry aspects of my work and for providing valuable proofreading.
- MARIUSZ KUBUS and JOHANNE MARIE NIELSEN for their help with training me on the use of the single-crystal X-ray diffractometer.
- KASPER ENEMARK RASMUSSEN for introducing me to the practical work with NMR machines and for lending a helping hand whenever advanced NMR techniques were required.
- Associate Professor RENÉ WUGT LARSEN for measuring the ATR-IR spectra.
- LARS EGEDE BRUHN, ANDERS GRAFF PEDERSEN, SHADI REDA WAHID and ISHAQ KHALIQDAD for being able to solve every single problem encountered with laboratory equipment.

I would also like to thank the entire BELLER/JUNGE workgroup at the Leibniz Institute for Catalysis (LIKAT) in Rostock/Germany, where I spent three and a half months as part of the external stay exchange program. Especially, I would like to thank the group leaders MATTHIAS BELLER and HENRIK JUNGE, for giving me a good introduction into a new field of chemistry, for their scientific advice during this project, and for making the brief stay there an overall joy.

Additionally, I would like to express gratitude towards the laboratory technicians at the University of Copenhagen (KU) who performed the elemental analysis (CHNS) for many of my novel compounds.

Of great importance was also the research of DENNIS UPPER, which helped me boost my motivation during times of severe cases of writer's block, proving that even short abstracts are worth publishing when done with exceptional quality.¹

As an international student, I would also like to thank the entire country of Denmark, for being a welcoming host nation during the times of the COVID-19 pandemic.

Finally, yet importantly, I would also like to thank my family and friends who supported me with encouragement and helped boost my motivation in the timeframe of my PhD studies. Words are not enough to express my gratitude.

Abstract

This thesis summarizes and discusses the results of six separate projects within the PhD studies and totals eight chapters, followed by ten appendices containing general instrumentation, synthesis protocols, spectroscopic data, and a list of planned publications and scientific disseminations based on this work.

After first opening up with a general introduction towards the topic of POP pincer complexes, the thesis discusses the synthesis of a family of related ruthenium(II) hydrido complexes containing POP pincer ligands. All of them were spectroscopically characterized and their structures confirmed by means of crystallography.

In the third chapter, the application of the previously synthesized family of Ru(II) complexes for the upgrading of ethanol to 1-butanol and related higher alcohols as a means of biofuel synthesis was investigated. At a temperature of 120 °C, they reached moderate yields of around 28% over two days after various condition screenings.

The complexes were then further tested for their activity in the dehydrogenation of formic acid using an ionic liquid as a solvent. This was an attempt to simplify the reaction conditions for formic acid dehydrogenation in order to make the reaction more industrially attractive. The set of complexes showed high activities at 90 °C and were active at temperatures as low as 60 °C.

In the fifth chapter, a new set of Ru(II)-POP complexes bearing nitrosyl groups was synthesized. This gives a fundamental insight into binding properties of POP pincer complexes, especially their hemilability between different binding modes. All complexes were investigated by spectroscopic techniques and their structures verified by crystallography.

The sixth chapter aimed to develop a novel set of previously unknown POP pincer complexes of manganese. Three catalysts could be synthesized and spectroscopically analyzed to various degrees. To my knowledge, this work represents the first reported example of Mn(I) POP pincer complexes. They were then used in formic acid dehydrogenation reactions in conditions identical to those used for the ruthenium complexes and showed moderate activity.

Finally, the seventh chapter, done in collaboration with the Leibniz Institute for Catalysis (LIKAT) in Rostock/Germany, investigates the reactivity of CO₂ adducts of very electron-rich phosphines. Breaking the molecule symmetry of CO₂, these adducts are interesting as co-catalysts for the hydrogenation of CO₂ to formic acid and other bulk chemicals in a future hydrogen economy. Catalytic reactions were attempted

using the commercially available Ru-MACHO-BH catalyst under harsh conditions, and small amounts of formate signals were detected, opening up the possibility of further investigation.

In conclusion, this thesis contributes to the further understanding of catalytic processes using POP pincer complexes of ruthenium and manganese for applications in the field of green chemistry, specifically biofuel development and energy storage solutions.

Resumé

I den nærværende afhandling præsenteres og diskuteres resultaterne af de arbejder, der er udført som led af ph.d.-uddannelsen ved Institut for Kemi, Danmarks Tekniske Universitet. Disse arbejder er inddelt i otte kapitler, hvilke efterfølges af ni bilag. Disse bilag indeholder tekniske informationer om instrumentering, synteseprotokoller, spektroskopiske data, liste over planlagte publikationer samt yderligere videnskabelig formidling hidrørende de i denne afhandling beskrevet arbejder.

Afhandlingen åbnes indledningsvis af en generel introduktion til begrebet om POP-ligander og ”pincer-komplekser”, hvorefter følger beskrivelse af syntese af en række strukturelt beslægtede hydridoruthenium(II)-forbindelser koordineret af førnævnte POP-ligander. Alle heri diskuterende forbindelser er karakteriseret strukturelt gennem spektroskopiske- og krystallografiske metoder.

I Kapitel 3 beskrives reaktionsprofilen af de i Kapitel 2 beskrevet forbindelser under anvendelse i den katalytiske omdannelse af ethanol til hovedsageligt butan-1-ol og samt tungere alkoholer, der heri beskrives som lovende kandidater til syntetisk biobrændsel. Det vises, at udbytter på 28% kan opnås ved en reaktionstid på to dage ved 120 °C efter optimering af reaktionsvariable. Herefter beskrives, ligeledes i Kapitel 4, hvorledes de for denne afhandling relevante forbindelser er blevet testet for katalytisk aktivitet i dehydrogeneringsreaktioner af myresyre under anvendelse af ioniske væsker som opløsningsmiddel. Dette beskrives som et forsøg på at simplificere reaktionsbetingelserne for derved at gøre denne proces mere attraktiv for den kemiske industri. Således vises det, at de i Kapitel 4 undersøgte koordinationsforbindelser udviser høj katalytisk aktivitet ved 90 °C, og katalytisk omsætning blev detekteret ved reaktionstemperature ned til 60 °C.

I Kapitel 5 fremsættes en generel protokol for syntesen af nye nitrosyl-forbindelser af ruthenium(II) flankeret af POP-ligander. Som vist gennem spektroskopisk- og krystallografisk strukturanalyse udviser POP-liganderne anderledes bindingsforhold til ruthenium(II), end hvad tilfældet er for alle ikke-nitrosyl-bærende forbindelser der præsenteres i den foreliggende afhandling.

Herpå følger i Kapitel 6 gennemgang af syntese og delvis karakterisering af tre nye POP-forbindelser af mangan(I), vis moderate katalytiske aktivitet i dehydrogeneringsreaktionen af myresyre er afprøvet under identiske reaktionsbetingelser for de i det foregående kapitel undersøgte ruthenium forbindelser.

Arbejder der er udført under udvekslingsopholdet på Leibniz Institut für Katalyse i Rostock, Tyskland, beskrives som det sidste i Kapitel 7. Undersøgelse af relativitetsmønstrene af carboxylatophosphonium-forbindelser, efter dannelse af disse gennem reaktion mellem særdeles elektronrige phosphiner og CO₂,

udgør en væsentlig del af dette kapitel. På grund af polariseringen af CO_2 er disse phosphin- CO_2 -addukter interessante emner, i et potentielt "hydrogendrevet" samfund, som katalytisk intermediat under direkte reduktion af CO_2 til myresyre og andre kemikalier. Ydermere undersøges muligheden for katalytisk omdannelse af førnævnte carboxylatophosphonium-forbindelser til myresyre gennem hydrogenering ved anvendelse af det kommercielle kompleks kendt som Ru-MACHO-BH. Dette viser sig ladsiggørligt under relativt hårde reaktionsbetingelser.

Afrundningsvis kan det konkluderes, at den foreliggende afhandling bidrager til den fundamentale forståelse af katalytiske processor, hvori POP-komplekser af ruthenium og mangan kan finde anvendelse med særlig fokus på metodisk udvikling af syntese af briobrændsel og energilagring.

Table of contents

Preface	I
Acknowledgements.....	III
Abstract.....	V
Resumé.....	VII
Table of contents.....	IX
List of figures.....	XIV
List of schemes	XIX
List of tables.....	XX
List of abbreviations and acronyms	XXI
1. General introduction	1
1.1 Pincer complexes	1
1.2.1 History and definition	1
1.2.2 POP pincer ligands.....	2
1.2.3 POP pincer complexes	6
1.2.4 Ruthenium POP pincer complexes: History and reactivity.....	8
1.3 POP and PNP pincer complexes compared	10
2. Ruthenium POP pincer complex synthesis and analysis.....	12
2.1 On the choice of POP ligands and precursors.....	12
2.2 Results and discussion	15
2.2.1 Synthesis of [RuHCl(POP)(PPh ₃)] complexes.....	15
2.2.2 Chloride abstraction and influence of POP backbone on structure of corresponding cations ...	24
2.2.3 Syntheses of azido complexes.....	29
2.3 Conclusions and outlook.....	32
3. Ethanol upgrading using Ru-POP pincer complexes	33
3.1 Biofuels as a future energy storage system.....	33

3.1.1 The need for efficient biofuels	33
3.1.2 Ethanol as a biofuel.....	33
3.1.3 Advanced biofuels and the case for 1-butanol	34
3.1.4 The GUERBET mechanism.....	36
3.1.5 Organometallic complexes for ethanol upgrading	38
3.1.6 Ethanol upgrading mechanisms	40
3.1.7 Aim of the project	43
3.2 Ethanol upgrading reactions using POP pincer complexes.....	44
3.2.1 Ethanol upgrading screening reactions	44
3.2.3 Base screenings	48
3.2.4 Stoichiometric reactions.....	49
3.2.5 On the catalytic cycle	51
3.3 Conclusions and outlook.....	54
4. Formic acid dehydrogenation using Ru-POP pincer complexes.....	55
4.1 General introduction	55
4.1.1 Liquid organic hydrogen carriers	55
4.1.2 Formic acid as a liquid organic hydrogen carrier.....	56
4.1.3 Formic acid dehydrogenation by homogeneous catalysis.....	57
4.1.4 Formic acid dehydrogenation mechanisms	59
4.1.5 Ionic liquids as solvents for formic acid dehydrogenation	61
4.1.6 Aim of the project	62
4.2 Formic acid dehydrogenation catalysis reactions	63
4.2.1 Activity screenings.....	63
4.2.2 Investigations into reaction mechanism and reaction of the complexes with the ionic liquid ...	69
4.2.3 On the catalytic cycle	75
4.3 Conclusions and outlook.....	76
5. Ruthenium-POP nitrosyl complexes	77

5.1 Nitrosyl: A non-innocent ligand	77
5.1.1 Nitrosyl as a non-innocent ligand in organometallic chemistry.....	77
5.1.2 Aim of the project	79
5.2 Results and discussion	81
5.2.1 Synthesis attempts of $[\text{Ru}(\text{POP})(\text{NO})\text{Cl}_2]\text{Cl}$	81
5.2.2 Chloride abstraction experiments.....	85
5.3 Conclusions and outlook.....	86
6. Manganese(I) POP pincer complexes for formic acid dehydrogenation in ionic liquids	87
6.1 General introduction	87
6.1.1 The case for 1 st row transition metal catalysts	87
6.1.2 Manganese complexes for formic acid dehydrogenation.....	87
6.1.3 Aim of the project	88
6.2 Synthesis of $\text{Mn}(\text{I})(\text{POP})$ complexes	89
6.3 Formic acid dehydrogenation experiments	94
6.4 Conclusions and outlook.....	97
7. Hydrogenation of carbon dioxide with electron-rich phosphine adducts	98
7.1 Introduction.....	99
7.1.1 Zwitterionic phosphine CO_2 adducts: Properties and use cases.....	99
7.1.2 Other types of phosphine CO_2 adducts	101
7.1.3 General proposal and aim of the project	101
7.2 Results and discussion	103
7.2.1 Low temperature investigations of phosphines.....	103
7.2.2 Hydrogenation catalysis using $\text{P}(\text{tmg})_3$ and Ru-MACHO-BH	104
7.3 Conclusions and outlook.....	105
8. Summary and perspectives.....	106
Bibliography	109
9. Appendices.....	123

Table of contents

Appendix A.	General instrumentation	124
Appendix B.	General synthesis protocols	126
Appendix C.	Chapter 2	128
	C1 Synthesis of precursors and ligands	128
	C2 Synthesis of [RuHCl(POP)(PPh ₃)]	128
	C3 Synthesis of [RuH(POP)(PPh ₃)(MeCN)]X	160
	C4 Synthesis of [RuH(N ₃)(POP)(PPh ₃)]	166
	C5 Crystallographic data.....	170
Appendix D.	Chapter 3	181
	D1 Product identification and calibration curves.....	181
	D1.1 GC and GC-MS spectra of reaction products.....	181
	D1.2 Calibration curves	183
	D2 General procedure for ethanol upgrading reactions	185
	D3 Ethanol upgrading experiments.....	186
	D4 Stoichiometric NMR experiments.....	189
Appendix E.	Chapter 4	192
	E1 General procedure for formic acid dehydrogenation in ionic liquid	192
	E2 Formic acid dehydrogenation experiments.....	193
	E3 Reaction mechanism investigations.....	200
	E4 Synthesis of [RuH(<i>i</i> Pr-DBFphos)(PPh ₃)(MeCN)]X.....	203
	E5 Crystallographic data.....	204
Appendix F.	Chapter 5	205
	F1 Synthesis of [Ru(POP)(NO)Cl ₃]	205
	F2 Crystallographic data	213
Appendix G.	Chapter 6	215
	G1 Synthesis of [Mn(POP)(CO) ₂ Br]	215
	G2 General procedure for formic acid dehydrogenation in ionic liquid	225

Table of contents

G3 Formic acid dehydrogenation in ionic liquid	226
G4 Crystallographic data	227
Appendix H. Chapter 7	228
H1 Phosphine synthesis	228
H2 General procedure for temperature-dependent NMR experiments	228
H3 Temperature-dependent NMR experiments	229
H4 General procedure for CO ₂ hydrogenation experiments	232
H5 CO ₂ hydrogenation experiments using P(tmg) ₃	232
Appendix I. Planned publications	234
Appendix J. Conferences and scientific exchanges.....	235

List of figures

Figure 1.1: Pincer ligand nomenclature.	2
Figure 1.2: POP pincer ligands first used in hydroformylation by van Leeuwen in 1995.	3
Figure 1.3: General structure of bis[(PR ₂)ethyl]ether POP pincer ligands.	4
Figure 1.4: Typical binding modes of POP ligands.	7
Figure 1.5: Examples of less common binding modes of POP pincer ligands.	7
Figure 1.6: Deactivation of PNP pincer complexes by <i>N</i> -methylation and POP pincers as the central subject of this work.	11
Figure 2.1: Overview over ligands L1-L12 chosen in this work.	12
Figure 2.2: [RuHCl(POP)(PPh ₃)] complexes Ru-1a to Ru-12a under investigation.	15
Figure 2.3: NMR spectra of Ru-8a	17
Figure 2.4: NMR spectra of crude Ru-12a in C ₆ D ₆ at 25 °C.	18
Figure 2.5: Hydride chemical shifts and P-P coupling constants in Ru-1a to Ru-11a	20
Figure 2.6: Overview of newly obtained crystal structures for Ru-4a to Ru-11a	22
Figure 2.7: Overview of newly obtained crystal structures for Ru-1b to Ru-10b	25
Figure 2.8: Reaction product of Ru-2a with NaBF ₄ in MeCN.	27
Figure 2.9: Crystal structures of Ru-7c and Ru-7d	28
Figure 2.10 Ruthenium(II) hydrido azido complexes.	29
Figure 2.11: Crystal structure of Ru-7e	30
Figure 3.1: Butanol fuel synthesis via ethanol upgrading.	36
Figure 3.2: Examples of ruthenium(II) catalysts for ethanol upgrading.	39
Figure 3.3: LIU and JONES'S manganese(I) PNP pincers for ethanol upgrading.	40
Figure 3.4: First ethanol upgrading screening.	45
Figure 3.5: Screening of phosphine substituents.	46
Figure 3.6: Temperature and time screening of Ru-2a	47
Figure 3.7: Base screening of Ru-2a and Ru-3a	48
Figure 3.8: Hydride region of the ¹ H NMR of a reaction between Ru-2a and NaOEt in EtOH-d ₆ after 2 hours.	49
Figure 3.9: 600 MHz ¹ H NMR spectrum of a reaction of Ru-2a with NaOEt in THF-d ₈ at 25 °C.	50
Figure 4.1: Liquid organic hydrogen carriers.	56
Figure 4.2: Examples of iridium-based catalysts for formic acid dehydrogenation.	58
Figure 4.3: Examples of ruthenium catalysts for formic acid dehydrogenation.	58

Figure 4.4: Typical cations and anions of ionic liquids.	61
Figure 4.5: Temperature screening of [RuHCl(PPh ₃) ₃] toluene adduct.	63
Figure 4.6: Catalyst screening of Ru-1a to Ru-11a	65
Figure 4.7: Temperature screening of Ru-1a and Ru-8a	66
Figure 4.8: ARRHENIUS plots of [RuHCl(PPh ₃) ₃] toluene adduct, Ru-1a and Ru-8a	67
Figure 4.9: Crystal structure of Ru-8c	68
Figure 4.10 Anion screening of Ru-8a-c	68
Figure 4.11: Hydride region of the ¹ H NMR spectrum of Ru-1a during formic acid dehydrogenation.	70
Figure 4.12: Hydride region of the ¹ H NMR spectrum of Ru-1a during formic acid dehydrogenation after 120 minutes.	71
Figure 4.13: Hydride region of the ¹ H NMR spectrum of Ru-2a during formic acid dehydrogenation.	72
Figure 4.14: Hydride region of the ¹ H NMR spectrum of Ru-2a during formic acid dehydrogenation after 120 minutes.	73
Figure 4.15: Reaction of Ru-1a with BMIM-OAc after 24 hours at 40 °C.	74
Figure 5.1: Ruthenium(II) nitrosyl complexes.	79
Figure 5.2: Solid state structure of Ru-NO-2	81
Figure 5.3: Disordered crystallographic model of Ru-NO-1	83
Figure 5.4: Solid state structure of Ru-NO-1	84
Figure 5.5: Crystal structure of Ru-NO-6	84
Figure 6.1: Mn(I) complexes for formic acid dehydrogenation.	88
Figure 6.2: Formic acid dehydrogenation using Mn(POP) complexes.	88
Figure 6.3: [Mn(POP)(CO) ₂ Br]Catalysts under investigation.	89
Figure 6.4: ATR-IR of Mn-3 and Mn-7	90
Figure 6.5 Temperature dependent ³¹ P{ ¹ H} NMR of Mn-7 in toluene-d ₈	91
Figure 6.6: Crystal structure of Mn-7	91
Figure 6.7: Crystal structure of degraded Mn-3	93
Figure 6.8: Attempted synthesis of Mn-1 and Mn-5	94
Figure 6.9 Catalyst screening of Mn-7 , Mn-3 and Mn-5	95
Figure 6.10: Concentration screening of Mn-5 and Mn-7	96
Figure 7.1: Equilibrium between highly electron-rich phosphine and CO ₂ , and their corresponding adduct.	99
Figure 7.2: Reaction of phosphazene base P ₁ - <i>t</i> Bu-tris(pyrrolidin) with CO ₂	101
Figure 8.1: POP and <i>N</i> -methylated PNP pincer complexes.	107
Figure 9.1: Autoclave reactor types used in this work.	127

Figure 9.2: 400 MHz ^1H NMR spectrum of Ru-1a in toluene- d_8 at 25 $^\circ\text{C}$	129
Figure 9.3: 162 MHz $^{31}\text{P}\{^1\text{H}\}$ NMR spectrum of Ru-1a in toluene- d_8 at 25 $^\circ\text{C}$	130
Figure 9.4: 400 MHz ^1H NMR spectrum of Ru-2a in C_6D_6 at 25 $^\circ\text{C}$	131
Figure 9.5: 162 MHz $^{31}\text{P}\{^1\text{H}\}$ NMR spectrum of Ru-2a in C_6D_6 at 25 $^\circ\text{C}$	131
Figure 9.6: 400 MHz ^1H NMR spectrum of Ru-3a in C_6D_6 at 25 $^\circ\text{C}$	132
Figure 9.7: 800 MHz ^1H NMR spectrum of Ru-4a in C_6D_6 at 25 $^\circ\text{C}$	134
Figure 9.8: 201 MHz ^{13}C NMR spectrum of Ru-4a in C_6D_6 at 25 $^\circ\text{C}$	134
Figure 9.9: 162 MHz $^{31}\text{P}\{^1\text{H}\}$ NMR spectrum of Ru-4a in C_6D_6 at 25 $^\circ\text{C}$	135
Figure 9.10: 800 MHz COSY spectrum of Ru-4a in C_6D_6 at 25 $^\circ\text{C}$	135
Figure 9.11: 800 MHz HSQC spectrum of Ru-4a in C_6D_6 at 25 $^\circ\text{C}$	136
Figure 9.12: 400 MHz ^1H NMR spectrum of Ru-5a in C_6D_6 at 25 $^\circ\text{C}$	138
Figure 9.13: 400 MHz ^{13}C NMR spectrum of Ru-5a in C_6D_6 at 25 $^\circ\text{C}$	138
Figure 9.14: 162 MHz $^{31}\text{P}\{^1\text{H}\}$ NMR spectrum of Ru-5a in C_6D_6 at 25 $^\circ\text{C}$	139
Figure 9.15 400 MHz ^1H NMR spectrum of Ru-6a in C_6D_6 at 25 $^\circ\text{C}$	141
Figure 9.16: 101 MHz ^{13}C NMR spectrum of Ru-6a in C_6D_6 at 25 $^\circ\text{C}$	141
Figure 9.17: 162 MHz $^{31}\text{P}\{^1\text{H}\}$ spectrum of Ru-6a in C_6D_6 at 25 $^\circ\text{C}$	142
Figure 9.18: 400 MHz ^1H NMR spectrum of Ru-7a in C_6D_6 at 25 $^\circ\text{C}$	144
Figure 9.19: 101 MHz ^{13}C NMR spectrum of Ru-7a in C_6D_6 at 25 $^\circ\text{C}$	144
Figure 9.20: 162 MHz $^{31}\text{P}\{^1\text{H}\}$ NMR spectrum of Ru-7a in C_6D_6 at 25 $^\circ\text{C}$	145
Figure 9.21: 400 MHz ^1H NMR spectrum of Ru-8a in C_6D_6 at 25 $^\circ\text{C}$	147
Figure 9.22: 101 MHz ^{13}C NMR spectrum of Ru-8a in C_6D_6 at 25 $^\circ\text{C}$	147
Figure 9.23: 162 MHz $^{31}\text{P}\{^1\text{H}\}$ NMR spectrum of Ru-8a in C_6D_6 at 25 $^\circ\text{C}$	148
Figure 9.24: 400 MHz ^1H NMR spectrum of Ru-9a in C_6D_6 at 25 $^\circ\text{C}$	150
Figure 9.25: 101 MHz ^{13}C NMR spectrum of Ru-9a in C_6D_6 at 25 $^\circ\text{C}$	150
Figure 9.26: 162 MHz $^{31}\text{P}\{^1\text{H}\}$ NMR spectrum of Ru-9a in C_6D_6 at 25 $^\circ\text{C}$	151
Figure 9.27: 400 MHz ^1H NMR spectrum of Ru-10a in C_6D_6 at 25 $^\circ\text{C}$	153
Figure 9.28: 101 MHz ^{13}C NMR spectrum of Ru-10a in C_6D_6 at 25 $^\circ\text{C}$	153
Figure 9.29: 162 MHz $^{31}\text{P}\{^1\text{H}\}$ NMR spectrum of Ru-10a in toluene- d_8 at 25 $^\circ\text{C}$	154
Figure 9.30: Variable temperature 243 MHz $^{31}\text{P}\{^1\text{H}\}$ NMR spectrum of Ru-10a in toluene- d_8	154
Figure 9.31: 400 MHz ^1H NMR spectrum of crude Ru-11a in $\text{DMSO}-\text{d}_6$ at 25 $^\circ\text{C}$	156
Figure 9.32: 162 MHz $^{31}\text{P}\{^1\text{H}\}$ NMR spectrum of crude Ru-11a in $\text{DMSO}-\text{d}_6$ at 25 $^\circ\text{C}$	156
Figure 9.33: 400 MHz ^1H NMR spectrum of crude Ru-12a in C_6D_6 at 25 $^\circ\text{C}$	158
Figure 9.34: 162 MHz $^{31}\text{P}\{^1\text{H}\}$ NMR spectrum of crude Ru-12a in C_6D_6 at 25 $^\circ\text{C}$	158
Figure 9.35: 162 MHz ^{31}P NMR spectrum of crude Ru-12a in C_6D_6 at 25 $^\circ\text{C}$	159

Figure 9.36: 400 MHz ^1H NMR spectrum of Ru-7e in C_6D_6 at 25 °C.	167
Figure 9.37: 101 MHz ^{13}C NMR spectrum of Ru-7e in C_6D_6 at 25 °C.	167
Figure 9.38: 162 MHz $^{31}\text{P}\{^1\text{H}\}$ NMR spectrum of Ru-7e in C_6D_6 at 25 °C.....	168
Figure 9.39: 81 MHz $^1\text{H}/^{15}\text{N}$ HMBC NMR spectrum of Ru-7e in C_6D_6 at 25 °C.....	168
Figure 9.40: ATR-IR spectrum of Ru-7e	169
Figure 9.41: Example of a gas chromatography spectrum of a reaction mixture.	181
Figure 9.42: Mass spectrum of 1-butanol.	182
Figure 9.43: Mass spectrum of 1-hexanol.....	182
Figure 9.44: 400 MHz ^1H NMR spectrum of the reaction of Ru-2a with NaOEt in ethanol- d_6 at 333 K (60 °C).....	189
Figure 9.45: 162 MHz $^{31}\text{P}\{^1\text{H}\}$ NMR spectrum of the reaction of Ru-2a with NaOEt in ethanol- d_6 at 333 K (60 °C).....	190
Figure 9.46: 600 MHz ^1H NMR spectrum of a reaction of Ru-2a with EtOAc in THF- d_8	191
Figure 9.47: ^1H NMR of FA, BMIM-OAc and catalyst in MeCN- d_3	192
Figure 9.48: ARRHENIUS plot of FA dehydrogenation using $[\text{RuHCl}(\text{PPh}_3)_3]\cdot\text{toluene}$	194
Figure 9.49: ARRHENIUS plot of FA dehydrogenation using Ru-1a	197
Figure 9.50: ARRHENIUS plot of FA dehydrogenation using Ru-8a	199
Figure 9.51: 400 MHz ^1H NMR spectrum of Ru-1a in BMIM-OAc at 25 °C.....	200
Figure 9.52: 162 MHz ^{31}P NMR spectrum of Ru-1a in BMIM-OAc at 25 °C.....	201
Figure 9.53: Hydride region of the ^1H NMR spectrum of FA dehydrogenation using Ru-1a	202
Figure 9.54: Hydride region of the ^1H NMR spectrum of FA dehydrogenation using Ru-2a	202
Figure 9.55: 400 MHz ^1H NMR spectrum of Ru-NO-1 in DMF- d_7 at 25 °C.	206
Figure 9.56: 101 MHz ^{13}C NMR spectrum of Ru-NO-1 in DMF- d_7 at 25 °C.	206
Figure 9.57: 162 MHz $^{31}\text{P}\{^1\text{H}\}$ NMR spectrum of Ru-NO-1 in DMF- d_7 at 25 °C.....	207
Figure 9.58: ATR-IR spectrum of Ru-NO-1	207
Figure 9.59: 400 MHz ^1H NMR spectrum of Ru-NO-2 in DMSO- d_6 at 25 °C.....	209
Figure 9.60: 162 MHz $^{31}\text{P}\{^1\text{H}\}$ NMR spectrum of Ru-NO-2 , revealing free ligand.	209
Figure 9.61: ATR-IR spectrum of Ru-NO-2	210
Figure 9.62: ATR-IR spectrum of Ru-NO-6	211
Figure 9.63: ATR-IR spectrum of Ru-NO-7	212
Figure 9.64: 800 MHz ^1H NMR spectrum of Mn-7 in CD_3CN at 25 °C.....	216
Figure 9.65: 201 MHz ^{13}C NMR spectrum of Mn-7 in CD_3CN at 25 °C.....	216
Figure 9.66: 162 MHz $^{31}\text{P}\{^1\text{H}\}$ NMR spectrum of Mn-7 in CD_3CN at 25 °C.	217
Figure 9.67 162 MHz temperature-dependent $^{31}\text{P}\{^1\text{H}\}$ NMR of Mn-7 in CD_3CN	217

Figure 9.68: ATR-IR spectrum of Mn-7	218
Figure 9.69: ^1H NMR spectrum of Mn-3 in C_6D_6 at 25 °C.	219
Figure 9.70: 162 MHz $^{31}\text{P}\{^1\text{H}\}$ NMR of Mn-3 in C_6D_6 at 25 °C.	220
Figure 9.71: ATR-IR spectrum of Mn-3	220
Figure 9.72: 400 MHz ^1H NMR spectrum of the attempted synthesis of Mn-1 in C_6D_6 at 25 °C.....	221
Figure 9.73: 152 MHz $^{31}\text{P}\{^1\text{H}\}$ NMR spectrum of the attempted synthesis of Mn-1 in C_6D_6 at 25 °C... 222	
Figure 9.74: 400 MHz ^1H NMR spectrum of Mn-5 in C_6D_6 at 25 °C.	223
Figure 9.75: $^{31}\text{P}\{^1\text{H}\}$ NMR spectrum of Mn-5 in C_6D_6 at 25 °C.....	224
Figure 9.76: ATR-IR spectrum of Mn-5	224
Figure 9.77: NMR of FA, BMIM-OAc and catalyst in DMSO- d_6	225
Figure 9.78: Variable temperature ^1H NMR spectrum of $\text{P}(\text{1-Ad})_3$ in THF- d_8	229
Figure 9.79: Variable temperature ^{13}C NMR spectrum of $\text{P}(\text{1-Ad})_3$ in THF- d_8	229
Figure 9.80: Variable temperature $^{31}\text{P}\{^1\text{H}\}$ spectrum of $\text{P}(\text{1-Ad})_3$ in THF- d_8	230
Figure 9.81: Variable temperature ^1H spectrum of BuPAd_2 in THF- d_8	230
Figure 9.82: Variable temperature ^{13}C spectrum of BuPAd_2 in THF- d_8	231
Figure 9.83: Variable temperature $^{31}\text{P}\{^1\text{H}\}$ spectrum of BuPAd_2 in THF- d_8	231
Figure 9.84: Downfield region of ^1H NMR spectrum of hydrogenation reaction.	233
Figure 9.85: 101 MHz ^{13}C NMR of hydrogenation reaction.	233

List of schemes

Scheme 1.1: Synthesis route to <i>i</i> Pr-xantphos via phosphination of 9,9-dimethylxanthene.	4
Scheme 1.2: Synthesis route to DiPrPEE via nucleophilic attack of diisopropyl phosphide on bis(2-chloroethyl)ether.	5
Scheme 1.3: Synthesis route to methylene-bridged xanthene-linked POP ligands.....	5
Scheme 1.4: P-substituent-dependent reactivity of POP pincer ligands according to GUSEV. ³⁹	8
Scheme 1.5: Transfer hydrogenation demonstrated by ESTERUELAS. ⁴¹	9
Scheme 2.1: Influence of precursor on binding mode.	14
Scheme 2.2: General synthesis of complexes Ru-1a to Ru-12a	16
Scheme 2.3: Chloride abstraction reaction applied to complexes Ru-1a to Ru-10a	24
Scheme 2.4: Observed reaction product of Ru-2a with NaBF ₄ in MeCN.....	26
Scheme 3.1: GUERBET-reaction to form 1-butanol from ethanol.....	36
Scheme 3.2: Possible side reactions during ethanol upgrading.	38
Scheme 3.3: Inner-sphere mechanism of ethanol dehydrogenation using a Ru-PNP pincer. ⁵¹	41
Scheme 3.4: Outer-sphere mechanism of ethanol dehydrogenation using an Mn-PNP pincer.	42
Scheme 3.5: First proposed catalytic cycle for ethanol dehydrogenation using [RuHCl(POP)(PPh ₃)] complexes.	51
Scheme 3.6: Second proposed catalytic cycle for ethanol dehydrogenation using [RuHCl(POP)(PPh ₃)] complexes.	52
Scheme 4.1: Formic acid as an LOHC.....	57
Scheme 4.2: Comparison between <i>N</i> -protonated and <i>N</i> -methylated PNP pincer complexes.	60
Scheme 4.3: Proposed inner-sphere catalytic cycle for FA dehydrogenation with a Ru-POP pincer complex.....	75
Scheme 5.1: Possible products of Ru(NO)Cl ₃ (H ₂ O) with a POP pincer ligand.....	80
Scheme 5.2: Proposed chloride abstraction using precipitation of insoluble halide salts.	85
Scheme 6.1: Redox reaction to form degraded Mn-3 in MeCN during crystallization attempt.	93
Scheme 7.1: Proposed catalytic cycle and thermal activation of Ru-MACHO-BH.	102

List of tables

Table 2.1: Important ^1H and ^{31}P chemical shifts and coupling constants in Ru-1a to Ru-11a	19
Table 2.2 : Important crystallographic parameters of complexes Ru-1a to Ru-11a	23
Table 2.3: Selected bond lengths, atom distances and angles of Ru-2b	27
Table 2.4: Selected bond lengths, atom distances and angles of Ru-7e	31
Table 3.1 : Physical properties of selected upgraded biofuels compared to gasoline and ethanol.	35
Table 5.1: Properties of linear and bent nitrosyl complexes.	78
Table 5.2: Selected bond lengths, atom distances and angles of Ru-NO-2	82
Table 6.1: Selected bond lengths, atom distances and angles of Mn-7	92
Table 7.1: Different phosphines and their behavior regarding the formation of CO_2 adducts in correlation to TEP.	100
Table 7.2: CO_2 hydrogenation experiments using phosphines as co-catalysts.	104
Table 9.1: Catalyst screening.	186
Table 9.2: Temperature and time screenings.	187
Table 9.3: Base screenings at $120\text{ }^\circ\text{C}$	188
Table 9.4: Temperature screening of $[\text{RuHCl}(\text{PPh}_3)_3]$ toluene adduct.	193
Table 9.5: ARRHENIUS plot data of FA dehydrogenation using $[\text{RuHCl}(\text{PPh}_3)_3]^*\text{toluene}$	194
Table 9.6: Screening of ruthenium catalysts for FA dehydrogenation.	195
Table 9.7: Temperature screening of Ru-1a	196
Table 9.8: ARRHENIUS plot data of FA dehydrogenation using Ru-1a	196
Table 9.9: Temperature screening of Ru-8a	198
Table 9.10: ARRHENIUS plot of FA dehydrogenation using Ru-8a	198
Table 9.11: Anion screening of Ru-8a-c	199
Table 9.12: Catalytic screening of manganese complexes.	226
Table 9.13: Hydrogenation experiments of Ru-MACHO and $\text{P}(\text{tmg})_3$	232

List of abbreviations and acronyms

1-Ad	1-Adamantyl
ABE	Acetone-butanol-ethanol
ATR	Attenuated total reflectance
a.u.	Arbitrary units
BDE	Bond dissociation energy
BEV	Battery-electric vehicle
BMIM-OAc	1-Butyl-3-methylimidazolium acetate
BuLi	Butyllithium
BuPAD ₂	Di(1-adamantyl)- <i>n</i> -butylphosphine
CCD	Charge-coupled device
CV	Cyclic voltammetry
Cy	Cyclohexyl
d	Doublet (NMR)
DBFphos	4,6-Bis(diphenylphosphino)dibenzofuran
DiPrPEE	bis[(2-diisopropylphosphino)ethyl]ether
DMF	Dimethylformamide
DMOA	<i>N,N</i> -dimethyloctylamine
DPEphos	[Oxydi(2,1-phenylene)]bis(diphenylphosphane)
DPPEE	bis[(2-diphenylphosphino)ethyl]ether
EA	Elemental analysis
Et ₂ O	Diethyl ether
EtOH	Ethanol
FA	Formic acid
FID	Flame ionization detector
GC	Gas chromatography
HMBC	Heteronuclear multiple bond coherence
HSAB	Hard and soft acids and bases
HSQC	Heteronuclear single quantum coherence
IAP	Imidazoline-2-ylidenamino substituted phosphine
ICE	Internal combustion engine
<i>i</i> Pr	Isopropyl

IR	Infrared
LOHC	Liquid organic hydrogen carrier
m	Multiplet (NMR)
MeCN	Acetonitrile
MLC	Metal-ligand-cooperation
MS	Mass spectrometry
Nixantphos	4,6-Bis(diphenylphosphino)-10 <i>H</i> -phenoxazine
NB <i>i</i> Pr	1,3-diisopropyl-benzimidazolin-2-ylidenamino
NHC	<i>N</i> -heterocyclic carbene
NMR	Nuclear Magnetic Resonance
N <i>i</i> Pr	1,3-diisopropyl-4,5-dimethylimidazolin-2-ylidenamino
ppm	Parts per million
q	Quartet (NMR)
s	Singlet (NMR)
SC-XRD	Single crystal X-ray diffractometry
SI	Spark-ignition
SILP	Supported ionic liquid-phase
t	Triplet (NMR)
<i>t</i> Bu	<i>tert</i> -Butyl
TEP	Tolman electronic parameter
TD	temperature-dependent (NMR)
THF	Tetrahydrofuran
TM	Transition metal
TMG, tmg	Tetramethylguanidine, tetramethylguanidyl
TMS	Tetramethylsilane
TOF	Turnover frequency
TON	Turnover number
VT	Variable temperature
Xantphos	(9,9-Dimethyl-9 <i>H</i> -xanthene-4,5-diyl)bis(diphenylphosphane)
XRD	X-ray diffractometry

1. General introduction

This first chapter of the thesis is meant to fulfil two purposes: First, it is meant to provide the reader with a general understanding of the history of POP pincer ligands and their binding properties, which play an important role in their catalytic activities. The second purpose is to outline the general motivation behind this work, which is to use the POP pincer complexes in various subfields of homogeneous catalysis in pursuit of catalytic conversions for the sustainability of energy storage. The main topics of this work will revolve around the chemistry of low valent coordination complexes of ruthenium(II) and manganese(I), their chemical and spectroscopic properties, and their activities in catalysis in the framework of the transition to sustainable energy sources. All compounds presented in this work will have a few common properties. First, they will all bear POP pincer ligands, with the goal of obtaining them in their three-coordinate meridional binding mode. Second, they will all have a set of three monodentate co-ligands, which means that they will all be obtained as d^6ML_6 complexes.

1.1 Pincer complexes

1.2.1 History and definition

From the simplest chlorido ligand to the most complex chiral phosphines for asymmetric hydrogenations in drug development, the choice of ligands has always been paramount for the successful application of organometallic chemistry. Due to their tuneability, the design and application of complexes bearing pincer ligands has become an important area of research recently. The term “pincer ligand” was first used by VAN KOTEN in 1989 to describe a tridentate NCN ligand utilized in a Ni(III) complex previously synthesized by the same workgroup.^{2,3} While originally referring to anionic tridentate ligands with a carbon atom as the central binding site, the modern definition has been broadened, and today, pincer ligands are typically understood as any tridentate ligands that bind in a meridional way.

Informal terminologies for the different parts of pincer ligands exist. They are listed in Figure 1.1. The first and arguably most important consists of the three atoms that coordinate to the metal center. Connecting them lies the organic backbone of the ligand, usually referred to as a “linker”, which itself contains the central “anchor”. The non-central coordinating atoms and organic substituents on them are usually referred to as the “wingtips” of the pincer ligand.

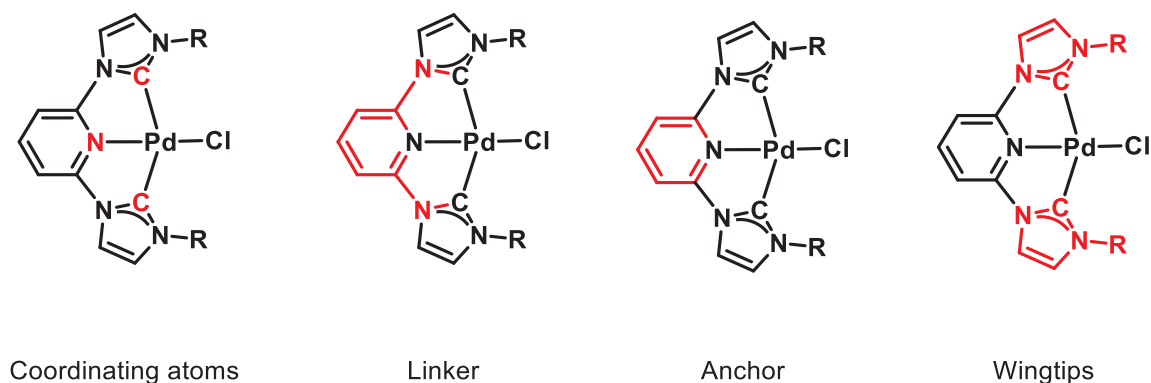


Figure 1.1: Pincer ligand nomenclature.

Example used: Pd-CNC pincer complex with two *N*-heterocyclic carbenes (NHCs) as wingtips.

The first example of a pincer complex was synthesized in 1976 by SHAW, more than a decade before the term was first mentioned.⁴ Their report also contains the first use of the now common acronym for pincers by abbreviating it as the list of metal-bound chelation sites in the sum formula of the complex, in this case “[NiCl(pcp)]”. While a narrow field of study in the beginning, the interest in pincer complexes has expanded significantly over the last five decades and they are now a common sight in homogeneous catalysis. A vast majority of complexes use nitrogen, oxygen, phosphorous, and carbon, in various combinations, as their metal binding sites, but more exotic main group elements have been investigated as well, including boron,⁵ silicon,⁶ arsenic,⁷ germanium,⁸ and the heavier chalcogenes sulphur,⁹ selenium,¹⁰ and tellurium.¹¹

A very common type of pincer ligand binds to a metal center through two phosphines that are connected by an ether bridge which contains the central binding oxygen atom. The standard naming convention refers to them as “POP pincers”. This work is solely dedicated to the investigation of POP pincer ligands and various of their complexes of ruthenium and manganese.

1.2.2 POP pincer ligands

The history of POP pincer complexes is strongly linked to efforts in improving hydroformylation reactions. The first Rh(I)-based hydroformylation catalysts, most notably those developed by OSBORN, EVANS, and WILKINSON, used monodentate phosphine ligands.¹² While reaching quantitative conversions with high activities, the regioselectivity between linear and branched hydroformylation products was suboptimal, with product ratios of only around 2.8:1. This necessitated reaction optimization. In 1992, CASEY reasoned that such selectivity could be improved by employing bidentate ligands.¹³ This would be accomplished by inducing the two phosphines into a diequatorial configuration, and would involve the

fine tuning of the P-M-P binding angle towards the metal, usually referred to as the “bite angle”. Natural bite angles of 120° , consistent with a diequatorial position in a trigonal bipyramidal complex, were shown to deliver optimal results in terms of selectivity. In 1995, KAMER and VAN LEEUWEN improved the concept by using ether linkers to link triphenylphosphine moieties together to form bidentate phosphine complexes with similar bite angles,¹⁴ using ligands which had been synthesized first in the same year by HAENEL.¹⁵ Specifically, they tested a set of five chelating phosphine ligands, all identical in their structure containing various interlinked 2,2'-bis(diphenylphosphino)-diphenyl ether moieties. They were named after the heterocyclic compound that forms their main structure, e.g. DBFphos from dibenzofuran and xantphos from 9,9-dimethylxanthene. An overview over their structures is shown in Figure 1.2.

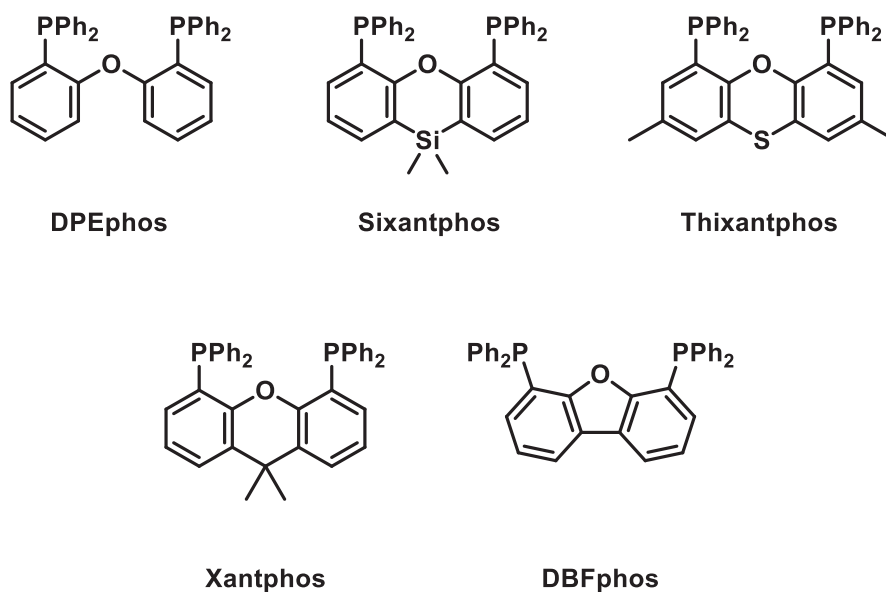
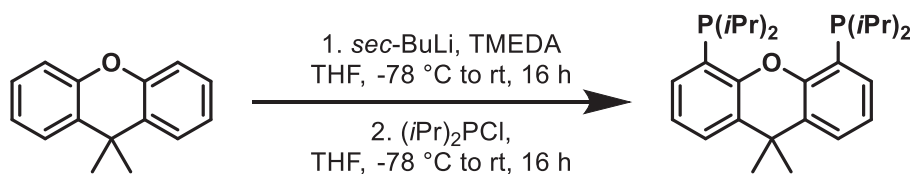


Figure 1.2: POP pincer ligands first used in hydroformylation by van Leeuwen in 1995.

Indeed, this approach proved successful, and the ratio of linear to branched products in hydroformylation improved immediately to about 54:1 under similar conditions. While later studies showed the influence of the bite angle on the reaction mechanism, specifically that of the ratio of diequatorial and equatorial-apical complex isomers, to be less straightforward than originally thought,¹⁶ VAN LEEUWEN's discovery sparked wide interest in this new group of phosphine ligands. Since then, modifications of this basic structure have allowed a large range of applications in catalysis and have unveiled some interesting novel reaction pathways previously unknown to literature.

The synthesis of this type of POP ligand is straightforward. The diaryl ether backbone is deprotonated and lithiated using organolithium compounds, typically *n*-BuLi or *sec*-BuLi. While the first published

synthesis route relied refluxing the precursor in heptane,¹⁵ today this is usually done in THF at -78 °C using TMEDA as an additive with subsequent warmup to room temperature. *Ortho*-dilithiation relative to oxygen has been found to be highly favoured and can be regarded as the only deprotonation site when no significant excess of base is used. The next step is a simple phosphination using the corresponding chlorophosphine.^{17,18} The synthesis route gives access to modified phenylphosphine moieties, as well as alkylphosphines such as ethyl, isopropyl, cyclohexyl and *tert*-butyl. A typical example is shown in Scheme 1.1.



Scheme 1.1: Synthesis route to *iPr*-xantphos via phosphination of 9,9-dimethylxanthene.

Based on this general synthetic strategy, xantphos-type POP ligands have been modified for several applications. These include, but are not limited to, the use of chiral phosphine moieties for various asymmetric catalytic reactions,^{19,20,21} chiral ligand backbone substituents for asymmetric catalysis,²² immobilization on several substrates by using the nitrogen linker on a phenoxazine backbone,^{23,24} and the attachment of anionic sulfonates on the backbone²⁵ or on the phosphine substituents²⁶ for improved water solubility in biphasic systems.

A related class of compounds bears a simple ethylene linker between the phosphines and the oxygen atom, shown in Figure 1.3. Due to the higher degree of freedom in the alkyl backbone, they are often more flexible and as their xantphos-type counterparts and the alkyl linker makes them slightly more electron-rich. Originally conceived as a means to circumvent metalation reactions in 1,5-bis(dialkylphosphino)pentane ligands which had been observed in rhodium complexes,²⁷ they were originally also primarily targeted as bidentate ligands for hydroformylation.

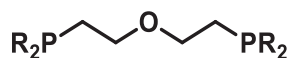
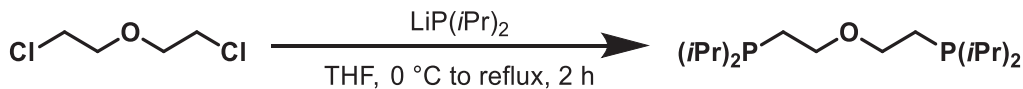


Figure 1.3: General structure of bis[(*PR*₂)ethyl]ether POP pincer ligands.

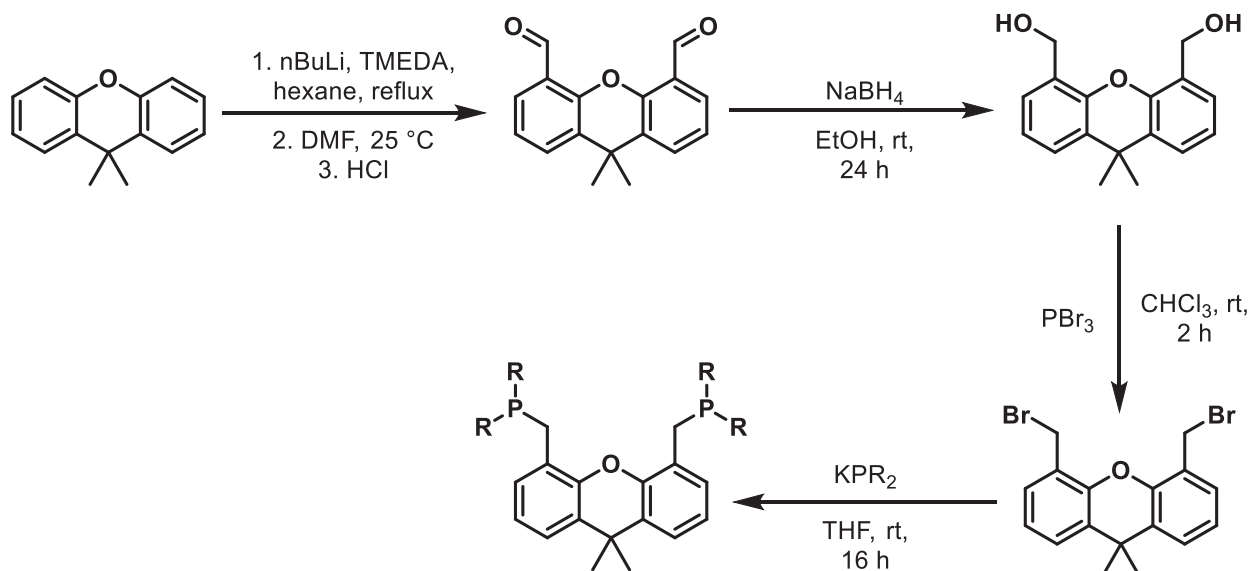
This class of POP pincers is synthesized by a nucleophilic substitution reaction, in which a dialkyl-, or diarylphosphide attacks the bis(2-chloroethyl) ether.²⁸ While commercially available, the phosphides are

instead often produced in situ by reduction of the chlorophosphines with lithium or potassium metal,²⁹ or alternatively by deprotonation of the dialkylphosphine.



Scheme 1.2: Synthesis route to DiPrPEE via nucleophilic attack of diisopropyl phosphide on bis(2-chloroethyl)ether.

Xanthene-based pincer ligands with longer, more flexible backbones are also known and have previously been used for the synthesis of gold(I) complexes³⁰ and for hydroformylation using rhodium complexes.³¹ Their syntheses start with the formylation of the corresponding ligand backbone at the *ortho* positions relative to the ether bridge by *ortho*-lithiation and addition of dimethyl formamide (DMF). This is then reduced to the alcohol using sodium borohydride, brominated with PBr₃, and finally phosphinated with the corresponding alkali metal phosphide salt.



Scheme 1.3: Synthesis route to methylene-bridged xanthene-linked POP ligands.

1.2.3 POP pincer complexes

POP pincer complexes can coordinate to metals in multiple different configurations. In many cases, the central oxygen atom binds well enough to ruthenium to make it possible to isolate the complex, but weakly enough to generate a vacant site for substrate coordination during a reaction. This behaviour, often referred to as hemilability, a term coined by JEFFREY and RAUCHFUSS,³² is caused by two factors: The first is the weak metal-oxygen bond, which can be explained by a mismatch between a soft late low-valent transition metal center and a hard oxygen ligand. Complexes containing POP pincer ligands can switch between two different binding modes within the same catalytic cycle and this has been invoked before to explain certain differences in reactivity in very similar POP ligands with only slight differences in backbone structure.³³ In comparison, PNP analogs are less hemilabile and bind stronger through the nitrogen atom, which corresponds to the amine's softer nature. The second explanation is their relatively flexible backbone, which allows for multiple geometries. The various binding modes of POP ligands can easily be differentiated by means of single-crystal X-ray diffraction (SC-XRD). Most compounds fall into one of four distinct groups, which cluster according to P-M-P bite angle and M-O distance,³⁴ summarized in Figure 1.4.

The most common group binds in a *cis*- κ^2 -P,P fashion through both phosphine atoms, with the oxygen atom not interacting with the metal center. This configuration leads to a very high metal-oxygen distance between 2.5 and 4 Å and P-M-P angles between 90 and 120°.

When an interaction between oxygen and the metal is observed, the complex binds in a facial κ^3 -P,O,P fashion. In this case, the M-O distance drops significantly to 2.0-2.5 Å, with P-M-P angles remaining identically low.

Increasing the P-M-P binding angle in bidentate complexes leads to the *trans*- κ^2 -P,P configuration. The missing interaction between the metal center and the oxygen atom leads to comparatively high M-O distances of 2.5-3.0 Å, and the *trans*-configuration of the chelating diphosphine causes P-M-P angles between 130 and 160°.

Finally, and most importantly for this work, the ligands can also bind in the *mer*- κ^3 -P,O,P configuration. This is the binding mode that classifies them as pincer ligands. These complexes are identified by their low M-O distance of 2.0-2.5 Å, while simultaneously showing very high P-M-P angles between 150 and 180°. The first example of this configuration was characterized and its structure studied by SC-XRD by ALCOCK in 1974 on a rhodium(I) center.³⁵

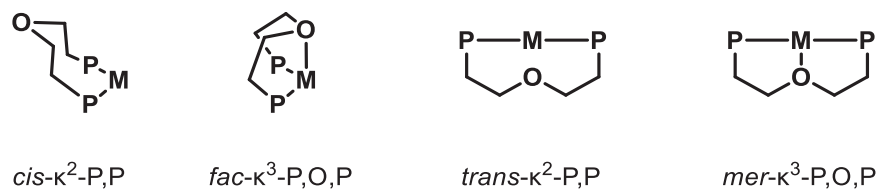


Figure 1.4: Typical binding modes of POP ligands.

The last one in this series, $mer-\kappa^3-P,O,P$, qualifies them as pincer ligands.

More exotic configurations have also previously been observed. POP pincers can occur as monodentate ligands (Figure 1.5A), binding through one of the phosphine atoms, with the other one being unbound. Fluxionality between tridentate and monodentate binding modes can be found within the same complex.³⁶ Additionally, their ditopic nature allows for bridging configurations, in which each ligand binds to two different metal centers through one phosphine each. They have been reported in gold³⁷ and cobalt³⁸ complexes (Figure 1.5B).

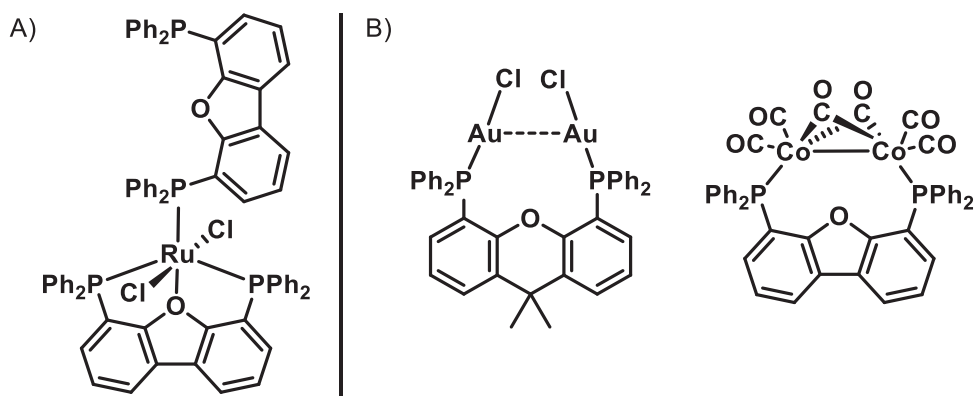


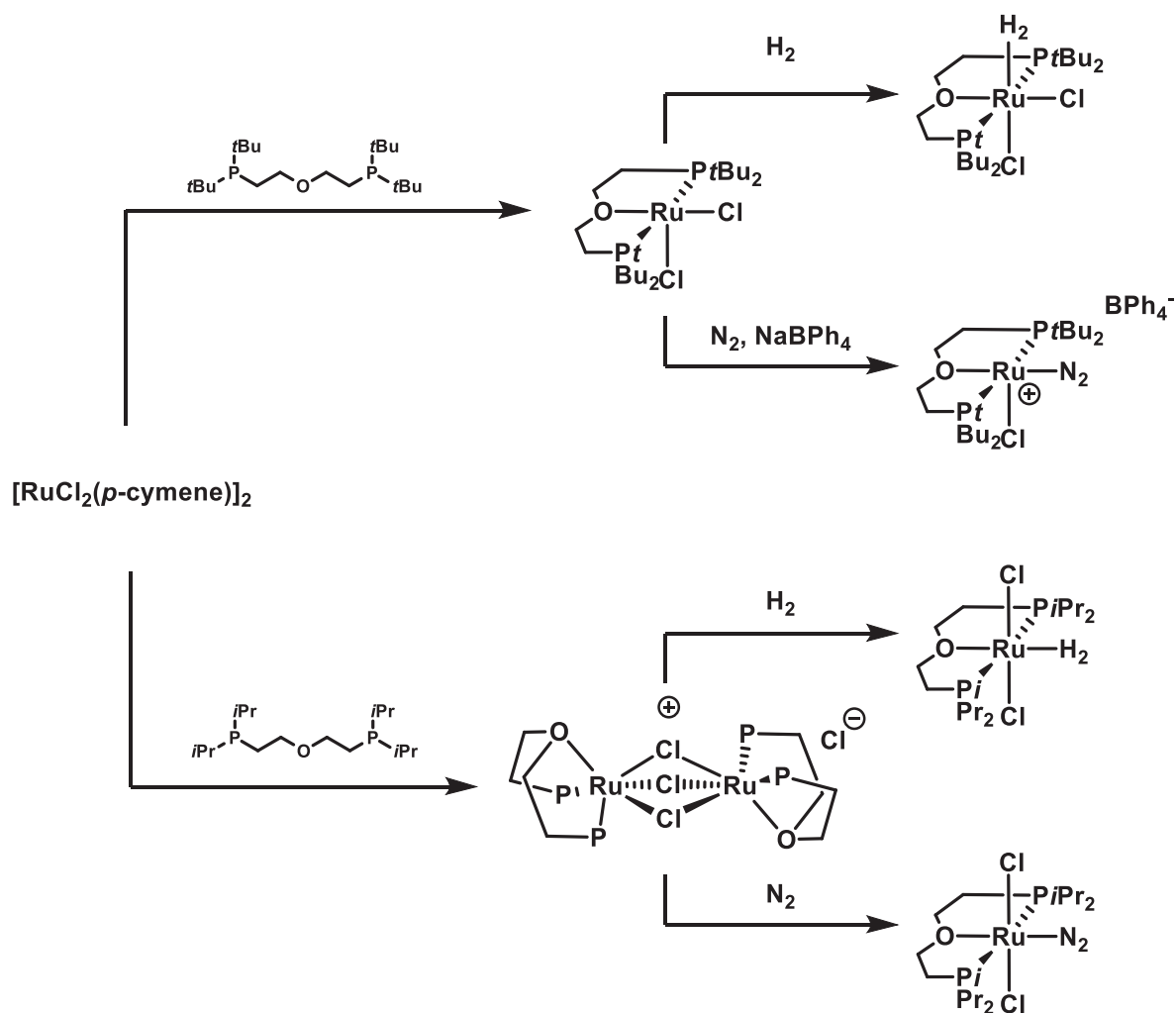
Figure 1.5: Examples of less common binding modes of POP pincer ligands.

A) Monodentate and tridentate DBFphos in the same complex

B) Bimetallic complexes of gold and cobalt with bridging POP ligands.

1.2.4 Ruthenium POP pincer complexes: History and reactivity

While still comparatively rare compared to PNP pincers, POP ligands have been used in various ruthenium complexes. First investigated by GUSEV in 2005 by reacting an ethylene bridged POP pincer complex with $[\text{RuCl}_2(\text{cymene})]_2$, complexes of the type $[\text{Ru}(\text{POP})\text{Cl}_2]$ were shown to obtain a tetragonal pyramidal structure with the ligands in the *mer*- κ^3 -P,O,P configuration, characterizing them as pincers (Scheme 1.4). They are stabilized by an agostic interaction between a terminal methyl group of the ligand and the ruthenium center.³⁹ This was highly dependent on the substituent at phosphorous, and the complexes could alternatively form a dimeric, cationic species with three bridging chlorido ligands and the POP ligand obtaining a facial binding mode. The authors also showed that such complexes readily react with N_2 and H_2 , forming the corresponding dihydrogen and dinitrogen complexes.

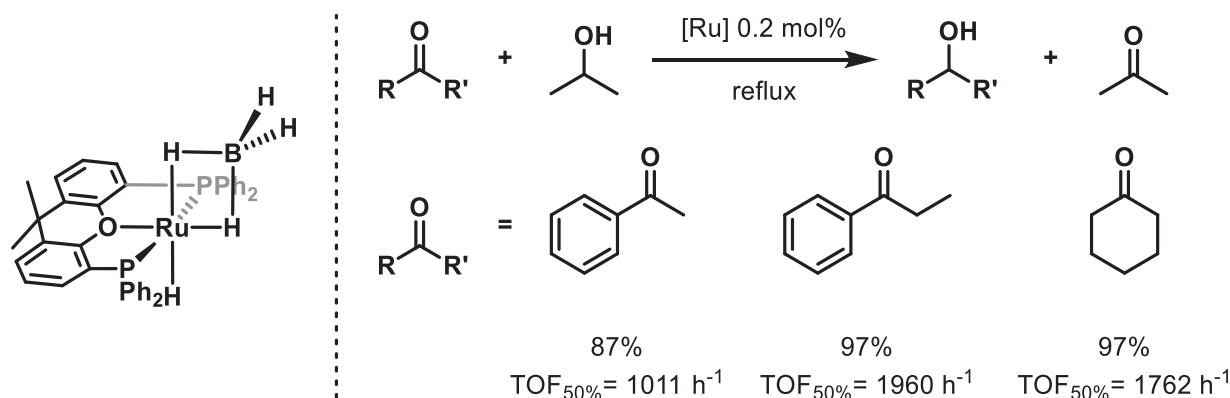


Scheme 1.4: P-substituent-dependent reactivity of POP pincer ligands according to GUSEV.³⁹

Substituents on P in the dimeric complex omitted for clarity.

Further investigation of this complex type was performed by WILLIAMS et al. in 2010.⁴⁰ This workgroup first synthesized ruthenium complexes of xantphos-type POP pincers with the general formula $[\text{Ru}(\text{POP})(\text{PPh}_3)\text{HCl}]$ and their reactivity in chloride abstraction reactions using silver salts. They synthesized the corresponding $[\text{Ru}(\text{POP})(\text{PPh}_3)(\text{H}_2\text{O})\text{H}]$ aqua complexes, in which the aqua ligand was found to be trans relative to hydrido, and observed reactions of these species with H_2 , N_2 and O_2 , the latter of which formed the corresponding peroxo complex.

Finally, in 2014, ESTERUELAS et al. used similar xantphos-type complexes for the first time in catalysis.⁴¹ Their dihydrido complex readily reacted with monoborane ammonia adduct to form the tetrahydridoborate complex, which was then successfully used for transfer hydrogenation experiments. Using isopropanol as a sacrificial agent and solvent, they reached high yields up to 97% and turnover frequencies of up to 1960 h^{-1} when reducing propiophenone, acetophenone and cyclohexanone to the corresponding alcohols. They speculated about the reaction pathway, likely involving an inner-sphere mechanism of ketone reduction, and thereby opened up a wide field of hydrogenation and dehydrogenation catalysis to be investigated.



Scheme 1.5: Transfer hydrogenation demonstrated by ESTERUELAS.⁴¹

1.3 POP and PNP pincer complexes compared

Comparing the catalytic activities of POP pincer complexes to their PNP counterparts is one of the main motivations behind this work. While PNPs have been used in several fields of catalysis for sustainable chemistry, particularly in hydrogenations and dehydrogenations of alcohols, aldehydes and ketones as sugar hydrogenations,⁴² similar complexes bearing POP pincers are currently comparatively unexplored. This is certainly due to the PNP's excellent properties due to their metal-ligand cooperation (MLC), enabling outer-sphere hydrogenation and dehydrogenation reactions with a plethora of substrates. Particularly ruthenium catalysts using MACHO-type ligands, first developed by KURIYAMA,^{43,44} have proven to be highly versatile and active.⁴⁵ One way of exploring the influence of MLC is to disable it on purpose and compare reactivity. Usually, this is done by methylating the nitrogen atom of the PNP pincer, in some cases severely reducing catalyst activity,⁴⁶ while in other cases increasing reactivity.⁴⁷ Compared the *N*-methylation, other deactivation methods are comparatively rare.

One simple way of removing the capability of the complexes to undergo MLC is to exchange the nitrogen atom in the center of the ligand backbone with a different atom, which is incapable of undergoing deprotonations. This work aims to explore this by exchanging the common PNP pincer ligands by POP pincers of the xantphos- and diethyl ether-types. The oxygen atom in the center of the ligand is incapable of MLC, and therefore comparisons to *N*-methylated and non-methylated PNP pincer complexes should yield interesting insight into the mechanisms of many catalytic cycles. It is important to note here that the hard-soft mismatch, and the resulting hemilability of the POP complexes also need to be taken into account when judging the catalytic activities. It could cause completely new reaction pathways in catalytic cycles that are unknown for PNP pincers.

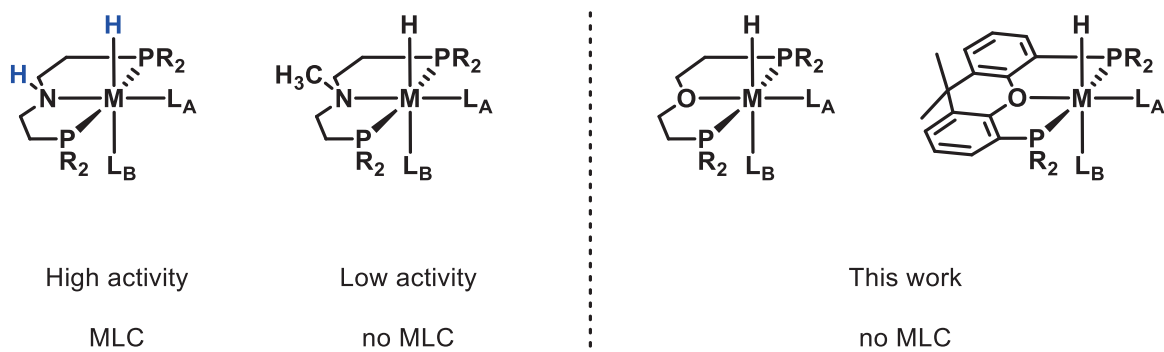


Figure 1.6: Deactivation of PNP pincer complexes by *N*-methylation and POP pincers as the central subject of this work.

The hydride ligand on the metal and a typical amine proton on the PNP pincer ligand capable of undergoing MLC are marked in blue.

2. Ruthenium POP pincer complex synthesis and analysis

The goal of the following chapter is the synthesis and spectroscopic characterization of two sets of organometallic complexes with the general formulae $[\text{Ru}(\text{POP})\text{PPh}_3\text{HCl}]$ and $[\text{Ru}(\text{POP})(\text{PPh}_3)\text{H}]\text{X}$, which will be investigated for their catalytic activities in the two following chapters of this thesis.

2.1 On the choice of POP ligands and precursors

To gain insight into the influence of POP ligand properties, a suitable set of ligands had to be chosen, differentiated in their bite angles, electronic properties at phosphorous, and flexibility. As a result, five different backbones were selected, and three different groups at P, phenyl, isopropyl and cyclohexyl, were chosen. The ligands are listed in Figure 2.1

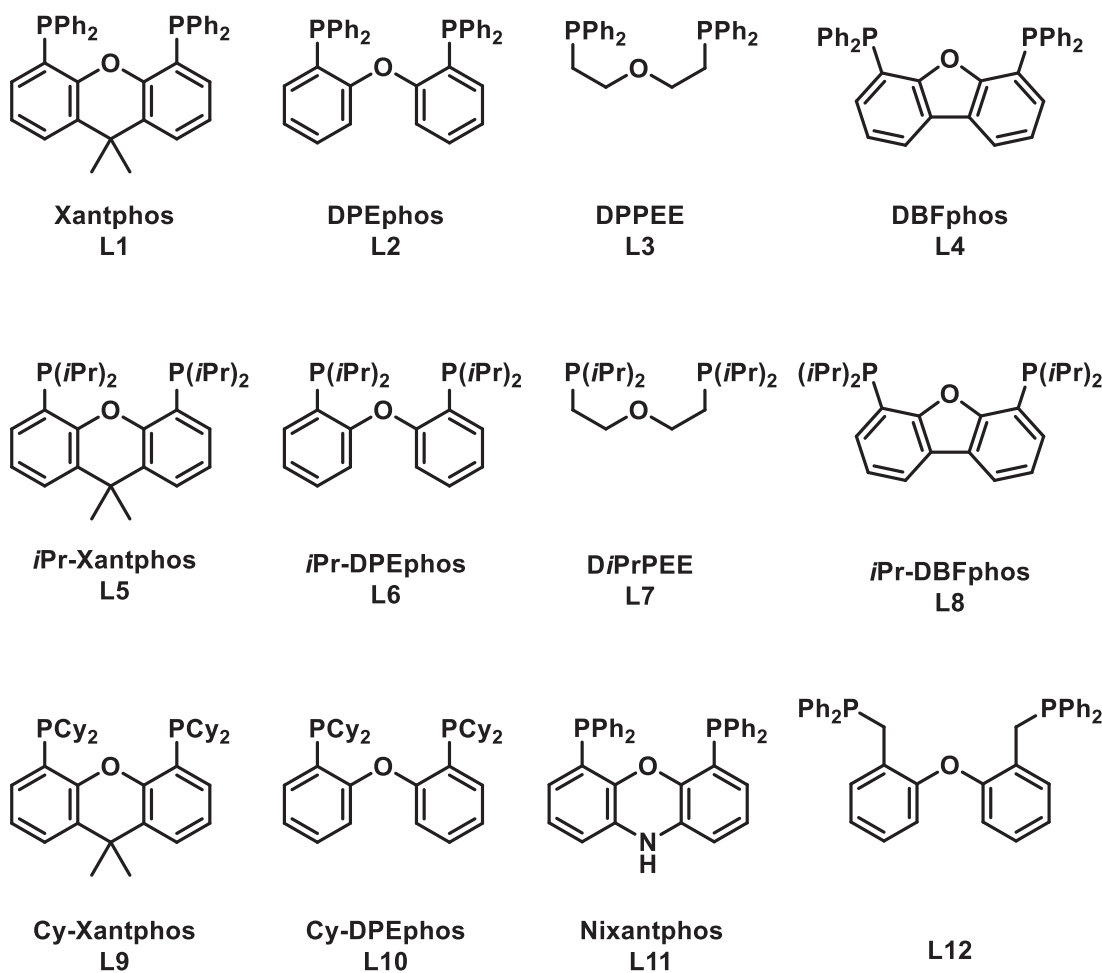


Figure 2.1: Overview over ligands L1-L12 chosen in this work.

This ligand set offers the opportunity to investigate reactivity dependence of ligand backbone flexibility, which is mainly dependent on the linkers between the central oxygen atom and the wingtip phosphine units. While the dibenzofurane (**L4**, **L8**) is very rigid and is not known to torque significantly out of plane,⁴⁸ the flexibility increases throughout this ligand series. The dimethyl xanthene moieties in the xantphos derivatives **L1**, **L5** and **L9** often show a boat-shaped central ring. Going further, the diphenyl ether backbone of **L2**, **L6** and **L10** is more flexible and can severely twist out of plane. This has been invoked before as the main reason for its increased performance over xantphos in a rhodium-catalyzed alkene hydroacylation.³³ The ethylene bridge of **L3** and **L7** is even more flexible than the previous ones, and complexes using this backbone are known to occur in all major four binding configurations shown earlier in Chapter 1.

Additionally, this dataset allows for the exploration of different electron densities on the ruthenium center. This tuneability has been explored before using monodentate phosphines in a wide variety of stoichiometric studies and catalytic transformations on various transition metals, including rhodium⁴⁹ and ruthenium.⁵⁰ The same modification can be performed on tridentate POP pincers, and therefore a variation in this parameter can give further insight into the catalytic properties of the complexes. While the ligands **L1**, **L2** and **L3** can be understood as two units of linked-together triphenylphosphine, their isopropyl, and cyclohexyl-substituted counterparts **L5**, **L6**, **L8**, **L9** and **L10** should resemble isopropylidiphenyl phosphine more in this regard. The ligands **L3** and **L4**, bearing a diethyl ether backbone, should even be more electron-dense to their counterparts.

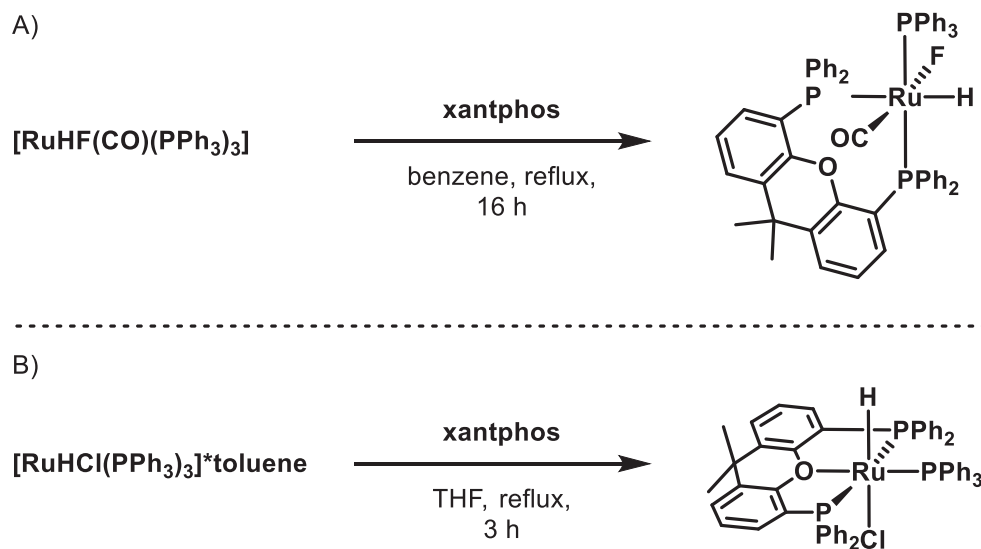
The ligand nixantphos (often also referred to as NiXantphos or *N*-Xantphos) **L11** was also included in this study. Its backbone has been used previously to immobilize active hydroformylation catalysts on dendrites and polymers,²³ and therefore would be a useful backbone for future industrial application. Additionally to its use in heterogenization, its amine proton could be envisioned as a site of metal-ligand cooperation.

Finally, a longer-chained POP ligand **L12**, previously synthesized by TSUI³¹ was also investigated. Its longer, more flexible linker could potentially facilitate complex reconfigurations, which have previously been invoked in PNP pincer complexes with similarly flexible backbones.⁵¹

Throughout the upcoming chapters, the complexes will be assigned numbers corresponding to the ligand numbers that were defined in Figure 2.1.

Of equal importance for this project is the choice of ligand precursor. It was decided to incorporate at least one hydrido ligand into the complex structure, as they play a significant role in catalyst activity. However, previous research shows that forcing a POP ligand into a *mer*- κ^3 -P,O,P configuration in Ru(II)

hydrido complexes is comparatively hard, and that they prefer to bind as *cis*- κ^2 -P,P chelates, especially when containing carbonyl ligands. For example, the addition of xantphos to the precursor $[\text{Ru}(\text{PPh}_3)_3(\text{CO})\text{HF}]$ reliably yielded $[\text{RuHF}(\text{xantphos})(\text{PPh}_3)(\text{CO})]$, in which xantphos bonded as a chelate.⁵² Therefore, it was decided to synthesize complexes of the general formula $[\text{RuHCl}(\text{POP})(\text{PPh}_3)]$ using the precursor $[\text{RuHCl}(\text{PPh}_3)_3]$ toluene adduct, which was shown to reliably produce pincer complexes when using xantphos-type and ethylene-linked POP pincer ligands.⁴⁰



Scheme 2.1: Influence of precursor on binding mode.

2.2 Results and discussion

2.2.1 Synthesis of $[\text{RuHCl}(\text{POP})(\text{PPh}_3)]$ complexes

To begin this project, the complexes **Ru-1a**, **Ru-2a**, and **Ru-3a**, which have previously been characterized in the literature,⁴⁰ were re-synthesized. Complex **Ru-5a** has been synthesized by a similar procedure,⁴¹ however the authors were unable to obtain crystalline material of the complex. Hence no crystal structure had been known of **Ru-5a** at the time of writing this work.

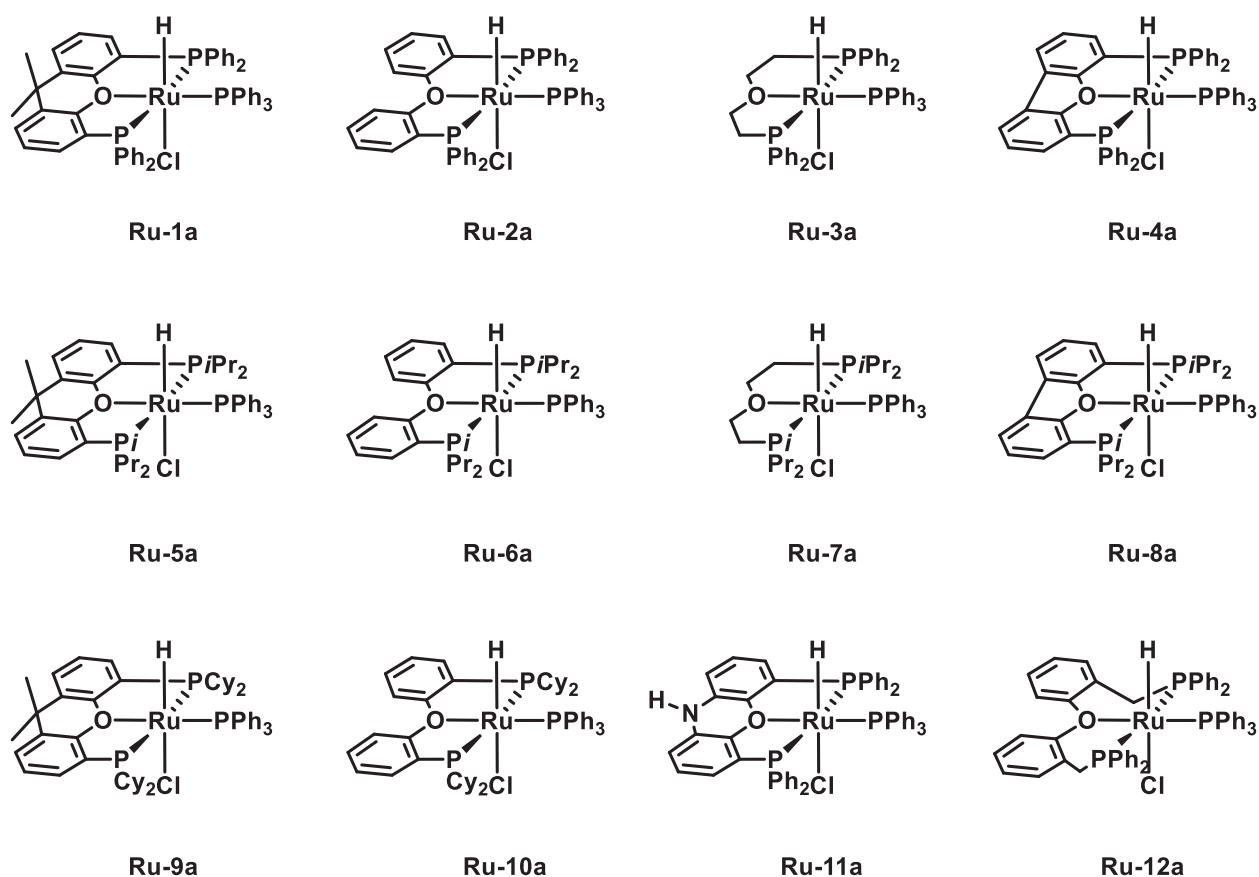
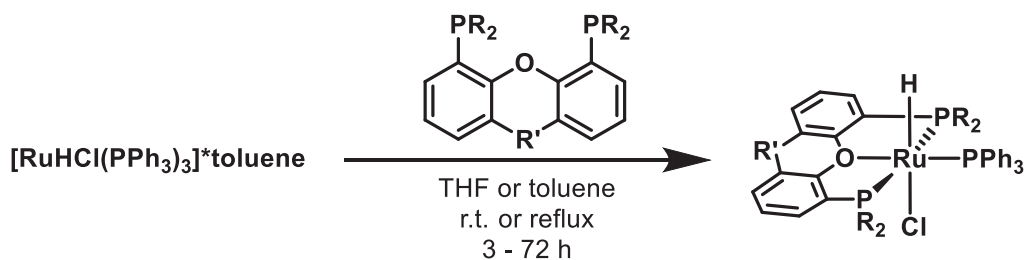


Figure 2.2: $[\text{RuHCl}(\text{POP})(\text{PPh}_3)]$ complexes **Ru-1a** to **Ru-12a** under investigation.

To synthesize the complexes **Ru-4a** to **Ru-11a**, the literature procedure previously used for the synthesis of the previously known **Ru-1a**, **Ru-2a** and **Ru-3a**⁴⁰ was adapted to the use of all available ligands. Starting from the precursor $[\text{RuHCl}(\text{PPh}_3)_3]$, specifically its toluene adduct, which was synthesized according to a procedure developed by WILKINSON,⁵³ the complexes are obtained by ligand addition, dissolution in THF or toluene, and stirring for prolonged periods of time at temperatures between ambient and refluxing. A general reaction overview can be found in Scheme 2.2. The reaction is accompanied by a strong colour change from the intense blackish purple of the dissolved precursor to yellow or orange once complete conversion is achieved. The phenyl derivatives **L1-L4** required high temperatures for complete conversion or alternatively very long reaction times of up to 72 hours at room temperature. In the case of **L4**, a switch from THF to toluene as solvent was required. Compared to this, the isopropyl derivatives **L5-L8** reacted readily at room temperature over the course of a maximum of six hours, with **L7** achieving complete colour change within 45 minutes. To ensure complete conversion, all reactions at room temperature were stirred for at least 3 hours after the colour of the solution had stabilized. After solvent removal in vacuo, freeze-drying from benzene was used to powderize the compounds when required.



Scheme 2.2: General synthesis of complexes **Ru-1a** to **Ru-12a**.

All complexes **Ru-1a** to **Ru-10a** obtained this way were insoluble in pentane, hexane, and diethyl ether, rendering purification by washing with these solvents feasible. Further purification was achieved via recrystallization by slow gas diffusion or layering. Detailed information can be found in Appendix C. All complexes were analyzed by NMR spectroscopy. ^1H NMR revealed the typical doublet of a triplet signal (often appearing as a quartet due to very similar $^2J_{\text{H-P}}$ coupling constants) in the far hydride region of the spectrum, at approximately -15.5 to -17.5 ppm relative to TMS. As an example, the hydride region of the ^1H -NMR spectrum of **Ru-8a** is shown in Figure 2.3A. In all cases, the $^2J_{\text{H-P}}$ coupling constants matched a configuration in which the hydride was located *cis* to all three phosphorous atoms. As expected, proton-decoupled $^{31}\text{P}\{^1\text{H}\}$ NMR revealed two signals, corresponding to the triphenyl phosphine ligand (triplet, near 75 ppm) and the phosphines of the POP ligand (doublet, between 40 and 60 ppm), shown in Figure 2.3B. The signal integrals correlated accordingly. $^2J_{\text{P-P}}$ coupling constants were found to be 25-32 Hz.

This confirmed the meridional configuration of the POP ligand (with both phosphorous atoms of the pincer being *cis*-configured relative to triphenyl phosphine).

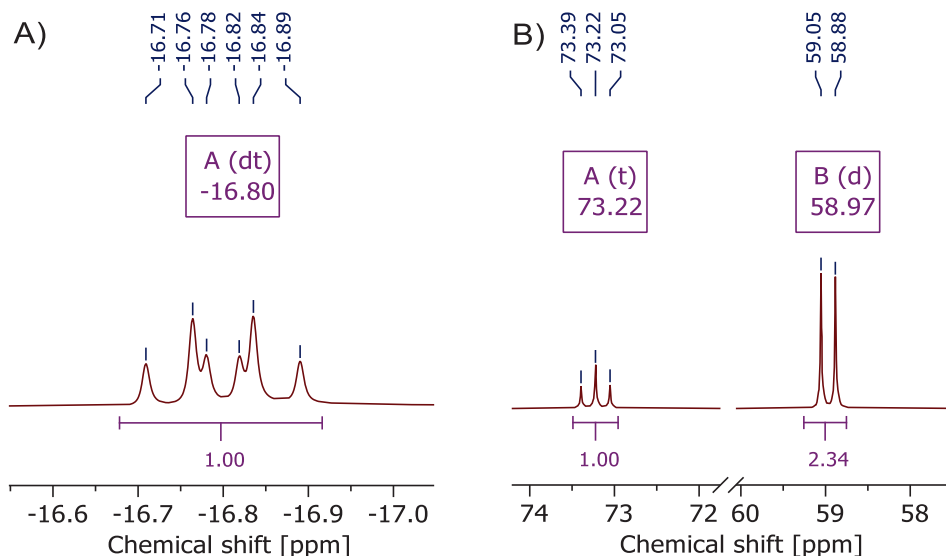


Figure 2.3: NMR spectra of **Ru-8a**.

A) Hydride region of ^1H NMR spectrum showing a dt signal for Ru-H.

B) $^{31}\text{P}\{^1\text{H}\}$ NMR spectrum, showing the signals for triphenyl phosphine (A) and the POP ligand (B).

Signals of the POP backbone were significantly broadened in ^1H and $^{31}\text{P}\{^1\text{H}\}$ spectra in the cases of **Ru-2a**, **Ru-6a** and **Ru-10a**, revealing a significant flexibility, or even fluxionality, of the DPEphos derived complexes. The aforementioned increased flexibility of DPEphos³³ is a possible explanation for this behaviour, causing the complexes to undergo fast exchange at room temperature. Variable-temperature $^{31}\text{P}\{^1\text{H}\}$ NMR was performed to investigate this behaviour in the case of **Ru-10a**, showing a clear temperature-dependence of the line broadening, which froze to a set of two doublets undergoing strong roofing effects at lower temperatures (see Figure 9.30 in Appendix C).

In the case of $[\text{RuHCl}(\text{nixantphos})(\text{PPh}_3)]$ **Ru-11a**, a different synthetic approach was required. When the previously established protocol was applied, the presumed product was obtained as a very insoluble, brown powder, which could not be dissolved in any hydrocarbons. Therefore, solvation was attempted in ethanol, methanol, diethyl ether, THF, DMF, DMSO, and chloroform. However, the solubility in DMSO merely sufficed to analyze the complex by means of ^1H NMR, which showed the presence of the typical doublet of a triplet in the hydride region. $^{31}\text{P}\{^1\text{H}\}$ NMR showed the two expected peaks, however, free PPh_3 was also found in significant quantities even after multiple cycles of washing with hexane. This

points to complex **Ru-11a** slowly decomposing in solution, and as a result, **Ru-11a** was excluded from all future experimentation in this project. No usable ^{13}C NMR spectrum could be obtained.

Finally, the synthesis of **Ru-12a** was attempted using the standard conditions. Already at room temperature, the reaction was accompanied by the typical colour change from the precursor's dark purple to bright yellow within 30 minutes. Removing the solvent, washing in hexane and drying in vacuo led to an off-white powder, which could be analyzed via NMR. The ^1H NMR showed four multiplets in the hydride region, which points either to the formation of multiple products, or to a single set of products undergoing slow exchange between multiple conformations. The latter case is certainly possible, and ligands of a similar linker have been observed to be highly flexible as discussed previously. In the ^{31}P NMR spectrum, a total of three peaks were found. The first, at 73.7 ppm, likely corresponds to the coordinated triphenylphosphine ligand. The other peaks around 55 and 41 ppm were found to be strongly roofed doublets. This effect is similar to the roofing peaks found in the spectra of **Ru-2a**, **Ru-6a** and **Ru-10a**. The integrals of all peaks correspond to a ratio of approximately 1:2, which would confirm the complex to bind the POP pincer and triphenylphosphine, albeit be significantly fluxional in solution.

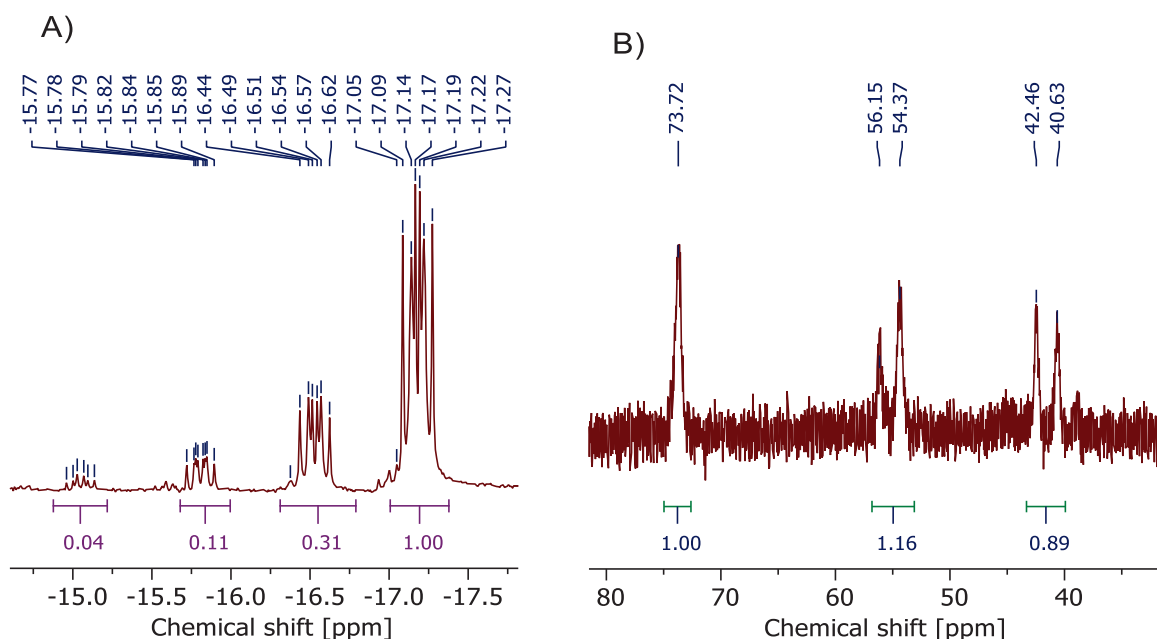


Figure 2.4: NMR spectra of crude **Ru-12a** in C_6D_6 at 25 °C.

A) Hydride region of ^1H NMR.

B) ^{31}P NMR spectrum, showing a roofing effect for the proposed peaks of the POP ligand.

2. Ruthenium POP pincer complex synthesis and analysis

Attempts at recrystallization were taken in multiple solvents (DMSO, THF, MeCN, Et₂O, toluene, benzene, hexane, and combinations thereof) but so far proved unsuccessful. As a result, this product could not be unequivocally confirmed, and it was decided to stop pursuing **Ru-12a** and concentrate the efforts on **Ru-1a** to **Ru-10a**.

In order to fully understand the catalytic activities of the complexes in relation to each other, trends can be derived from their NMR signals. The following table shows a selection of NMR datapoints taken of this set of catalysts:

Table 2.1: Important ¹H and ³¹P chemical shifts and coupling constants in **Ru-1a** to **Ru-11a**.

Complex	¹ H δ Hydride [ppm]	² J _{H-P} [Hz]	² J _{H-P} [Hz]	³¹ P δ POP [ppm]	² J _{P-P} [ppm] [*]
Ru-1a	-16.29	27.4	23.9	42.1	32.6
Ru-2a	-15.50	27.2	24.2	36 wide/roofed***	31.4
Ru-3a	-17.37	28.5	21.6	42.3**	32.3**
Ru-4a	-15.91	29.8	20.9	41.7	30.0
Average Ru-1a to Ru-4a	-16.27	28.2	22.7	42.0	31.6
Ru-5a	-16.66	27.3	24.3	52.3	31.6
Ru-6a	-16.40	29.6	21.5	48.4***	30.4
Ru-7a	-17.62	27.6	23.5	52.6	29.9
Ru-8a	-16.80	28.6	22	59.0	27.6
Average Ru-5a to Ru-8a	-16.87	28.3	22.8	54.6	29.9
Ru-9a	-16.70	25.0	25.0	44.2	28.3
Ru-10a	-16.68	32.0	20.0	41 wide/roofed***	30.6
Average Ru-9a to Ru-10a	-16.69	28.5	22.5	---	29.5
Ru-11a	-17.47	28.1	22.6	42.25	32.3

NMRs taken in C₆D₆ (Toluene-d₈ for **Ru-1a**, DMSO-d₆ for **Ru-11a**) at room temperature.

*Value taken from the average of both coupling phosphorous signals when possible.

** Value taken from literature; measured in CD₂Cl₂.⁵²

*** Data excluded from averages. Very wide broadening of the peaks made clear centering imprecise in **Ru-2a** and **Ru-10a**.

Several trends can be found. For once, the increased electron-density on the ruthenium center causes the chemical shift of the hydride peaks to move upfield. From an average -16.27 ppm in the phenyl-substituted complexes, this increases to -16.87 ppm for their isopropyl counterparts. The same is the case for the two cyclohexyl-substituted complexes **Ru-9a** and **Ru-10a** (-16.69 ppm for **Ru-9a** and **Ru-10a** compared to -15.90 ppm in **Ru-1a** and **Ru-2a** and -16.53 ppm in **Ru-5a** and **Ru-6a**). Secondly, the $^2J_{P-P}$ coupling constants decrease from the phenyl-derivatives (average 31.6 Hz) to the isopropyl counterparts (average 29.9 Hz). The same is the case for the two cyclohexyl complexes (average 29.5 Hz vs. 32.0 Hz in **Ru-1a** and **Ru-2a** and 31.0 Hz in **Ru-5a** and **Ru-6a**). The coupling constants in the DBFphos-derived **Ru-4a** and **Ru-5a** are the smallest within their respective groups, which is likely caused by central five-ring of DBFphos, causing comparatively long Ru-P bonds and therefore weaker interactions between the POP ligand and the PPh_3 moiety. Interestingly, the hydride chemical shifts and coupling constants in the nixantphos complex **Ru-11a** are very similar to those found in **Ru-3a**. This result might be skewed due to the need for DMSO as a solvent in case of **Ru-11a**. An illustration of these trends is shown below:

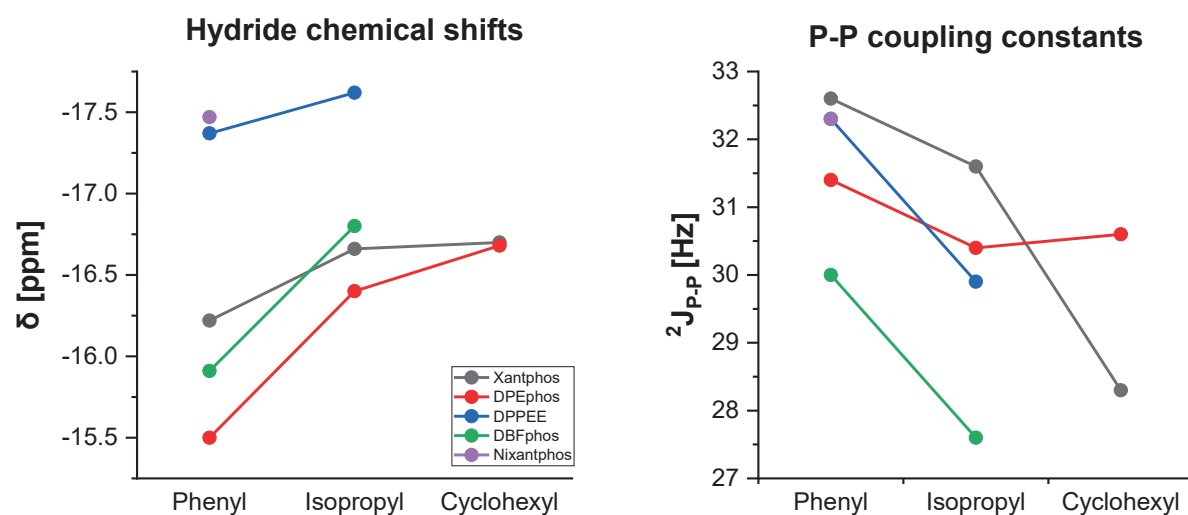


Figure 2.5: Hydride chemical shifts and P-P coupling constants in **Ru-1a** to **Ru-11a**.

The literature-unknown complexes (all except **Ru-1a**, **Ru-2a**, and **Ru-3a**) were further analyzed by SC-XRD. **Ru-4a** to **-8a** could be grown by layering or gas diffusion from toluene/hexane. **Ru-9a** crystallized directly after adding polybutene oil to a toluene solution of the complex. In all cases, the *mer*- κ^3 -P,O,P pincer configuration was confirmed. No complexes were found to crystallize as chelates or in other unpredicted configurations. An overview of their crystal structures is shown below in Figure 2.6, and a complete overview of all crystal structures and crystallographic details of the group can be found in Appendix C. While most complexes showed symmetrical ligand backbones, the DPEphos-derived **Ru-6a** and **Ru-10a** were both found to significantly twist their ligand backbones out of plane, crystallizing in chiral space groups. In the case of **Ru-6a**, crystals of both chiral configurations could be obtained, albeit in significantly different crystal qualities.

Ru-11a was previously obtained as a very insoluble powder, and any attempts at recrystallization had failed. So, to confirm its *mer*- κ^3 -P,O,P configuration, a small-scale crystallization experiment was performed in which **L11** and the precursor were dissolved in 0.5 mL THF each, filtered twice each to avoid any inclusion of possible nucleation sites, and very carefully layered on top of each other in an NMR tube with 0.5 mL of pure THF in between, which was then stored in a vibration-free environment. Very slow diffusion allowed for clean crystallization of **Ru-11a**, which was obtained as orange crystals and which co-crystallized with two THF molecules per complex. It crystallized in a monoclinic crystal system of the space group $P2_1/c$ and showed a slightly distorted octahedral geometry. Of great interest in **Ru-11a** was the geometric configuration of the amine group. Like in free Nixantphos,⁵⁴ the phenoxazine ring in **Ru-11a** is essentially planar and the CNC angle was found to be 119.73 °. This points to an sp^2 hybridization on the nitrogen atom. In the future, this might prove useful for metal-ligand cooperation in catalysis experiments due to the increased acidity of sp^2 -hybridized amines over sp^3 -hybridized amines, albeit with a long metal-nitrogen distance of 5.016 Å. Typical catalysts that rely on MLC are assumed to require a *cis*-configuration of the hydride ligand and the proton in the pincer ligand backbone. However, to the best of my knowledge, no MLC experiments have been undertaken using a catalyst with a geometric configuration comparable to that found in **Ru-11a**, and neither have they been reported with nixantphos complexes, which means that this area should be investigated in the future.

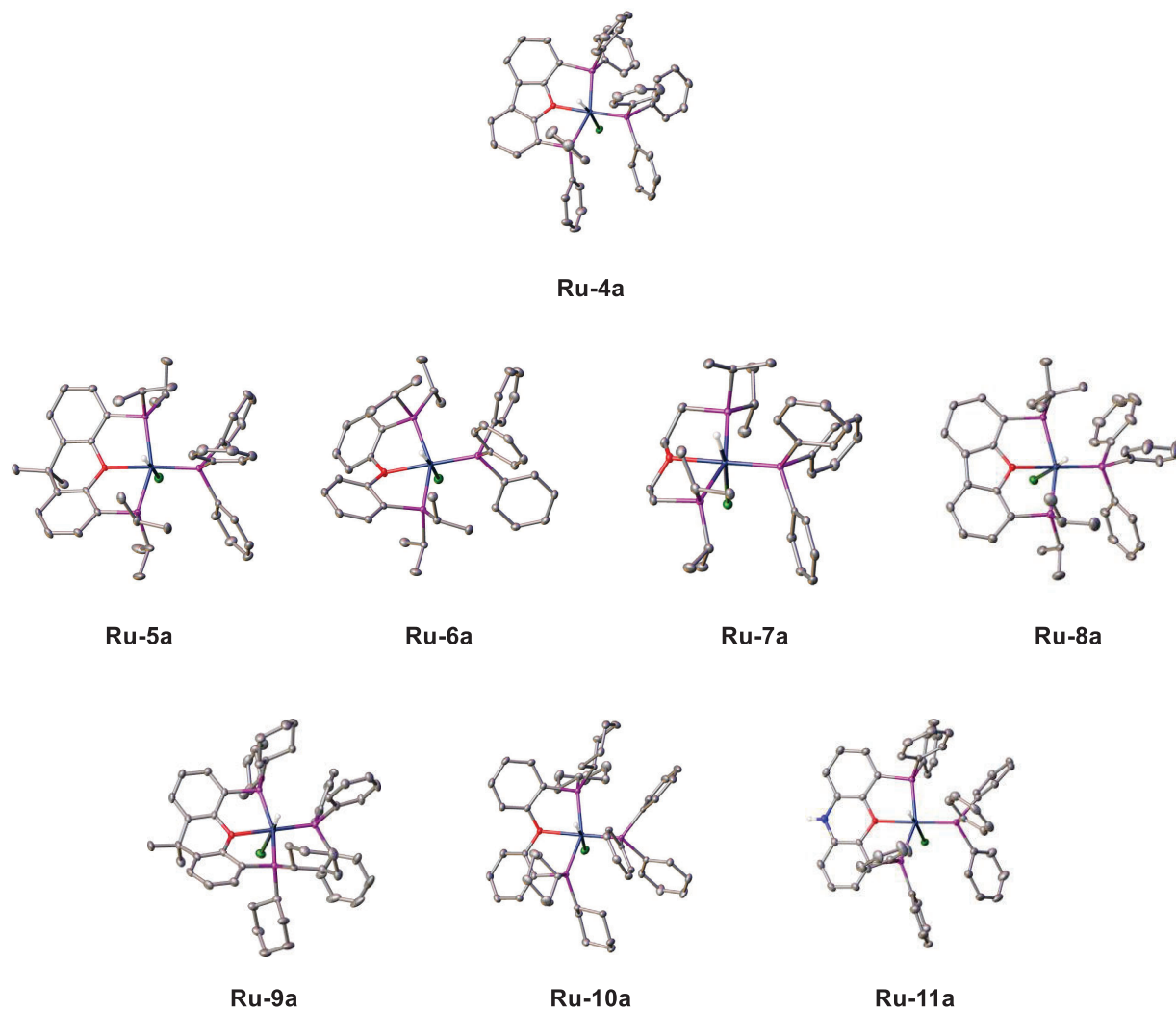


Figure 2.6: Overview of newly obtained crystal structures for **Ru-4a** to **Ru-11a**.

Hydrogen atoms on C and co-crystallized solvents omitted for clarity. Thermal ellipsoids are shown at 50% probability level.

In cases of two molecules crystallizing per unit cell, only one is shown.

2. Ruthenium POP pincer complex synthesis and analysis

Table 2.2 : Important crystallographic parameters of complexes **Ru-1a** to **Ru-11a**.

Complex	Distances [Å]				Angles [°]	
	Ru-P _{POP} **	Ru-P _{PPh₃}	Ru-Cl	Ru-O	P-Ru-P	P _{POP} -Ru-O**
Ru-1a*	2.305	2.228	2.520	2.251	156.393	80.155
Ru-2a*	2.312	2.227	2.512	2.248	156.523	79.57
Ru-3a*	2.323	2.229	2.519	2.278	158.32	80.02
Ru-4a	2.364	2.245	2.539	2.141	154.492	79.221
Ru-5a	2.322	2.235	2.558	2.255	153.512	80.930
Ru-6a	2.353	2.232	2.551	2.208	150.641	77.314
Ru-7a	2.332	2.222	2.557	2.226	155.210	80.178
Ru-8a***	2.393	2.225	2.562	2.100	153.84	78.053
Ru-9a	2.331	2.236	2.554	2.251	155.597	80.752
Ru-10a	2.352	2.228	2.540	2.244	153.268	78.077
Ru-11a	2.318	2.246	2.549	2.233	152.742	79.915

*Values taken from literature.⁴⁰

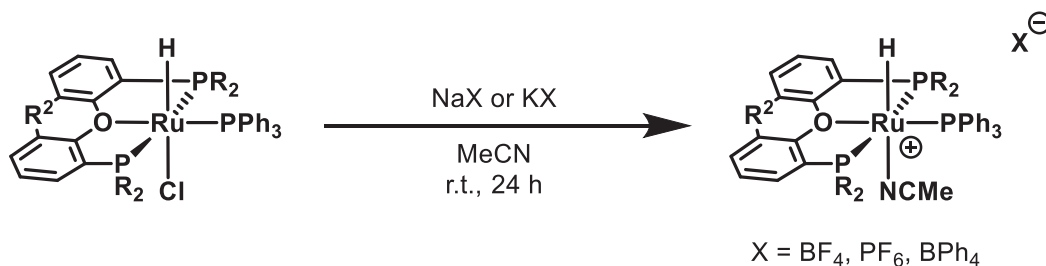
** Average between the two coordinating phosphines in the POP ligand.

*** Two molecules per unit cell, averages taken.

As was the case previously, a few trends in this setup become apparent. First, in all three cases, the xantphos-derivatives have the smallest average Ru-P bond length between the POP ligand and the metal center in their respective groups. The longest Ru-P_{POP} bond lengths are found in the DBFphos derivatives **Ru-4a** and **Ru-8a**. With all the other ligands constant, this is certainly a consequence of their backbone structure, with the two P-C bonds from the dibenzofuran moiety to the phosphines pointing slightly apart and is in agreement with the smaller ²J_{H-P} coupling constants in the DBFphos ligands discussed above. The Ru-O bond lengths show the opposite trends, with the DBFphos derivatives having a bond length that is in all cases more than 0.1 Å shorter than for the other complexes.

2.2.2 Chloride abstraction and influence of POP backbone on structure of corresponding cations

Since all complexes **Ru-1a** to **Ru-11a** contain a saturated d^6ML_6 18 electron ruthenium center, an activation to form the catalytically active species must occur first in a catalytic cycle. This occurs via a complex reconfiguration to generate a vacant coordination site. Multiple different pathways of this are conceivable. The most obvious ones are the abstraction of the chlorido or triphenylphosphine ligands followed by reactant association. The second option is a reconfiguration of the backbone to a κ^2 -P,P chelate configuration. While all of these are possible in situ, having an unsaturated complex already before dissolution eliminates the requirement for solvolysis. Therefore, it was decided to investigate the abstraction reactions of chloride by replacing it with only weakly binding anions such as tetrafluoroborate (BF_4^-), hexafluorophosphate (PF_6^-) and tetraphenylborate (BPh_4^-), depicted below.



Scheme 2.3: Chloride abstraction reaction applied to complexes **Ru-1a** to **Ru-10a**.

This reaction was first attempted in THF using the corresponding silver salts $AgBF_4$ and $AgPF_6$, but this proved unsuccessful, even when the reactions were performed under light exclusion. The same silver salts also did not produce clean products using other solvents such as toluene and benzene. When the sodium or potassium salts were utilized and the solvent was replaced by MeCN, the reaction yielded pure products over 24 hours. Using THF as a solvent did not yield any successful reactions even when using the sodium and potassium salts. The reaction was accompanied by slight colour loss, changing from lemon yellow to pale yellow, and by precipitation of NaCl and KCl. This general approach worked well for complexes **Ru-1b**, **Ru-3b** to **Ru-8b**, and **Ru-10b**. The products were herein only analyzed via SC-XRD to confirm their structures. A complete overview over their crystal data can be found in Appendix C.

2. Ruthenium POP pincer complex synthesis and analysis

Unfortunately, this dataset is currently incomplete. No crystallization effort was yet successful for **Ru-9b**. It is possible that other crystallization conditions will be needed.

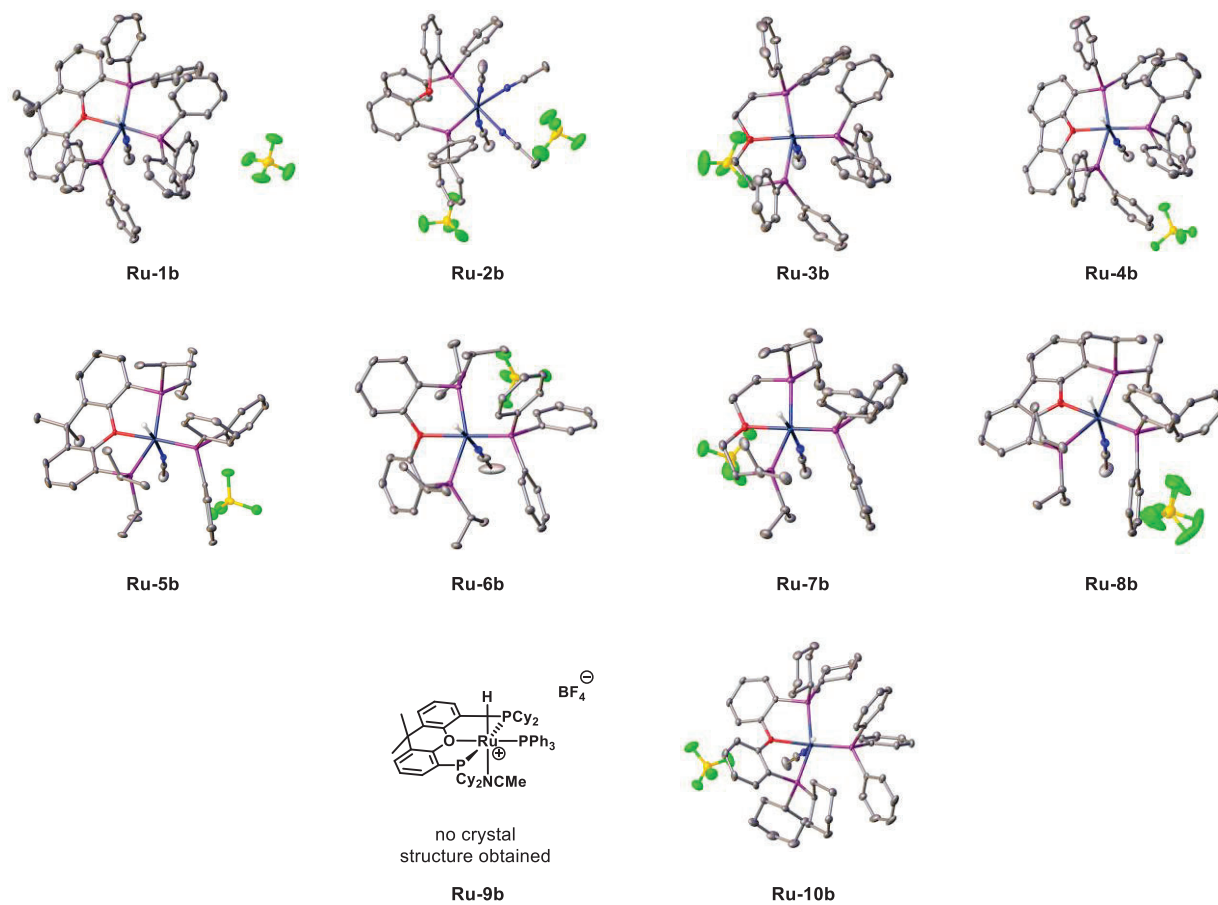
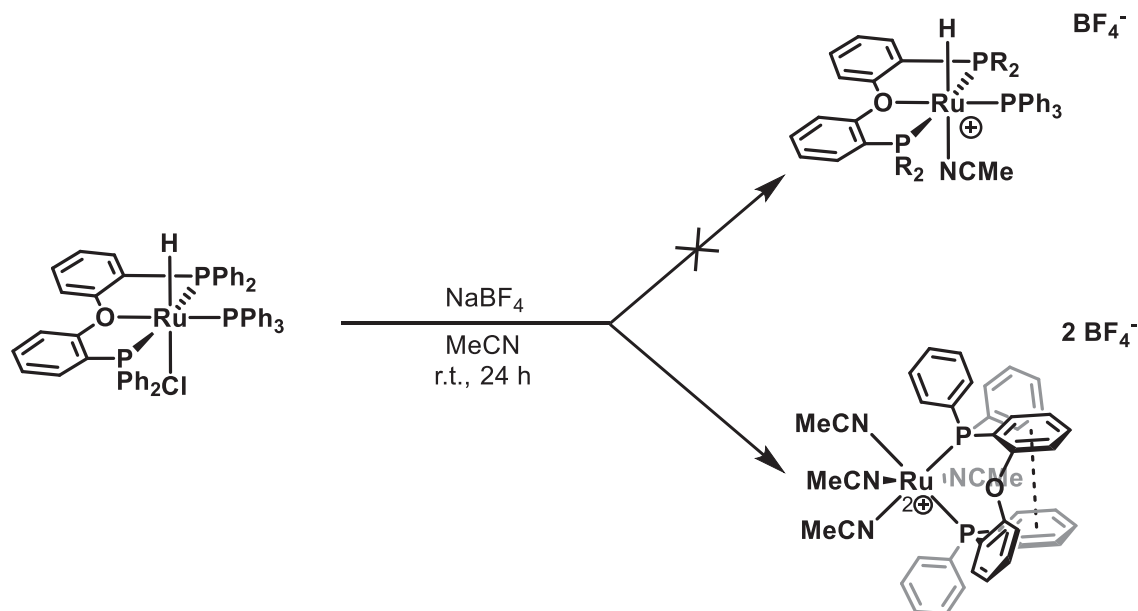


Figure 2.7: Overview of newly obtained crystal structures for **Ru-1b** to **Ru-10b**.

Hydrogen atoms on C and co-crystallized solvents omitted for clarity. Thermal ellipsoids are shown at 50% probability level.

In cases of two molecules crystallizing per unit cell, only one is shown.

Curiously, the reaction towards **Ru-2b** did not yield the desired product. Instead, the reaction product showed a different solubility and was, unlike the others, completely colourless. It was therefore analyzed by SC-XRD, which revealed the alternative reaction path (Scheme 1.2): Instead of the POP pincer complex, the ligand had instead transformed into a κ^2 -P,P-chelate. While the chlorido ligand had been abstracted as planned, the same occurred for the hydrido and triphenylphosphine ligands, yielding a complex of the sum formula $[\text{Ru}(\text{POP})(\text{MeCN})_4](\text{BF}_4)_2$. The complex crystallized in a monoclinic crystal system of the space group $\text{P}2_1/\text{n}$ and showed a slightly distorted octahedral geometry. Important bond lengths and angles are listed in Table 2.3.



Scheme 2.4: Observed reaction product of **Ru-2a** with NaBF_4 in MeCN.

Its crystal structure (Figure 2.8) clearly revealed a severe twisting of the diphenyl ether linker out of plane, in which one of the bridging phenyl groups of the POP backbone π -stacks with one of the non-bridging phenyls of the other phosphine. The planes of the phenyl groups are not completely coplanar with an angle between the planes of 28° and they have a distance of approximately 3.36 \AA (centroid of one ring towards the closest carbon of the other ring). This corresponds well to the layer distance of 3.35 \AA found in graphite.⁵⁵ In graphite, the stacking layers are also shifted towards one another, with the centroid of one plane stacking directly on the carbon atom of the next. All of this suggests that the energy gain from π -stacking is enough to overcome the Ru-O binding energy. For catalytic applications, this could suggest an activity of complexes bearing the ligand DPEphos **L2** unlike that for the other ligands of the set. The hydride abstraction mechanism is as of yet unclear and will be subject to further investigation going forward.

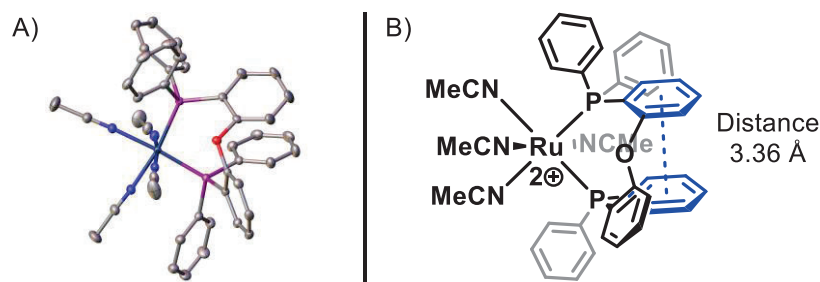


Figure 2.8: Reaction product of **Ru-2a** with NaBF₄ in MeCN.

Sum formula [Ru(dpephos)(MeCN)₄](BF₄)₂; 2×BF₄[−] omitted for clarity

A) Crystal structure. Hydrogen atoms on C omitted for clarity. Thermal ellipsoids shown at 50% probability level.

B) Illustration of the complex. Planes of stacking phenyl groups are marked in blue. Counterions omitted for clarity.

Table 2.3: Selected bond lengths, atom distances and angles of **Ru-2b**.

Ru-2b						
Atom	Atom	Distance [Å]	Atom	Atom	Atom	Angle [°]
Ru	P1	2.3282(5)	P1	Ru	P2	96.908(19)
Ru	P2	2.3458(5)	N3	Ru	N4	172.16(7)
Ru	N1	2.0983(19)				
Ru	N2	2.0893(19)				
Ru	N3	2.0344(19)				
Ru	N4	2.0182(19)				

To test if the chloride abstraction was dependent on the counteranion, the same reactions were tested for the counterions PF_6^- and BPh_4^- using complex **Ru-7a**. The reaction worked equally well, giving the products **Ru-7c** and **Ru-7d** in high yields.

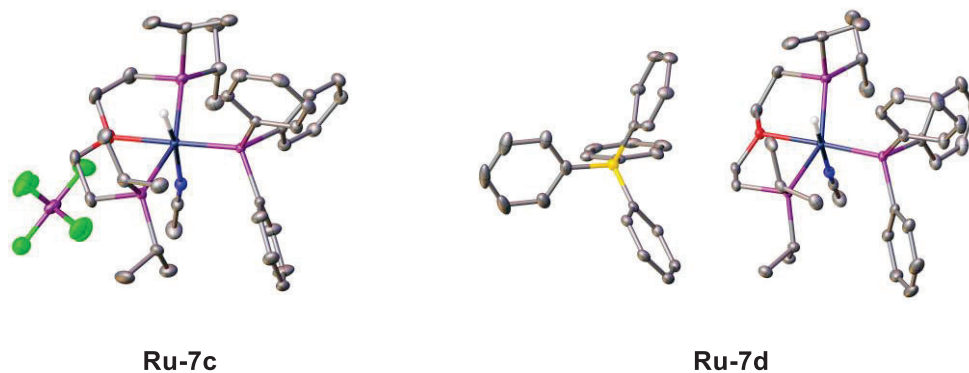


Figure 2.9: Crystal structures of **Ru-7c** and **Ru-7d**.

Hydrogen atoms on C and co-crystallized solvents omitted for clarity. Thermal ellipsoids are shown at 50% probability level.

In cases of two molecules crystallizing per unit cell, only one is shown.

2.2.3 Syntheses of azido complexes

Azido complexes of ruthenium(II) complexes are relatively rare, and only two examples of an N_3 ligand binding trans to the hydride have been described as of yet. The first was described by MAŁECKI containing two triphenylphosphine, one 4-pyrrolidinopyridine and a CO co-ligand.⁵⁶ The second example was synthesized in this workgroup by PhD student MIKE S. B. JØRGENSEN (now postdoc in the same group), and contained a *i*Pr-MACHO type PNP pincer ligand in a meridional configuration, thereby being the first example of a pincer complex with this configuration.⁵⁷ They are listed in Figure 2.10A. The POP counterpart of this (albeit with PPh_3 instead of CO) is therefore synthetically interesting and was the primary focus of this subchapter. It was chosen to attempt the ligand exchange from chloride to a corresponding azido complex using **Ru-7a**.

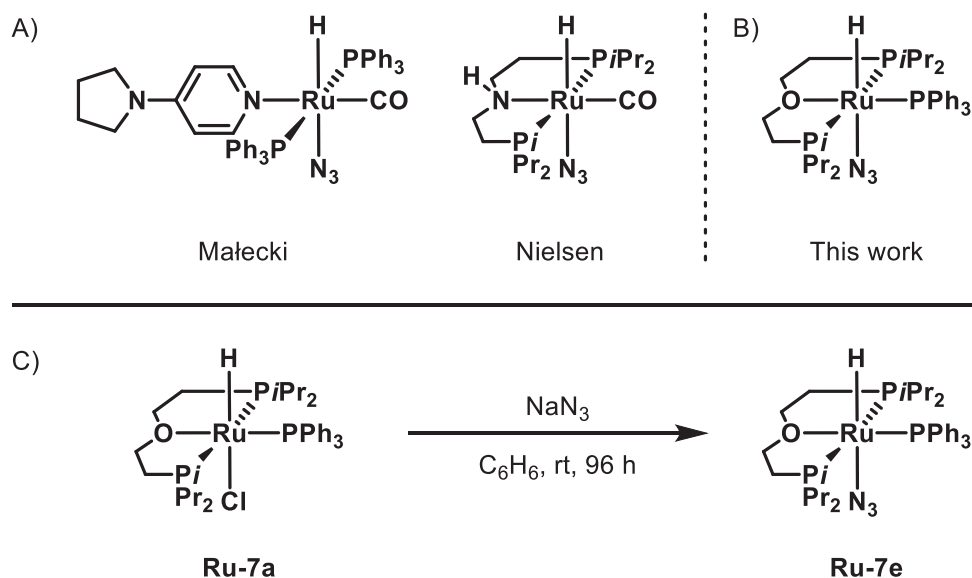


Figure 2.10 Ruthenium(II) hydrido azido complexes.

A) Previously described examples.

B) Synthetic goal of this subchapter.

C) Synthetic route towards **Ru-7e**.

Using the slight solubility of sodium azide in benzene, chloride abstraction could be forced even at room temperature to obtain the complex. To achieve complete conversion at room temperature, the reaction needed to be stirred for 96 hours, shorter reaction times showed mixtures of product and starting material. The complex was analyzed by means of ^1H , ^{13}C , ^{31}P NMR spectroscopy. Compared to **Ru-7a**, the hydride of **Ru-7e** signal was slightly shifted from -17.62 ppm to -17.49 ppm. To investigate the azido ligand, a

$^{15}\text{N}/^1\text{H}$ HMBC experiment was performed (Appendix C, Figure 9.39). The coupling could be detected and provided a ^{15}N chemical shift value of 50.04 ppm for what is likely the nitrogen atom bonded to ruthenium. A second ^{15}N signal coupling to hydride could barely be detected at 259.89 ppm. It is reasonable to assume that this corresponds to the central nitrogen atom of the azido ligand, and that the low signal intensity is due to the weaker three-bond coupling. A third signal, which would correspond to the terminal nitrogen atom, could not be detected. The IR spectrum revealed a strong band at 2043 cm^{-1} , corresponding to the N_3 stretching, significantly lower than free azide at 2140 cm^{-1} (measured as sodium azide),⁵⁸ but similar to the two stretching frequencies of 2057 and 2027 cm^{-1} found on the PNP counterpart.⁵⁷ This falls within the range of N_3 stretching bands previously observed on Ru(II) complexes.^{59,60,61} The Ru-H stretching band could not be clearly determined.

The complex was further analyzed by means of SC-XRD. Suitable crystals could be grown by dissolving in benzene and layering with hexane at room temperature. It was found to crystallize with the ligand in a meridional $\kappa^3\text{-P,O,P}$ binding mode, confirming it as a pincer structure. The complex crystallized in a monoclinic crystal system of the space group $\text{P}2_1/\text{c}$ and showed a slightly distorted octahedral geometry. Important bond lengths and angles are listed in Table 2.4.

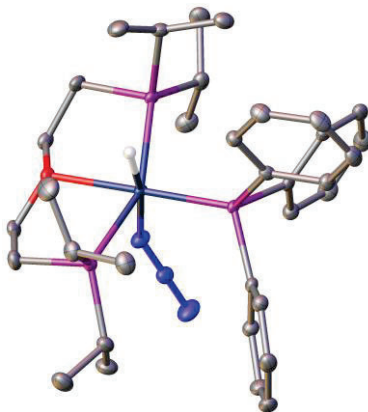


Figure 2.11: Crystal structure of **Ru-7e**.

Hydrogen atoms on C omitted for clarity. Thermal ellipsoids are shown at 50% probability level.

2. Ruthenium POP pincer complex synthesis and analysis

With a Ru-N₃ bond length of 2.245 Å and a Ru-N-N angle of 144.88°, the azido ligand showed a very similar geometry to the PNP counterpart synthesized previously. It is 0.04 Å longer than the Ru-N₃ bond in MAŁECKI'S complex. Its Ru-O bond to the pincer is 0.07 Å longer than the corresponding Ru-N bond in the previously synthesized PNP pincer.⁵⁷ This significant difference is likely caused by the stronger π -acidity of the carbonyl group *trans* to the amino ligand on the PNP pincer complex.

Table 2.4: Selected bond lengths, atom distances and angles of **Ru-7e**.

Ru-7e						
Atom	Atom	Distance [Å]	Atom	Atom	Atom	Angle [°]
Ru	P1	2.3403(5)	P1	Ru	P2	154.650(19)
Ru	P2	2.3340(5)	P3	Ru	O	177.81(3)
Ru	P3	2.2284(5)	H	Ru	N1	170.43
Ru	O	2.2597(10)	Ru	N1	N2	144.88(11)
Ru	N1	2.2245(13)	N1	N2	N3	178.97(16)
N1	N2	1.1796(19)				
N2	N3	1.172(2)				

The same reaction was attempted for **Ru-3a**. At room temperature, no reaction towards the azido complex could be observed after 72 h as evident by a missing N₃ stretching IR band in the expected region around 2100 cm⁻¹.

2.3 Conclusions and outlook

In summary, three sets of catalysts of the general formula $[\text{Ru}(\text{POP})(\text{PPh}_3)\text{HCl}]$, totaling 11 complexes, were synthesized, with five different ligand backbones and three types of phosphine substituents. Their properties were investigated by multiple spectroscopic techniques, mainly NMR of the ^1H , ^{13}C and ^{31}P nuclei and EA, and their structures were determined by SC-XRD, confirming the previously proposed configuration of **Ru-5a**.⁴¹ This set of complex provides a good basis for the catalytic transformations performed in the upcoming chapters, allowing for reaction screening dependent on ligand backbone configuration and electron density of the phosphines.

Chloride abstraction reactions were performed using sodium and potassium salts, revealing a novel pathway of hydride abstraction in the case of **Ru-2a** towards a $\kappa^2\text{-P,P}$ chelate configuration with a π -stacked backbone. The investigation of its mechanism for hydride abstraction has so far not been a particular focus of this work, but a future evaluation of this behaviour and its relation towards the structure of the POP pincer backbone is warranted from a fundamental standpoint.

Finally, a novel azido complex was synthesized by direct chloride abstraction, preserving the hydride functionality of the complex. ^1H - ^{15}N -HMBC was used to investigate chemical shifts of the azido ligand. To my knowledge, this complex represents the first published example of a Ru(II) POP pincer complex with an azido ligand in *trans*-position to a hydride. From a fundamental point of view, the synthesized azido complex could open up synthetic pathways to amido complexes, for example by means of intramolecular STAUDINGER reactions or by demobilizing the complex by formation of triazoloto complexes.^{60,62}

3. Ethanol upgrading using Ru-POP pincer complexes

3.1 Biofuels as a future energy storage system

3.1.1 The need for efficient biofuels

One of the major challenges for chemists in the 21st century is the development of efficient biofuels. As fossil fuel prices,⁶³ global temperatures,⁶⁴ and atmospheric CO₂ contents rise,⁶⁵ a practical solution must be found for personal transport as well as cargo shipping on land and in the air. Since automobiles have an average lifetime between one to two decades,⁶⁶ being able to use existing internal combustion engine (ICE) technology and vehicle stock with a carbon-neutral fuel without major retrofitting would greatly help the fight against a changing climate. While battery-powered vehicles will certainly be a large part of a solution due to their high well-to-wheel efficiency,⁶⁷ some applications will continue to require liquid fuels even after a complete switch from ICE cars to battery electric vehicles (BEVs). The high energy density of liquid fuels will be required for the aviation industry, cargo shipping, cargo transport on roads, as well as any type of operation not allowing for connectivity to the electric grid.

In order to achieve the goal of a CO₂ neutral economy with the help of carbon-neutral liquid biofuels, both a good carbon source from renewable materials, as well as an efficient catalytic system for upgrading to the desired product or products need to be developed.

3.1.2 Ethanol as a biofuel

As ethanol can be easily achieved by means of biomass fermentation, it is one of the best candidates for a C₂ building block for sustainable industrial chemistry, and also an obvious liquid biofuel. It can be fermented from food crops such as sugar cane,⁶⁸ sugar beet,⁶⁹ potatoes,⁷⁰ and corn.⁷¹ Since all of these examples are food crops and in competition with food supply, alternatives such as fermentation from cellulosic biomass such as agricultural waste are under investigation as well.⁷² With a very high research octane number (RON) of around 109-130,^{73,74} greatly exceeding that of common gasoline blends (usually between 95 and 100), ethanol offers good combustion properties for internal combustion engines currently in service, severely reducing the probability of engine knock. Engine knock is the spontaneous self-ignition of gasoline-type fuel during the compression cycle of spark-ignition (SI) engines.⁷⁵ For this reason, ethanol is the de-facto standard fuel for light vehicles in several countries that have access to readily available fermentable feedstock, such as Brazil.⁷⁶

Unfortunately, the good combustion properties of ethanol are offset by multiple chemical and physical disadvantages:

- Ethanol is infinitely miscible with water. When blended into gasoline, high water concentrations in ethanol can lead to a phase separation between an EtOH/H₂O phase and a gasoline phase in the fuel tank of the vehicle. This can cause engine malfunction and possibly vehicle damage. Water contamination can also lead to engine corrosion.⁷⁷
- The volatility of ethanol can be a problem when handling large quantities of it. Its high vapour pressure, very low flash point and low boiling point compared to other liquid fuels, specifically gasoline (see Table 3.1), pose potential risk of violent combustion during fueling and storing operations.
- The high heat of vaporization of ethanol can cause problems during cold-starts.⁷⁸ Some gasoline cars that can be operated with high ethanol blends require extended engine and fuel intake pre-heating during cold weather. During the warm-up phase, bad drivability can also occur.⁷⁹
- Ethanol can be corrosive to parts of the fuel injection system of a vehicle as well as engine parts made from certain aluminium alloys.⁸⁰

3.1.3 Advanced biofuels and the case for 1-butanol

To solve the problems of ethanol as a biofuel, other alternatives must be investigated. A desirable fuel would have combustion properties similar or superior to gasoline, while not having the disadvantages of ethanol. *n*-Butanol for example has an energy density similar to gasoline and significantly superior to ethanol. It combines a low vapour pressure, high flash point and very low miscibility with water with a significantly lower heat of vapourization compared to ethanol.^{74,81} With a value of 94-96,⁸² its RON also lies within the range of standard gasoline blends. Similar properties are found in the other butanol isomers, as well as even higher alcohols, such as *n*-hexanol and octanols. All of these substances are therefore regarded as suitable replacements for ethanol in gasoline blends and can be used with the current ICE vehicle stock. An overview over 1-butanol's properties compared to gasoline and ethanol can be found in Table 3.1.

3. Ethanol upgrading using Ru-POP pincer complexes

Table 3.1 : Physical properties of selected upgraded biofuels compared to gasoline and ethanol.

Property	gasoline	EtOH	1-BuOH
RON	95-100	106-130	94-96
boiling point	~200 °C	78 °C	117 °C
vapour pressure (~38-40 °C)	62-90 kPa	17 kPa	1.61 kPa
flash point	-43 °C	13 °C	34 °C
heat of vapourization	0.36 MJ/kg	0.92 MJ/kg	0.43 MJ/kg
energy content	32 MJ/L	20 MJ/L	29 MJ/kg
miscibility with H ₂ O	None	Fully miscible	7.7 wt%

Currently, many of these potential biofuels are under investigation with a particular focus lying on 1-butanol. The traditional method to synthesize butanol, called acetone-butanol-ethanol (ABE) fermentation,⁷⁴ has not been shown to deliver results good enough for applications without the need for expensive upstream and downstream processing. The fermentation uses bacteria from the *Clostridium* family. Product formation is however halted because *Clostridium*'s metabolism is severely inhibited by butanol.⁸³ This has so far disqualified any bacterial fermentation processes directly to butanol from being used as a viable production method for liquid fuel from renewable feedstock.

Therefore, another process for sustainable 1-butanol synthesis is needed. Genetic modification of *Clostridium* has been discussed,⁸⁴ but a direct conversion of biofeedstock using non-biological catalysis might be more efficient. Due to ethanol's availability from plant matter, an upgrading process can be envisioned in which ethanol is obtained via efficient fermentation, and then catalytically converted into 1-butanol, along with potential side products. After fractional distillation, the 1-butanol could then be used in gasoline blends. The process of ethanol upgrading to advanced biofuel is depicted below:

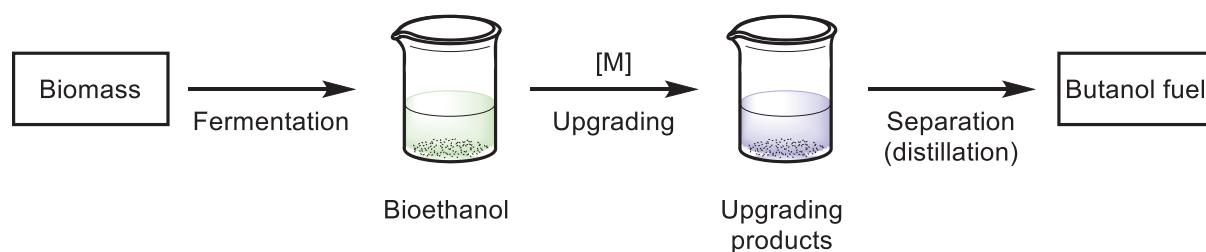
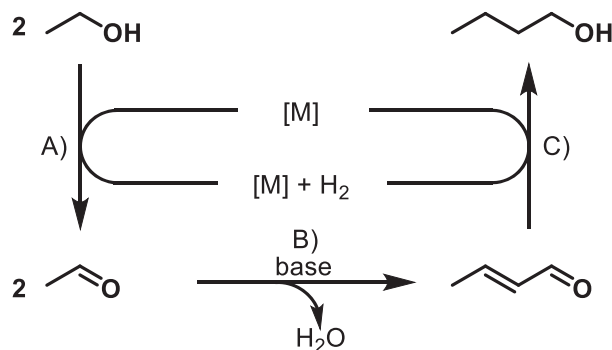


Figure 3.1: Butanol fuel synthesis via ethanol upgrading.

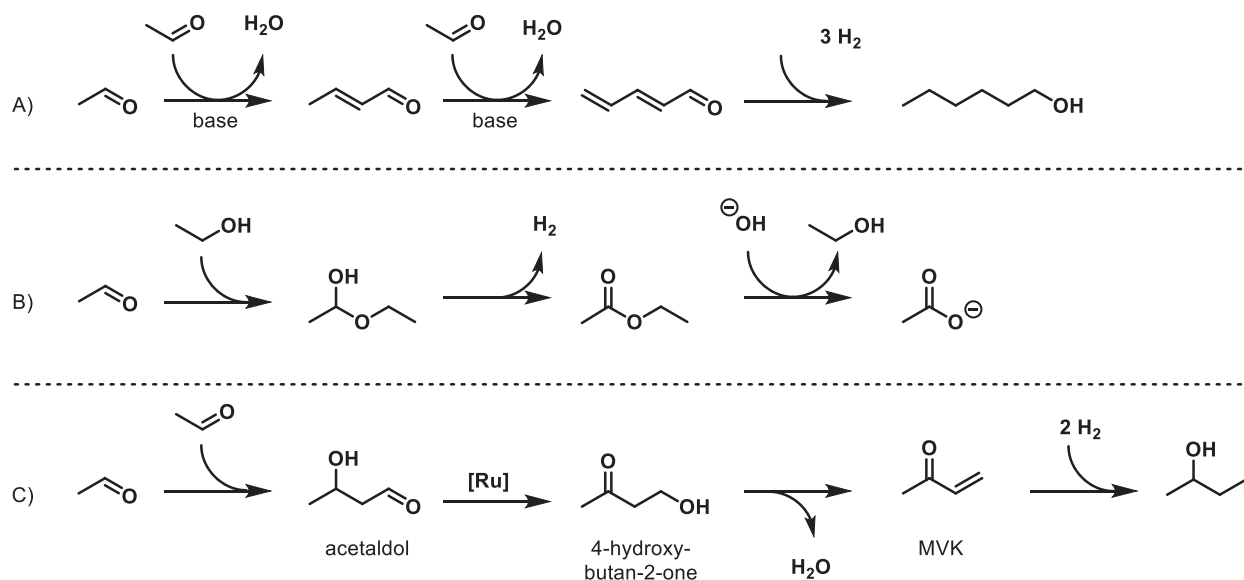
3.1.4 The GUERBET mechanism

For this upgrading, a chemical process is required that can convert ethanol directly into longer linear alcohols. The most well-described mechanism by which this can be achieved was first described by GUERBET in 1899,⁸⁵ now collectively known as the GUERBET-reaction. Based on it, an industrial-scale process can be envisioned. An overview of the reaction from ethanol to 1-butanol is shown in Scheme 3.1. In the first step of the reaction (A), ethanol is dehydrogenated. This can be done with homogeneous or heterogeneous catalysts, and the reaction forms acetaldehyde and hydrogen. H_2 can be either completely liberated and occur in gaseous form in the atmosphere over the reaction mixture, or it can stay chemically bonded in a hydrogenated form of the catalyst. A following base-catalyzed aldol condensation (B) between two molecules of acetaldehyde leads to the formation of crotonaldehyde and water as a side product. Finally, the crotonaldehyde is rehydrogenated using the previously liberated hydrogen to form 1-butanol (C). The process of hydrogen abstraction by (alcohol) dehydrogenation, followed by rehydrogenation in a series of reactions is usually referred to as “hydrogen borrowing” or “hydrogen auto-transfer”, and has been used in various areas of homogeneous catalysis.^{86,87} Therefore, while the reaction is ongoing, it can also be envisioned as a transfer hydrogenation between ethanol and crotonaldehyde.



Scheme 3.1: GUERBET-reaction to form 1-butanol from ethanol.

Other reaction cascades can occur in this mixture, so this reaction usually forms multiple side products. Three of them are depicted below in Scheme 3.2. After the formation of crotonaldehyde, a second condensation can lead to longer carbon chains, which are rehydrogenated to form longer linear alcohols such as 1-hexanol and 1-octanol (A). For biofuel synthesis, this is not necessarily a problem, as those longer alcohols are also similar to gasoline in their combustion properties yet offer slightly higher energy densities than 1-butanol due to their lower oxygen content and therefore lower average carbon oxidation state.⁸⁸ The formation of acetals is also possible (B), in which acetaldehyde reacts with ethanol. Three reaction pathways are possible, and all of them lead to the formation of acetate. The first is promoted by free hydroxide ions in solution and is called the CANNIZARRO pathway.⁸⁹ The second one is promoted by ethoxide, and is called the TISHCHENKO pathway.^{90,91} Both can be understood as disproportionations of acetaldehyde into ethoxide and acetate. The TISHCHENKO pathway yields ethyl acetate, which can be hydrolyzed to acetate ions, while the CANNIZARRO pathway leads directly to acetate ions.⁹² A third pathway, called the dehydrogenative pathway, oxidizes ethanol directly to acetic acid.⁹³ In general, the reaction towards acetate is strongly favoured by low reaction pressures and in setups where hydrogen is purposefully allowed to escape, usually by simple refluxing, causing a slow net oxidation by hydrogen removal. Ethyl acetate synthesis through this pathway known as acceptorless dehydrogenation. However, constituting a competitive reaction in butanol synthesis, acceptorless dehydrogenation is undesired, as the hydrolysis of ethyl acetate can lead to the formation of acetic acid, which will quench the base, hampering reactivity. Finally, it has recently been shown in our workgroup that secondary alcohols can also be formed via a novel pathway (C).⁹⁴ This is due to an aldol reaction, which does not condensate water and thereby forms acetaldol (3-hydroxybutanal). A hydrogenation and dehydrogenation by the catalyst isomerizes this to 4-hydroxy-2-butanone, which dehydrates to methyl vinyl ketone (MVK). Double hydrogenation of MVK finally leads to 2-butanol. The same reaction pathway also yields small amounts of hydrocarbon gases (2-butene and butane), and products of retro-aldol reactions of 4-hydroxy-2-butanone such as acetone and formaldehyde.



Scheme 3.2: Possible side reactions during ethanol upgrading.

A) Formation of longer primary alcohols due to repeated condensation reactions (simplified).

B) Direct acceptorless dehydrogenation to ethyl acetate (simplified).

C) 2-butanol formation due to formation of MVK.

3.1.5 Organometallic complexes for ethanol upgrading

The interest in GUERBET-type ethanol upgrading first began in 2013, when WASS reported a system for 1-butanol synthesis from ethanol using a ruthenium(II) dichloride complex bearing diphosphine ligands.⁹⁵ By screening of several related complexes, they achieved turnover numbers (TONs) up to 1300 and turnover frequencies of up to 65 h⁻¹. At a temperature of 150 °C, their system achieved up to 23.3% of 1-butanol yield, with the remaining converted ethanol mainly found as GUERBET alcohols. The system was improved by synthesizing the active complex before the start of the reaction, which led to a yield of 35.5% 1-butanol at a selectivity of 85%. To explain the catalytic activity, they invoked a beta hydrogen elimination step, turning a Ru-coordinated ethoxide ligand into acetaldehyde and a hydride. This was verified by in-situ ¹H NMR spectroscopy, finding the presence of a triplet in the hydride region of the spectrum.

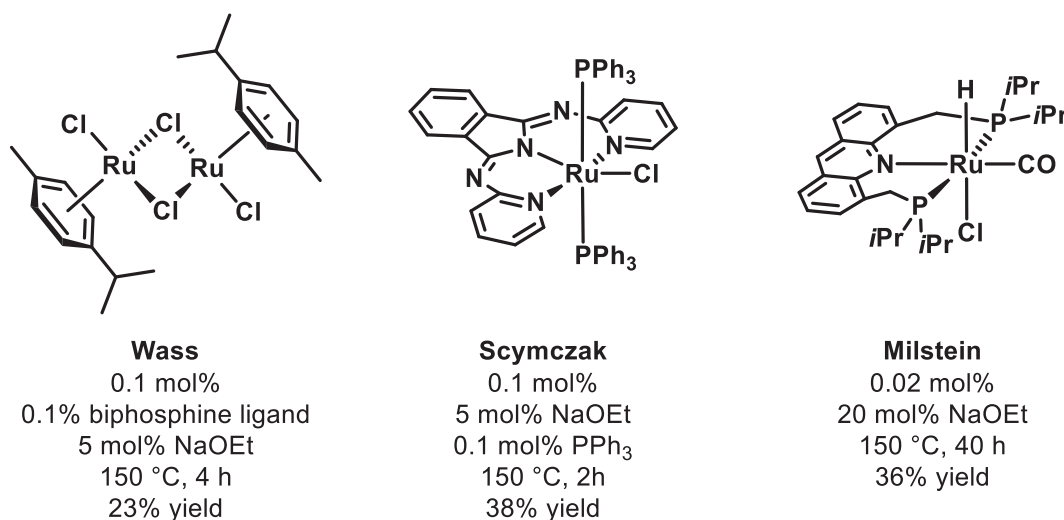


Figure 3.2: Examples of ruthenium(II) catalysts for ethanol upgrading.

Since then, multiple workgroups have taken on the task of improving on these results. In 2016, SZYMCAK developed an air-stable ruthenium complex bearing an NNN pincer ligand, which showed up to 38% yield, around 50% conversion and selectivities over 80% at 150 °C within 2 hours when triphenylphosphine was used as an additive in low concentrations.⁹⁶ MILSTEIN used a PNP pincer ligand with a very flexible backbone in a hydrido complex reaching up to 36% yield, and high turnover numbers of up to 18209 at 150 °C. His catalyst was already slightly active at a temperature of 110 °C, where up to 22% 1-butanol was obtained.

While work in this field still continues to concentrate on ruthenium catalysts, manganese complexes for this reaction are also known. The research groups of LIU and JONES reported catalysts of the type [Mn(PNP)(CO)₂Br] in 2017 and 2018, respectively.^{46,97} This complex type had previously been used by BELLER for hydrogenation reactions of nitriles, ketones and aldehydes.⁹⁸ LIU found high catalytic activities in a GUERBET-type reaction pathway to butanol with yields up to 23% and high selectivities at a temperature of 160 °C over 96 hours using 0.01 mol% of catalyst. Alternatively, high turn-over numbers of up to 114120 could be achieved by decreasing catalyst loading to 1.0 ppm and increasing reaction time to 168 hours.⁴⁶ While LIU only investigated the activity of the isopropyl- and cyclohexyl-substituted phosphines, JONES varied the electron density on the manganese center and steric bulk further by screening through the corresponding complexes bearing phosphines of isopropyl, cyclohexyl, phenyl, *tert*-butyl and 1-adamantyl. Both groups also investigated the influence of the proton on the secondary amine moiety. Methylating the complex at this position significantly reduced yields (reduction to only 6% 1-butanol compared to over 30% for JONES and 0.5% 1-butanol compared to 6.7% for LIU), which points to a strong influence of the proton in the catalytic cycle.

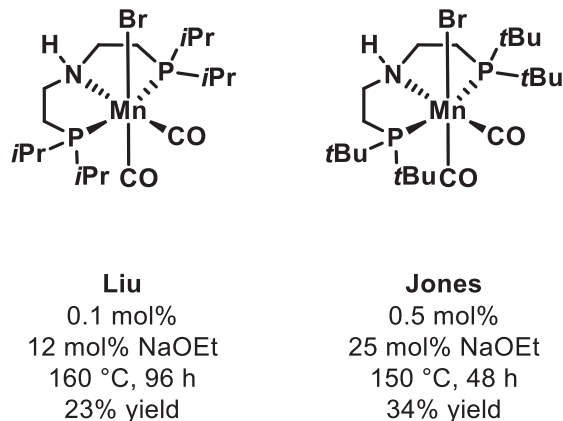
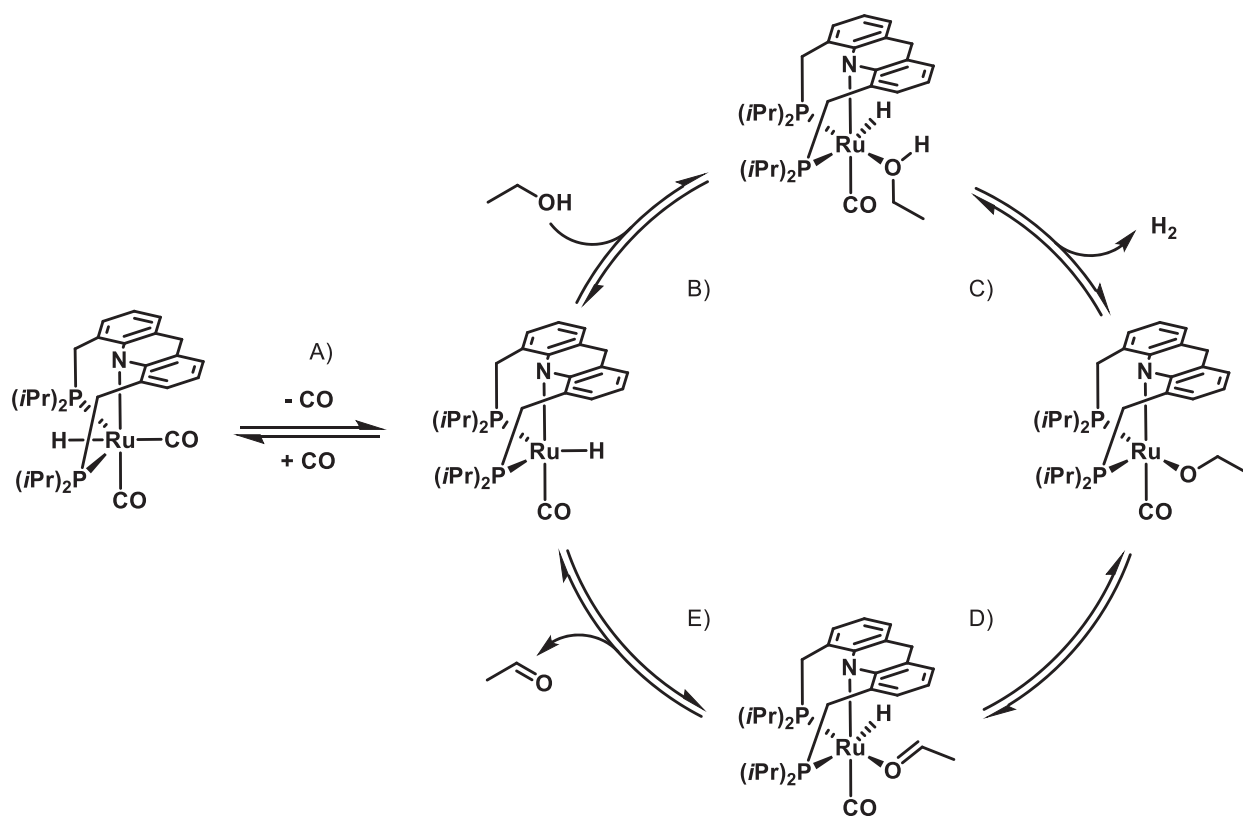


Figure 3.3: LIU and JONES's manganese(I) PNP pincers for ethanol upgrading.

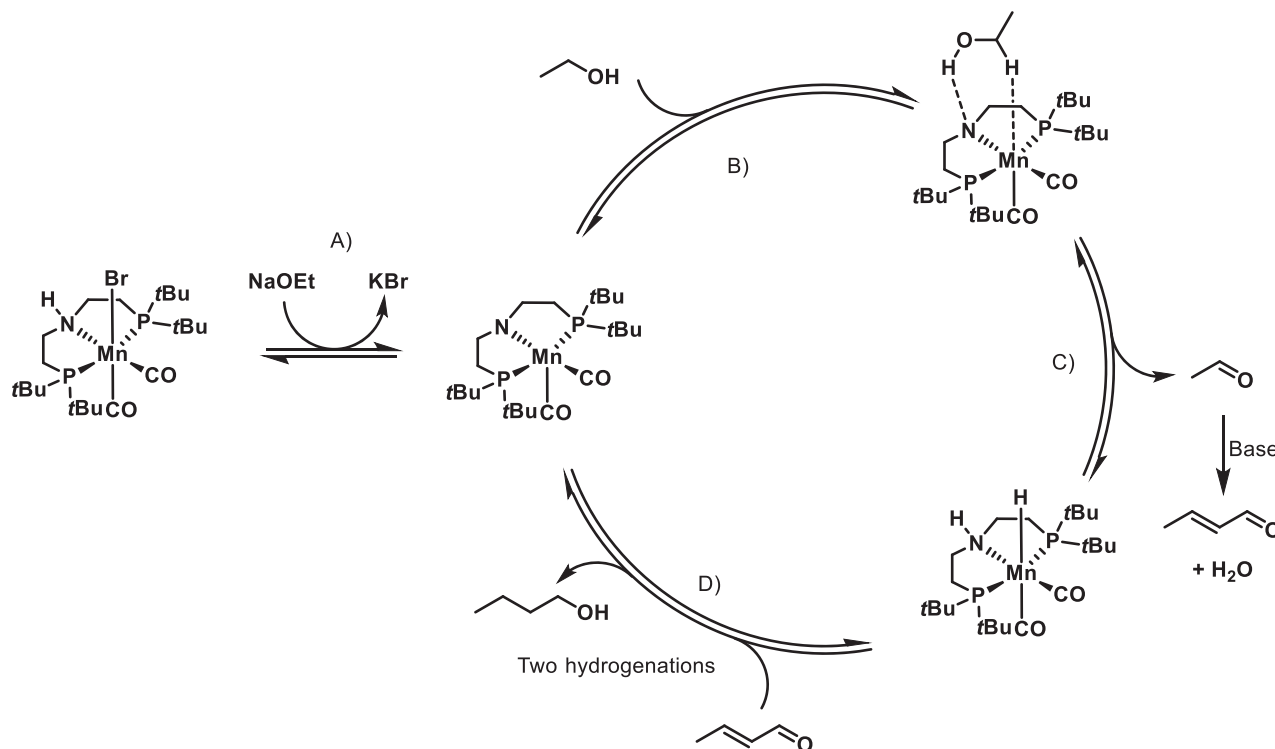
3.1.6 Ethanol upgrading mechanisms

The oxidation of ethanol to acetaldehyde typically follows one of two mechanisms. The first one uses an inner-sphere mechanism in which ethanol is oxidized via beta hydride elimination. A typical example of the ethanol dehydrogenation catalytic cycle was proposed by MILSTEIN.⁵¹ and is depicted in Scheme 3.3. In the first step (A), the complex liberates a carbonyl ligand to form the unsaturated active species. Coordination of ethanol in a position *cis* to the hydrido ligand (B) follows. Hydrogen is then eliminated (C) in a rather unusual α -abstraction in which the hydride ligand deprotonates the coordinated ethanol. The same elimination mechanism had been proposed by WASS as described earlier,⁹⁵ and is speculated to form a dihydrogen ligand intermediate in theoretical studies of the related methanol dehydrogenation, albeit with a high reaction barrier.⁹⁹ This transforms the ethanol moiety to the corresponding ethoxido ligand. After the β -hydrogen elimination which restores the hydrido ligand (D), acetaldehyde dissociates, thereby restoring the active species and closing the catalytic cycle. In the case of MILSTEIN'S PNP ligand, the methylene bridges between the phosphines and the ligand backbone significantly increase ligand flexibility, which allows this specific ligand type to switch easily between facial and meridional configurations. It must be noted here that for the rehydrogenation of crotonaldehyde to 1-butanol, this catalytic cycle can be imagined as running in reverse. This would mean that crotonaldehyde binds *cis* to the hydride signal (reverse step E), then be hydrogenated (reverse D,C), and finally liberated (reverse B).

Scheme 3.3: Inner-sphere mechanism of ethanol dehydrogenation using a Ru-PNP pincer.⁵¹

The second mechanism involves an interaction between a hydrido ligand on the metal center and an acidic proton on the ligand. The most common type of ligand showing this behaviour uses a secondary amine, the central binding amine in PNP pincers, and is usually referred to as a “NOYORI-type”,^{100,101} The activation of hydrogen with a metal-amido bond was first described by FRYZUK in an iridium(III) PNP pincer complex.^{102,103} However, deprotonation on carbon can also occur.¹⁰⁴ The totality of interactions between hydrido ligands and a proton of the ligand backbone is typically called “metal-ligand cooperation” (MLC). A good example of this behaviour is the complex used by JONES et al., which was described earlier. In a typical reaction cycle, the complex is first activated by the formal elimination of a hydrogen halide, typically HBr or HCl, with the use of a base such as an alkoxide(A). Due to their synthesis from easily available $[\text{Mn}(\text{CO})_5\text{Br}]$, manganese(I) complexes usually eliminate HBr whereas ruthenium complexes such as Ru-MACHO are typically activated by HCl elimination. Since a base is required for the aldol condensation later in the GUERBET reaction, alkoxides are used, and regularly show the best performance during base screenings. This elimination transforms the amine group in the ligand backbone to an amido ligand. The amide acts as a proton acceptor during the following outer-sphere oxidation of ethanol to acetaldehyde (B and C), which condenses in an aldol condensation to crotonaldehyde. A strong interaction is assumed to occur between the acidic proton on the hydroxy group

of ethanol and the amide ligand. Another interaction is assumed to occur between the free coordination site at the metal center and the hydrogen atom on C1 of ethanol. This formally transfers H_2 to the complex and oxidizes ethanol to acetaldehyde. As a result, the complex is found to bear a hydrido ligand on the metal center and a proton on the amine, which finally reduce the crotonaldehyde to 1-butanol in two hydrogenation cycles (D).



Scheme 3.4: Outer-sphere mechanism of ethanol dehydrogenation using an Mn-PNP pincer.

Proposed catalytic cycle based on the work of JONES et al.⁹⁷

The presence of both catalytic cycles in the same reaction is possible as they are not mutually exclusive. Indeed, both examples mentioned above are potentially capable of either reaction mechanism. MILSTEIN speculated about the presence of an O-H activation using the amido group of his complex, but believed this to be unlikely due to the comparatively low basicity of the amide caused by its integration into the aromatic system of the ligand backbone. In the case of JONES'S complex, an *N*-methylation of the PNP ligand did not completely eliminate catalytic activity, hinting at the presence of some type of inner-sphere mechanism being present, albeit slow compared to the mechanism undergoing MLC.

3.1.7 Aim of the project

Unfortunately, the currently available catalysts for GUERBET-type ethanol upgrading require very harsh reaction conditions of 150-160 °C (see the examples shown above in Figure 3.2 and Figure 3.3). The long-term goal of researchers active in this field is the development of a catalyst active at lower temperatures, ideally even below the boiling point of ethanol. This would have two main advantages. Firstly, the energy required for this process would be reduced significantly, due to, among others, less requirements for heating processes and reactor vessel thermal insulation. Secondly, the risks associated with pressure vessels, mainly thermal explosions, would be eliminated. Overall, production costs of upgraded biofuels would drop as a result, making this process more economically viable.

It is therefore the goal of this first catalysis project to investigate the activities of the previously synthesized complexes **Ru-1a** to **Ru-10a** for their activity in GUERBET-type ethanol upgrading. To better understand this catalyst class's properties in this reaction, it is also the goal to run stoichiometric reactions between the complexes and some of the substrates present in the reaction mixture.

3.2 Ethanol upgrading reactions using POP pincer complexes

Using the Ru-POP complexes synthesized in Chapter 2 of this thesis, GUERBET-type ethanol upgrading reactions were investigated. It is important to note here that the alternative acceptorless dehydrogenation route for the synthesis of ethyl acetate has not been purposefully studied in this work, as it would require drastically different reaction design to destroy the hydrogenation/dehydrogenation equilibrium by allowing H₂ gas to escape.

3.2.1 Ethanol upgrading screening reactions

The investigation of the complexes began with a screening of the previously synthesized, phenyl-substituted complexes **Ru-1a** to **Ru-4a**, as well as two control experiments, one without any catalyst, and one using the precursor [RuHCl(PPh₃)₃] toluene adduct. No conversion towards 1-butanol was observed for the experiment without any catalyst. The precursor was completely insoluble in basic ethanolic solutions even at high temperatures, so the reaction was abandoned. Due to an unavailability of high temperature capable autoclaves, the reactions began to be screened at 120 °C, using 250 ppm of catalyst and 10 mol% of base relative to ethanol with a reaction time of 48 hours. The complexes were already partially soluble in ethanol at room temperature, and at increased temperatures, complete dissolution was observed upon prolonged heating. It is important to note here that the complexes are extremely oxygen sensitive when in solution. The simple act of opening a valve on a J-Young tube for a few seconds under air and resealing it is enough to cause the complexes dissolved in degassed solvents to degrade within short amounts of time, which is visible by a striking colour change from yellow to dark grey.

The first screening immediately revealed significant differences in catalytic performance between the different complexes (Figure 3.4A). An overview over the reaction conditions, yields, as well as turn-over numbers and frequencies can be found in Table 9.1 in Appendix D. While the xantphos complex **Ru-1a** only produced 2.3% of 1 butanol, **Ru-2a** showed to be the best of the set with a yield of 15.1% (TON 1224, TOF 25.5 h⁻¹). Complexes **Ru-3a** and **Ru-4a** showed results in between those two extremes, yielding 12.1 and 8.9% 1-butanol, respectively. The longer linear alcohol 1-hexanol was obtained in low quantities as well, yielding up to 0.6% in the case of **Ru-3a**. The pressures in the reaction vessels were monitored through the autoclave-integrated manometers (Figure 3.4B). **Ru-2a** produced pressures as high as 12 bar, and the pressure continued to rise until the end of the experiment. In contrast, **Ru-1a** did not show pressures higher than 2 bar, and the pressure stagnated after less than 10 hours. Either of these pressures is significantly lower than what would be expected for the development of significant amounts of dehydrogenated products,⁹⁴ which points towards high selectivities of GUERBET-type products. The

most likely side product to form in a dehydrogenative pathway to explain this behaviour would be the formation of acetate according to Scheme 3.2B.

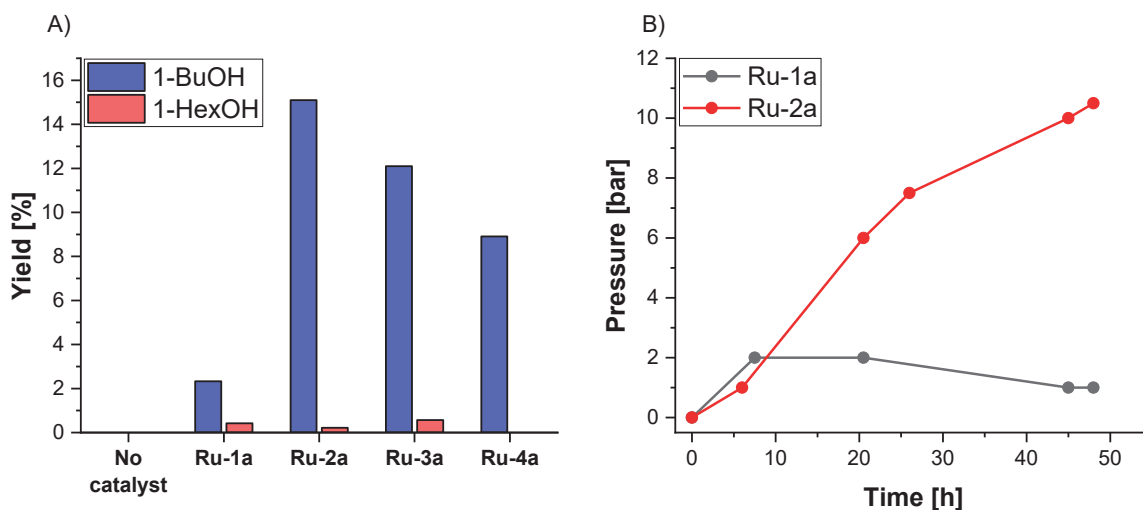


Figure 3.4: First ethanol upgrading screening.

Reaction conditions: 2.5 mL (42.8 mmol) EtOH, 291 mg (10 mol%) NaOEt, 10.7 μ mol (250 ppm) catalyst, 48 h, 120 $^{\circ}$ C.

A) Reaction yields. Determined by GC-FID.

B) Reactor pressures in **Ru-1a** and **Ru-2a** compared.

The first screening was followed by the comparison between different substituents at phosphorous (Table 9.1 in Appendix D). Starting with the xantphos-derivatives **Ru-1a**, **Ru-5a** and **Ru-9a**. The reaction improved slightly from yielding 2.3% 1-butanol with the phenyl-derived **Ru-1a** to 4.3 and 4.0% for **Ru-5a** and **Ru-9a**, respectively, however no yields could be achieved that got close to the results of **Ru-2a** previously achieved. Interestingly, for the DPEphos derivatives, the opposite trend was observed. The yield of 1-butanol reduced from 15.1% in **Ru-2a** to 7.7% in **Ru-6a**. **Ru-10a** did not dissolve in basic ethanol at elevated temperatures and was therefore not investigated. While 0.4% of 1-hexanol were found in **Ru-2a**, no 1-hexanol could be detected for **Ru-6a**. The ether-bridged complexes **Ru-3a** and **Ru-7a** delivered very similar results of 1-butanol of 12.1% and 11.6%, respectively. This most likely lies within the margin of error of the laboratory procedures, meaning that no major influence of the substituents at P can be described for this set. Finally, the DBFphos derivatives also showed a significant reduction in activity from the phenyl-substituted **Ru-4a** with 8.9% yield of 1-butanol towards 4.9% in **Ru-8a**. Overall, the change from phenyl-derived ligands towards alkylphosphines slightly reduces the activity of the complexes. This points towards more electron-poor catalysts being more adequate for this reaction, and therefore, attention was focused on them.

3. Ethanol upgrading using Ru-POP pincer complexes

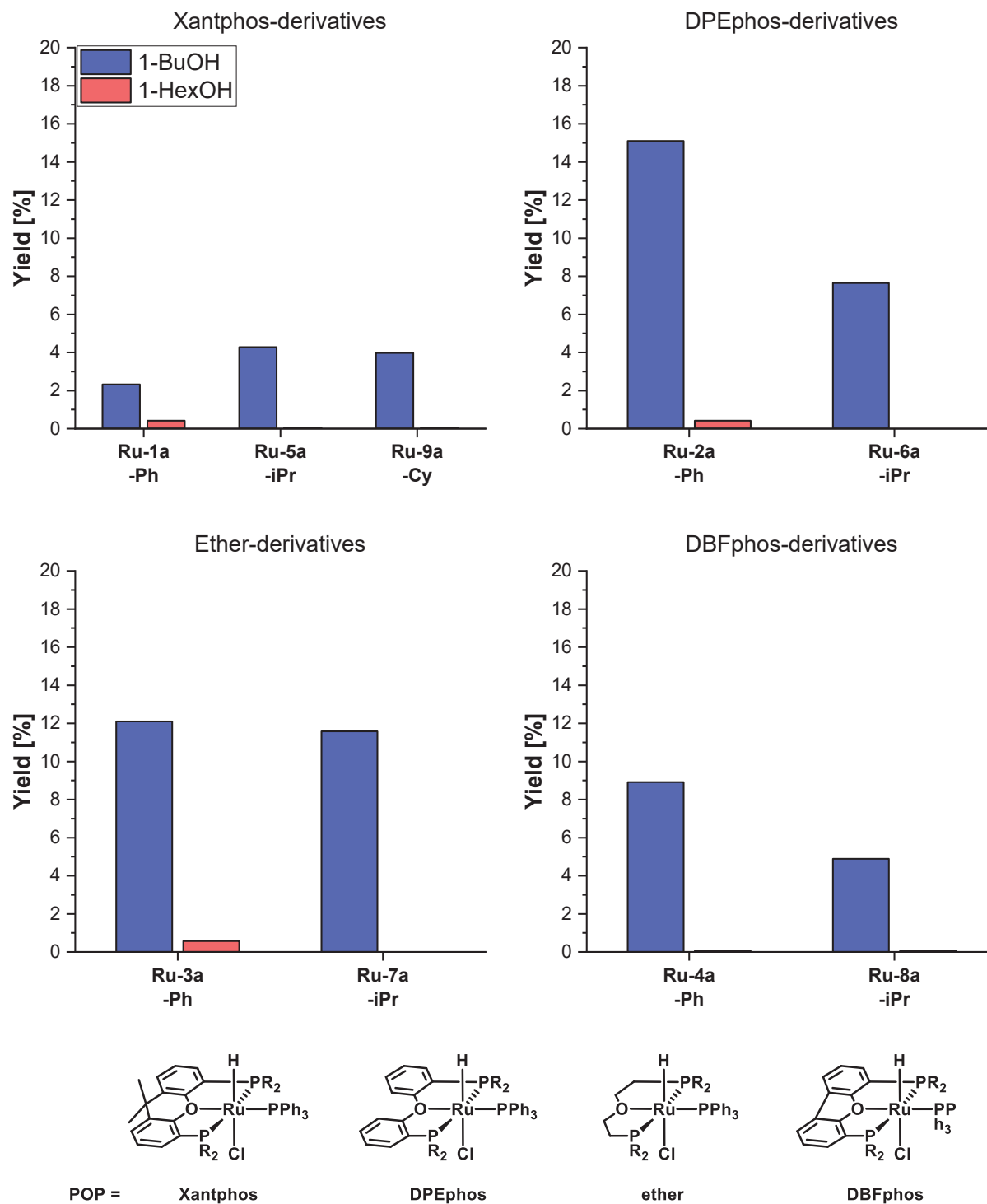


Figure 3.5: Screening of phosphine substituents.

Reaction conditions: 2.5 mL (42.8 mmol) EtOH, 291 mg (10 mol%) NaOEt, 10.7 μ mol (250 ppm) catalyst, 48 h, 120 $^{\circ}$ C.

Yields determined by GC-FID.

3.2.2 Time and temperature screenings

Reaction times and temperatures have a large effect on the formation of products. Therefore, a few select complexes were investigated for varying reaction times between 24 and 96 hours at 120 °C, and at varying temperatures between 90 and 150 °C. An overview over the reaction conditions, yields, as well as turn-over numbers and frequencies can be found in Table 9.2 in Appendix D. Starting with **Ru-2a**, a high yield of over 10% of 1-butanol could already be observed over 24 hours at 120 °C. Longer reaction times of 48 and 96 hours caused the yield to stagnate, and only slight increases in formation of 1-hexanol was observed after 96 hours, while the amount of 1-butanol slightly decreased within the margin of error. It is therefore likely that the reaction stops due to catalyst deactivation in a timeframe between 24 and 48 hours. For the same catalysts, the temperatures 90, 120 and 150 °C were screened. At 90 °C, less than 1% 1-butanol could be detected for **Ru-2a** after 48 hours reaction time. A reaction time increase to 96 hours at 90 °C only marginally improved the amount (1.3%) of 1-butanol. Additionally, the reaction was also tested at 150 °C. For this, a new autoclave type had to be used (Type B, see Appendix B), which required the downscaling of the reaction by a factor of two. At 150 °C, only 4.7% of 1-butanol were obtained, which suggests a deactivation of the catalyst by thermal decomposition. A different behaviour was found for **Ru-1a**, which showed an increase to 8.8% 1-butanol at 150 °C over 48 h (Appendix D).

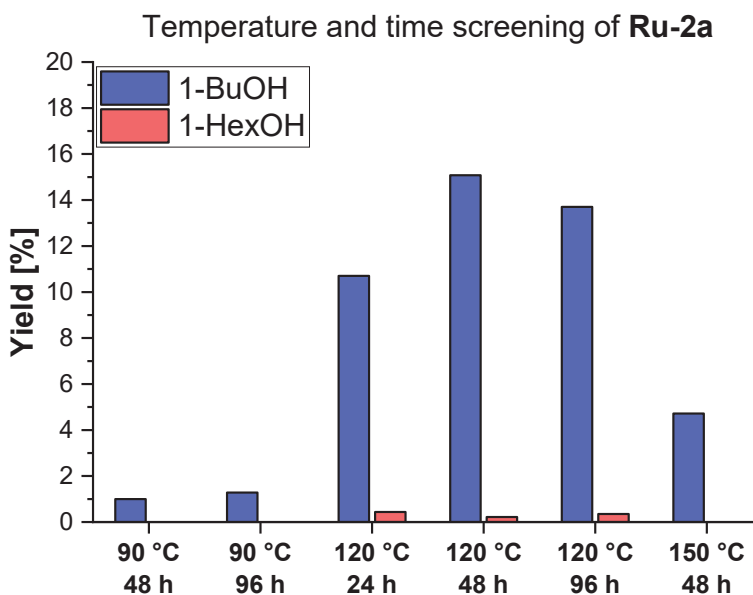


Figure 3.6: Temperature and time screening of **Ru-2a**.

Reaction conditions:

90 and 120 °C: 2.5 mL (42.8 mmol) EtOH, 291 mg (10 mol%) NaOEt, 10.7 µmol (250 ppm) catalyst

150 °C: 1.25 mL (21.4 mmol) EtOH, 145 mg (10 mol%) NaOEt, 5.35 µmol (250 ppm) catalyst. Yields determined by GC-FID.

3.2.3 Base screenings

In the next step, the best performing catalyst, **Ru-2a**, was screened for different bases. An overview over the reaction conditions, yields, as well as turn-over numbers and frequencies can be found in Table 9.3 in Appendix D. A reaction without any basic additives was performed first, and only traces of 1-butanol were found. Then, multiple alkoxides were screened. When using ethoxides, the corresponding lithium salt delivered a butanol yield of 9.3% compared to the previously achieved 15.1% using sodium ethoxide. The doubling of the base concentration was attempted, but the reaction was only successful for sodium ethoxide. When using 20% sodium ethoxide in **Ru-2a**, the yield of 1-butanol stayed at 13.0%, while more 1-hexanol (0.7%) was found. When sodium *tert*-butoxide was used, the yield dropped to 8.5%. However, when using potassium *tert*-butoxide, a significantly higher yield of 28.2% 1-butanol and 1.6% 1-hexanol could be observed, translating to a TON of 2382 and a TOF of 49.6 h⁻¹, representing the best result. Potassium ethoxide (KOEt) should be screened in the future to investigate the influence of the potassium cation. The same screening was performed for **Ru-3a**. Here, the highest yield was observed with sodium ethoxide, reaching 12.1% yield. The influence of the base was much weaker with this catalyst, the yield ranging only between 7.9 and 12.1%.

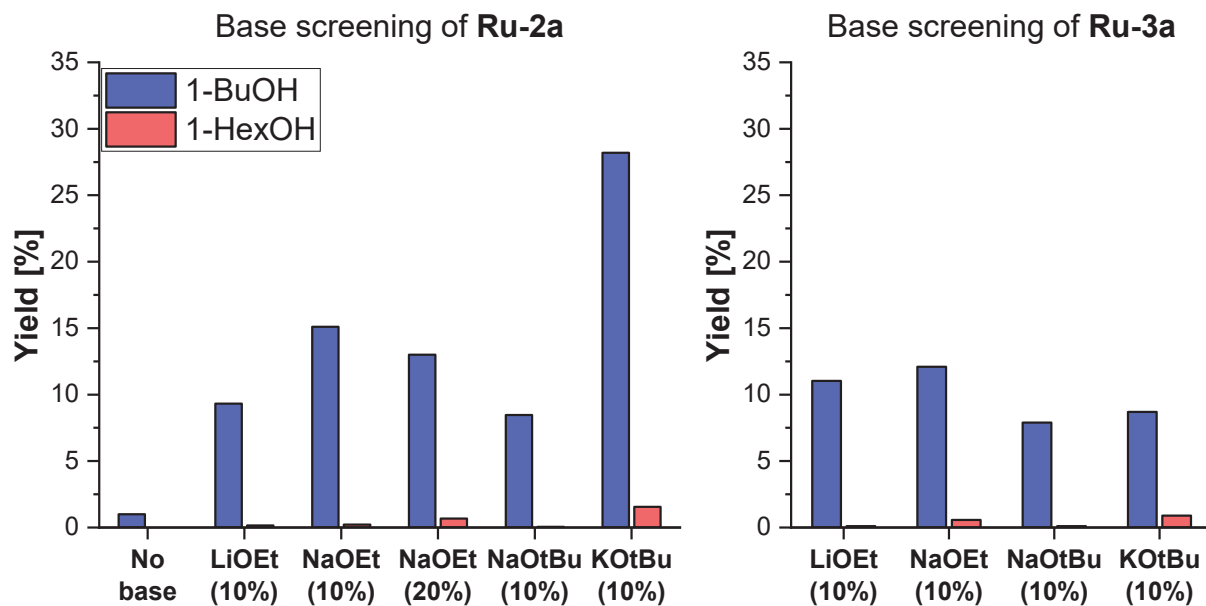


Figure 3.7: Base screening of **Ru-2a** and **Ru-3a**.

Reaction conditions: 2.5 mL (42.8 mmol) EtOH, 10 mol% base, 10.7 μ mol (250 ppm) catalyst, 48 h, 120 $^{\circ}$ C.

Yields determined by GC-FID.

3.2.4 Stoichiometric reactions

Stoichiometric reactions were performed to better understand the catalytic cycle of the system. With **Ru-2a** turning out to be the best performing catalyst of the set, all stoichiometric reactions were performed using it. Sodium ethoxide is barely soluble in many organic solvents, so ethanol- d_6 was chosen for the first experiment. In this experiment, **Ru-2a** was dissolved in ethanol- d_6 , together with 10 equivalents of sodium ethoxide. While not completely homogeneous at room temperature, complete dissolution was observed at 60 °C, and NMR measurements could be taken. In the ^1H NMR spectrum, two distinct peaks could be observed in the hydride regions of the spectrum, at -6.8 and -8.9 ppm, respectively. Due to the low signal-to-noise ratio, exact multiplicities could not be determined, however the peak at -8.9 ppm appears to show a wide coupling constant of around 77 Hz, pointing towards a phosphine atom coordinated *trans* to a hydrido ligand. No signal was found in the range between -15 and -18 ppm, which shows complete conversion of **Ru-2a**. To exclude the possibility of any proton/deuterium exchanges of the hydrido, the corresponding positions in the ^2H NMR spectrum were investigated as well, but no deuterido ligand signals were detected. The $^{31}\text{P}\{^1\text{H}\}$ spectrum revealed multiple signals in the region expected for ruthenium-bound phosphines of 70-20 ppm, and two signals were found in the regions expected for free triphenylphosphine and free ligand (see Appendix D).

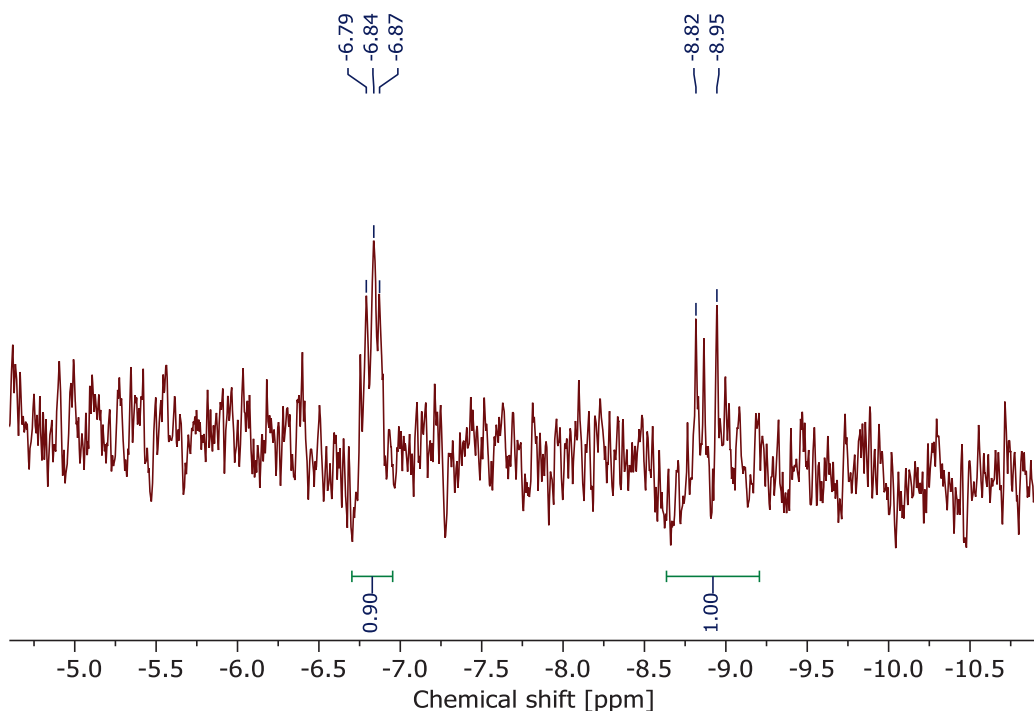


Figure 3.8: Hydride region of the ^1H NMR of a reaction between **Ru-2a** and NaOEt in EtOH- d_6 after 2 hours.

Conditions: 400 MHz, EtOH- d_6 , 10 eq. NaOEt, 60 °C (333 K).

In the next step, a stoichiometric reaction between **Ru-2a** and sodium ethoxide was repeated in THF- d_8 over a time of 24 hours at room temperature. The hydride region of the ^1H NMR revealed three distinct peaks (Figure 3.9A). The first, found at -15.85 ppm, exhibits a clear dt multiplicity, and likely corresponds to either unreacted complex **Ru-2a**, or to ethoxide coordinating *trans* to the hydride. The two additionally found peaks were observed at chemical shift of -6.8 and -8.9 ppm, respectively, confirming the observation made in the previous experiment. The peak at -8.9 ppm shows coupling constants of 78 and 31 Hz, while the coupling constants for the peak at -6.8 ppm could not be determined. It is possible that this peak corresponds to the *trans*-dihydrido complex. To establish whether the two peaks correspond to a single dihydrido species, which would be suggested by the integrals shown earlier in Figure 3.8, or whether they correspond to two distinct molecules, the phosphorous-decoupled $^1\text{H}\{^{31}\text{P}\}$ NMR spectrum was measured (Figure 3.9B). All three peaks observed therein collapse to singlets, which means that no *cis*-dihydrido species with magnetically non-equivalent protons is detectable in the mixture. From this, the complex structures, listed in Figure 3.9C, can be proposed.

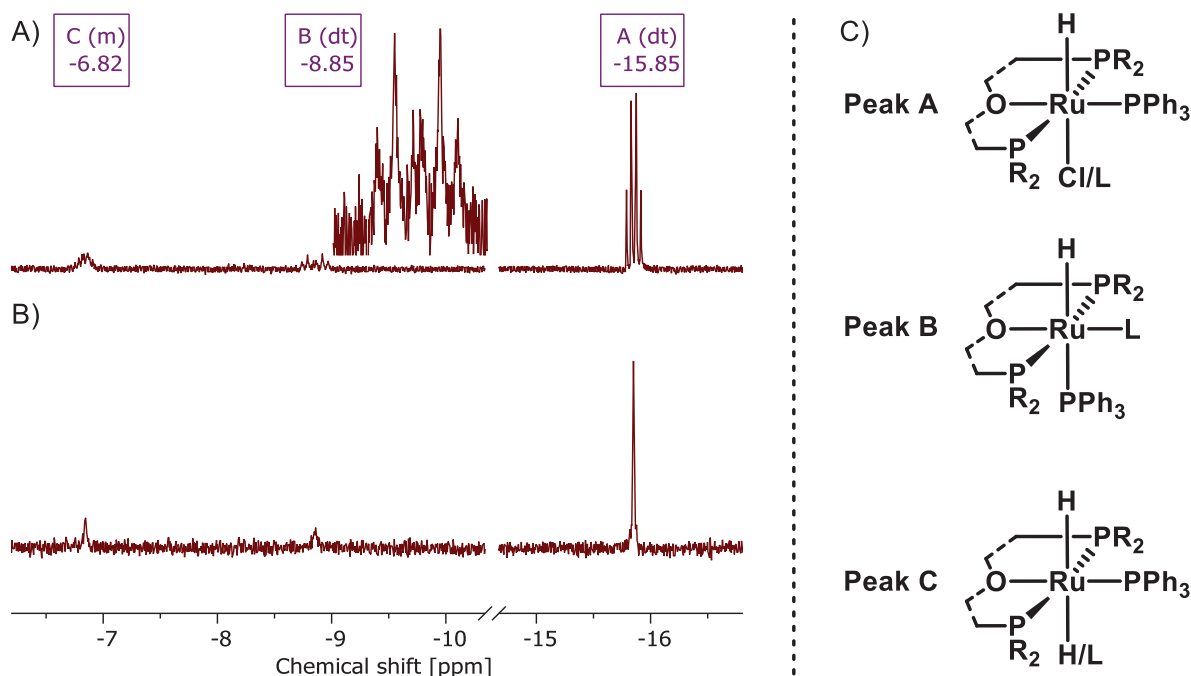


Figure 3.9: 600 MHz ^1H NMR spectrum of a reaction of **Ru-2a** with NaOEt in THF- d_8 at 25 °C.

Reaction time 24 hours at room temperature.

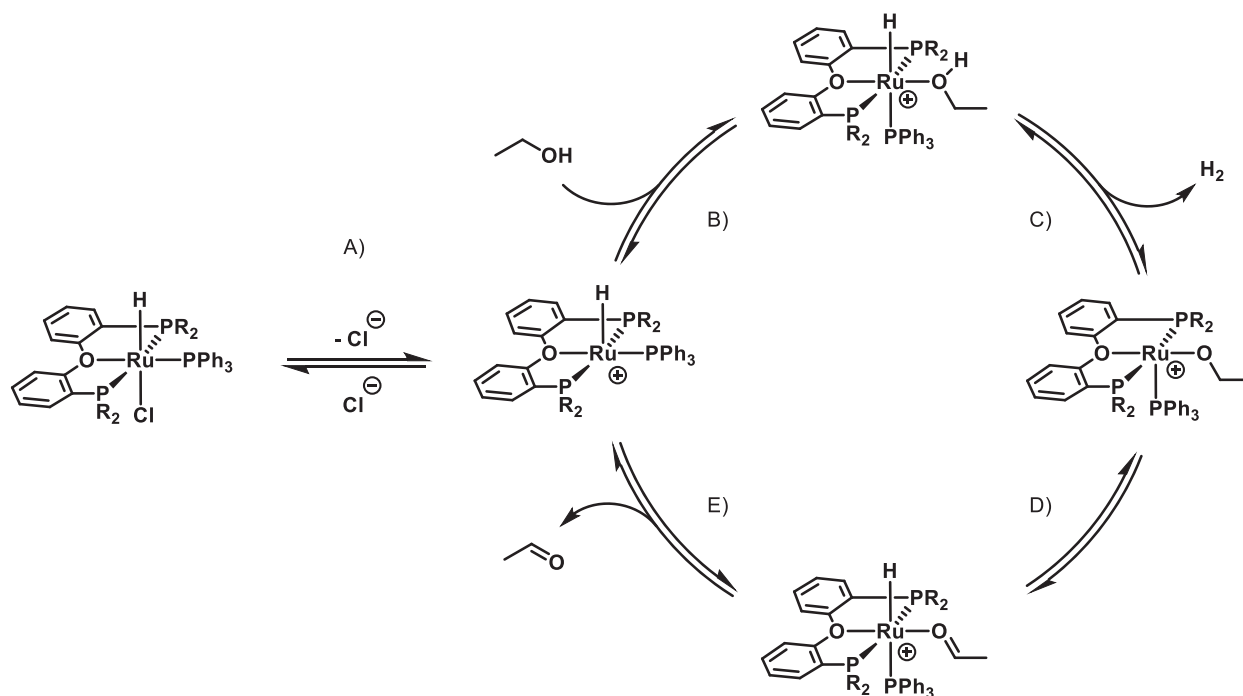
A) ^1H spectrum.

B) $^1\text{H}\{^{31}\text{P}\}$ spectrum. Signals collapse to singlets.

C) Suggested molecule fragments for the signals.

3.2.5 On the catalytic cycle

Using this information gained previously, two catalytic cycles can be proposed. The first one generally follows the mechanism proposed by MILSTEIN depicted earlier in Scheme 3.3 and contains a series of cationic species. It is not dependent on the hemilability of POP pincers and their reconfigurations to bidentate chelates. The entire catalytic cycle is depicted below. In the first step (A), the chlorido ligand is abstracted and a cationic species is formed. This reaction is possible in polar media such as ethanol and should be accelerated by the presence of alkali metal cations to form only very slightly soluble chloride salts such as NaCl in analogy to the abstraction of the chloride ligand in complexes **Ru-1b** to **Ru-10b** discussed earlier. Ethanol then coordinates to the complex (B) in the position *cis* to the hydrido ligand. This allows for the liberation of hydrogen in the following step (C). A β -hydride elimination regenerates the hydrido ligand (D), and finally, the active species is regenerated by dissociation of acetaldehyde.

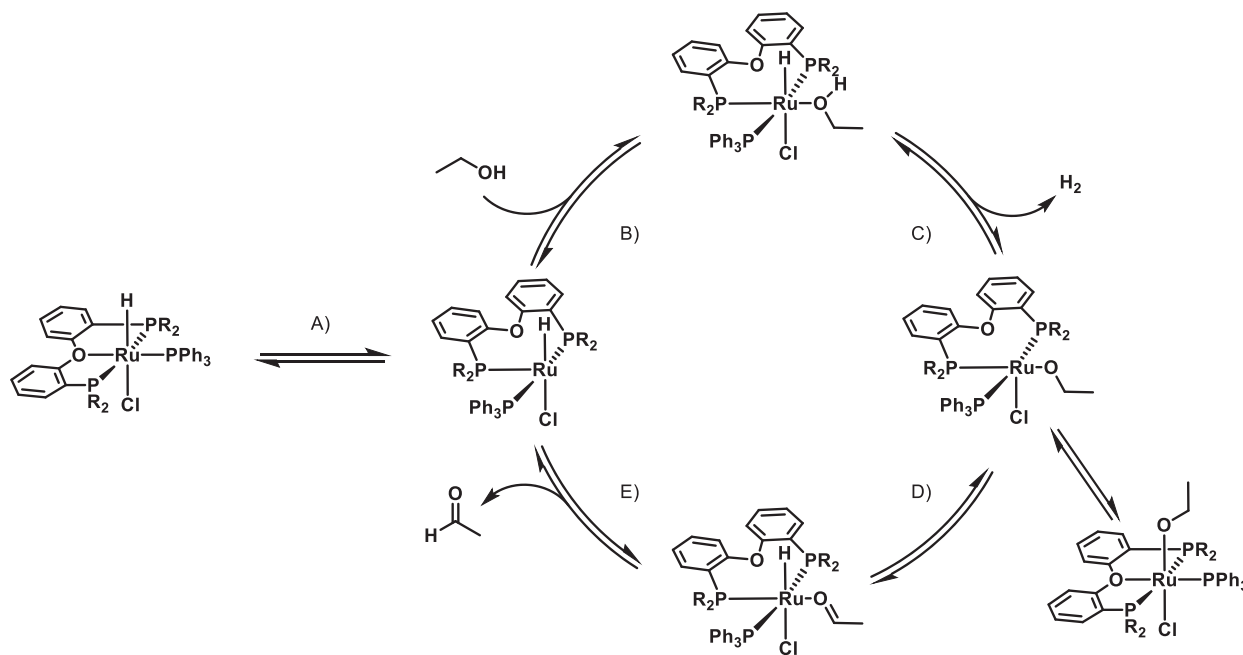


Scheme 3.5: First proposed catalytic cycle for ethanol dehydrogenation using $[\text{RuHCl}(\text{POP})(\text{PPh}_3)]$ complexes.

Example used: **Ru-2a**.

The second proposed catalytic cycle relies on the POP ligands' hemilability. This could explain the significant difference in catalytic activity between the complexes **Ru-1a** and **Ru-2a**, which mainly differ in their ligand backbone flexibility. The main difference to the first catalytic cycle lies in the absence of

chloride abstraction. Instead, the complex is desaturated and transformed into the active species by decooordination of the oxygen ligator in the ether link of the POP pincer ligand (A). After the coordination of ethanol at the vacant site (B) the same hydrogen elimination occurs (C). The ethoxido complex may be stabilized by oxygen coordinating on ruthenium. By β -hydride elimination, the hydrido ligand is regenerated (D), and dissociation of acetaldehyde regenerates the active species (E).



Scheme 3.6: Second proposed catalytic cycle for ethanol dehydrogenation using $[\text{RuHCl}(\text{POP})(\text{PPh}_3)]$ complexes.

Example used: **Ru-2a**.

To validate or rule out one catalytic cycle over the other, several control experiments can be envisioned. Due to the relatively low solubility of sodium chloride in ethanol, the abstraction of chloride during the reaction is likely. This suggests that desaturation of the complex occurs through that route, favouring the first proposed catalytic cycle. It could alternatively however lead to the formation of the ethoxido complex in a *trans*-configuration relative to the hydride, which should not be catalytically active. This must be investigated in stoichiometric reactions with sodium ethoxide, using multiple different ligand backbones. If *trans*-configurations are repeatedly observed independently of the linker, then this particular catalytic cycle might be disfavoured. The usage of the solvato complexes such as **Ru-1b** compared to **Ru-1a** in ethanol upgrading experiments could give valuable insight into this behaviour, as it could favour the formation of the complex with ethoxido *trans* to the hydrido ligand. A different ethoxide salt such as tetrabutylammonium ethoxide could be used in ethanol upgrading to make the precipitation of

sodium chloride impossible. No change in catalytic performance in this experiment compared to using an alkali metal ethoxide would suggest that the liberation of chloride by precipitation is not the primary driving force of the catalyst activation, and that the reaction might occur primarily through the hemilability of the POP pincer ligand or the abstraction of triphenylphosphine.

The ancillary phosphine ligand might also play a role in determining the role of the catalytic cycle. In the first cycle, the phosphine is proposed to coordinate *trans* to the hydrido. As a result, a modification of the electron density on the phosphine, and a resulting stronger or weaker sigma-type electron donation into the ruthenium center might strongly influence the properties of the hydrido ligand. This effect is not expected for the second catalytic cycle, in which the ancillary ligand is expected *cis* to hydrido.

3.3 Conclusions and outlook

In conclusion, the catalysts synthesized in Chapter 2 of this work were tested for their catalytic performance in the GUERBET-type upgrading of ethanol to 1-butanol as a means of biofuel synthesis. The complexes showed activities at 120 °C and higher. Significant dependence of reactivity depending on the linker of the POP pincer complex was found, with **Ru-2a** yielding the best results during catalyst screenings. A following conditions screening revealed a reaction time of 48 hours to be optimal at a temperature of 120 °C. The following base screening showed potassium *tert*-butoxide to be the most promising base in this screening, and a yield of 28.2% 1-butanol (TON=2382, TOF=49.6 h⁻¹) could be achieved when using complex **Ru-2a**. This surpasses the state-of-the-art using non-NOYORI-type complexes at a comparable temperature range. MILSTEIN found 1-butanol yields of 20.9% using his PNP pincer complex at a temperature of 110 °C (TON 1171, 16 h).⁵¹

Finally, stoichiometric reactions on the best-performing complex were conducted. New hydrido signals were found at -6.8 and -8.9 ppm respectively, showing a direct reaction between the complex **Ru-2a** and sodium ethoxide. Based on this data, two catalytic cycles were proposed.

Multiple pathways for further investigations can be envisioned. For one, the synthesis of the ethoxido complexes and their complete characterization would give further insight into the catalytic cycle. While a clean conversion directly from the chlorido complexes yielded a mixture of different products, other pathways towards the products are possible. Additional information could also be gathered using deuterated ethanol in the upgrading reaction and the analysis of deuterated products to investigate potential exchange reactions.

4. Formic acid dehydrogenation using Ru-POP pincer complexes

The following chapter describes my efforts to apply the catalysts synthesized in Chapter 2 for formic acid dehydrogenation. This project was designed as a collaboration between myself and my colleague BRENDA RABELL MONTIEL, who is working on a similar project using PNP pincer complexes.

4.1 General introduction

4.1.1 Liquid organic hydrogen carriers

One pathway to synthetic fuels is to use hydrogen gas as an energy storage medium. In times of excess renewable electricity from sources such as wind and solar, hydrogen gas can be created with great efficiency by means of electrolysis¹⁰⁵ or via direct thermochemical processes.¹⁰⁶ Unfortunately, the physical properties of hydrogen pose certain risks. As a highly flammable gas with a very low boiling point of only 21 K ($-252\text{ }^{\circ}\text{C}$),¹⁰⁷ hydrogen must be either cryogenically stored as a liquid or compressed and stored in pressure vessels to achieve energy densities necessary for applications in the transport sector. Both methods, however, involve the disadvantages of specialized vessels for transport.

As a result, the use of liquid organic hydrogen carriers, or LOHCs, has been proposed. LOHCs are defined as liquid, or low melting point solid, organic compounds that can be catalytically hydrogenated and to act as hydrogen storage media.¹⁰⁸ In their hydrogenated form, they can be transported using common infrastructure such as fuel trucks, ships, and pipelines. They are then passed over a second catalyst for dehydrogenation, liberating hydrogen gas, and restored to their dehydrogenated form. Proposed LOHCs include among others toluene,¹⁰⁹ naphthalene,¹¹⁰ (di)benzyltoluene derivatives,¹¹¹ indoles and indolines,¹¹² as well as *N*-alkyl carbazoles.^{113,114} An overview of the entire lifecycle of LOHCs, as well as examples of LOHCs can be found in Figure 4.1.

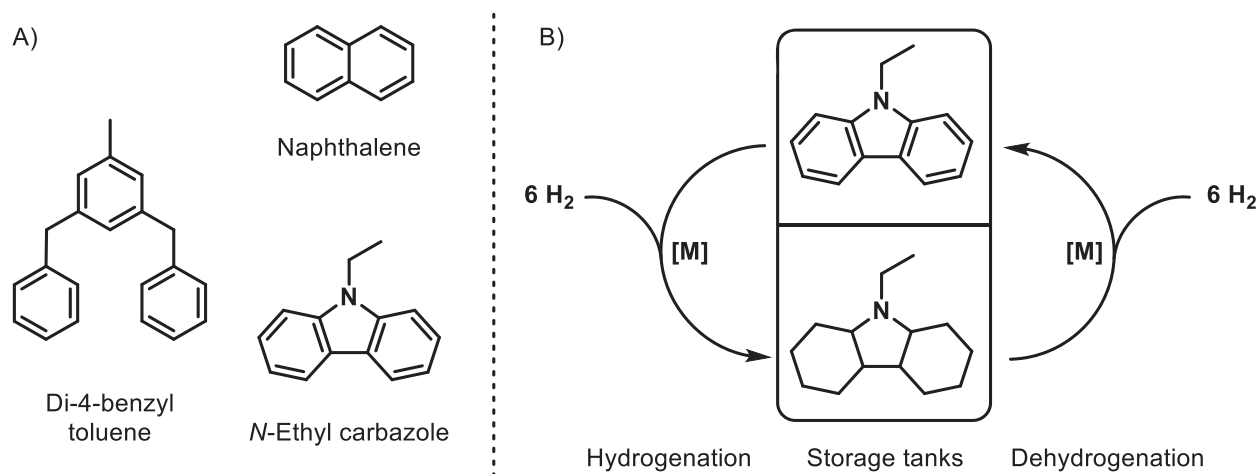


Figure 4.1: Liquid organic hydrogen carriers.

A) Examples of LOHCs.

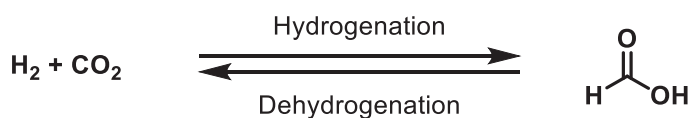
B) Hydrogen storage cycle with an LOHC with the example of *N*-ethyl carbazole using an organometallic catalyst.

A serious disadvantage of most LOHCs is that their dehydrogenated form needs to be stored in the LOHC-powered vehicle until the end of the travel. In practice, this means that a vehicle fueled by an LOHC will have to contain two fuel tanks, one for the hydrogenated LOHC, and one for the dehydrogenated LOHC.¹¹⁵ An increase in vehicle complexity, weight, and volume follows, all of which make this setup less attractive for implementation and are associated with an overall higher cost, higher number of failure points, and lower energy efficiency.

4.1.2 Formic acid as a liquid organic hydrogen carrier

One way to overcome this issue is the use of formic acid (FA) as an LOHC. FA has a long history of usage as a hydrogen carrier in various fields of organic and inorganic chemistry, such as secondary amine methylations with formaldehyde first described by ESCHWEILER,¹¹⁶ or the reductive amination of ketones using ammonium formate in the LEUCKART reaction.¹¹⁷ While the vast quantity is industrially produced by hydrolysis of methyl formate from methanol and carbon monoxide,¹¹⁸ it can also be synthesized by equimolar hydrogenation of carbon dioxide with hydrogen, see Scheme 4.1. With a hydrogen capacity of 4.38 weight%, it offers a very high energy density of 6.34 MJ/L, which supersedes that of pressurized hydrogen gas (5.04 MJ/L at 700 bar) without the disadvantages of a pressure vessel.¹¹⁹ After dehydrogenation, CO_2 can be released into the atmosphere, which means that no second tank is required for LOHC recycling. If the CO_2 is produced from non-fossil sources, such as in a powerplant burning biogas or biowaste, this cycle is CO_2 -neutral. With a melting point of 8.4°C and a boiling point of

100.8 °C at ambient pressure,¹²⁰ FA can be easily transported in its liquid state using current technology. Formic acid is flammable and has been proposed as a liquid fuel in reciprocating engines¹²¹ and liquid-fueled turbines.¹²² Additionally, it has been studied extensively in fuel cells.¹²³ Together, these technologies potentially open up applications in the shipping, automotive, and aviation industries.



Scheme 4.1: Formic acid as an LOHC.

4.1.3 Formic acid dehydrogenation by homogeneous catalysis

Homogeneous catalysis has previously been shown to be a viable means of formic acid dehydrogenation, using various metals in a plethora of different conditions. In 1967, COFFEY reported the first instance of this reaction, using complexes of Pt(II), Ru(II) and Ir(III), out of which the latter showed the highest activity in the initial screening.¹²⁴ Since then, this field has steadily gained momentum in the endeavour to create a practical system, yielding evermore improving activities at continuously milder reaction conditions. While COFFEY's original work performed this reaction in acetic acid, the reaction is now known to work in organic solvents, water,^{125,126,127} and also in neat formic acid.¹²⁸ Most catalysts reported for this transformation still use ruthenium or iridium complexes, showing excellent performance under a variety of conditions. Iridium complexes are usually cationic and use bidentate amine ligands, such as the systems by LI and HIMEDA depicted below,^{125,129} the latter showing extraordinary activity at temperatures as low as 50 °C.

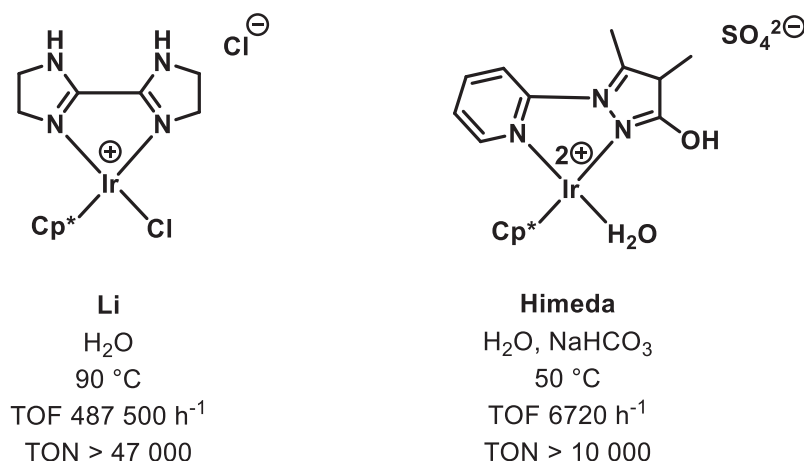


Figure 4.2: Examples of iridium-based catalysts for formic acid dehydrogenation.

When it comes to ruthenium catalysts, three examples should be mentioned, they are listed below in Figure 4.3. In 2014, PIKDO used a pyridine-type PNP pincer, which showed extreme TOFs of up to 257000 h⁻¹ when adding a basic trialkylamine.¹³⁰ Very recently in 2021, MILSTEIN applied the same catalyst shown previously for ethanol upgrading in formic acid dehydrogenation, reaching high turn-over numbers of 1.7 million in neat formic acid.¹³¹ Unfortunately, both of these systems required additives/solvents or the treatment of the catalysts under inert conditions. Both of these problems were solved in our workgroup by using the commercially available catalyst Ru-MACHO-BH in an ionic liquid as a solvent.¹³² In the next subchapter, I will therefore give a brief introduction into ionic liquids, mainly focusing on their properties and use cases.

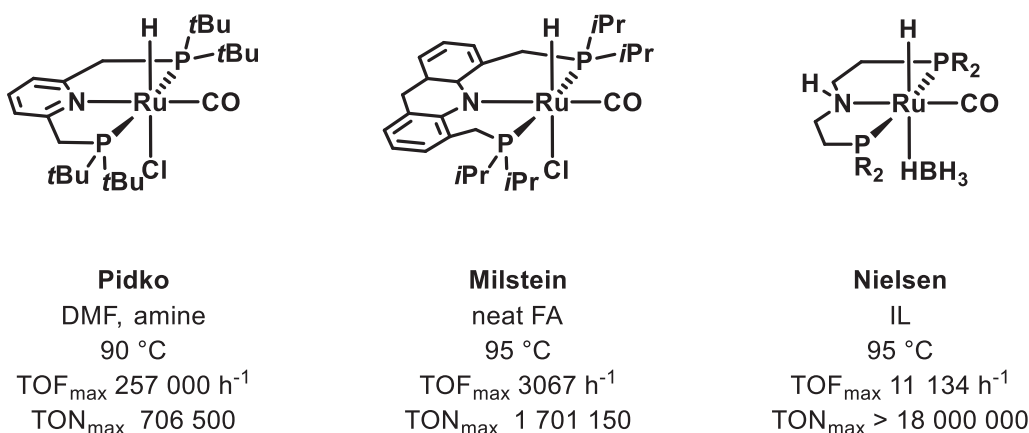


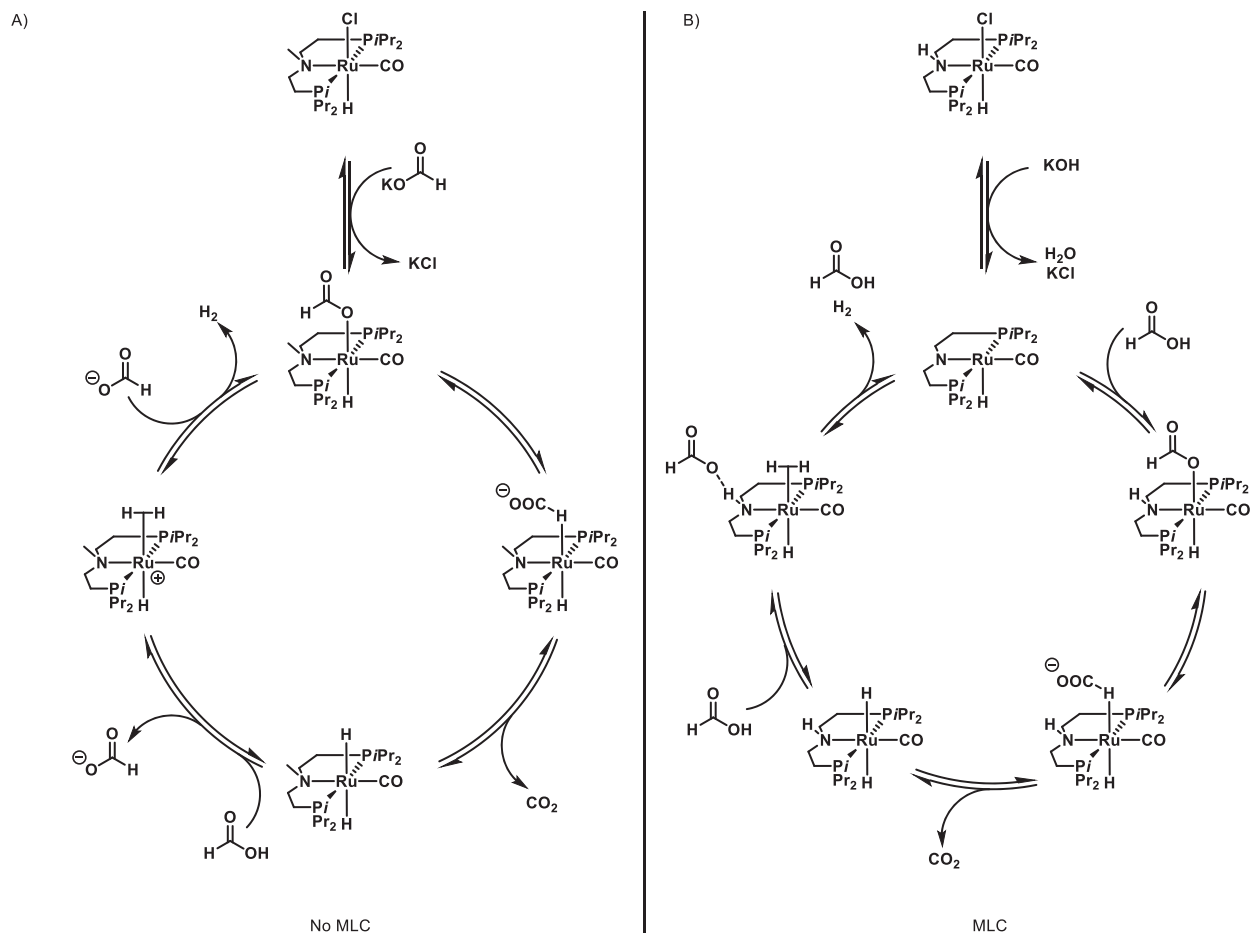
Figure 4.3: Examples of ruthenium catalysts for formic acid dehydrogenation.

4.1.4 Formic acid dehydrogenation mechanisms

Similar to the dehydrogenation of ethanol in GUERBET-type ethanol upgrading, the dehydrogenation of formic acid to carbon dioxide usually follows two different subtypes. In the first route, the ligand plays no active role in the dehydrogenation of the formic acid, and the reaction is completely inner-sphere. The second route occurs through the formation of activated dearomatized, imido, or amido species, as described earlier, using the principle of metal-ligand cooperation. A good comparison can be given by the following example using a Ru-PNP pincer system, depicted in Scheme 4.2.

In 2019, BELLER investigated the influence of an *N*-methylation of the pincer complex of a typical Ru-MACHO complex in formic acid dehydrogenation.⁴⁷ Their results showed an increased activity of the *N*-methylated complex over the non-methylated analogue. While the authors proposed two completely different reaction mechanisms, they reasoned that the protonation of a dihydrido species to form a dihydrogen complex, which then liberates hydrogen gas, was the key step of both reaction pathways. Their complexes were first activated by ligand exchange using potassium formate, and the corresponding formato complexes were considered to be the active species. At a temperature of 92 °C, they observed TOFs of up to 6800 h⁻¹ for the *N*-methylated species.

4. Formic acid dehydrogenation using Ru-POP pincer complexes



Scheme 4.2: Comparison between *N*-protonated and *N*-methylated PNP pincer complexes.

A) *N*-methylated pincer.

B) Non-methylated pincer.

Higher activity with methylated pincer, according to BELLER.⁴⁷

4.1.5 Ionic liquids as solvents for formic acid dehydrogenation

In recent years, the new solvent class of ionic liquids has gained interest throughout multiple fields of chemistry. Typically, the term “ionic liquid” is defined as any organic or inorganic salt that has a melting point below 100 °C.¹³³ Due to some of their chemical and physical properties, they are often seen as a green alternative to commonly used organic and inorganic solvents. One of their main advantages consists of their very low vapour pressure at room temperature, caused by their ionic nature. This means that ILs are not flammable and that no refluxing setups are needed for reactions using them as solvents. Additionally, they are thermally and chemically stable towards many reagents and can often be recycled from reaction mixtures by various techniques such as distillation of the reaction products,¹³⁴ extraction of hydrophilic products out of hydrophobic ILs using water,¹³⁵ or by nanofiltration using selectively permeable membranes.¹³⁶ Due to their ionic nature, their properties are highly tunable towards the desired reactions as their cat- and anions can be mixed and matched accordingly. Typical cations are phosphonium,^{137,138} ammonium,^{139,140} pyridinium¹⁴¹ and imidazolium ions,¹⁴² out of which the last group certainly plays the biggest role. These are combined with anions such as triflates,¹⁴³ alkylsulfates and alkylsulfonates,^{144,145} carbonates,¹⁴⁶ carboxylates,¹³⁹ (alkyl)phosphates and phosphinates,¹⁴⁰ hexafluorophosphate,¹⁴⁷ tetrafluoroborate,¹⁴⁷ halogenides and even hydroxide.¹³⁷

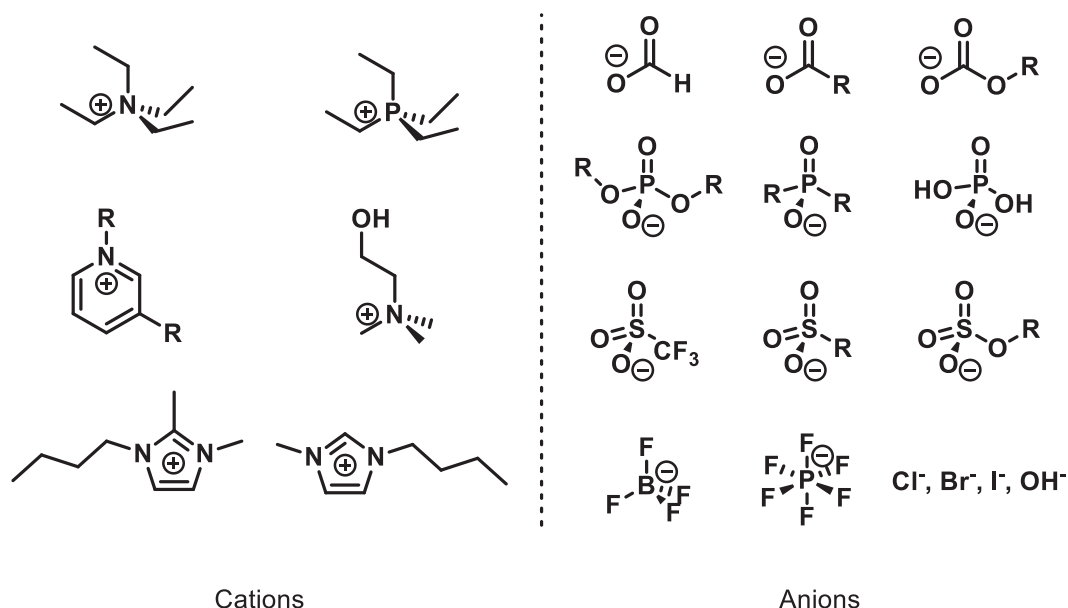


Figure 4.4: Typical cations and anions of ionic liquids.

4.1.6 Aim of the project

As previously described, our workgroup extensively studied ionic liquids as a solvent medium for formic acid dehydrogenation using Ru-PNP pincer complexes.¹³² In batch reactions at a temperature 80 °C, turnover frequencies of up to 1260 h⁻¹ were observed using the commercially available catalyst Ru-MACHO-BH and its *i*Pr-derivatives, and commercially available ionic liquids. The reaction could be improved further by a continuous formic acid feeding setup, which led to turnover numbers exceeding 18 million. The same catalyst system, albeit the corresponding *trans*-dihydrido complex, was also shown to be active in the opposite reaction, efficiently hydrogenating CO₂ to formic acid already at ambient temperatures and low gas pressures of up to 30 bar.

It is the aim of this project to investigate the previously synthesized Ru-POP pincer complexes **Ru-1a** to **Ru-10a** described in Chapter 2 of this thesis for their utility in the dehydrogenation of formic acid using ionic liquids as a solvent. This is meant as a way to investigate the findings by e.g. BELLER,⁴⁷ showing that MLC is not a requirement for high activity, even in the same catalyst family, as other factors such as ease of protonation might be a more relevant concern. The project begins with the screening of the previously synthesized complexes. The optimization of reaction conditions using the best of the complexes will follow. During these steps, investigations into the reaction mechanism will take place, mainly by NMR spectroscopy.

4.2 Formic acid dehydrogenation catalysis reactions

4.2.1 Activity screenings

To assess the value of synthesizing the POP pincer complexes **Ru-1a** to **Ru-10a** for formic acid dehydrogenation, it is important to understand the catalytic capabilities of their precursor first. Therefore, a temperature screening of $[\text{RuHCl}(\text{PPh}_3)_3]$ toluene adduct was performed. For this, BMIM-OAc was chosen as the ionic liquid due previously obtained data showing high reaction conversions in it when using Ru-PNP catalysts such as Ru-MACHO-BH.¹³² Using 1.0 mL of BMIM-OAc (5.35 mmol), 13 μmol of the precursor was dissolved and after 10 minutes of stirring, formic acid (13.25 mmol, ~1020 equivalents relative to the catalyst) was injected. Figure 4.5 shows the calculated conversions obtained at reaction timeframes between 10 and 180 minutes.

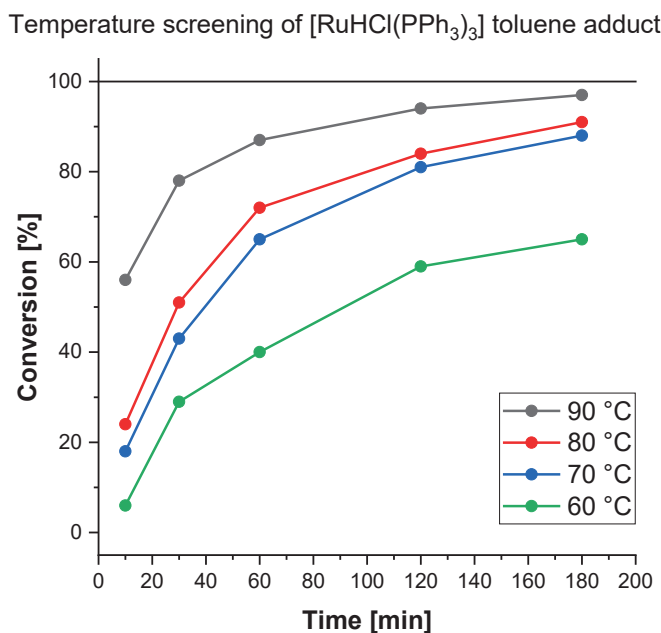


Figure 4.5: Temperature screening of $[\text{RuHCl}(\text{PPh}_3)_3]$ toluene adduct.

Reaction conditions: 0.5 mL formic acid, 1.0 mL ionic liquid, 13.0 μmol catalyst.

Conversion calculated from $^1\text{H-NMR}$ using IL as internal reference.

In all cases, no major induction periods are observed, meaning that the catalyst is unlikely to undergo a slow transformation into an active species, or that this conversion is too fast to be observable with this dataset. At 90 °C, 56% conversion ($\text{TOF} = 3425 \text{ h}^{-1}$) is reached after only 10 minutes, which increases to almost quantitative 97% conversion after three hours. Reducing the temperature to 80 °C reduces the

conversion after 10 minutes by more than half to 24% (TOF = 1468 h⁻¹), and reductions to 70 and 60 °C continue this trend to 18% (TOF = 1101 h⁻¹) and 6% (TOF = 366 h⁻¹), respectively.

The precursor's dataset serves as a baseline to determine the value of the additional synthetic step to the POP pincer complexes. To investigate the catalysts' activity compared to their precursor, screening experiments of them in the IL using the same conditions were performed. Catalysts **Ru-1a** to **Ru-9a** proved to be completely soluble under these reaction conditions even at room temperature, but the systems were kept at the chosen screening temperature of 90 °C for 10 minutes to assure a complete solution before the formic acid was injected. **Ru-10a** did not dissolve in pure BMIM-OAc even after prolonged heating to 90 °C, but immediately dissolved upon injection of formic acid. An overview of the catalyst screening can be found below, and exact data as well as the experimental setup are listed and described in Table 9.6 in Appendix E.

In the screening of the diphenylphosphine containing complexes, **Ru-1a** turned out to be the best, delivering 74% conversion within the first 10 minutes of the experiment time (TOF = 4525 h⁻¹). The reactivity of **Ru-4a** was slightly lower. Unfortunately, **Ru-2a** was shown to be significantly less active than its counterparts, and only delivered 27% conversion within 10 minutes, stagnating at 84% after 3 hours.

When it comes to the diisopropylphosphine-containing complexes, **Ru-8a** was significantly faster than the other complexes, with 60% conversion (TON = 3670 h⁻¹) after 10 minutes and 90% conversion after 30 minutes. Full conversion at over 99% was reached after only 60 minutes, after which the experiment was stopped. Interestingly in this dataset, the ethylene-bridged **Ru-7a** was by far the slowest, showing no conversion after only 10 minutes.

Both cyclohexyl phosphine containing complexes **Ru-9a** and **Ru-10a** were significantly outcompeted by their precursor and showed slow activity compared to their isopropyl counterparts **Ru-5a** and **Ru-6a**. This could point towards the bulkiness of the dicyclohexylphosphines slowing catalytic performance. They were subsequently no longer investigated in this project.

4. Formic acid dehydrogenation using Ru-POP pincer complexes

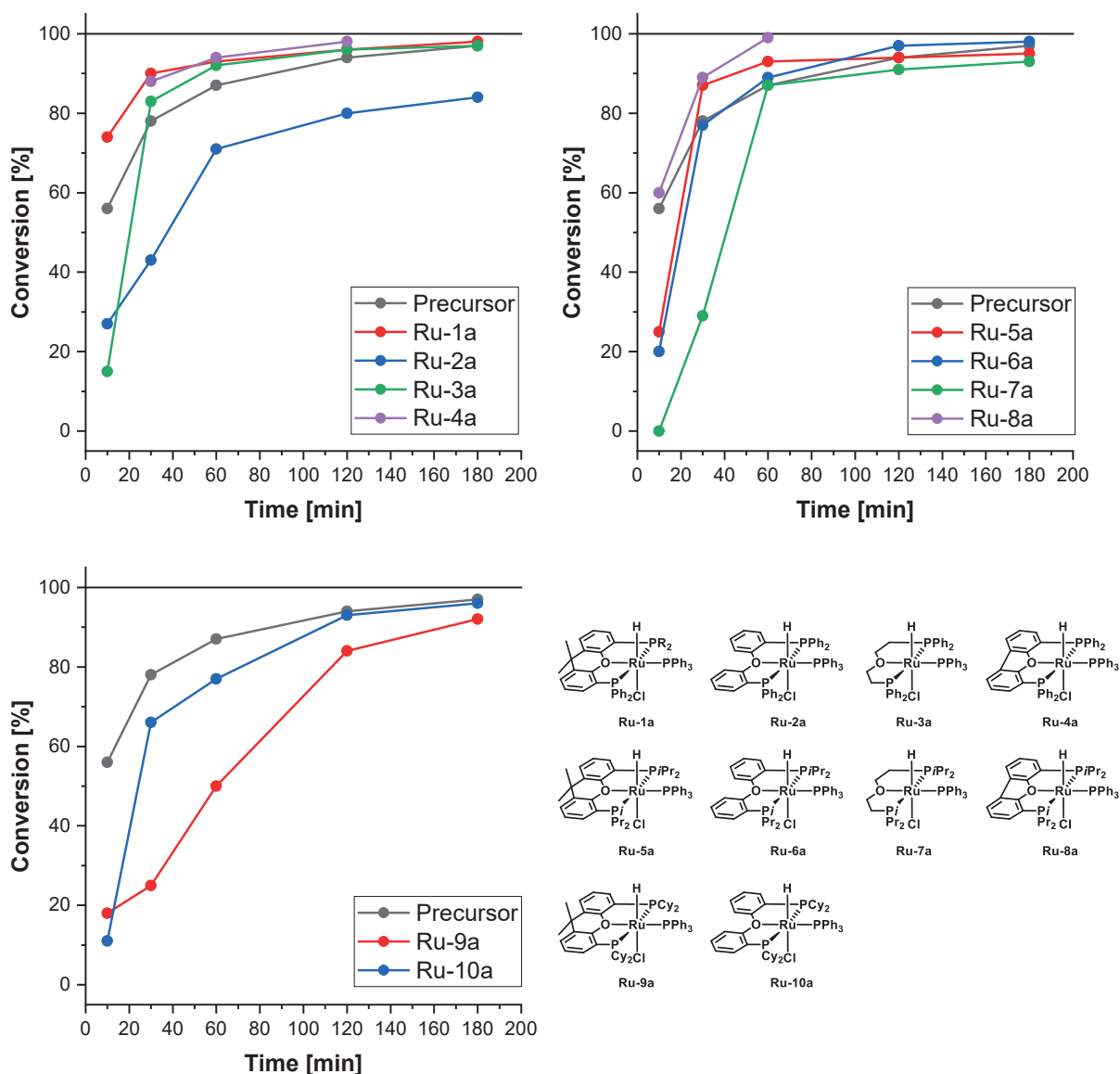


Figure 4.6: Catalyst screening of **Ru-1a** to **Ru-11a**.

Reaction conditions: 0.5 mL formic acid, 1.0 mL ionic liquid, 13.0 μmol catalyst, 90 $^{\circ}\text{C}$.

Conversion calculated from ^1H NMR using IL as internal reference.

In the next step, the catalytic activities of the best catalysts **Ru-1a** and **Ru-8a** were investigated further. Their reaction temperatures were reduced in steps of 10 $^{\circ}\text{C}$. While **Ru-1a** was instantly active at 90 $^{\circ}\text{C}$, yielding quantitative conversions in about one hour, this activity fell drastically at lower temperatures. At 80 and 70 $^{\circ}\text{C}$, low conversions around of 18 and 23% were observed after 10 minutes, but this increased

to high conversions of 88 and 73% respectively after 30 minutes and both experiments showed conversions over 90% within two hours. After a further temperature reduction to 60 °C, no conversion was found in the first 30 minutes of the experiment. A corresponding diagram can be found below, and all data is listed in Appendix E.

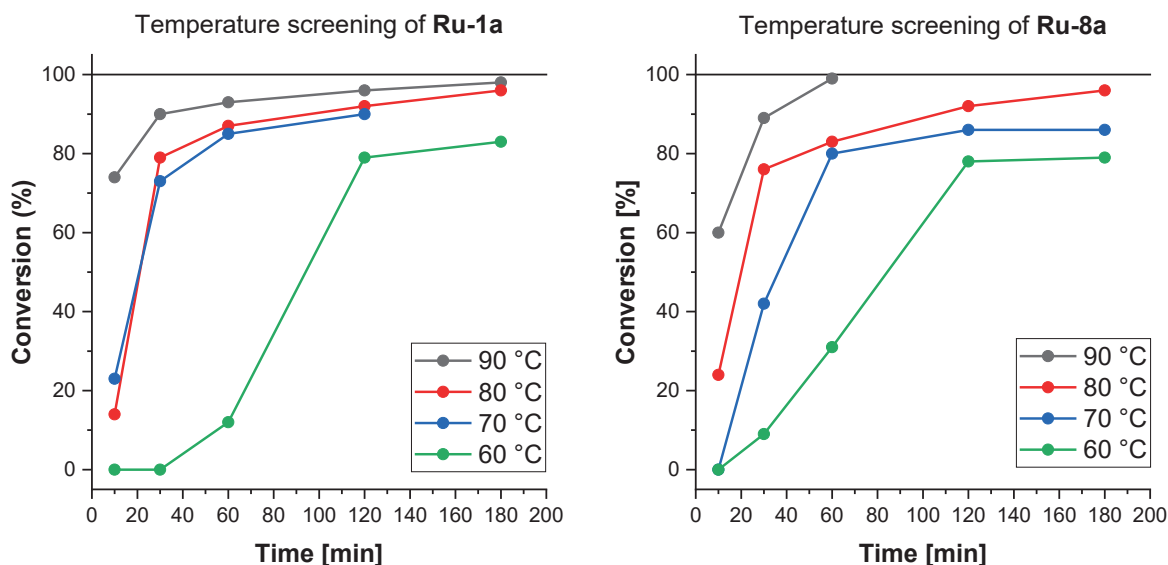


Figure 4.7: Temperature screening of **Ru-1a** and **Ru-8a**.

Reaction conditions: 0.5 mL formic acid, 1.0 mL ionic liquid, 13.0 μmol catalyst.

Conversion calculated from ^1H NMR using IL as internal reference.

The apparent inactivity of **Ru-1a** at 60 °C (and also at 70 and 80 °C after 10 minutes) compared to the precursor points towards the requirement for a catalyst activation period, in which the pre-catalyst **Ru-1** is transformed into the active species. It is reasonable to assume that this activation period is present at all temperatures, however cannot be detected with a temporal resolution of 10 minutes after formic acid injection. In contrast to this, the temperature screening of **Ru-8a** revealed no apparent activation period. Compared to **Ru-1a**, **Ru-8a** showed higher activities at 30 and 60 minutes at 60 °C.

The temperature screenings of the precursor, **Ru-1a**, and **Ru-8a** can be used to calculate the activation energies with an ARRHENIUS plot.⁴⁷ Details can be found in Appendix E. The linear fits of the natural logarithm of the turnover frequency over the reciprocal absolute temperature are directly proportional to the activation energies. The data suggests activation energies of 50.4 kJ/mol for the precursor, 59.7 kJ/mol for **Ru-1a** and 63.7 kJ/mol for **Ru-8a**. Unfortunately, due to the measurement method, the R^2 values of the linear fits are rather large, and therefore no definitive conclusions should be taken from them. To obtain more precise values, the experiments should be upscaled in the future, and gas volumetry should be used to determine conversions instead of NMR measurements.

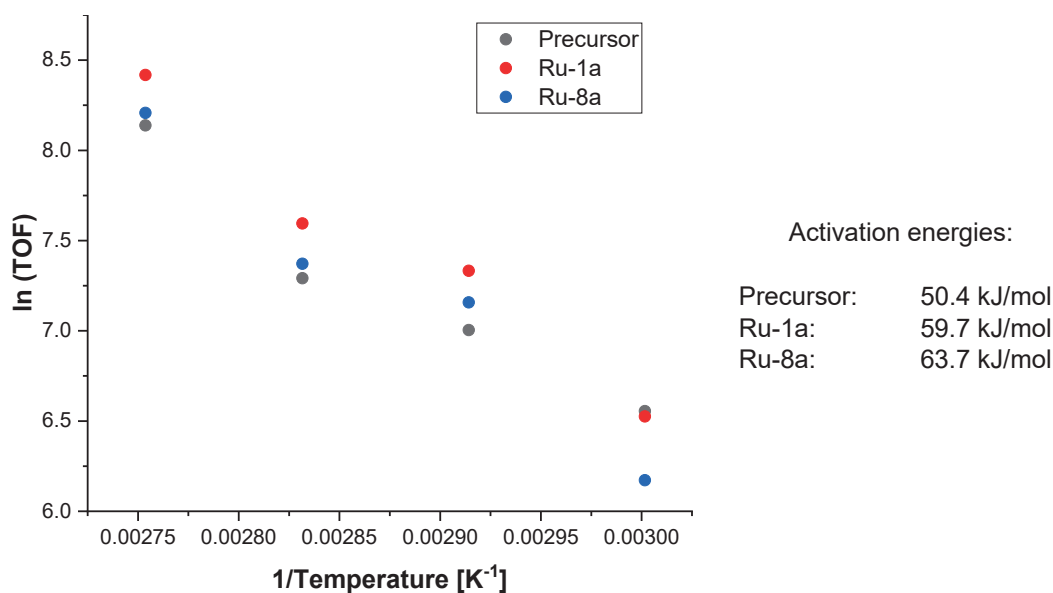


Figure 4.8: ARRHENIUS plots of $[\text{RuHCl}(\text{PPh}_3)_3]$ toluene adduct, **Ru-1a** and **Ru-8a**.

Linear fits, calculations and methodology can be found in Appendix E.

In order to fully understand the activation process of these two catalysts, it was decided to attempt screenings of the chlorido-abstracted complex cation. Therefore, another chloride abstraction was performed on **Ru-8a**, synthesizing the additional PF_6^- and BPh_4^- salts **Ru-8c** and **Ru-8d**. The same synthesis protocol was used as for the BF_4^- salt **Ru-8b**, as described previously in chapter 2 of this work. As of the time of writing, only **Ru-8c** could be analyzed by crystallographic means, so only it was tested for formic acid dehydrogenation.

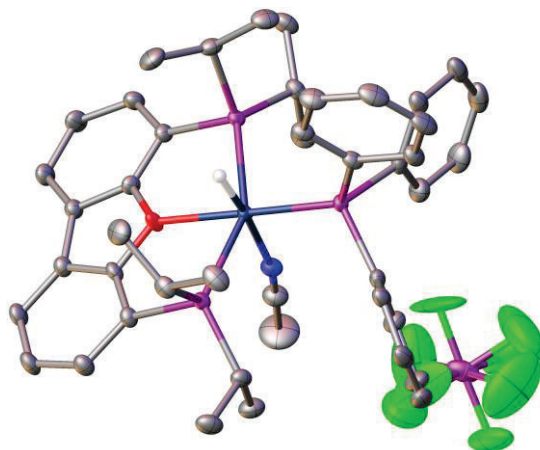


Figure 4.9: Crystal structure of **Ru-8c**.

Hydrogen atoms on C and co-crystallized solvents omitted for clarity. Thermal ellipsoids are shown at 50% probability level.

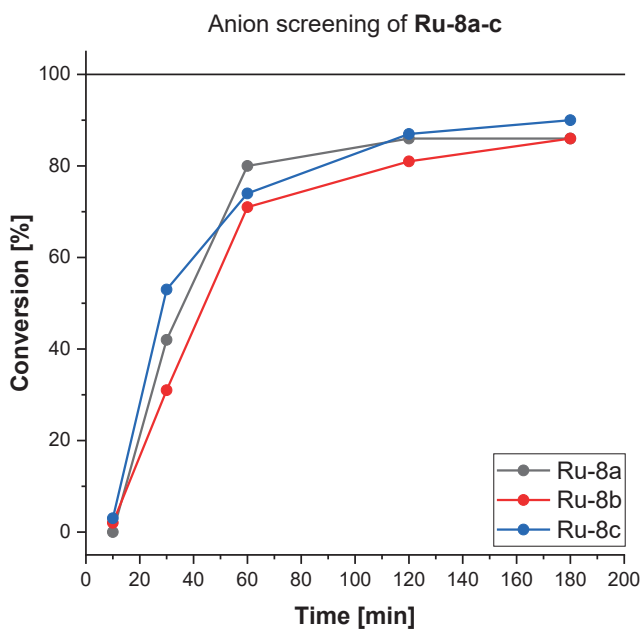


Figure 4.10 Anion screening of **Ru-8a-c**.

Reaction conditions: 0.5 mL formic acid, 1.0 mL ionic liquid, 13.0 μmol catalyst, 70 $^{\circ}\text{C}$.

Conversion calculated from ^1H NMR using IL as internal reference.

In this experiment, the average reaction rate stayed approximately the same between the chlorido complex **Ru-8a**, and the cationic species **Ru-8b** and **Ru-8c**. This points to the abstraction of the chloride ion as not being a major factor in catalyst reactivity. It is likely that the chloride abstraction in the ionic liquid happens too fast for chloride abstraction to be worth the additional synthetic step.

4.2.2 Investigations into reaction mechanism and reaction of the complexes with the ionic liquid

A few different methods were attempted to investigate the reaction mechanism of formic acid dehydrogenation with the complexes. First, a quick experiment was run in which neat formic acid was dehydrogenated with complex **Ru-7a** under conditions otherwise identical to the previous catalytic screening. No gas formation at all was observed, which points to the ionic liquid playing an integral role in the catalytic cycle. This suggests the absence of mechanisms in which only the ruthenium complex itself is catalytically active, such as proposed by MILSTEIN.¹³¹ More likely, an influence by the ionic liquid is present, such as protonations and deprotonations.

To investigate the reaction mechanism, samples of the reaction mixtures were analyzed using NMR. It was decided to concentrate only on the best catalysts, **Ru-1a** and **Ru-8a**, for further investigations. The signals of the hydrido ligands on the catalysts were the primary focus of this investigation, due to the very clear differences in $^2J_{H-P}$ between the hydrides and the phosphine ligands. As the concentration of the catalyst in the ionic liquids were very low, NMR acquisition times had to be severely increased. In the case of **Ru-1a**, the typical doublet of a triplet pattern was observed for the first 60 minutes of the reaction. While shifted significantly downfield from -16.29 to -13.35 ppm, it showed coupling constants to phosphine of 27.2 and 18.4 Hz, respectively (Figure 4.11 peak A). This is compatible with all three phosphines being in a *cis*-configuration to the hydrido ligand and shows that the ligand configuration is somewhat stable in the ionic liquid over the course of approximately one hour during the experiment. The strong downfield shift might be explained by the abstraction of chloride and its exchange by MeCN in the NMR tube or by the formation of the corresponding acetato and formato complexes. Over the course of this experiment, the intensity of this signal decreases, and after 180 minutes of reaction time, it disappears completely. Instead, two new signals were detected. The first shows an apparent dt pattern and occurs at -6.4 ppm (peak B). With a coupling constant of around 130 Hz, this suggests that one of the phosphines is moved to a *trans*-position relative to hydrido. This would make sense in a step of the catalytic cycle, as it would free the active *cis*-position. Alternatively, the low chemical shift suggests that this might be a dihydrido species. The second new peak is found at -17.5 ppm. While its multiplicity is not clear, it is suggested to be a triplet with a small coupling constant of 17.3 Hz, suggesting the liberation of triphenylphosphine (peak C).

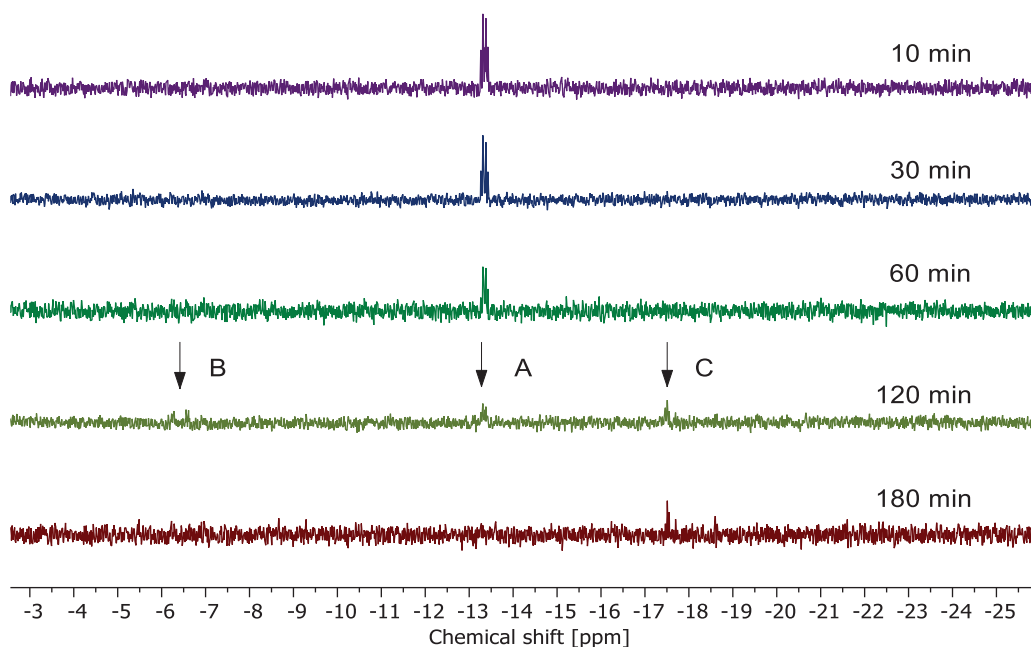


Figure 4.11: Hydride region of the ^1H NMR spectrum of **Ru-1a** during formic acid dehydrogenation.

Reaction conditions: 0.5 mL formic acid, 1.0 mL BMIM-OAc, 13.0 μmol catalyst, 90 $^\circ\text{C}$.

NMR taken in MeCN-d_3 , 500 μL deuterated solvent, $\sim 10\mu\text{L}$ reaction mixture.

Interestingly, once the quartet at -13 ppm is starting to diminish around one hour after the beginning of the experiment, the activity of the catalyst seems to drop as well. This suggests that the configuration of three phosphines *cis* to hydride is the more reactive active species. It could therefore be useful for catalysis to stabilize this configuration by the addition of phosphine to the solution, or by exchanging PPh_3 by a more electron-rich phosphine, binding more stably to the ruthenium center.

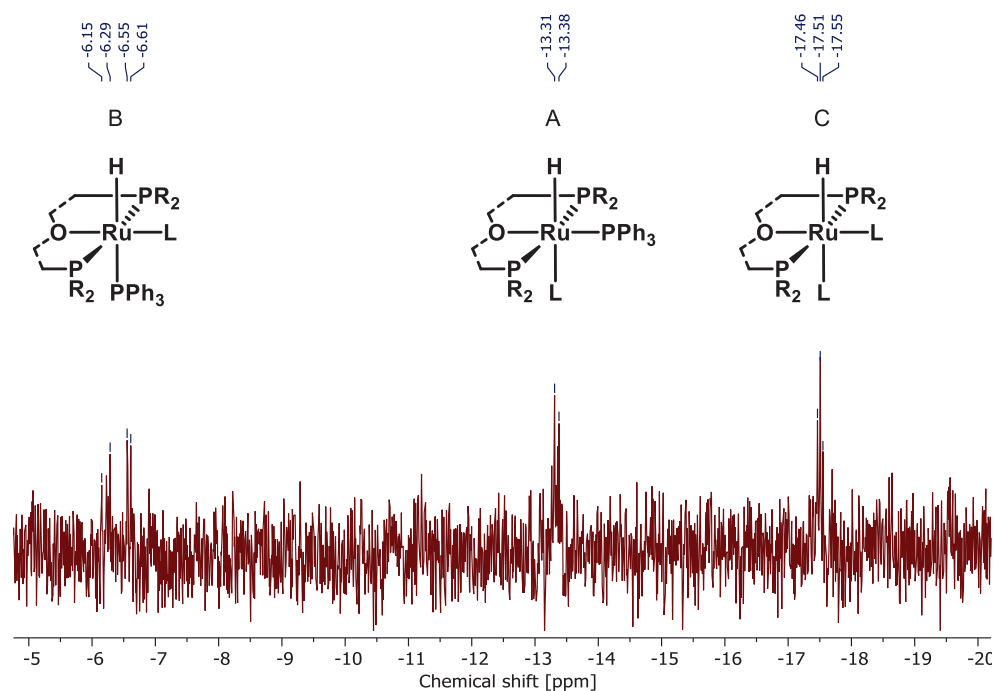


Figure 4.12: Hydride region of the ^1H NMR spectrum of **Ru-1a** during formic acid dehydrogenation after 120 minutes.

Suggested complex configurations for the different signals.

Reaction conditions: 0.5 mL formic acid, 1.0 mL BMIM-OAc, 13.0 μmol catalyst, 90 $^\circ\text{C}$.

NMR taken in MeCN-d_3 , 500 μL deuterated solvent, $\sim 10\mu\text{L}$ reaction mixture.

To gain insight into the catalytic activity, the complex with the lowest activity, **Ru-2a**, was investigated the same way. In contrast to the relatively stable quartet of **Ru-1a**, the spectrum of **Ru-2a** already shows a complete loss of the hydride quartet corresponding to the starting material after 30 minutes. Instead, two new peaks form between 30 and 60 minutes. The first is a quartet at -6.6 ppm ($J = 26.1$ Hz) and a doublet of a triplet at -8.8 ppm ($J = 76.6, 28.8$ Hz) are found. The turnover number of this complex significantly lowers after approximately 60 minutes of reaction time (see Figure 4.6), which points to the two peaks shown below corresponding to a catalytically inactive species. While the peak integrals are roughly 1:1, similar stoichiometric NMR experiments previously done in Chapter 3 propose that these signals correspond to two distinct species.

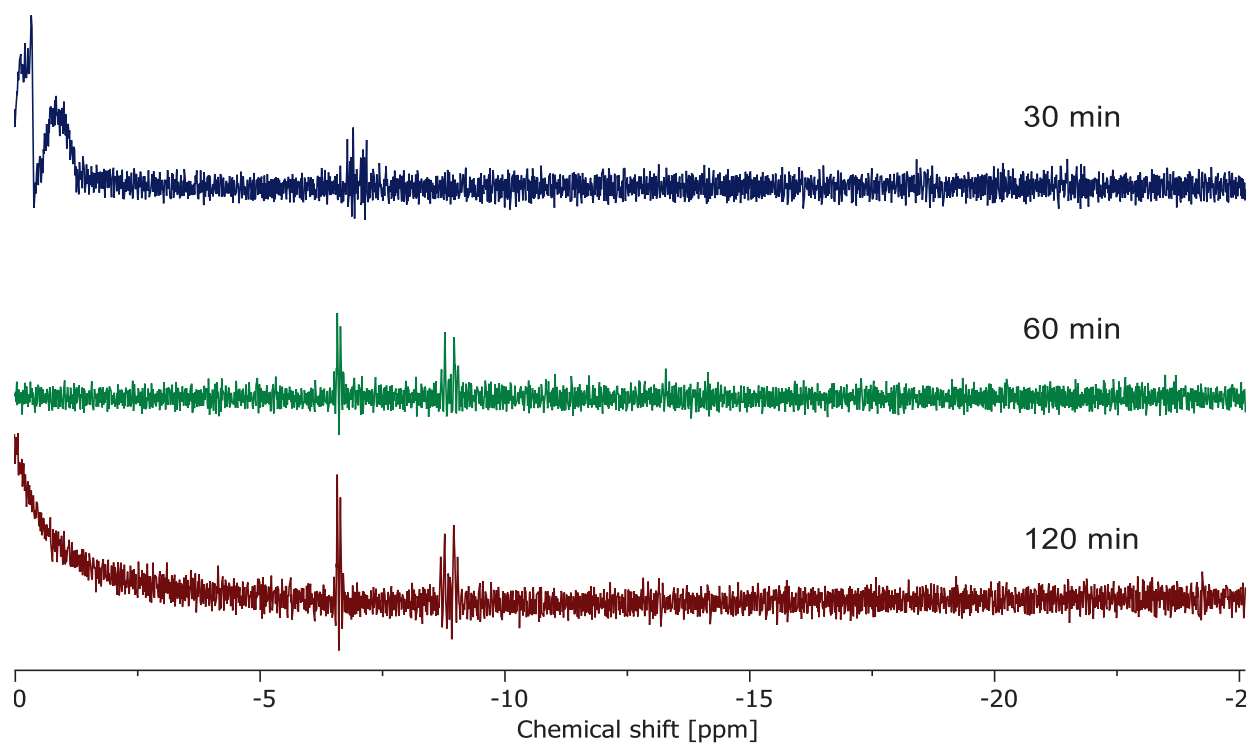


Figure 4.13: Hydride region of the ^1H NMR spectrum of **Ru-2a** during formic acid dehydrogenation.

Reaction conditions: 0.5 mL formic acid, 1.0 mL BMIM-OAc, 13.0 μmol catalyst, 90 $^\circ\text{C}$.

NMR taken in MeCN-d_3 , 500 μL deuterated solvent, $\sim 10\mu\text{L}$ reaction mixture.

Peak A in Figure 4.14 at -6.6 ppm likely corresponds to the complex in which all phosphorous atoms are *cis* to the hydrido ligands. The downfield position in the hydride region suggests that this signal might be the *trans*-dihydrido complex. The large coupling constant of 76.6 Hz at the second peak at -8.8 ppm likely corresponds to one of the three two atoms being *trans* to the hydride. Attempts were made at screening the ^{31}P nucleus to determine the exact configurations, but with the available maximal acquisition times, no useable signals could be differentiated from background noise.

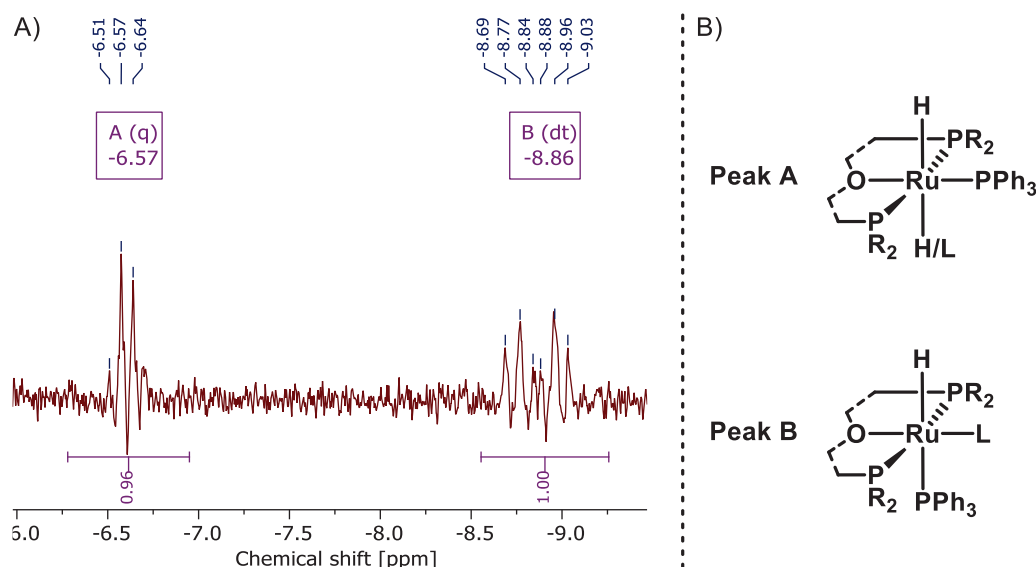


Figure 4.14: Hydride region of the ^1H NMR spectrum of **Ru-2a** during formic acid dehydrogenation after 120 minutes.

A) ^1H NMR spectrum.

B) Suggested structure of forming complex. Linker omitted for clarity.

To investigate the reactivity of the complex with the ionic liquid independently from the formic acid reactions, an experiment was performed in which **Ru-1a** was dissolved in BMIM-OAc. After dissolution and slight warming, the reaction was left standing for 24 hours. The following NMR experiment (Figure 4.15) gave insight into the reaction products of BMIM-OAc with the catalyst. Due to the low mobility of the ionic liquid as a solvent, all peaks were severely broadened and no multiplicities could be investigated. In the ^1H spectrum, two peaks were observed at -19.28 ppm (major) and -19.75 ppm (minor). The ^{31}P spectrum showed three expected peaks. The first, at 70.47 ppm, likely corresponds to ruthenium-coordinated triphenylphosphine. The second one at 44.27 ppm likely corresponds to the POP ligand when bound to ruthenium in a $\kappa^3\text{-P,O,P}$ pincer configuration. A third major peak was found at -7.14 ppm, close to the chemical shift of free triphenylphosphine at 4.7 ppm in C_6D_6 ,¹⁴⁸ confirming the

previously suspected dissociation of the PPh_3 ligand during the reaction. Two very small peaks at 50 and 55 ppm were also found, yet so far their corresponding structure is unknown.

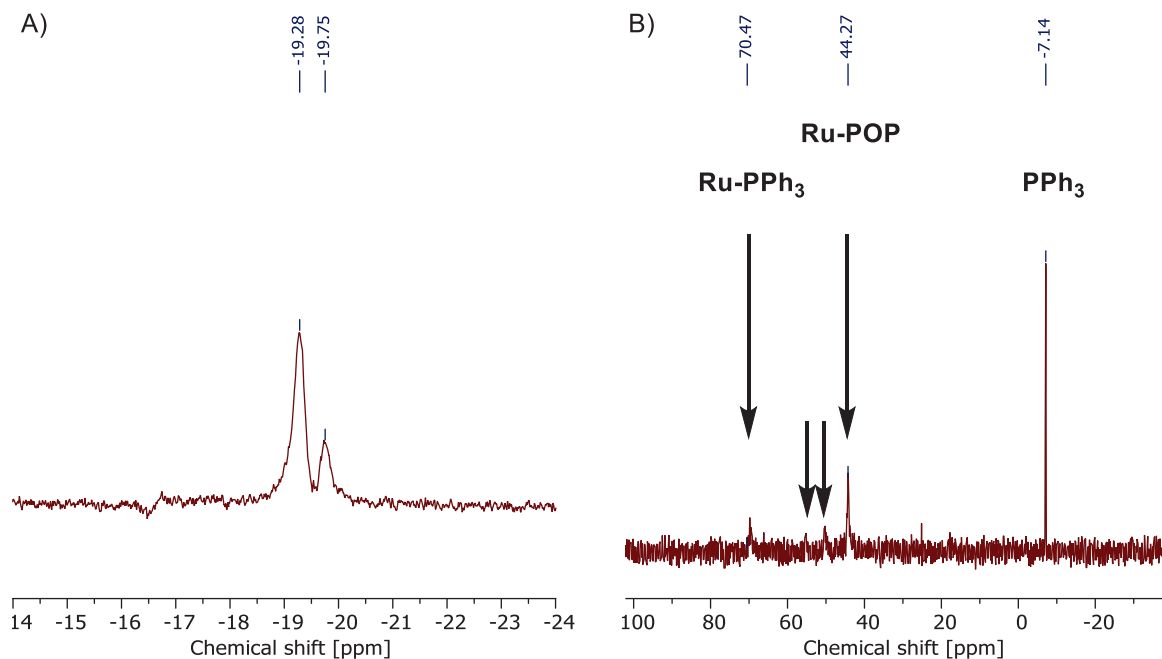
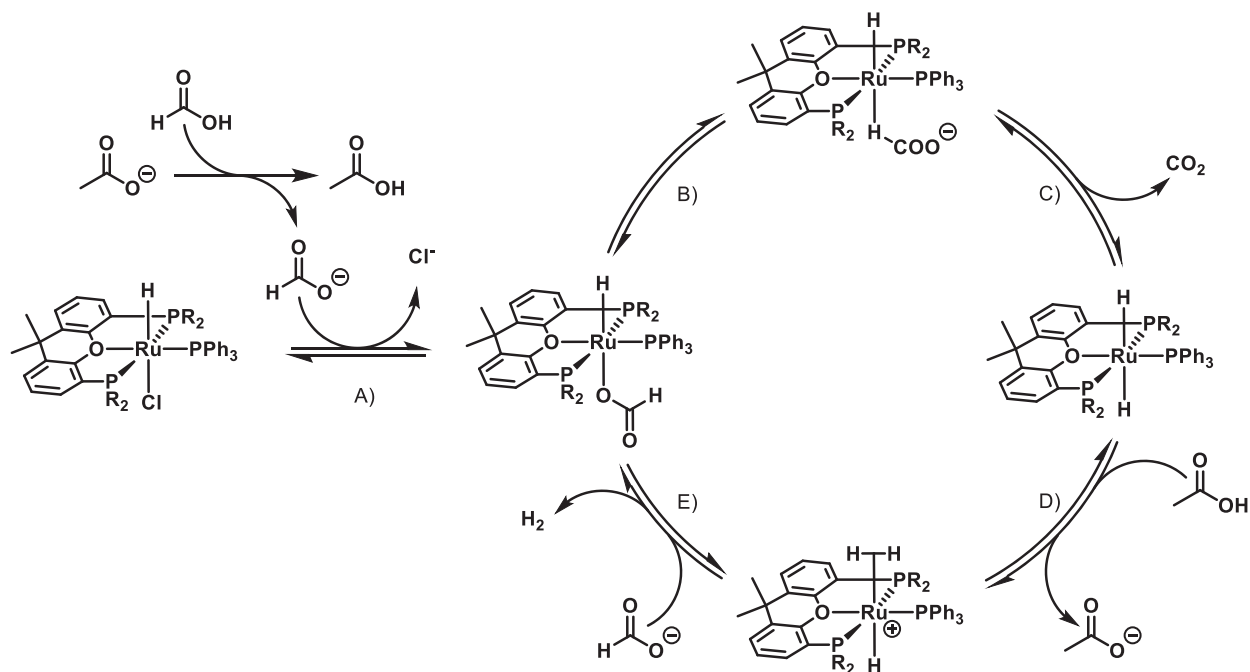


Figure 4.15: Reaction of **Ru-1a** with BMIM-OAc after 24 hours at 40 °C.

- A) Hydride region of the ^1H spectrum
 B) $^{31}\text{P}\{^1\text{H}\}$ spectrum of in BMIM-OAc after 24 hours.

4.2.3 On the catalytic cycle

Based on this information, possible catalytic cycles can be proposed. One possibility is a cycle similar to that proposed previously by BELLER using an *N*-methylated Ru-PNP pincer complex.⁴⁷ The analogous reaction mechanism using **Ru-1a** as catalyst is depicted in Scheme 4.3. Since the complexes show no activity without the presence of the ionic liquid, its involvement must be necessary. The basicity of the free acetate to deprotonate formic acid is one likely pathway. Since formic acid is more acidic than acetic acid,¹⁴⁹ formate ions are present. These can undergo ligand exchange with chloride, yielding a formato complex (A). Reconfiguration of this complex (B) leads to CO₂ liberation (C), forming a *trans*-dihydrido species. The low chemical shift of a species found in situ presented earlier might point towards the presence of this dihydrido complex. The following protonation towards a dihydrogen complex with the previously formed acetic acid (D) was proposed to be the key step in BELLER's reaction using an analogous *N*-methylated PNP pincer. Additionally, the proposed dihydrogen complex [RuH(H₂)(xantphos)(PPh₃)]⁺ has previously been synthesized in stoichiometric reactions using **Ru-1a** under a hydrogen atmosphere after chloride abstraction by a sodium salt.⁵² Elimination of hydrogen gas and coordination of formate (E) then completes the cycle.



Scheme 4.3: Proposed inner-sphere catalytic cycle for FA dehydrogenation with a Ru-POP pincer complex.

4.3 Conclusions and outlook

To summarize this project, the complexes previously synthesized were screened for their activity for formic acid dehydrogenation using the ionic liquid BMIM-OAc as a solvent and co-catalyst. Complex **Ru-1a** and **Ru-8a** achieved high conversions at low timespans, being close in performance to the Ru-PNP pincers investigated previously in this workgroup in similar conditions, with a conversion of 99% within the first hour of the experiment, translating TOF of around 4525 h^{-1} in the first 10 minutes of the experiment at $90\text{ }^{\circ}\text{C}$. Their high reactivity was also observed after temperature reduction to 80 and $70\text{ }^{\circ}\text{C}$. ARRHENIUS activation energies were obtained, showing activation energies of the best complexes of approximately 60 kJ/mol . This work represents, to my knowledge, the first example of a use of this complex type in formic acid dehydrogenation, and also the first use of POP pincer complexes in ionic liquids. The hydride regions of the spectra were monitored, and suggest the *in situ* formation of various hydrido and dihydrido species with different configurations between phosphorous and the hydride ligand/ligands. A catalytic cycle was proposed.

Based on this data, multiple pathways for further investigation can be envisioned. For one, the hydricity manipulation of the hydrido ligand in the pre-catalyst could be the focus of future research to optimize the dihydrogen abstraction step of the catalytic cycle. This could be achieved by further screening of ligands *trans* to the hydrido, or by electron density manipulation at the ruthenium center by the use of different phosphines. As the increased bulkiness of the cyclohexylphosphines appears to be negatively influencing reactivity, a less bulky phosphine moiety, such as $-\text{P}(\text{Et})_2$ or $-\text{P}(\text{Me})_2$ could be chosen for future investigation.

The stoichiometric synthesis of the corresponding acetato and formato complexes could also be envisioned as a future endeavour and will likely prove paramount to completely understanding the catalytic cycle. Since the highest activity of this catalyst is recorded when the ^1H NMR spectrum shows the typical dt pattern, the addition of a more stable monodentate phosphine, either *in situ*, or stoichiometrically by phosphine exchange reactions could be envisioned to stabilize this configuration in the ionic liquid. Suitable candidates might be trialkylphosphines such as tricyclohexylphosphine or tri-1-adamantylphosphine. Additionally, the high conversions certainly warrant a screening of different ionic liquids, both with and without basic anions. This is interesting not only for their practical use in the industry, but also to gather further insight into their catalytic cycle, as NMR investigations could show the presence or absence of the proposed formato-complex hydride peaks around -17.5 ppm . Lastly, a future project could investigate the long-term stability of this reaction by switching from a batch system to a setup with continuous formic acid addition (for example via syringe pump injection).

5. Ruthenium-POP nitrosyl complexes

The following chapter describes my efforts to synthesize a new set of Ru(II) nitrosyl complexes bearing POP pincer ligands. In the context of my work, this project was a collaboration between myself and my colleague MIKE JØRGENSEN, who had previously developed similar complexes bearing PNP pincer ligands, which were then applied in fundamental investigations in his PhD thesis,⁵⁷ as well as transfer hydrogenations by other members of the workgroup.

5.1 Nitrosyl: A non-innocent ligand

5.1.1 Nitrosyl as a non-innocent ligand in organometallic chemistry

Redox-active ligands fulfill an important role in multiple fields of organometallic chemistry and are paramount to many biological functions in living organisms.¹⁵⁰ Termed as “non-innocent”, “suspect” and “guilty” by JØRGENSEN,¹⁵¹ their properties are in sharp contrast to those of “innocent” ligands, such as halogenides. The oxidation states of non-innocent ligands may not be immediately obvious from a trivial analysis of the complex’s structure formula, and due to this ambiguity, the oxidation state of the central metal atom as well as the ligand charges are equally ambiguous. Examples include polydentate ligands such as pyridine diamine pincers,¹⁵² π -systems of porphyrines,¹⁵³ but also very simple ligands like dioxygen.¹⁵⁴

One of the most important non-innocent ligands is the NO ligand. The system of this ligand and the metal center it coordinates to has previously been described as an “electron reservoir”, with very facile redox events occurring, either induced by co-reactants or electrochemically.¹⁵⁵ Complexes containing nitrosyl ligands are described as $\{MNO\}^n$ according to the ENEMARK-FELTHAM notation, first proposed in 1974.¹⁵⁶ In this model, n equals the sum of all electrons in the d orbitals of the metal and the π^* orbitals of the NO ligand. The most common complexes of this type fall under the categories of $n=6,7,8$, but $n=9$ and $n=10$ complexes are also known, the latter being proposed as intermediates in various bioinorganic reactions and studied *in silico*.^{157,158,159,160}

In mononuclear complexes, NO is observed to bond in two main configurations. The general trends of their properties are listed in Table 5.1.

The first group consists of the linear nitrosyl complexes. Electronically, they can be thought of as NO^+ ligands with an NO triple bond, called nitrosonium ligands, and are isoelectronic to carbon monoxide.

They are counted as three-electron donors in the covalent bonding model. The triple bond character causes high N-O stretching frequencies of 1620-1900 cm^{-1} and very short N-O bond lengths of 1.05-1.20 Å.^{161,162}

The second group consists of the bent nitrosyl complexes. These can be thought of as NO^- ligands with an NO double bond, isoelectronic to the dioxygen diradical. Counted as single electron donors in the covalent bonding model, the reduction of bond order compared to linear complexes leads to slightly longer bond lengths of 1.16-1.22 Å, and the free electron pair causes the ligand to bend.

Table 5.1: Properties of linear and bent nitrosyl complexes.

	Linear NO	Bent NO
Structure		
M-N-O angles	110-140°	160-180°
N-O bond length	1.05-1.20 Å	1.16-1.22 Å
NO stretching mode	smaller than 1620 cm^{-1}	1610-1900 cm^{-1}

A simple way to differentiate between the two modes can be achieved by means of X-ray crystallography, in which bond lengths and M-N-O angles become directly visible. Linear nitrosyl complexes are easily recognized by their high M-N-O angles approaching 180°. This angle is significantly lower in the bent complexes, with values ranging from 115-155°. Unfortunately, complications can arise when the NO group is crystallographically disordered. Specifically, a rotational disorder of the oxygen atom around the M-N axis can give the appearance of a linear configuration.

5.1.2 Aim of the project

Previously, our workgroup showed the high activity of ruthenium(II) nitrosyl complexes with a general formula of $[\text{Ru}(\text{PNP})(\text{NO})\text{Cl}_2]\text{X}$ in transfer hydrogenations.⁵⁷ Using 10 mol% NaOH as an additive, the complex reached a conversion of 96% within 30 minutes in the reduction of acetophenone to 1-phenylethanol using isopropanol as a hydrogen donor. To compare reactivities with POP complexes, it was therefore the goal of this project to synthesize complexes of the general structure $[\text{Ru}(\text{POP})(\text{NO})\text{Cl}_2]\text{Cl}$ (see Figure 5.1B), to analyze their spectroscopic properties with focus on the properties of the nitrosyl ligand and the oxidation state of the metal. This serves as a preparation for their future use in homogeneous catalysis.

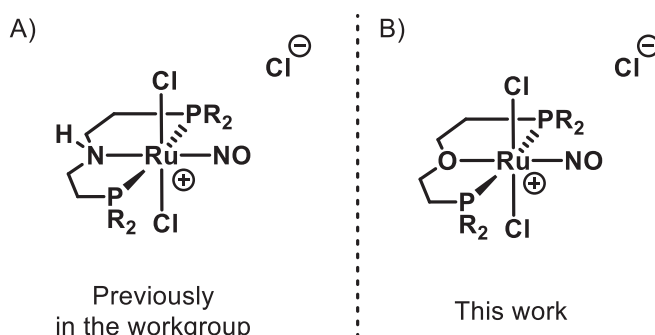
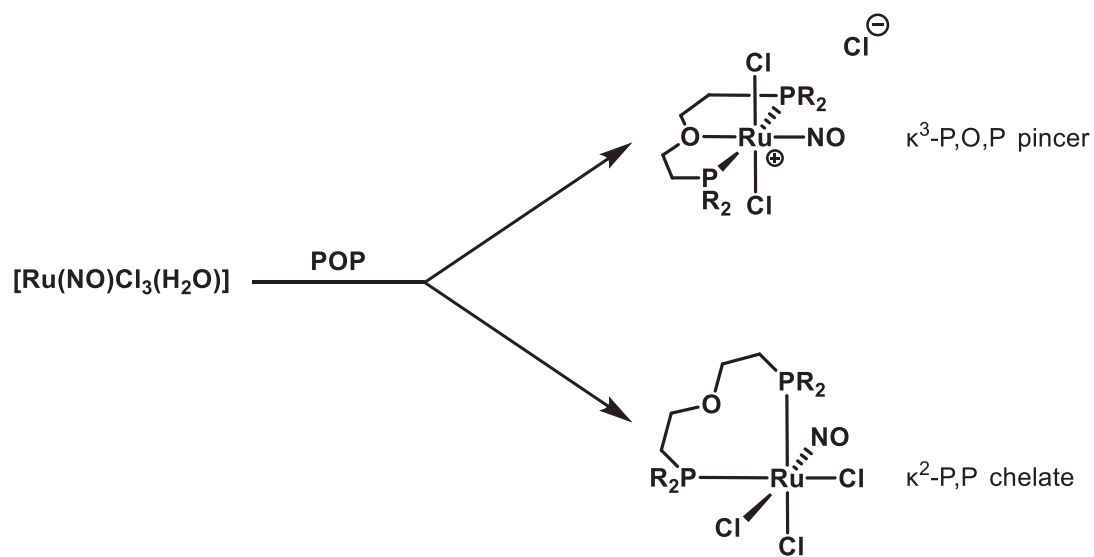


Figure 5.1: Ruthenium(II) nitrosyl complexes.

A) Bearing PNP ligands previously synthesized in this workgroup and used for transfer hydrogenation reactions.

B) Bearing POP ligands as the aim of this project

Due to the different possible binding modes of the POP pincer ligands caused by the comparatively weak Ru-O bond discussed previously, several products can be envisioned. While the pincer configuration has been exclusively found for PNP analogs, it is also possible that the POP pincers will bind as a $\kappa^2\text{-P,P}$ chelates. The general structure of the possible configurations is shown in Scheme 5.1.



Scheme 5.1: Possible products of $\text{Ru}(\text{NO})\text{Cl}_3(\text{H}_2\text{O})$ with a POP pincer ligand.

5.2 Results and discussion

5.2.1 Synthesis attempts of $[\text{Ru}(\text{POP})(\text{NO})\text{Cl}_2]\text{Cl}$

In analogy to the corresponding ruthenium nitrosyl complexes bearing PNP ligands, synthesis attempts were performed using slight excess of the ligands **L1**, **L2**, **L6** and **L7** in a THF solution under inert conditions at room temperature. Over the course of 24 hours, the reaction yielded off-white powders. The complexes were insoluble in aliphatic hydrocarbons, so for purification they were washed multiple times in hexane and obtained as off-white to beige powders.

Unfortunately, not all complexes could as of yet be obtained as single crystals and the work in this endeavour is still ongoing. The first crystals could be obtained for **Ru-NO-2** after dissolving in MeCN and layering with diethyl ether at room temperature. This mixture precipitated as an orange powder upon layering, however over a time of approximately two weeks, crystals of sufficient quality for SC-XRD grew from the solution phase. The complex crystallized in a triclinic crystal system of the P-1 space group and showed a clear distorted octahedral geometry. The crystal structure and an illustration of the complex can be found in Figure 5.2. In contrast to the expectation of a $\kappa^3\text{-P,O,P}$ pincer configuration with a chloride anion of the formula $[\text{Ru}(\text{dpephos})(\text{NO})\text{Cl}_2]\text{Cl}$, which is observed in the PNP analogs, the complex showed a $\kappa^2\text{-P,P}$ chelate configuration with all three chloride ligands facially coordinated to ruthenium, $[\text{Ru}(\text{dpephos})(\text{NO})\text{Cl}_3]$ **Ru-NO-2**, similar to the reaction product of **Ru-2a** and NaBF_4 , earlier described in Chapter 2. Important atom distances and bond angles are listed in Table 5.2. An atom distance of more than 3.4 Å confirmed that no interaction between ruthenium and the oxygen atom on the pincer is likely to take place.

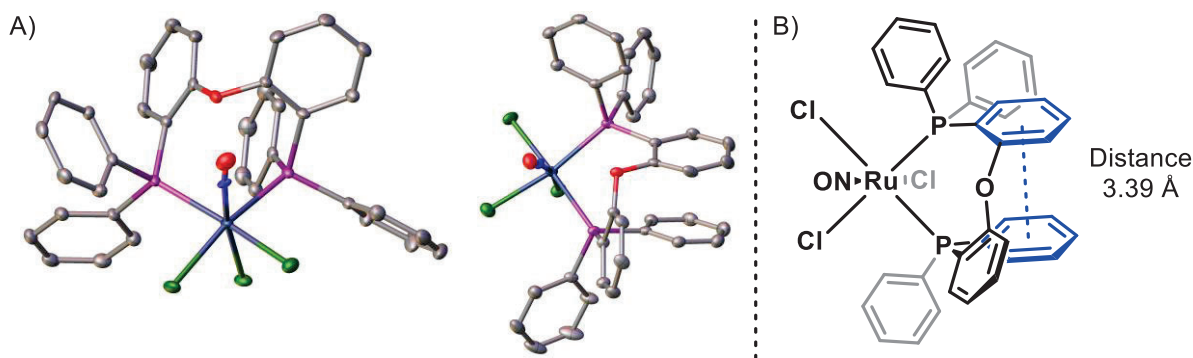


Figure 5.2: Solid state structure of **Ru-NO-2**.

A) Crystal structure obtained by SC-XRD. Hydrogen atoms are omitted for clarity. Thermal ellipsoids shown at 50% probability.

B) Illustration of the complex. Planes of stacking phenyl groups are marked in blue.

One possible explanation of this configuration can be found in the three-dimensional parallel alignment of one of the phenyl group substituents on one phosphine and the bridging phenyl group between the other phosphorous atom and the ether bridge. With a medium plane distance of about 3.39 Å, this is comparable to the layer distance in graphite at 3.35 Å.⁵⁵ This strongly suggests stabilization by intramolecular π -stacking. The very linear Ru-N-O angle of 174.7° and the short N-O distance of 1.07 Å clearly indicate an NO⁺ configuration of the nitrosyl ligand and an {MNO}⁶ electronic configuration according to the ENEMARK-FELTHAM notation.

Table 5.2: Selected bond lengths, atom distances and angles of **Ru-NO-2**.

Ru-NO-2						
Atom	Atom	Distance [Å]	Atom	Atom	Atom	Angle [°]
Ru	N	1.804(2)	P1	Ru	P2	94.66(2)
Ru	Cl1	2.3382(6)	Cl1	Ru	N	169.74(7)
Ru	Cl2	2.3977(6)	P1	Ru	Cl3	168.71(2)
Ru	Cl3	2.4540(7)	P2	Ru	Cl2	166.91(2)
Ru	P1	2.4350(7)	Ru	N	O1	174.7(2)
Ru	P2	2.4355(6)				
Ru	O2	3.415				
N	O1	1.070(3)				

This twisted geometry is only made possible by the ability of **L2** to significantly bend its ligand backbone out of plane. In **Ru-NO-2**, the planar angle between the two bridging phenyl groups is found to be 80°. As previously described in Chapter 2 of this work, this behaviour of **L2** is literature-known and has previously been suggested to be a major influence on catalyst activity compared to other evaluated ligands without this capability.³³

To eliminate the possibility of stabilization through means of backbone π -stacking, the same reaction was attempted using **L1**, which due to its bridged linker is incapable of bending out of plane like **L2** is observed to do. As previously, the complex would precipitate as a powder from acetonitrile layered with

diethyl ether, but suitable crystals would grow after prolonged standing at room temperature. The crystal structure obtained this way showed complex **Ru-NO-1** to also obtain a κ^2 -P-P chelate binding mode to the ruthenium center. Instead of π -stacking a bridging phenyl group of the diphenyl ether linker, the non-bridging phenyl groups are π -stacking. Like in **Ru-NO-2**, even though the stacked phenyl rings are not completely parallel (5.66° angle between planes), the average distance between the two planes of the phenyl rings was 3.43 Å, slightly longer than the layer distance in graphite at 3.35 Å. This leads to the conclusion that a configuration like this is likely to occur with all POP ligands of similar P-P distance bearing phenyl groups on P, meaning **L1**, **L2**, **L3**, **L4** and possibly **L11**. In this specific experiment, the nitrosyl group was disordered over two positions: *Trans* to chloride or *trans* to phosphorous, as shown below. Interestingly, the disorder was not observed throughout all three coordination sites despite the chemical equivalence of the third site to one of the disordered sites.

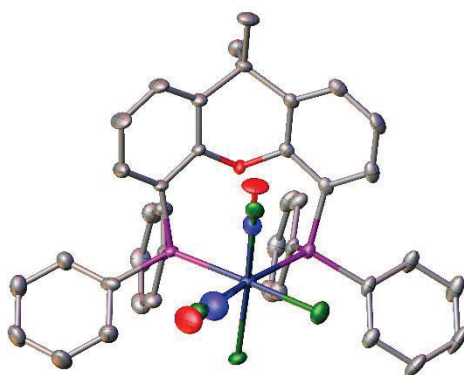
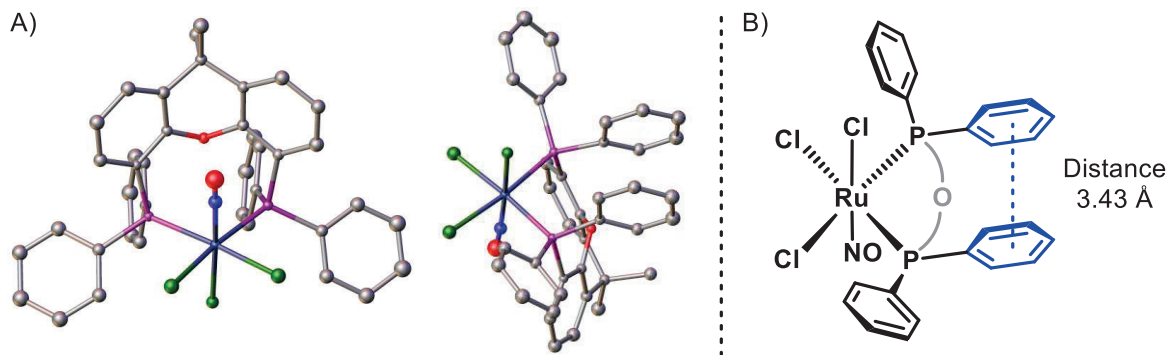


Figure 5.3: Disordered crystallographic model of **Ru-NO-1**.

Hydrogen atoms are omitted for clarity. Thermal ellipsoids shown at 50% probability.

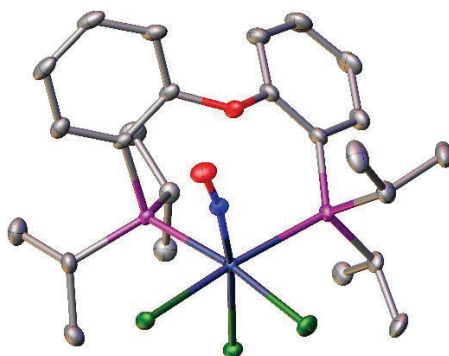
When the compound was synthesized in benzene instead of THF, a beige powder was obtained, which dissolves in DMSO and DMF as a red solution. Layering either solution with diethyl ether yielded crystals suitable for SC-XRD studies, which did not show the scrambling of the nitrosyl group (Figure 5.4).

Figure 5.4: Solid state structure of **Ru-NO-1**.

A) Hydrogen atoms are omitted for clarity. Thermal ellipsoids shown at 50% probability.

B) Illustration of the complex. Planes of π -stacking phenyl groups are marked in blue. The backbone of the complex is omitted for clarity.

To avoid the possibility of π -stacking, a similar synthesis was attempted using the *i*Pr-DPEphos ligand **L6**. The synthesis of the complex **Ru-NO-6** was performed in THF at room temperature and yielded beige powder. It could be crystallized from DMSO/diethyl ether by layering and showed the same chelating configuration of **L6** (see Figure 5.5), with its diphenyl ether backbone twisted out of plane, as in **Ru-NO-2**. This suggests that π -stacking is not the primary cause of the chelate configuration in this set of complexes and therefore all POP ligands bearing aromatic backbones related to xantphos as expected to bind in this matter. Multiple other reasons are possible. Charge separation by salt formation might already be sufficient to overcome the energy gains of the formation of the weak ruthenium oxygen bond. The same applies for the relation between Ru-O and Ru-Cl bond strengths (as measured by the bond dissociation energies), which is significantly stronger for the latter.¹⁶³

Figure 5.5: Crystal structure of **Ru-NO-6**.

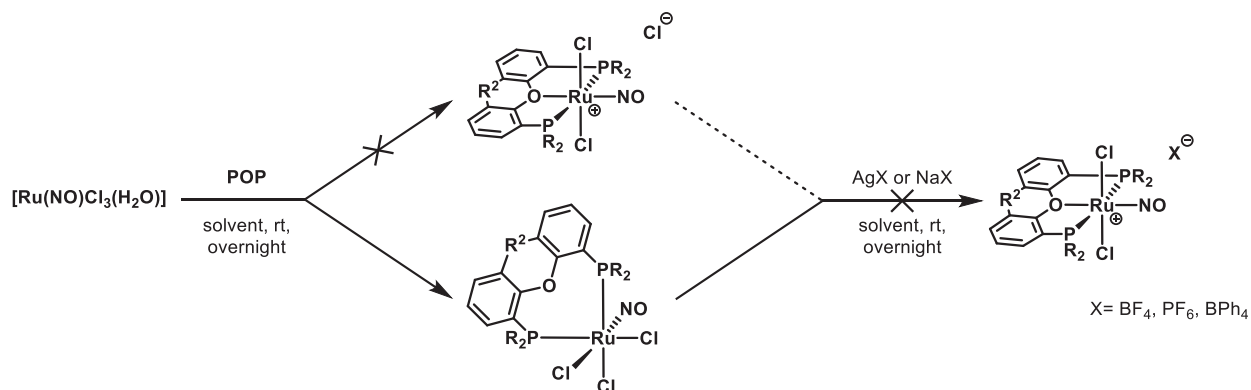
Hydrogen atoms are omitted for clarity. Thermal ellipsoids are shown at 50% probability.

To further investigate the properties of the complexes, ATR-IR analysis was performed for **Ru-NO-1**, **Ru-NO-2** and **Ru-NO-6**. Strong NO stretching bands were found at 1874, 1868 and 1863 cm^{-1} , respectively, which both strongly fall into the region of linear, triple-bonded nitrosonium ligands, confirming the NO^+ -character of the ligands, and thereby the oxidation state of the metal center as Ru(II). The structures of **Ru-NO-1** and **Ru-NO-2** were further confirmed by elemental analysis and analyzed via NMR. $^{31}\text{P}\{^1\text{H}\}$ NMR of **Ru-NO-1** and **Ru-NO-2** in DMF-d_7 and DMSO-d_6 revealed clean singlets at 9.39 ppm and 13.58 ppm, respectively.

The same synthesis was attempted using the ether-bridged ligand **L7**, but no crystal could be grown, and hence no structure could as of yet be obtained. The product of this reaction, **Ru-NO-7**, shows an NO stretching band at 1836 cm^{-1} , significantly redshifted compared to the other complexes. This fits in line with the significantly higher electron density due to the diethyl ether backbone of the ligand and the isopropyl substituents. This complex was not soluble in any tested solvent, so no NMR spectra could be obtained.

5.2.2 Chloride abstraction experiments

One method to force the complexes into a pincer configuration is the selective abstraction of one of the three chloride ligands, to liberate one of the available coordination sites for the weak Ru-O bond according to Scheme 5.2. For this, experiments were undertaken using the $\kappa^2\text{-P,P}$ chelate complexes.



Scheme 5.2: Proposed chloride abstraction using precipitation of insoluble halide salts.

This reaction was attempted using complex **Ru-NO-2**. Several different reaction conditions were attempted, using the silver, sodium, and potassium salts of BF_4^- and PF_6^- . Unfortunately, in neither case could clean product formation be observed. Interestingly, the attempted chloride abstraction in acetonitrile

led to the formation of small quantities of $[\text{Ru}(\text{POP})(\text{MeCN})_4](\text{BF}_4)_2$, the same complex observed previously in Chapter 2 during chloride abstraction experiments of **Ru-2a**. This was confirmed by XRD. So far, the mechanism to explain this finding remains undetermined.

5.3 Conclusions and outlook

In summary, a novel set of ruthenium nitrosyl complexes bearing POP pincer ligands was synthesized. The ligands were found to exclusively bind in a $\kappa^2\text{-P,P}$ chelate configuration and an electronic structure likely to correspond to $\{\text{RuNO}\}^6$. They were characterized by multiple different techniques including NMR, IR, EA and XRD. To my knowledge, these complexes represent the first examples of Ru-POP complexes with nitrosyl ligands and are as of time of writing subject to first catalytic screening experiments in the workgroup. Unfortunately, the efforts of obtaining them in their $\kappa^3\text{-P,O,P}$ pincer configuration by means of chloride abstraction have as of yet not been successful.

To further investigate these complexes, solid-state NMR could be used to compare the solid-state chemical shifts to those in DMSO solution, in order to investigate possible complex reconfigurations. Specifically for **Ru-NO-7**, this will be needed for determining the complex structure.

One possibility of addressing the issue of chloride abstraction might be the choice of a different precursor, such as $[\text{Ru}(\text{NO})\text{Cl}_2(\text{H}_2\text{O})]\text{BF}_4$, by attempting chloride abstraction in a one-pot synthesis upon ligand addition, or by circumventing potential redox pathways with silver salts by using redox inactive thallium salts instead. The use of PSP pincers compared to POP pincers in the future might be an option to force a pincer configuration due to the better HSAB match between ruthenium and sulphur. Additionally, further investigations into the properties of the nitrosyl complexes could be performed by synthesizing the isotope-marked ^{15}NO complex for ^{15}N NMR studies.

6. Manganese(I) POP pincer complexes for formic acid dehydrogenation in ionic liquids

The following chapter describes the relatively short, yet interesting final project of my work at DTU. In the context of my work, it was meant as a collaboration between myself and my colleague RAJIB PRAMANIK, who, simultaneously to my efforts in Mn(I)(POP) complex synthesis and application for catalysis, investigated closely related compounds bearing PNP ligands in an effort to better understand the mechanism of this reaction.

6.1 General introduction

6.1.1 The case for 1st row transition metal catalysts

Due to their high abundance in the earth's crust compared to their heavier counterparts,¹⁶⁴ 1st row transition metals, often referred to as “base metals”, have recently become a valuable field of interest in transition metal catalysis. Their affordable price combined with generally lower toxicities makes them ideal for applications in which 2nd and 3rd row TMs have previously been used. Particular focus lies on complexes of manganese and iron. Unfortunately, these advantages are offset somewhat by their tendency to undergo single-electron redox reductions, which are untypical for 2nd and 3rd row TMs. As a result, reaction pathways otherwise impossible can occur.

6.1.2 Manganese complexes for formic acid dehydrogenation

Manganese complexes have previously been used for formic acid dehydrogenation with good catalytic properties. In 2019, TONDREAU presented an acid-resistant Mn(I) complex bearing a MLC-capable PNNOP ligand, which dehydrogenated FA with TOFs of up to 8500 h⁻¹ at temperatures as low as 80 °C.¹⁶⁵ A year later, BELLER reported a 2,2'-bisimidazole *N,N*-chelate complex which dehydrogenated formic acid with TONs of over 7500 within 12 hours.¹⁶⁶ Very recently, a PNNNP pincer complex was reported that yielded TONs of 15200 and TOFs of up to 2086 h⁻¹ by HUANG.¹⁶⁷

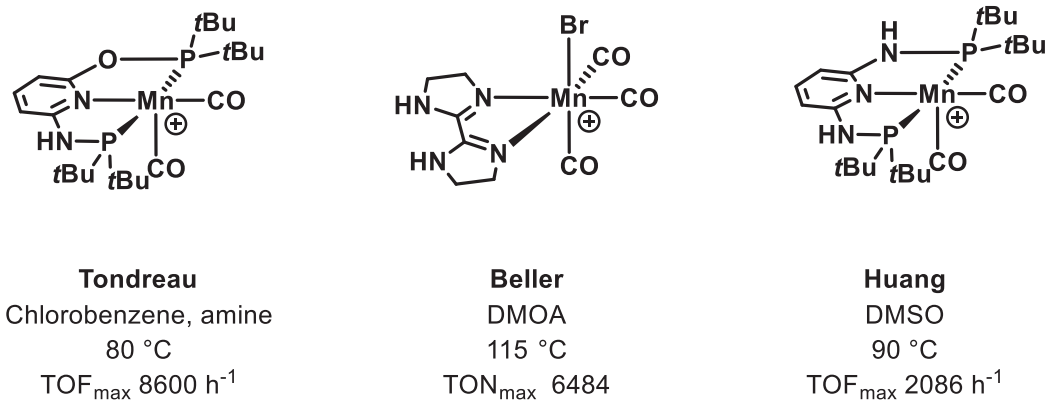


Figure 6.1: Mn(I) complexes for formic acid dehydrogenation.

6.1.3 Aim of the project

To further compare the POP pincer complexes to their corresponding PNP counterparts, it was therefore the aim of the project to synthesize a set of previously unknown manganese(I) complexes bearing a POP pincer ligands of the general formula $[\text{Mn}(\text{POP})(\text{CO})_2\text{Br}]$. The complexes in question were to be analyzed for their structural and spectroscopic properties, and then to be used in formic acid dehydrogenation reactions using an ionic liquid as a solvent. Since no Mn(I) complexes with POP ligands binding in the pincer configuration are as of yet known, their intrinsic properties are of general interest in catalyst development.

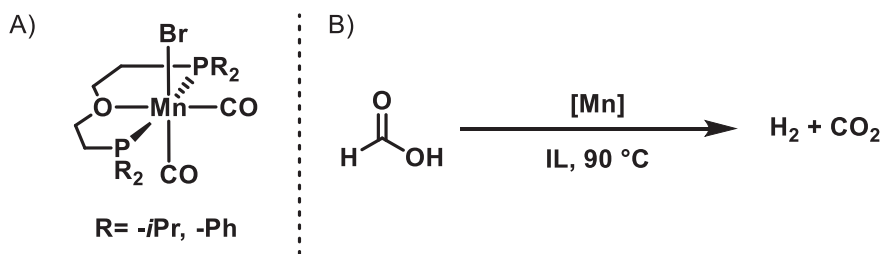


Figure 6.2: Formic acid dehydrogenation using Mn(POP) complexes.

A) General structure of complexes under investigation.

B) Formic acid dehydrogenation using Mn(POP) complexes.

6.2 Synthesis of Mn(I)(POP) complexes

To keep comparability with the corresponding PNP pincer complexes that were under investigation in the workgroup, the effort was started by focusing on POP pincers bearing an ethylene bridge backbone instead of a xantphos derivative. As a result, **Mn-7** and **Mn-3** were chosen as primary targets for synthesis.

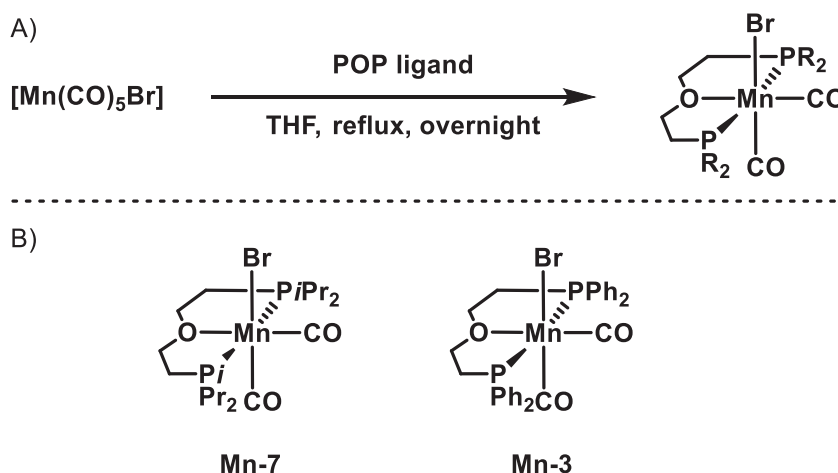


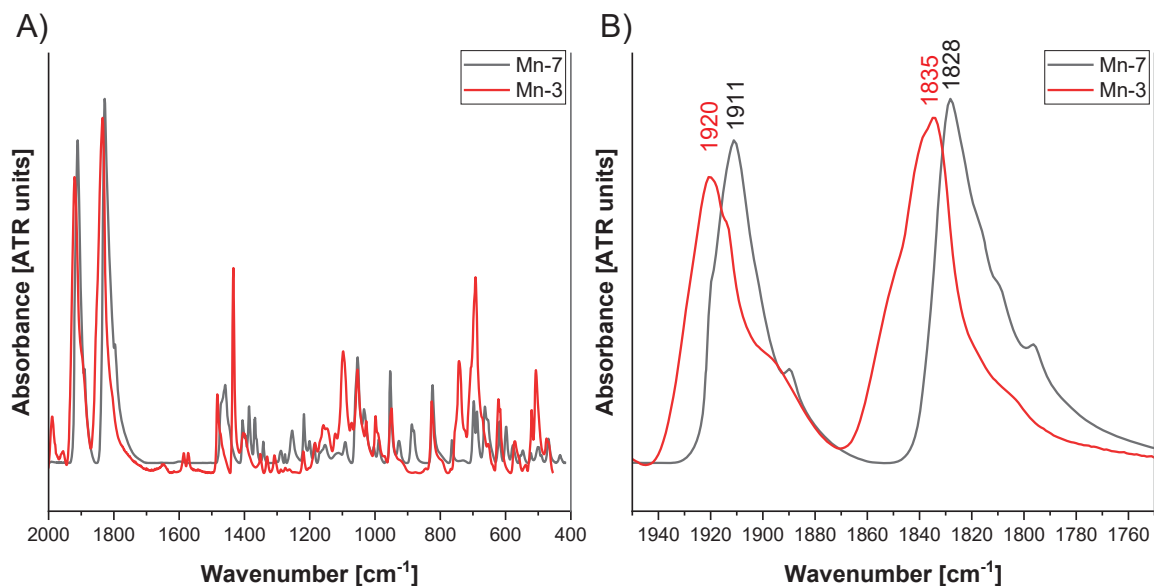
Figure 6.3: $[\text{Mn}(\text{POP})(\text{CO})_2\text{Br}]$ Catalysts under investigation.

A) General synthesis route

B) List of $[\text{Mn}(\text{POP})(\text{CO})_2\text{Br}]$ complexes first synthesized in this project

The synthesis of the Mn(I) complexes was performed by an addition of the POP ligand to the commercially available $\text{MnBr}(\text{CO})_5$ precursor. In the cases of **Mn-3** and **Mn-7**, the injection of the ligand into the solution of the precursor complex was immediately accompanied by gas formation, pointing at the decoordination of carbonyl ligands from the complex to form CO gas. This hints at the reaction being feasible at room temperature over prolonged periods of time. The reactions were refluxed overnight to ensure complete conversion. A slight colour change from yellow to orange was observed. Removal of the solvent via vacuum drying followed by washing in hexane produced complexes **Mn-3** and **Mn-7** in high yields. The complexes were insoluble in hydrocarbons, making washing in hexane feasible.

ATR-IR of the complexes (Figure 6.4) revealed sharp carbonyl stretching bands at 1920 and 1835 cm^{-1} for **Mn-3**, indicating the coordination of two carbonyl ligands at the manganese center. Compared to this, the peaks of **Mn-7** were found to be slightly redshifted at 1911 and 1828 cm^{-1} , which corresponds to **Mn-7**'s slightly more electron-rich metal center due to the more electron-rich alkylphosphine moieties.

Figure 6.4: ATR-IR of **Mn-3** and **Mn-7**.

77 K, Diamond surface.

A) Full spectrum.

B) Carbonyl stretching peaks in the region around 1950-1750 cm⁻¹.

¹H-NMR yielded generally very broad peaks with indistinct multiplicities (see appendix G), which did not allow for full characterization of **Mn-3**. In the case of **Mn-7**, the ¹H, ¹³C and ³¹P{¹H} NMR spectra appeared to show the formation of two isomers in the ratio 85:15 at room temperature with peaks in the ³¹P{¹H} NMR spectrum at 79.87 and 75.87 ppm, respectively. This was investigated by variable temperature ³¹P{¹H} NMR spectroscopy at a temperature range of 258 to 338 K, clearly demonstrating a temperature-dependence of the ratio of peak integrals (Figure 6.5). By varying the temperature back and forth, this reaction was shown to be reversible. It's therefore probable that two isomers occur in the liquid phase, which likely correspond to slow configurational flipping of the ligand backbone. The ³¹P{¹H} spectrum for **Mn-3** produced a sharp singlet at 65.76 ppm, which lies within the expected range.

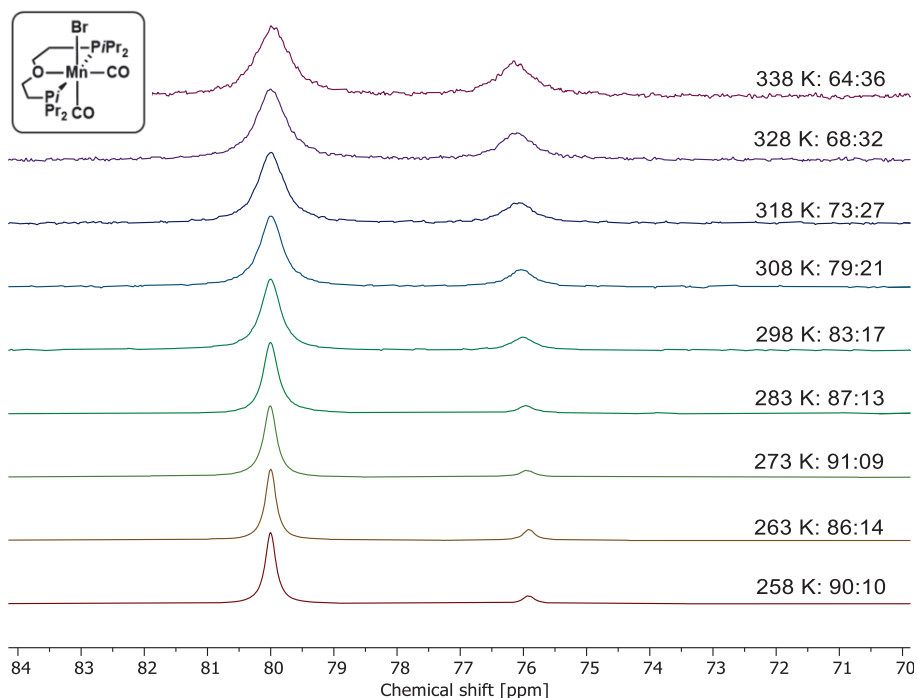


Figure 6.5 Temperature dependent $^{31}\text{P}\{^1\text{H}\}$ NMR of **Mn-7** in toluene- d_8 .

Isomer ratios are marked on the right side.

To gain further insight into the properties of the complexes, attempts at crystal growth were made. **Mn-7** could be grown as orange crystals by dissolving in acetonitrile and layering with diethyl ether in an NMR tube at room temperature. The complex crystallized in an orthorhombic crystal system of the space group $P2_12_12_1$ and showed a distorted octahedral geometry expected for a d^6 Mn(I) complex (see Figure 6.6). Important bond lengths, atom distances and bond angles are listed in Table 6.1.

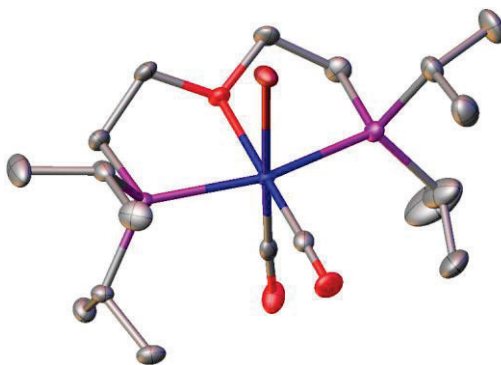


Figure 6.6: Crystal structure of **Mn-7**.

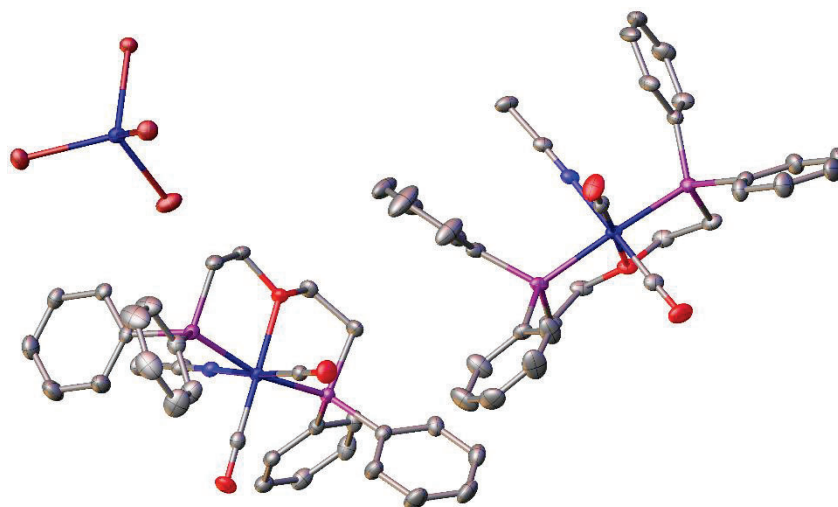
Hydrogen atoms are omitted for clarity. Thermal ellipsoids shown at 50%.

Compared to the PNP counterpart synthesized by BELLER,⁹⁸ the Ru-P bonds were about 0.01 Å longer. With a P-Ru-P angle of 163.79°, the bite angle of the pincer complex was slightly reduced compared to the PNP pincer (average value 165.93°). The Ru-Br bond was slightly shorter than in the PNP pincer (average 2.576 Å).

Table 6.1: Selected bond lengths, atom distances and angles of **Mn-7**.

Mn-7						
Atom	Atom	Distance [Å]	Atom	Atom	Atom	Angle [°]
Ru	C1	1.766(3)	P1	Ru	P2	163.79(4)
Ru	C2	1.770(3)	Br	Ru	C2	177.82(10)
Ru	O3	2.145(2)	C1	Ru	O3	177.50(12)
Ru	P1	2.3089(9)				
Ru	P2	2.3060(9)				
Ru	Br	2.5573(6)				
C1	O1	1.162(4)				
C2	O2	1.130(4)				

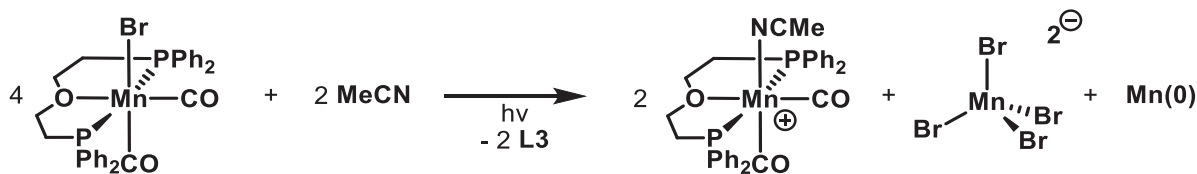
In the case of **Mn-3**, crystals of suitable quality could also be obtained from MeCN layered with diethyl ether. The crystal structure, shown in Figure 6.7, showed a degradation of the complex to $[\text{Mn}(\text{DPPEE})(\text{CO})_2(\text{MeCN})]_2[\text{MnBr}_4]$.

Figure 6.7: Crystal structure of degraded **Mn-3**.

General structure $[\text{Mn}(\text{DPPEE})(\text{CO})_2(\text{MeCN})]_2[\text{MnBr}_4]$

Hydrogen atoms as well as co-crystallized solvents omitted for clarity. Thermal ellipsoids shown at 50%.

Typical for 1st row transition metals, manganese is known to undergo single-electron redox reactions, so it is likely that this caused the degradation of the crystallization experiment of **Mn-3**. No measures against light intrusion had been taken, as this was not necessary for **Mn-7**. A suggested reaction equation is shown below. As of yet, no crystals of suitable quality for XRD studies for non-degraded **Mn-3** could be obtained.

Scheme 6.1: Redox reaction to form degraded **Mn-3** in MeCN during crystallization attempt.

In addition to the synthesis of the two ethylene-backbone-bearing complexes **Mn-7** and **Mn-3**, I also attempted to synthesize two complexes with a xantphos-type POP pincer ligand. This is interesting due to the complex's significantly decreased electron density, which could be a major factor in its catalytic activity. When the same synthetic conditions were applied as before, formation of **Mn-1** was not indicated by carbon monoxide formation. Even after 72 hours of refluxing, no product formation could be observed and NMR analysis of the reaction towards **Mn-1** confirmed that the reaction was not successful. ¹H spectra of the reaction mixtures only yielded very broad peaks, hinting at the presence of a paramagnetic species. ³¹P{¹H} NMR analysis showed very slight formation of the product, with most

xantphos being unconverted in solution. Interestingly, a total of three peaks were found in the region between 50 and 85 ppm, which points to the formation of more than one product.

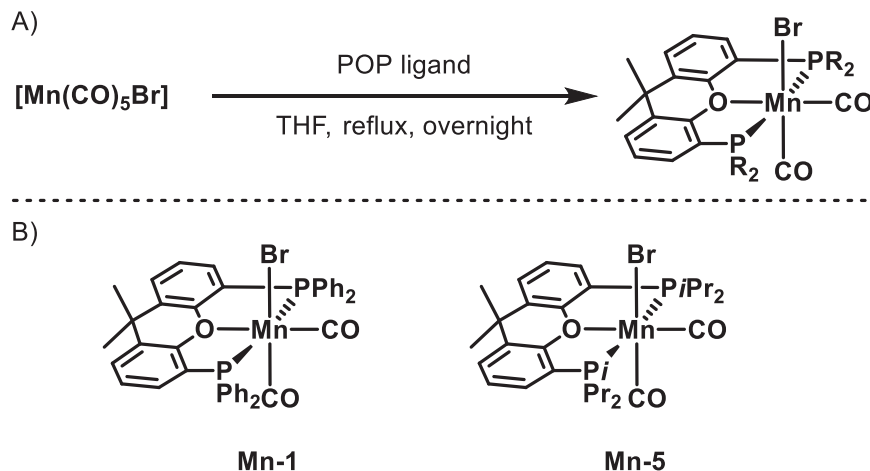


Figure 6.8: Attempted synthesis of **Mn-1** and **Mn-5**.

A) General synthesis route.

B) List of [Mn(POP)(CO)₂Br] complexes first synthesized in this project.

For **Mn-5**, slight CO evolution was observed upon dissolving ligand and precursor, and the reaction yielded a yellow powder after 72 hours of refluxing in THF and solvent removal. The product was insoluble in hydrocarbons, making washing in hexane feasible. While the ¹H NMR of the solution produced again only broad peaks, a single clean singlet ppm was found at 73.21 in the ³¹P{¹H} spectrum after washing in hexane, hinting at a clean formation of **Mn-5**. ATR-IR revealed two CO stretching bands at 1930 and 1848 cm⁻¹, further blueshifted relative to **Mn-3**. This confirms the even lower suspected lower electron density of the complex due to the xantphos ligand. No crystals of **Mn-5** suitable for XRD studies could as of yet be obtained.

6.3 Formic acid dehydrogenation experiments

To investigate the catalysts' performance in formic acid dehydrogenation, the complexes were dissolved in 1-butyl-3-methylimidazolium acetate (BMIM-OAc). All manganese complexes under investigation showed excellent solubility, with slow dissolution even happening at room temperature. The reaction protocol was adapted from the ruthenium complexes previously investigated in chapter 4. To maintain comparability with experiments run by my colleagues in the workgroup, the NMR experiments were analysed in DMSO-d₆ instead of MeCN-d₃.

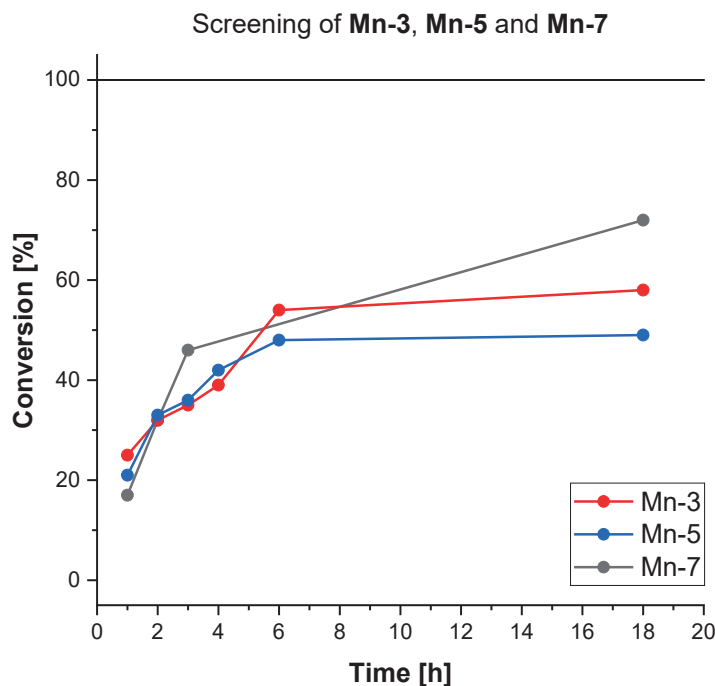


Figure 6.9 Catalyst screening of **Mn-7**, **Mn-3** and **Mn-5**.

Reaction conditions: 0.5 mL formic acid, 1.0 mL ionic liquid, 13.0 μmol catalyst, 90 $^{\circ}\text{C}$.

Conversion calculated from ^1H NMR using IL as internal reference.

The complexes **Mn-3**, **Mn-5** and **Mn-7** and immediately proved to be active in FA dehydrogenation at 90 $^{\circ}\text{C}$, but severely less so than the ruthenium complexes tested in chapter 4. Upon injection of formic acid, only slight gas formation was observed, and as a result, the NMR samples were only taken after 1 h of experiment time. After one hour, conversions of only 25% (**Mn-3**), 21% (**Mn-5**) and 17% (**Mn-7**) were found. Running the experiments for prolonged periods of time only showed moderate conversions of formic acid, with the conversions stagnating at 58% for **Mn-3**, 49% for **Mn-5** and 72% for **Mn-7** after a reaction time of 18 h.

In the next step, the catalyst concentrations were doubled for **Mn-5** and **Mn-7**. Conversions immediately rose, with the highest conversion achieved being 79% for 26 μmol of **Mn-7** after 18 hours.

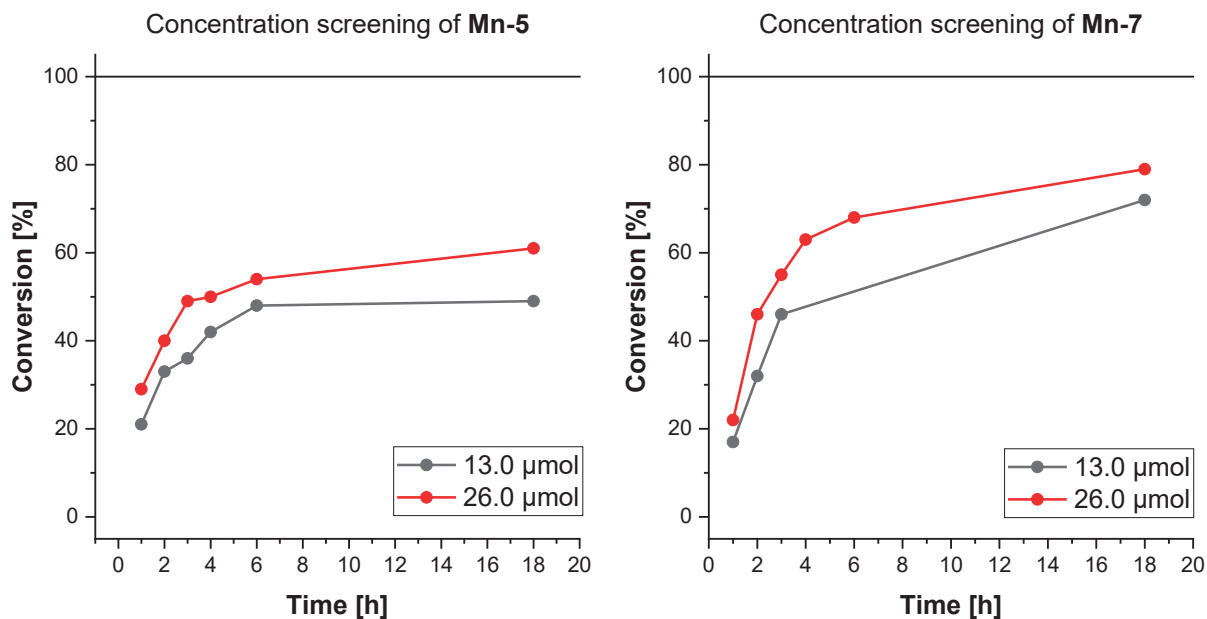


Figure 6.10: Concentration screening of **Mn-5** and **Mn-7**.

Reaction conditions: 0.5 mL formic acid, 1.0 mL ionic liquid, 90 °C.

Conversion calculated from ^1H NMR using IL as internal reference.

Brief attempts have so far been made to investigate the catalytic cycle of this reaction. The hydride regions of the NMR spectra were monitored for hydride formation as a result as was done previously in Chapter 4. Manganese hydride complexes are literature-known, and have recently been investigated for their properties in metal-ligand cooperation.¹⁶⁸ They yield signals in the range of -8 ppm relative to TMS. Unfortunately, no signals could be detected in this study, so the catalytic reaction mechanism remains as of yet elusive. The integral of the ^1H peak of the acetate anion was found to reduce over time, with it disappearing completely overnight.

6.4 Conclusions and outlook

To conclude this chapter, a set of novel Mn-POP pincer was synthesized. To my knowledge, these complexes represent the first Mn(I) complexes bearing POP pincer ligands of the DPPEE and xantphos types. The complexes were characterized by multiple different techniques, mainly NMR, IR and SC-XRD. It is important to mention here that this data is as of yet incomplete, and that further characterizations are needed for a more complete understanding. Particularly electrochemical experiments such as cyclic voltammetry (CV) and UV-VIS spectroscopy are of great interest due to the tendency of manganese to undergo single-electron redox events, shown by the quick oxidation of **Mn-3** during crystallization attempts.

The first catalytic screening of these complexes already revealed their ability to catalyze formic acid dehydrogenation in the ionic liquid BMIM-OAc, albeit with significantly lower reaction rates than the ruthenium counterparts studied in Chapter 4, only reaching turn-over frequencies of around 250 h⁻¹. It is to be noted here that catalysis experiments of this class were very preliminary, and the reaction conditions are as of yet not optimized. A full screening of conditions is needed to fully understand the capability of these catalysts for this reaction. Apart from a change of ionic liquid, additional changes can be made to the catalyst structures. All of this is work to be carried out in the NIELSEN group in the future. Additionally, further work is needed to investigate the catalytic cycle of the reaction. Possibilities include the performance of stoichiometric reactions, the synthesis of a hydrido complex and its use in the reaction, as well as isotopic labelling experiments.

7. Hydrogenation of carbon dioxide with electron-rich phosphine adducts

The research summarized in the following brief chapter was done in collaboration between the NIELSEN workgroup at DTU and the H. JUNGE workgroup at the Leibniz institute for Catalysis (LIKAT) in Rostock/Germany. It summarizes the results that were obtained during this research stay. All of the syntheses and parts of the catalytic reactions were performed at LIKAT as part of the recommended external research stay exchange program for PhD students at DTU. The project was co-supervised by Professor MATTHIAS BELLER, scientific director of LIKAT. It must be noted here that the ruthenium catalyst used in the following chapter (Ru-MACHO-BH) was commercially achieved and is not related to the POP pincer complexes used in all other subprojects of this thesis. Therefore, this subproject should be seen as an addendum to the overarching themes laid out in the previous chapters, and that its results are very preliminary and subject to revisions in the future. I would like to again thank my colleagues at LIKAT for their help and cooperation in this short, albeit interesting project.

7.1 Introduction

7.1.1 Zwitterionic phosphine CO₂ adducts: Properties and use cases

To bind CO₂, a Lewis base can be utilized to form a corresponding adduct. Previously, this has been performed with carbenes,¹⁶⁹ nitrogen bases,¹⁷⁰ and even amino acids such as lysin.¹⁷¹ Recently, DIELMANN proved that very electron-rich phosphines can also react with carbon dioxide to reversibly form zwitterionic adducts (see Figure 7.1).¹⁷²

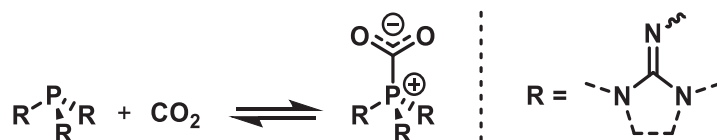


Figure 7.1: Equilibrium between highly electron-rich phosphine and CO₂, and their corresponding adduct.

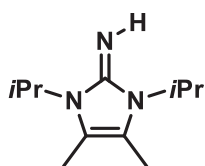
Substituents on phosphorous for this are condensed guanidines.

While this behavior is so far unknown for any trialkylphosphine, it has been observed in multiple different species bearing even more electron-rich substituents bearing guanidino groups. Research first focused on imidazoline-2-ylidenamino-substituted phosphines (IAPs),¹⁷² but the even more electron-rich tris(tetramethylguanidinyl)phosphine P(tmg)₃ was recently shown to be capable of the same reaction.¹⁷³ A strong correlation between the phosphine's Lewis acidity and the reaction with CO₂ has been observed. It can be visualized and quantified by comparing the stability of the adducts in question to the Tolman electronic parameter (TEP) of the corresponding phosphine. The TEP is the A₁ stretching frequency of a carbonyl ligand in a complex of the general formula [Ni(CO)₃L], which can be used to determine the ligand's electron donation strength.¹⁷⁴ While the adducts of the most electron-rich phosphines with a low TEP show extraordinary stability towards higher temperatures and vacuum conditions, higher TEPs were shown to correspond to easier decarboxylations and their presence could only be shown under low-temperature NMR conditions. It is important to note here that TEP changes are a result of σ- and π-interactions in complexes, while the bonding situation in the CO₂ adducts is only of the σ-type. An overview of phosphines capable of CO₂ adduct formation is found below:

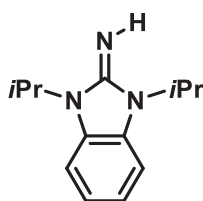
7. Hydrogenation of carbon dioxide with electron-rich phosphine adducts

Table 7.1: Different phosphines and their behavior regarding the formation of CO₂ adducts in correlation to TEP.

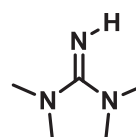
Phosphine	Formation of CO ₂ adduct	TEP (conditions) [cm ⁻¹]
P(Ph)₃	None	2068.9 (in CH ₂ Cl ₂) ^{174,175}
P(<i>i</i>Pr)₃	None	2059.2 (in CH ₂ Cl ₂) ^{174,175}
P(<i>t</i>Bu)₃	None	2056.1 (in CH ₂ Cl ₂) ^{174,175}
P(<i>n</i>-Bu)(1-Ad)₂	Investigated in this project	---
P(1-Ad)₃	Investigated in this project	2052.1 ¹⁷⁶ (calculated after ¹⁷⁷)
P(<i>i</i>Pr)(NB<i>i</i>Pr)₂	Low temperature NMR ¹⁷²	2049.2 (in CH ₂ Cl ₂) ¹⁷⁸
P(<i>i</i>Pr)₂(N<i>i</i>Pr)	Low temperature NMR ¹⁷²	2047.5 ¹⁷²
P(NB<i>i</i>Pr)₃	Stable at room temperature ¹⁷²	2044.3 (in CH ₂ Cl ₂) ¹⁷⁸
P(<i>i</i>Pr)(N<i>i</i>Pr)₂	Stable at room temperature ¹⁷²	2038.6 ¹⁷²
P(tmg)₃	Stable at room temperature under vacuum ¹⁷³	2036.5 (neat) ¹⁷³ 2041.1 (toluene) 2048.6 (THF) 2049.1 (DCM) 2054.1 (MeOH)



H-N*i*Pr



H-NB*i*Pr



H-tmg

This property of electron-rich phosphines has so far been only used for protecting the corresponding phosphines for the simplification of complex synthesis.¹⁷² In fact, several of the adducts were shown to be air stable for several months whereas the corresponding phosphines decomposed immediately.

7.1.2 Other types of phosphine CO₂ adducts

Although the zwitterionic adducts of phosphines to CO₂ generally represent the more common group in current research, other modes of adduct formation are known. For example, FONTAINE et al., while investigating phosphazene bases as catalysts for hydrosilylation of CO₂, discovered a reaction between the phosphazenes and CO₂ with an intermediate adduct. The reaction pathway strongly resembled a WITTIG-type reaction mechanism (see Figure 7.2).^{179,180} This reaction is likely driven by the exothermic formation of the corresponding phosphoric acid triamide.

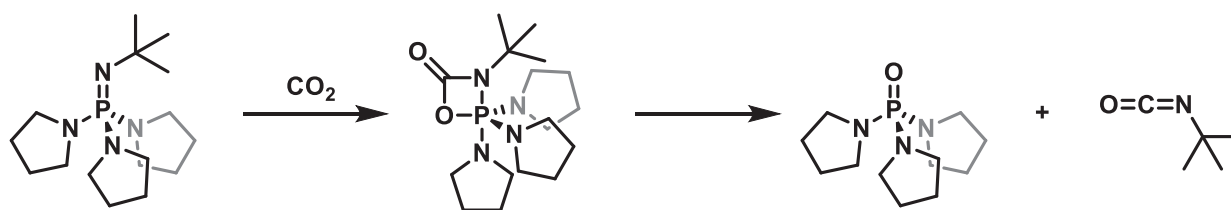


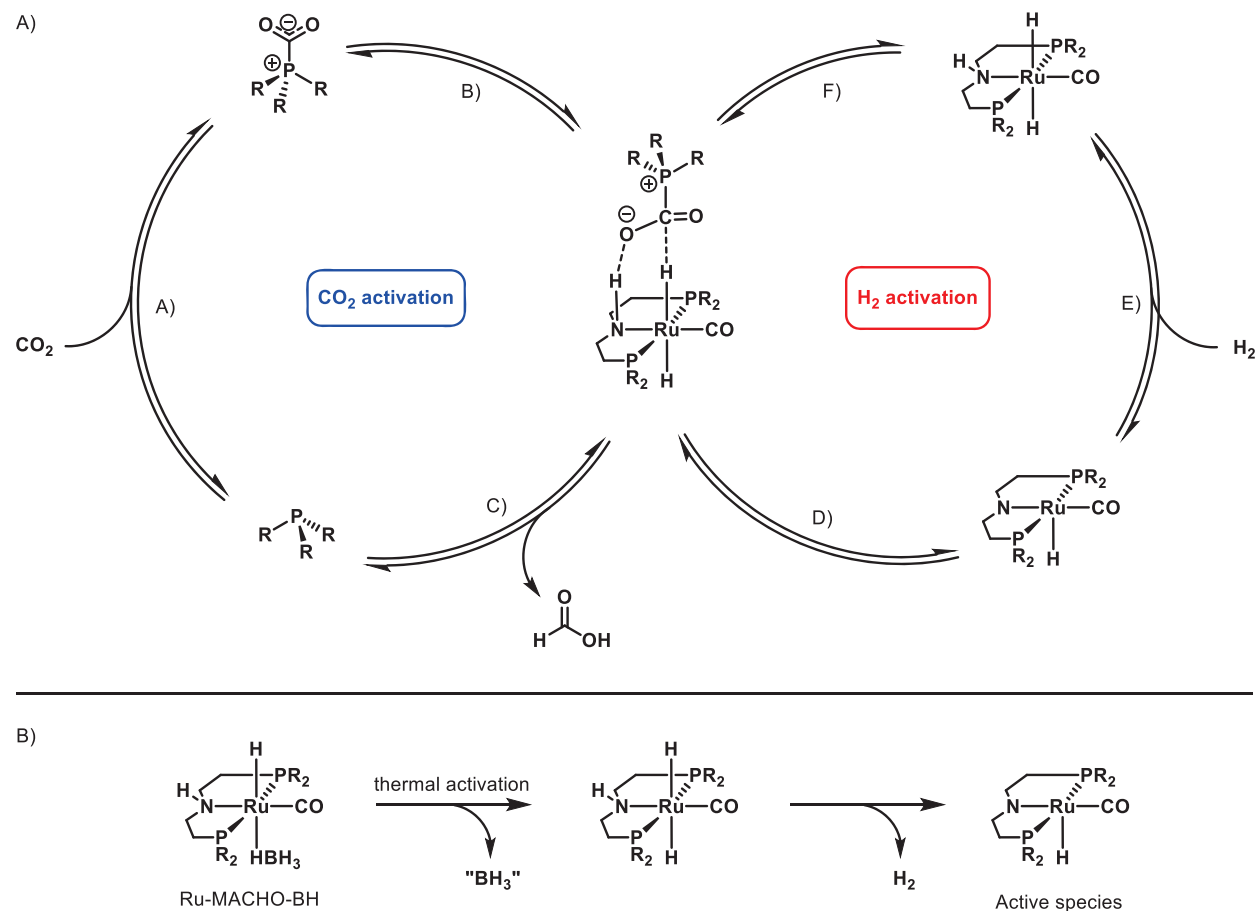
Figure 7.2: Reaction of phosphazene base P_1 -*t*Bu-tris(pyrrolidin) with CO₂.

Reaction products are the corresponding phosphoric acid triamide and *tert*-butyl isocyanate.

7.1.3 General proposal and aim of the project

Although phosphine CO₂ adducts have so far only been used in the field of complex synthesis, specifically as a means to protect the otherwise impractically reactive phosphines,¹⁷² another purpose might become evident from this work. One important step of the activation of CO₂ is the bending of the molecule accompanied by the reduction in symmetry from $D_{\infty h}$ to C_{2v} and induction of electric dipole moment.¹⁸¹ As evident by the spectroscopic properties of the zwitterion, both of these changes in molecular structure already occur in the adduct formation reaction. This potentially lowers the activation barriers for any further transformation of CO₂. With this energy barrier overcome, catalytic hydrogenation of the carbon dioxide might be facilitated, reducing the need for harsh reaction conditions. A proposed bicatalytic cycle for formic acid formation is shown below, employing activation of CO₂ via phosphine adduct formation and activation of H₂ with a ruthenium pincer complex. It starts with the activation of CO₂ (A) to form the zwitterionic adduct, which then coordinates to a Ru-MACHO-type complex (B and F). This hydrogenates the CO₂ to formic acid, regenerating the phosphine and the dehydrogenated active species of the catalyst containing an amido ligand (C and D), the latter is then finally rehydrogenated (E),

completing the cycle. The complex must first be activated by thermal cleavage of the borohydride ligand, followed by hydrogen abstraction.



Scheme 7.1: Proposed catalytic cycle and thermal activation of Ru-MACHO-BH.

A) Proposed bicatalytic cycle.

Blue: CO₂ activation using zwitterionic phosphine adducts

Red: H₂ activation with a Ru-MACHO complex

B) Activation of Ru-MACHO-BH to active species

Therefore, two goals of this project arise. The first is to investigate the possibility of adduct formation in the currently most electron-rich alkylphosphine P(1-Ad)₃, whose TEP suggests that adduct formation lies within the range of possibility under pressurized CO₂ atmospheres at low temperatures. The second goal of this project is to use the CO₂ adducts for the hydrogenation of carbon dioxide to formic acid, using them as co-catalysts in conjunction with already established hydrogenation catalysts such as Ru-MACHO-BH. An interaction can be envisioned in which the adduct interacts with the hydrogenated

active species of Ru-MACHO-BH, thereby transforming CO₂ to formic acid, according to the reaction mechanism discussed above. Due to the short timeframe of the project, only a few select molecules are to be screened. Specifically, the most electron-rich alkyl phosphines, and P(tmg)₃.

7.2 Results and discussion

7.2.1 Low temperature investigations of phosphines

As a first attempt to simplify a potential catalytic system, it was decided to investigate the possibility of adduct formation of the most electron-rich alkyl phosphines. Tri(1-adamantyl)phosphine was therefore synthesized according to a protocol by CARROW, starting from 1-adamantyl acetate.^{176,182} Unlike the related compound P(*t*Bu)₃ and very untypical for trialkyl phosphines, 1-adamantyl phosphine is stable under ambient conditions as a solid, albeit showing decomposition when stored in aerobic solutions.¹⁷⁶ To investigate whether a CO₂ adduct could be formed at room temperature, P(1-Ad)₃ was dissolved in benzene, and a stream of CO₂ was bubbled through the solution. As expected, no precipitation was detected, showing that if it was to form adducts, these would likely only occur at significantly lower temperatures than ambient. Therefore, an experiment was performed in which P(1-Ad)₃ was dissolved in THF-*d*₈ inside a heavy-walled NMR tube, and a pressure of 2 bar CO₂ was applied. This enabled the screening of the ¹H, ¹³C and ³¹P{¹H} NMR spectra at a temperature range from ambient to 200 K, which is close to the freezing point of CO₂ at 195 K. The NMR spectra can be found in Appendix H. In the ¹H NMR spectrum, a rearrangement of the adamantyl groups between 282 and 215 K was found during the cooldown, which points to the adamantyl groups changing their rotational behaviour at lower temperatures. To further monitor the formation of the CO₂ adduct, ¹³C NMR measurements were taken at temperatures of 199, 237 and 298 K during warmup. While the CO₂ signal remained visible throughout the entire temperature range, no characteristic signals for the CO₂ adducts were observed (expected in the range of 160 to 170 ppm with large phosphorous-carbon coupling constants of 130 Hz).¹⁷² In the ³¹P NMR spectrum, no major new peak formation around 0 ppm was found, which would coincide with the adduct, and no line broadening was observed for the phosphine peak. Combined, these experiments show that no adduct formation occurs under the given conditions for P(1-Ad)₃.

The same set of experiments was repeated for the commercially available di(1-adamantyl)-*n*-butylphosphine (BuPAd₂), first developed by BELLER and sold commercially as cataCXium® A.¹⁸³ At room temperature, no precipitation of product was observed when CO₂ was bubbled through a benzene solution of the compound. In low temperature experiments, no major peak formation of any peaks was found. In conclusion, even the most electron-rich alkylphosphine currently

known to literature ($\text{P}(\text{1-Ad})_3$) and a very closely related compound BuPAD_2 are not capable of forming zwitterionic adducts, neither at room temperature nor at lower temperatures down to 200 K in CO_2 -pressurized environments.

7.2.2 Hydrogenation catalysis using $\text{P}(\text{tmg})_3$ and Ru-MACHO-BH

Since all simpler alkylphosphines showed no activity in the formation of CO_2 adducts, the focus of this project shifted towards the use of $\text{P}(\text{tmg})_3$ as a co-catalyst. Since the $\text{P}(\text{tmg})_3\text{-CO}_2$ adduct is stable at room temperature for prolonged periods of time, it was decided to synthesize it, and directly use it as a co-catalyst instead of using the free phosphine. Using the commercially available catalyst Ru-MACHO-BH, the adduct was screened for their activity in CO_2 hydrogenation. These reactions were performed in autoclaves (type B, see Appendix A). First, a reference experiment was conducted, in which no additive was added to the solution. In following experiments, 10 equivalents of the CO_2 adduct were added to the solutions. ^1H and ^{13}C analysis was performed to search for traces of formate. In all cases, small peaks at the expected value around 171.7 ppm (reference measured in D_2O)¹⁸⁴ were detected. Quantification was performed using imidazole as an added internal standard. The reactions were additionally followed by monitoring the pressure decrease in the vessels. No pressure decrease was detected, pointing to very low activity. The results are tabularized below.

Table 7.2: CO_2 hydrogenation experiments using phosphines as co-catalysts.

$\text{H}_2 + \text{CO}_2 \xrightarrow[\text{THF (2.0 mL), 90 }^\circ\text{C 24 h}]{\text{Ru-MACHO-BH (0.01 mmol), Additive (0.1 mmol)}} \text{H}-\text{C}(=\text{O})-\text{OH}$			
Catalyst	Additive	Yield	TON (relative to Ru-MACHO-BH)
Ru-MACHO-BH	no additive	traces	<1
Ru-MACHO-BH	$\text{P}(\text{tmg})_3\text{-CO}_2$	0.56 eq. relative to $\text{P}(\text{tmg})_3$	5.6
Ru-MACHO-BH	$\text{P}(\text{tmg})_3\text{-CO}_2$	0.63 eq. relative to $\text{P}(\text{tmg})_3$	6.3

The reference experiment using no additive yielded very small quantities of formic acid that correspond to less than one TON relative to the catalyst. In all experiments with added adduct, slightly higher amounts of formate were detected, but no TON exceeded 6.3 relative to Ru-MACHO-BH. This points to the catalytic cycle being active, yet severely hindered. It is likely that the highest possible TON in this experiment is only 10, corresponding to 1.0 equivalents relative to the $\text{P}(\text{tmg})_3 \text{CO}_2$ adduct. This is due to the adduct performing one catalytic cycle, transforming 1 equivalent of CO_2 to formic acid, but then being protonated to $\text{HP}(\text{tmg})_3^+$ by the formic acid and thereby inactivated.

7.3 Conclusions and outlook

In conclusion, the properties of the most electron-rich alkyl phosphines in regards to their ability to form CO_2 adducts were investigated. Temperature-variable NMR experiments show that the currently most electron-rich trialkylphosphine $\text{P}(\text{1-Ad})_3$ and the similar compound BuPAD_2 are not capable of forming any detectable zwitterionic CO_2 adducts under the investigated reaction conditions. This means that the further increase of electron density with the use of a condensed guadynyl group is paramount for the adducts to form even at temperatures too low to be practical for catalysis.

Additionally, the properties of the highly electron rich phosphine $\text{P}(\text{tmg})_3$ regarding its use as co-catalysts in the ruthenium-catalyzed hydrogenation of CO_2 towards formic acid were investigated. Formic acid was detected in low quantities in ^1H and ^{13}C spectra, pointing to a slight activity of the catalytic system that exceeds that of Ru-MACHO-BH without the addition of additives under the same conditions. As a result, a future project could be envisioned in which stoichiometric amounts of a strong base would be added to keep the co-catalyst phosphine deprotonated and therefore active. Since Ru-MACHO type complexes typically are activated by either thermal activation (for Ru-MACHO-BH) or by the formal elimination of HCl by a base, this future system would have to be compared to reactions without the presence of the phosphine. Additionally, the reaction could be screened for other types of CO_2 activation, such as for the synthesis of methanol.

8. Summary and perspectives

To summarize, this PhD project investigated the synthesis and analysis of novel transition metal complexes of ruthenium and manganese bearing POP pincer ligands, as well as their activity in catalytic transformations necessary for a future sustainable energy system.

In Chapter 2, previously developed synthetic protocols for a class of ruthenium pincer complexes of the formula $[\text{RuHCl}(\text{POP})(\text{PPh}_3)]$ were generalized, and a set of complexes has been synthesized and characterized by means of NMR, EA and SC-XRD. Their NMR-spectroscopic and crystallographic properties gave insight into the electronic structure on the ruthenium center. The chloride abstraction revealed an untypical reaction pathway for the case of the ligand DPEphos. Finally, a new complex was synthesized bearing an azido ligand *trans* towards the hydride. This complex was analyzed by means of $^{15}\text{N}/^1\text{H}$ HMBC NMR at natural abundance. The latter offers the opportunity to anchor this type of POP pincer complex to a substrate using a triazolium moiety.

In Chapter 3, the complexes were used for GUERBET-type catalytic upgrading of ethanol to 1-butanol. They showed moderate activity at a temperature of 120 °C, yielding up to 28.2% 1-butanol over a timeframe of 48 hours after several screenings for optimal conditions. This corresponds to a TON of 2382 and a TOF of 49.6 h⁻¹ at 120 °C. Stoichiometric reactions suggest the formation of various hydrido and dihydrido products, however no isolation of any species formed *in situ* was as of achieved. Overall, the complexes unfortunately did not prove particularly active in this reaction, however the distinct difference in activity based on the POP linker warrants further research. Continuing this project, different catalytic pathways and transition states could be analyzed *in silico*.

Following their use for ethanol upgrading, the same complexes were investigated for their activity in formic acid dehydrogenation in Chapter 4. They were active at reaction temperatures as low as 60 °C, and showed turnover frequencies up to 4525 h⁻¹ at 90 °C. In the future, the system of a Ru-POP pincer complex in an ionic liquid could be implemented in several industrial applications, out of which fueling vehicles such as cargo trucks and ships is certainly the most attractive. Coupling the dehydrogenation catalyst system with a hydrogen fuel cell might circumvent the disadvantages of purely electric drivetrains, especially the problematically high weight and low energy density of lithium-ion batteries. Due to the ability of imidazolium to form *N*-heterocyclic carbenes, the same system might be used to also capture the CO₂ that forms during the hydrogen liberation, keeping it as an adduct in the IL solution until the system can be rehydrogenated at a fueling station. For this, the POP pincer catalysts presented in this thesis will also have to be screened for their activity in CO₂ hydrogenation to formic acid. Their PNP

analogues have been shown to be active under these conditions at temperatures as low as 25 °C.¹³² As a means to stabilize the complexes for future use in this applications, the complexes should be tested in supported ionic liquid-phase (SILP) catalysis, in which the catalysts, dissolved in ionic liquid, are applied to the surface of a solid support structure, such as a silicate, thereby combining the advantages of homogeneous and heterogeneous catalysis.^{185,186}

In general, the activity of the complexes synthesized in Chapter 2, and investigated in Chapters 3 and 4 points towards future applications of this complex type in homogeneous catalysis and suggests that the metal-ligand cooperation often cited for extraordinarily high catalytic activities may not be the only property that investigative work should concentrate on. To further compare their activity and to investigate MLC, the *N*-methylated PNP analog, specifically with the MACHO-type linker, [RuHCl(Me-PNP)(PPh₃)] (Figure 8.1), could be synthesized.

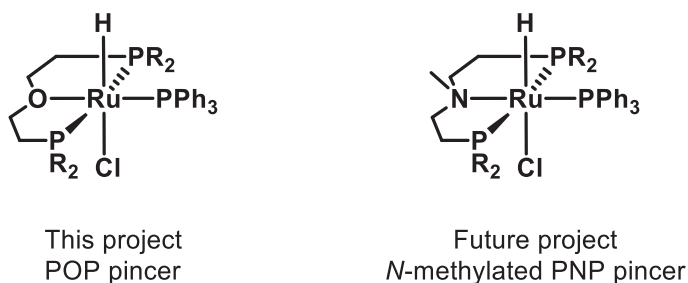


Figure 8.1: POP and *N*-methylated PNP pincer complexes.

For future experiments of the new complexes, classic hydrogenations of imines and ketones come to mind. These could be either performed using hydrogen gas, or alternatively as transfer hydrogenations using a sacrificial agent such as isopropanol. In the same way, asymmetric catalytic hydrogenation reactions could be investigated, using chiral substituents at the pincer wingtip phosphine atoms.

In Chapter 5, a series of novel Ru-POP complexes with nitrosyl ligands has been synthesized and characterized by X-ray crystallography, elemental analysis and ATR-infrared spectroscopy. Unlike their PNP counterparts previously investigated in this workgroup, the ligands solely coordinated to ruthenium as chelates, and all attempts at forcing them into a meridional tridentate configuration have been unsuccessful. However, the complexes could still prove useful in the future, as the hemilability typical for POP ligands is often a key factor in their reactivity. Additionally, POP pincer ligands have historically been mainly used as chelates and prove excellent catalytic properties in a wide variety of fields. At the time of writing this thesis, the new complexes are being tested for their reactivity in transfer hydrogenation of ketones to alcohols, and in the hydrogenation of carbon dioxide to formic acid. While

first tests indicate a low activity in transfer hydrogenations compared to similar experiments with their PNP counterparts (albeit under very unoptimized conditions), the complexes seem to be promising candidates for CO₂ hydrogenation even at very low temperatures.

In Chapter 6, the first examples of a manganese(I) pincer complex bearing a POP ligand has been synthesized and characterized by NMR, EA and SC-XRD. An oxidation product of a second example has been characterized by SC-XRD. In formic acid dehydrogenation experiments using BMIM-OAc as solvent, they show low activities with turn-over frequencies of only up to 255 h⁻¹. Like their Mn-PNP counterparts, they should be investigated for other catalytic transformations as well and warrant a full reaction condition screening.

Finally, the catalytic activity of highly electron-rich phosphines in an attempt to use them as co-catalysts for the hydrogenation of carbon dioxide to formic acid was explored. While only stoichiometric amounts of formic acid were obtained, this project opens up this field of research for future endeavours. A system could be envisioned in which formic acid is immediately deprotonated by a base, keeping the catalytic cycle of the reaction of carbon dioxide with the phosphine active. For this, the addition of a strong base in stoichiometric amounts should be considered going forward, and the reactivities of this system compared to a system without added phosphine.

Hopefully, these small steps can lead to a further understanding of transition metal chemistry as a whole. I hope it contributes to the research in sustainable chemistry to transition our society away from fossil energy sources, as well as motive further research into the interesting chemistry of POP pincer ligands and their complexes.

Bibliography

- (1) Upper, D. The Unsuccessful Self-Treatment of a Case of “Writer’s Block.” *J. Appl. Behav. Anal.* **1974**, 7 (3), 497–497. <https://doi.org/10.1901/jaba.1974.7-497a>.
- (2) van Koten, G. Tuning the Reactivity of Metals Held in Rigid Ligand Environment. *Pure Appl. Chem.* **1989**, 61 (10), 1681–1694. <https://doi.org/10.1351/pac198961101681>.
- (3) Grove, D. M.; van Koten, G.; Zoet, R.; Murrall, N. W.; Welch, A. J. Unique Stable Organometallic Nickel(III) Complexes: Syntheses and the Molecular Structure of Ni[C₆H₃(CH₂NMe₂)₂-o,O]I₂. *J. Am. Chem. Soc.* **1983**, 105 (5), 1379–1380.
- (4) Moulton, C. J.; Shaw, B. L. Transition Metal–Carbon Bonds. Part XLII. Complexes of Nickel, Palladium, Platinum, Rhodium and Iridium with the Tridentate Ligand 2,6-Bis[(Di-*t*-Butylphosphino)Methyl]Phenyl. *J. Chem. Soc. Dalt. Trans.* **1976**, No. 11, 1020–1024. <https://doi.org/10.1039/DT9760001020>.
- (5) Shih, W. C.; Gu, W.; MacInnis, M. C.; Timpa, S. D.; Bhuvanesh, N.; Zhou, J.; Ozerov, O. V. Facile Insertion of Rh and Ir into a Boron-Phenyl Bond, Leading to Boryl/Bis(Phosphine) PBP Pincer Complexes. *J. Am. Chem. Soc.* **2016**, 138 (7), 2086–2089. <https://doi.org/10.1021/jacs.5b11706>.
- (6) Suárez, E.; Plou, P.; Gusev, D. G.; Martín, M.; Sola, E. Cationic, Neutral, and Anionic Hydrides of Iridium with PSiP Pincers. *Inorg. Chem.* **2017**, 56 (12), 7190–7199. <https://doi.org/10.1021/acs.inorgchem.7b00833>.
- (7) Kihara, H.; Tanaka, S.; Imoto, H.; Naka, K. Phenylidquinolinyarsine as a Nitrogen-Arsenic-Nitrogen Pincer Ligand. *Eur. J. Inorg. Chem.* **2020**, 2020 (38), 3662–3665. <https://doi.org/10.1002/ejic.202000542>.
- (8) Cabeza, J. A.; Fernández-Colinas, J. M.; García-Álvarez, J.; García-Álvarez, P.; Laglera-Gándara, C. J.; Ramos-Martín, M. Dipyrromethane-Based PGeP Pincer Germyl Rhodium Complexes. *Chem. - A Eur. J.* **2022**, 28 (45). <https://doi.org/10.1002/chem.202200847>.
- (9) Toriumi, N.; Lyu, Y.; Iwasawa, N. Photohemilabile PSP-Rhodium Pincer Catalysts for Dehydrogenative C–H Bond Activation of Arenes. *ChemCatChem* **2023**, 202300139, 6–11. <https://doi.org/10.1002/cctc.202300139>.
- (10) Yao, Q.; Kinney, E. P.; Zheng, C. Selenium-Ligated Palladium(II) Complexes as Highly Active Catalysts for Carbon-Carbon Coupling Reactions: The Heck Reaction. *Org. Lett.* **2004**, 6 (17), 2997–2999. <https://doi.org/10.1021/ol0486977>.
- (11) Kumar, S.; Rao, G. K.; Kumar, A.; Singh, M. P.; Singh, A. K. Palladium(II)-(E,N,E) Pincer Ligand (E = S/Se/Te) Complex Catalyzed Suzuki Coupling Reactions in Water via in Situ Generated Palladium Quantum Dots. *Dalt. Trans.* **2013**, 42 (48), 16939–16948. <https://doi.org/10.1039/c3dt51658j>.
- (12) Evans, D.; Osborn, J. A.; Wilkinson, G. Hydroformylation of Alkenes by Use of Rhodium Complex Catalysts. *J. Chem. Soc. A Inorganic, Phys. Theor.* **1968**, 3133–3142. <https://doi.org/10.1039/J19680003133>.
- (13) Casey, C. P.; Whiteker, G. T.; Melville, M. G.; Petrovich, L. M.; Gavney, J. A.; Powell, D. R.

- Diphosphines with Natural Bite Angles near 120° Increase Selectivity for N-Aldehyde Formation in Rhodium-Catalyzed Hydroformylation. *J. Am. Chem. Soc.* **1992**, *114* (14), 5535–5543. <https://doi.org/10.1021/ja00040a008>.
- (14) Kranenburg, M.; van der Burgt, Y. E. M.; Kamer, P. C. J.; van Leeuwen, P. W. N. M.; Goubitz, K.; Fraanje, J. New Diphosphine Ligands Based on Heterocyclic Aromatics Inducing Very High Regioselectivity in Rhodium-Catalyzed Hydroformylation: Effect of the Bite Angle. *Organometallics* **1995**, *14* (6), 3081–3089. <https://doi.org/10.1021/om00006a057>.
- (15) Hillebrand, S.; Bruckmann, J.; Krieger, C.; Haenel, M. W. Bidentate Phosphines of Heteroarenes : 9,9-Dimethyl-4,5-Bis(Diphenylphosphino)Xanthene). *Tetrahedron Lett.* **1995**, *36* (1), 75–78. [https://doi.org/10.1016/0040-4039\(94\)02206-Q](https://doi.org/10.1016/0040-4039(94)02206-Q).
- (16) Van Der Veen, L. A.; Boele, M. D. K.; Bregman, F. R.; Kamer, P. C. J.; Van Leeuwen, P. W. N. M.; Goubitz, K.; Fraanje, J.; Schenk, H.; Bo, C. Electronic Effect on Rhodium Diphosphine Catalyzed Hydroformylation: The Bite Angle Effect Reconsidered. *J. Am. Chem. Soc.* **1998**, *120* (45), 11616–11626. <https://doi.org/10.1021/ja981969e>.
- (17) Asensio, G.; Cuenca, A. B.; Esteruelas, M. A.; Medio-Simón, M.; Oliván, M.; Valencia, M. Osmium(III) Complexes with POP Pincer Ligands: Preparation from Commercially Available OsCl₃·3H₂O and Their X-Ray Structures. *Inorg. Chem.* **2010**, *49* (19), 8665–8667. <https://doi.org/10.1021/ic101498h>.
- (18) Veits, Y. A.; Mutsenek, E. V.; Neganova, E. G.; Beletskaya, I. P. New Bidentate Diphosphine Ligands on the Basis of Diphenyl Ether. *Russ. J. Org. Chem.* **2001**, *37* (11), 1583–1586. <https://doi.org/10.1023/A:1013808220187>.
- (19) Hamada, Y.; Matsuura, F.; Oku, M.; Hatano, K.; Shioiri, T. Synthesis and Application of New Chiral Bidentate Phosphine, 2,7-Di-Tert-Butyl-9,9-Dimethyl-4,5-Bis (Methylphenylphosphino)Xanthene. *Tetrahedron Lett.* **1997**, *38* (52), 8961–8964. [https://doi.org/10.1016/S0040-4039\(97\)10363-X](https://doi.org/10.1016/S0040-4039(97)10363-X).
- (20) Chikkali, S. H.; Bellini, R.; De Bruin, B.; Van Der Vlugt, J. I.; Reek, J. N. H. Highly Selective Asymmetric Rh-Catalyzed Hydroformylation of Heterocyclic Olefins. *J. Am. Chem. Soc.* **2012**, *134* (15), 6607–6616. <https://doi.org/10.1021/ja210117z>.
- (21) Dierkes, P.; Ramdeehul, S.; Barloy, L.; De Cian, A.; Fischer, J.; Kamer, P. C. J.; Van Leeuwen, P. W. N. M.; Osborn, J. A. Versatile Ligands for Palladium-Catalyzed Asymmetric Allylic Alkylation. *Angew. Chemie - Int. Ed.* **1998**, *37* (22), 3116–3118. [https://doi.org/10.1002/\(SICI\)1521-3773\(19981204\)37:22<3116::AID-ANIE3116>3.0.CO;2-S](https://doi.org/10.1002/(SICI)1521-3773(19981204)37:22<3116::AID-ANIE3116>3.0.CO;2-S).
- (22) Czauderna, C. F.; Jarvis, A. G.; Heutz, F. J. L.; Cordes, D. B.; Slawin, A. M. Z.; Vlugt, J. I. Van Der; Kamer, P. C. J. Chiral Wide-Bite-Angle Diphosphine Ligands: Synthesis, Coordination Chemistry, and Application in Pd-Catalyzed Allylic Alkylation. **2015**. <https://doi.org/10.1021/om5008055>.
- (23) Ricken, S.; Osinski, P. W.; Eilbracht, P.; Haag, R. A New Approach to Dendritic Supported NIXANTPHOS-Based Hydroformylation Catalysts. *J. Mol. Catal. A Chem.* **2006**, *257*, 78–88. <https://doi.org/10.1016/j.molcata.2006.04.037>.
- (24) Sandee, A. J.; Reek, J. N. H.; Kamer, P. C. J.; Van Leeuwen, P. W. N. M. A Silica-Supported, Switchable, and Recyclable Hydroformylation - Hydrogenation Catalyst. *J. Am. Chem. Soc.* **2001**, *123* (35), 8468–8476. <https://doi.org/10.1021/ja010150p>.
- (25) Schreuder Goedheijt, M.; Kamer, P. C. J.; Van Leeuwen, P. W. N. M. A Water-Soluble

- Diphosphine Ligand with a Large “natural” Bite Angle for Two-Phase Hydroformylation of Alkenes. *J. Mol. Catal. A Chem.* **1998**, *134* (1–3), 243–249. [https://doi.org/10.1016/S1381-1169\(98\)00042-9](https://doi.org/10.1016/S1381-1169(98)00042-9).
- (26) Goedheijt, M. S.; Hanson, B. E.; Reek, J. N. H.; Kamer, P. C. J.; Van Leeuwen, P. W. N. M. Accelerated Biphasic Hydroformylation by Vesicle Formation of Amphiphilic Diphosphines. *J. Am. Chem. Soc.* **2000**, *122* (8), 1650–1657. <https://doi.org/10.1021/ja9925610>.
- (27) Crocker, C.; Errington, R. J.; Markham, R.; Moulton, C. J.; Odell, K. J.; Shaw, B. L. Large-Ring and Cyclometalated Rhodium Complexes from Some Medium-Chain- α,ω -Diphosphines. *J. Am. Chem. Soc.* **1980**, *102* (13), 4373–4379. <https://doi.org/10.1021/ja00533a014>.
- (28) Zhang, Q. F.; Williard, P. G.; Wang, L. S. Polymorphism of Phosphine-Protected Gold Nanoclusters: Synthesis and Characterization of a New 22-Gold-Atom Cluster. *Small* **2016**, *12* (18), 2518–2525. <https://doi.org/10.1002/sml.201600407>.
- (29) Abdur-Rashid, K.; Graham, T.; Tsang, C.-W.; Chen, X.; Guo, R.; Jia, W.; Amoroso, D.; Sui-Seng, C. The Generation of Hydrogen from Ammonia Borane through Catalytic Hydrolysis. WO2008/141439 A1, 2008.
- (30) Besenyei, G.; Bitter, I.; Párkányi, L.; Szalontai, G.; Baranyai, P.; Kunsági-Máté, É.; Faigl, F.; Grün, A.; Kubinyi, M. A New Xantphos-Type Ligand and Its Gold(I) Complexes: Synthesis, Structure, Luminescence. *Polyhedron* **2013**, *55*, 57–66. <https://doi.org/10.1016/j.poly.2013.02.052>.
- (31) Tsuji, T. Bisphosphine, Process for Producing the Same, and Use Thereof, October 2, 2003.
- (32) Jeffrey, J. C.; Rauchfuss, T. B. Metal Complexes of Hemilabile Ligands. Reactivity and Structure of Dichlorobis(o-(Diphenylphosphino)Anisole)Ruthenium(II). *Inorg. Chem.* **1979**, *18* (10), 2658–2666. <https://doi.org/10.1021/ic50200a004>.
- (33) Moxham, G. L.; Randell-Sly, H. E.; Brayshaw, S. K.; Woodward, R. L.; Weller, A. S.; Willis, M. C. A Second-Generation Catalyst for Intermolecular Hydroacylation of Alkenes and Alkynes Using β -S-Substituted Aldehydes: The Role of a Hemilabile P-O-P Ligand. *Angew. Chemie - Int. Ed.* **2006**, *45* (45), 7618–7622. <https://doi.org/10.1002/anie.200603133>.
- (34) Adams, G. M.; Weller, A. S. POP-Type Ligands: Variable Coordination and Hemilabile Behaviour. *Coord. Chem. Rev.* **2018**, *355*, 150–172. <https://doi.org/10.1016/j.ccr.2017.08.004>.
- (35) Alcock, N. W.; Brown, J. M.; Jeffery, J. C. Structural and Chemical Aspects of Phosphino-Ethers as Chelating Ligands in Rhodium(I) Cationic Complexes. X-Ray Crystal Structures of Two Phosphino Ether Rhodium Carbonyl Complexes. *J. Chem. Soc. Chem. Commun.* **1974**, No. 20, 829–830. <https://doi.org/10.1039/C39740000829>.
- (36) Vogl, E. M.; Bruckmann, J.; Kassier, M.; Krüger, C.; Haenel, M. W. The Remarkable Tridentate Coordination of 4,6-Bis(Diphenylphosphanyl)Dibenzofuran in Ruthenium(II) Complexes. *Chem. Ber.* **1997**, *130* (9), 1315–1319. <https://doi.org/10.1002/cber.19971300922>.
- (37) Pintado-Alba, A.; De La Riva, H.; Nieuwhuyzen, M.; Bautista, D.; Raithby, P. R.; Sparkes, H. A.; Teat, S. J.; López-De-Luzuriaga, J. M.; Lagunas, M. C. Effects of Diphosphine Structure on Auophilicity and Luminescence in Au(I) Complexes. *Dalt. Trans.* **2004**, 2 (21), 3459–3467. <https://doi.org/10.1039/b410619a>.
- (38) Vogl, E. M.; Bruckmann, J.; Krüger, C.; Haenel, M. W. Bidentate Phosphines of Heteroarenes: Effective Stabilization of the Co₂(CO)₆ Fragment by 4,6-Bis(Diphenylphosphino)Dibenzofuran. *J. Organomet. Chem.* **1996**, *520* (1–2), 249–252. [https://doi.org/10.1016/0022-328X\(96\)06266-3](https://doi.org/10.1016/0022-328X(96)06266-3).

- (39) Major, Q.; Lough, A. J.; Gusev, D. G. Substituents Effects in POP Pincer Complexes of Ruthenium. *Organometallics* **2005**, *24* (10), 2492–2501. <https://doi.org/10.1021/om050053v>.
- (40) Ledger, A. E. W.; Moreno, A.; Ellul, C. E.; Mahon, M. F.; Pregosin, P. S.; Whittlesey, M. K.; Williams, J. M. J. Pincer Phosphine Complexes of Ruthenium : Formation of Ru(P-O-P)(PPh₃)HCl(P-O-P=xantphos , DPEphos , (Ph₂PCH₂CH₂)₂O) and Ru(Dppf)(PPh₃)HCl and Characterization of Cationic Dioxygen , Dihydrogen , Dinitrogen , and Arene Coordinated Phosphine Products. *Inorg. Chem.* **2010**, *49* (16), 7244–7256. <https://doi.org/10.1021/ic100438d>.
- (41) Alós, J.; Bolaño, T.; Esteruelas, M. A.; Oliván, M.; Oñate, E.; Valencia, M. POP-Pincer Ruthenium Complexes: D6 Counterparts of Osmium d 4 Species. *Inorg. Chem.* **2014**, *53* (2), 1195–1209. <https://doi.org/10.1021/ic402795g>.
- (42) Ishikawa, H.; Touge, T.; Kuriyama, W.; Kida, M.; Matsumura, K. Highly Efficient and Selective Hydrogenation of Sugars Catalyzed by Ru-MACHO-BH: Practical Synthesis of Sugar Alcohols. *Org. Process Res. Dev.* **2022**. <https://doi.org/10.1021/acs.oprd.2c00047>.
- (43) Kuriyama, W.; Matsumoto, T.; Ogata, O.; Ino, Y.; Aoki, K.; Tanaka, S.; Ishida, K.; Kobayashi, T.; Sayo, N.; Saito, T. Catalytic Hydrogenation of Esters. Development of an Efficient Catalyst and Processes for Synthesising (R)-1,2-Propanediol and 2-(1-Menthoxy)Ethanol. *Org. Process Res. Dev.* **2012**, *16* (1), 166–171. <https://doi.org/10.1021/op200234j>.
- (44) Kuriyama, W.; Matsumoto, T.; Ino, Y.; Ogata, O. Novel Ruthenium Carbonyl Complex Having Tridentate Ligand and Manufacturing Method and Usage Therefor. WO/2011/048727, 2011.
- (45) Alberico, E.; Lennox, A. J. J.; Vogt, L. K.; Jiao, H.; Baumann, W.; Drexler, H. J.; Nielsen, M.; Spannenberg, A.; Checinski, M. P.; Junge, H.; Beller, M. Unravelling the Mechanism of Basic Aqueous Methanol Dehydrogenation Catalyzed by Ru-PNP Pincer Complexes. *J. Am. Chem. Soc.* **2016**, *138* (45), 14890–14904. <https://doi.org/10.1021/jacs.6b05692>.
- (46) Fu, S.; Shao, Z.; Wang, Y.; Liu, Q. Manganese-Catalyzed Upgrading of Ethanol into 1-Butanol. *J. Am. Chem. Soc.* **2017**, *139* (34), 11941–11948. <https://doi.org/10.1021/jacs.7b05939>.
- (47) Agapova, A.; Alberico, E.; Kammer, A.; Junge, H.; Beller, M. Catalytic Dehydrogenation of Formic Acid with Ruthenium-PNP-Pincer Complexes: Comparing N-Methylated and NH-Ligands. *ChemCatChem* **2019**, *11* (7), 1910–1914. <https://doi.org/10.1002/cctc.201801897>.
- (48) Hölscher, M.; Leitner, W. Low Activation Barriers in N₂ Reduction with H₂ at Ruthenium Pincer Complexes Induced by Ligand Cooperativity: A Computational Study. *Eur. J. Inorg. Chem.* **2014**, *2014* (35), 6126–6133. <https://doi.org/10.1002/ejic.201402706>.
- (49) Simpson, M. C.; Cole-Hamilton, D. J. Catalytic Applications of Rhodium Complexes Containing Trialkylphosphines. *Coord. Chem. Rev.* **1996**, *155* (96), 163–207. [https://doi.org/10.1016/s0010-8545\(96\)90181-2](https://doi.org/10.1016/s0010-8545(96)90181-2).
- (50) Leising, R. A.; Ohman, J. S.; Takeuchi, K. J. Ligand Substitution Studies of Aquo (Phosphine) Ruthenium (II) Complexes. *Inorg. Chem.* **1988**, *27* (21), 3804–3809. <https://doi.org/10.1021/ic00294a026>.
- (51) Xie, Y.; Ben-David, Y.; Shimon, L. J. W.; Milstein, D. Highly Efficient Process for Production of Biofuel from Ethanol Catalyzed by Ruthenium Pincer Complexes. *J. Am. Chem. Soc.* **2016**, *138* (29), 9077–9080. <https://doi.org/10.1021/jacs.6b05433>.
- (52) Ledger, A. E. W. Chelating Phosphine Complexes of Ruthenium for the Coordination and Activation of Small Molecules, University of Bath, 2011.

- (53) Schunn, R. A.; Wonchoba, E. R.; Wilkinson, G. Chlorohydridotris(Triphenylphosphine)Ruthenium(II). *Inorganic Syntheses*. January 1, 1972, pp 131–134. <https://doi.org/doi:10.1002/9780470132449.ch26>.
- (54) Marimuthu, T.; Bala, M. D.; Friedrich, H. B. 4,6-Bis(Diphenyl-Phosphino)Phenoxazine (Nixantphos). *Acta Crystallogr. Sect. E Struct. Reports Online* **2008**, *64* (4). <https://doi.org/10.1107/S1600536808006648>.
- (55) Chung, D. D. L. Review Graphite. *J. Mater. Sci.* **2002**, *37* (8), 1475–1489. <https://doi.org/10.1023/A:1014915307738>.
- (56) Małecki, J. G.; Maroń, A. Chloride and Pseudohalide Hydride-Carbonyl Ruthenium(II) Complexes with 4-Pyrrolidinopyridine as Co-Ligand. *Transit. Met. Chem.* **2013**, *38* (2), 133–142. <https://doi.org/10.1007/s11243-012-9670-8>.
- (57) Jørgensen, M. S. B. Synthesis, Characterisation and Analysis of Ruthenium Pincer Complexes with Strongly π -Acidic Ligands, Technical University of Denmark, 2022.
- (58) Fraser, A. T. M. Sodium Azide as an Internal Standard for Quantitative Infrared Analysis. *Anal. Chem.* **1959**, *31* (9), 1602–1603. <https://doi.org/https://doi.org/10.1021/ac60153a005>.
- (59) Makino, M.; Ishizuka, T.; Ohzu, S.; Hua, J.; Kotani, H.; Kojima, T. Synthesis and Characterization of an Azido-Bridged Dinuclear Ruthenium(II) Polypyridylamine Complex Forming a Mixed-Valence State. *Inorg. Chem.* **2013**, *52* (9), 5507–5514. <https://doi.org/10.1021/ic400412f>.
- (60) Nongbri, S. L.; Das, B.; Rao, K. M. Arene Ruthenium β -Diketonato Triazolato Derivatives: Synthesis and Spectral Studies (β -Diketones: 1-Phenyl-3-Methyl-4-Benzoyl Pyrazol-5-One, Acetylacetone Derivatives). *J. Organomet. Chem.* **2009**, *694* (24), 3881–3891. <https://doi.org/10.1016/j.jorganchem.2009.08.006>.
- (61) Che, C.-M.; Lai, T.-F.; Lau, K.; Mak, T. C. W. Studies on Ruthenium(II) Macrocyclic Amine Complexes. Synthesis and X-Ray Structure of the (R,S,R,R) Isomer of Trans-[Ru(L)(N₃)(NCMe)]PF₆(L = 1,4,8,11-Tetramethyl-1,4,8,11-Tetra-Azacyclotetradecane). *J. Chem. Soc. Dalt. Trans.* **1988**, No. 1, 239–241. <https://doi.org/10.1039/DT9880000239>.
- (62) Chang, C. W.; Lee, G. H. Synthesis of Ruthenium Triazolato and Tetrazolato Complexes by 1,3-Dipolar Cycloadditions of Ruthenium Azido Complex with Alkynes and Alkenes and Regiospecific Alkylation of Triazolates. *Organometallics* **2003**, *22* (15), 3107–3116. <https://doi.org/10.1021/om030079r>.
- (63) Shafiee, S.; Topal, E. A Long-Term View of Worldwide Fossil Fuel Prices. *Appl. Energy* **2010**, *87* (3), 988–1000. <https://doi.org/10.1016/j.apenergy.2009.09.012>.
- (64) Mann, M. E.; Bradley, R. S.; Hughes, M. K. Northern Hemisphere Temperatures during the Past Millennium: Inferences, Uncertainties, and Limitations. *Geophys. Res. Lett.* **1999**, *26* (6), 759–762. <https://doi.org/10.1029/1999GL900070>.
- (65) Neftel, A.; Moor, E.; Oeschger, H.; Stauffer, B. Evidence from Polar Ice Cores for the Increase in Atmospheric CO₂ in the Past Two Centuries. *Nature* **1985**, *315*, 45–47. <https://doi.org/10.1038/315045a0>.
- (66) Bento, A.; Roth, K.; Zuo, Y. Vehicle Lifetime and Scrappage Behavior: Trends in the U.S. Used Car Market. *Energy J.* **2018**, *39* (1), 159–183. <https://doi.org/10.5547/01956574.39.1.aben>.
- (67) Van Mierlo, J.; Maggetto, G. Fuel Cell or Battery: Electric Cars Are the Future. *Fuel Cells* **2007**, *7* (2), 165–173. <https://doi.org/10.1002/fuce.200600052>.

-
- (68) Basso, T. O.; Gomes, F. S.; Lopes, M. L.; De Amorim, H. V.; Eggleston, G.; Basso, L. C. Homo- and Heterofermentative Lactobacilli Differently Affect Sugarcane-Based Fuel Ethanol Fermentation. *Antonie van Leeuwenhoek, Int. J. Gen. Mol. Microbiol.* **2014**, *105* (1), 169–177. <https://doi.org/10.1007/s10482-013-0063-6>.
- (69) Gumienna, M.; Szambelan, K.; Jeleń, H.; Czarnecki, Z. Evaluation of Ethanol Fermentation Parameters for Bioethanol Production from Sugar Beet Pulp and Juice. *J. Inst. Brew.* **2014**, *120* (4), 543–549. <https://doi.org/10.1002/jib.181>.
- (70) Izmirlioglu, G.; Demirci, A. Ethanol Production from Waste Potato Mash by Using *Saccharomyces Cerevisiae*. *Appl. Sci.* **2012**, *2* (4), 738–753. <https://doi.org/10.3390/app2040738>.
- (71) Bothast, R. J.; Schlicher, M. A. Biotechnological Processes for Conversion of Corn into Ethanol. *Appl. Microbiol. Biotechnol.* **2005**, *67* (1), 19–25. <https://doi.org/10.1007/s00253-004-1819-8>.
- (72) Zertuche, L.; Zall, R. R. A Study of Producing Ethanol from Cellulose Using *Clostridium Thermocellum*. *Biotechnol. Bioeng.* **1982**, *24* (1), 57–68. <https://doi.org/10.1002/bit.260240106>.
- (73) Foong, T. M.; Morganti, K. J.; Brear, M. J.; Da Silva, G.; Yang, Y.; Dryer, F. L. The Octane Numbers of Ethanol Blended with Gasoline and Its Surrogates. *Fuel* **2014**, *115*, 727–739. <https://doi.org/10.1016/j.fuel.2013.07.105>.
- (74) Lee, S. Y.; Park, J. H.; Jang, S. H.; Nielsen, L. K.; Kim, J.; Jung, K. S. Fermentative Butanol Production by Clostridia. *Biotechnol. Bioeng.* **2008**, *101* (2), 209–228. <https://doi.org/10.1002/bit.22003>.
- (75) Zhen, X.; Wang, Y.; Xu, S.; Zhu, Y.; Tao, C.; Xu, T.; Song, M. The Engine Knock Analysis - An Overview. *Appl. Energy* **2012**, *92*, 628–636. <https://doi.org/10.1016/j.apenergy.2011.11.079>.
- (76) Anderson, L. G. Ethanol Fuel Use in Brazil: Air Quality Impacts. *Energy Environ. Sci.* **2009**, *2* (10), 1015–1037. <https://doi.org/10.1039/b906057j>.
- (77) Jafari, H.; Idris, M. H.; Ourdjini, A.; Rahimi, H.; Ghobadian, B. EIS Study of Corrosion Behavior of Metallic Materials in Ethanol Blended Gasoline Containing Water as a Contaminant. *Fuel* **2011**, *90* (3), 1181–1187. <https://doi.org/10.1016/j.fuel.2010.12.010>.
- (78) Davis, G. W.; Heil, E. T.; Rust, R. Ethanol Vehicle Cold Start Improvement When Using a Hydrogen Supplemented E85 Fuel. In *Collection of Technical Papers. 35th Intersociety Energy Conversion Engineering Conference and Exhibit (IECEC) (Cat. No.00CH37022)*; 2000; Vol. 1, pp 303–308. <https://doi.org/10.1109/IECEC.2000.870702>.
- (79) Krenus, R.; Passos, M. R. V.; Ortega, T.; Mowery, K.; Kim, Y. J.; Lavan, L. G.; Lee, K.; Park, C. J.; Han, K. Ethanol Flex Fuel System with Delphi Heated Injector Application. *SAE Tech. Pap.* **2014**. <https://doi.org/10.4271/2014-01-1369>.
- (80) Aperador, W.; Caballero-Gómez, J.; Delgado, A. Corrosion Behavior of the AA2124 Aluminium Alloy Exposed to Ethanol Mixtures. *Int. J. Electrochem. Sci.* **2013**, *8* (5), 6154–6161. [https://doi.org/10.1016/S1452-3981\(23\)14749-3](https://doi.org/10.1016/S1452-3981(23)14749-3).
- (81) Kemme, H. R.; Kreps, S. I. Vapor Pressure of Primary N-Alkyl Chlorides and Alcohols. *J. Chem. Eng. Data* **1969**, *14* (1), 98–102. <https://doi.org/10.1021/je60040a011>.
- (82) Kremer, F.; Blank, L. M.; Jones, P. R.; Akhtar, M. K. A Comparison of the Microbial Production and Combustion Characteristics of Three Alcohol Biofuels: Ethanol, 1-Butanol, and 1-Octanol. *Front. Bioeng. Biotechnol.* **2015**, *3* (AUG), 1–7. <https://doi.org/10.3389/fbioe.2015.00112>.

-
- (83) Ellefson, W. L.; Bowles, L. K. Effects of Butanol on *Clostridium Acetobutylicum*. *Appl. Environ. Microbiol.* **1985**, *50* (5), 1165–1170. <https://doi.org/10.1128/aem.50.5.1165-1170.1985>.
- (84) Woods, D. R. The Genetic Engineering of Microbial Solvent Production. *Trends Biotechnol.* **1995**, *13* (7), 259–264. [https://doi.org/10.1016/S0167-7799\(00\)88960-X](https://doi.org/10.1016/S0167-7799(00)88960-X).
- (85) Guerbet, M. Action Des Alcools Éthylique, Isobutylique, Isoamylique Sur Leurs Dérivés Sodés. *Comptes rendus académie des Sci.* **1899**, 1002–1004.
- (86) Hamid, M. H. S. A.; Slatford, P. A.; Williams, J. M. J. Borrowing Hydrogen in the Activation of Alcohols. *Adv. Synth. Catal.* **2007**, *349* (10), 1555–1575. <https://doi.org/10.1002/adsc.200600638>.
- (87) Shen, D.; Poole, D. L.; Shotton, C. C.; Kornahrens, A. F.; Healy, M. P.; Donohoe, T. J. Hydrogen-Borrowing and Interrupted-Hydrogen-Borrowing Reactions of Ketones and Methanol Catalyzed by Iridium. *Angew. Chemie - Int. Ed.* **2015**, *54* (5), 1642–1645. <https://doi.org/10.1002/anie.201410391>.
- (88) De Pours, M. V.; Sathiyagnanam, A. P.; Rana, D.; Rajesh Kumar, B.; Saravanan, S. 1-Hexanol as a Sustainable Biofuel in DI Diesel Engines and Its Effect on Combustion and Emissions under the Influence of Injection Timing and Exhaust Gas Recirculation (EGR). *Appl. Therm. Eng.* **2017**, *113*, 1505–1513. <https://doi.org/10.1016/j.applthermaleng.2016.11.164>.
- (89) Cannizzaro, S. Ueber Den Der Benzoësäure Entsprechenden Alkohol. *Justus Liebigs Ann. Chem.* **1853**, *88* (1), 129–130. <https://doi.org/10.1002/jlac.18530880114>.
- (90) Seki, T.; Nakajo, T.; Onaka, M. The Tishchenko Reaction: A Classic and Practical Tool for Ester Synthesis. *Chem. Lett.* **2006**, *35* (8), 824–829. <https://doi.org/10.1246/cl.2006.824>.
- (91) Idriss, H.; Seebauer, E. G. Reactions of Ethanol over Metal Oxides. *J. Mol. Catal. A Chem.* **2000**, *152* (1–2), 201–212. [https://doi.org/10.1016/S1381-1169\(99\)00297-6](https://doi.org/10.1016/S1381-1169(99)00297-6).
- (92) Cook, J.; Hamlin, J. E.; Nutton, A.; Maitlis, P. M. Pentamethylcyclopentadienyl-Rhodium and -Iridium Complexes. Part 33. The Metal-Catalysed Disproportionation of Acetaldehyde into Acetic Acid and Ethanol. *J. Chem. Soc. Dalt. Trans.* **1981**, 2343–2353.
- (93) Sponholz, P.; Mellmann, D.; Cordes, C.; Alsabeh, P. G.; Li, B.; Li, Y.; Nielsen, M.; Junge, H.; Dixneuf, P.; Beller, M. Efficient and Selective Hydrogen Generation from Bioethanol Using Ruthenium Pincer-Type Complexes. *ChemSusChem* **2014**, *7* (9), 2419–2422. <https://doi.org/10.1002/cssc.201402426>.
- (94) Ni, Z.; Padilla, R.; dos Santos Mello, L.; Nielsen, M. Tuning Ethanol Upgrading toward Primary or Secondary Alcohols by Homogeneous Catalysis. *ACS Catal.* **2023**, *13* (8), 5449–5455. <https://doi.org/10.1021/acscatal.2c06322>.
- (95) Dowson, G. R. M.; Haddow, M. F.; Lee, J.; Wingad, R. L.; Wass, D. F. Catalytic Conversion of Ethanol into an Advanced Biofuel: Unprecedented Selectivity for n-Butanol. *Angew. Chemie - Int. Ed.* **2013**, *52* (34), 9005–9008. <https://doi.org/10.1002/anie.201303723>.
- (96) Tseng, K. N. T.; Lin, S.; Kampf, J. W.; Szymczak, N. K. Upgrading Ethanol to 1-Butanol with a Homogeneous Air-Stable Ruthenium Catalyst. *Chem. Commun.* **2016**, *52* (14), 2901–2904. <https://doi.org/10.1039/c5cc09913g>.
- (97) Kulkarni, N. V.; Brennessel, W. W.; Jones, W. D. Catalytic Upgrading of Ethanol to N-Butanol via Manganese Mediated Guerbet Reaction. *ACS Catal.* **2018**, *8* (2), 997–1002. <https://doi.org/10.1021/acscatal.7b03653>.

- (98) Elangovan, S.; Topf, C.; Fischer, S.; Jiao, H.; Spannenberg, A.; Baumann, W.; Ludwig, R.; Junge, K.; Beller, M. Selective Catalytic Hydrogenations of Nitriles, Ketones, and Aldehydes by Well-Defined Manganese Pincer Complexes. *J. Am. Chem. Soc.* **2016**, *138* (28), 8809–8814. <https://doi.org/10.1021/jacs.6b03709>.
- (99) Johansson, A. J.; Zuidema, E.; Bolm, C. On the Mechanism of Ruthenium-Catalyzed Formation of Hydrogen from Alcohols: A DFT Study. *Chem. - A Eur. J.* **2010**, *16* (45), 13487–13499. <https://doi.org/10.1002/chem.201000593>.
- (100) Dub, P. A.; Gordon, J. C. Metal-Ligand Bifunctional Catalysis: The “Accepted” Mechanism, the Issue of Concertedness, and the Function of the Ligand in Catalytic Cycles Involving Hydrogen Atoms. *ACS Catal.* **2017**, *7* (10), 6635–6655. <https://doi.org/10.1021/acscatal.7b01791>.
- (101) Noyori, R.; Ohkuma, T. Asymmetric Catalysis by Architectural and Functional Molecular Engineering: Practical Chemo- and Stereoselective Hydrogenation of Ketones. *Angew. Chemie - Int. Ed.* **2001**, *40* (1), 40–73. [https://doi.org/10.1002/1521-3773\(20010105\)40:1<40::AID-ANIE40>3.0.CO;2-5](https://doi.org/10.1002/1521-3773(20010105)40:1<40::AID-ANIE40>3.0.CO;2-5).
- (102) Fryzuk, M. D.; MacNeil, P. A. Stereoselective Formation of Iridium(III) Amides and Ligand-Assisted Heterolytic Splitting of Dihydrogen. *Organometallics* **1983**, *2* (5), 682–684. <https://doi.org/10.1021/om00077a020>.
- (103) Fryzuk, M. D.; Bhangu, K. Activation of Dihydrogen by Organo-Iridium-Phosphido Complexes. Evidence for α -Hydrogen Abstraction by a Terminal Phosphide Ligand. *J. Am. Chem. Soc.* **1988**, *110* (3), 961–963. <https://doi.org/10.1021/ja00211a044>.
- (104) Zhang, J.; Leitus, G.; Ben-David, Y.; Milstein, D. Efficient Homogeneous Catalytic Hydrogenation of Esters to Alcohols. *Angew. Chemie - Int. Ed.* **2006**, *45* (7), 1113–1115. <https://doi.org/10.1002/anie.200503771>.
- (105) Zeng, K.; Zhang, D. Recent Progress in Alkaline Water Electrolysis for Hydrogen Production and Applications. *Prog. Energy Combust. Sci.* **2010**, *36* (3), 307–326. <https://doi.org/10.1016/j.pecs.2009.11.002>.
- (106) Steinfeld, A. Solar Hydrogen Production via a Two-Step Water-Splitting Thermochemical Cycle Based on Zn/ZnO Redox Reactions. *Int. J. Hydrogen Energy* **2002**, *27* (6), 611–619. [https://doi.org/10.1016/S0360-3199\(01\)00177-X](https://doi.org/10.1016/S0360-3199(01)00177-X).
- (107) Zhang, Y. H.; Jia, Z. C.; Yuan, Z. M.; Yang, T.; Qi, Y.; Zhao, D. L. Development and Application of Hydrogen Storage. *J. Iron Steel Res. Int.* **2015**, *22* (9), 757–770. [https://doi.org/10.1016/S1006-706X\(15\)30069-8](https://doi.org/10.1016/S1006-706X(15)30069-8).
- (108) Rao, P. C.; Yoon, M. Potential Liquid-Organic Hydrogen Carrier (Lohc) Systems: A Review on Recent Progress. *Energies* **2020**, *13* (22). <https://doi.org/10.3390/en13226040>.
- (109) Niermann, M.; Beckendorff, A.; Kaltschmitt, M.; Bonhoff, K. Liquid Organic Hydrogen Carrier (LOHC) – Assessment Based on Chemical and Economic Properties. *Int. J. Hydrogen Energy* **2019**, *44* (13), 6631–6654. <https://doi.org/10.1016/j.ijhydene.2019.01.199>.
- (110) Hodoshima, S.; Takaiwa, S.; Shono, A.; Satoh, K.; Saito, Y. Hydrogen Storage by Decalin/Naphthalene Pair and Hydrogen Supply to Fuel Cells by Use of Superheated Liquid-Film-Type Catalysis. *Appl. Catal. A Gen.* **2005**, *283* (1–2), 235–242. <https://doi.org/10.1016/j.apcata.2005.01.010>.
- (111) Huynh, N. D.; Hur, S. H.; Kang, S. G. Tuning the Dehydrogenation Performance of Dibenzyl Toluene as Liquid Organic Hydrogen Carriers. *Int. J. Hydrogen Energy* **2021**, *46* (70), 34788–

34796. <https://doi.org/10.1016/j.ijhydene.2021.08.039>.
- (112) Bachmann, P.; Schwarz, M.; Steinhauer, J.; Späth, F.; Düll, F.; Bauer, U.; Nascimento Silva, T.; Mohr, S.; Hohner, C.; Scheuermeyer, M.; Wasserscheid, P.; Libuda, J.; Steinrück, H. P.; Papp, C. Dehydrogenation of the Liquid Organic Hydrogen Carrier System Indole/Indoline/Octahydroindole on Pt(111). *J. Phys. Chem. C* **2018**, *122* (8), 4470–4479. <https://doi.org/10.1021/acs.jpcc.7b12625>.
- (113) Yang, M.; Dong, Y.; Fei, S.; Pan, Q.; Ni, G.; Han, C.; Ke, H.; Fang, Q.; Cheng, H. Hydrogenation of N-Propylcarbazole over Supported Ruthenium as a New Prototype of Liquid Organic Hydrogen Carriers (LOHC). *RSC Adv.* **2013**, *3* (47), 24877–24881. <https://doi.org/10.1039/c3ra44760j>.
- (114) Pez, G. P.; Scott, A. R.; Cooper, A. C.; Cheng, H.; Wilhelm, F. C.; Abdourazak, A. H. Hydrogen Storage by Reversible Hydrogenation of Pi-Conjugated Substrates. US 7351395, 2008.
- (115) Teichmann, D.; Arlt, W.; Wasserscheid, P.; Freymann, R. A Future Energy Supply Based on Liquid Organic Hydrogen Carriers (LOHC). *Energy Environ. Sci.* **2011**, *4* (8), 2767–2773. <https://doi.org/10.1039/c1ee01454d>.
- (116) Eschweiler, W. Ersatz von an Stickstoff Gebundenen Wasserstoffatomen Durch Die Methylgruppe Mit Hilfe von Formaldehyd. *Chem. Ber.* **1905**, *38*, 880–882.
- (117) Alexander, E. R.; Bowman Wildman, R. Studies on the Mechanism of the Leuckart Reaction. *J. Am. Chem. Soc.* **1948**, *70* (3), 1187–1189. [https://doi.org/10.1016/S0140-6736\(00\)62619-3](https://doi.org/10.1016/S0140-6736(00)62619-3).
- (118) Hietala, J.; Vuori, A.; Johnson, P.; Pollari, I.; Reutemann, W.; Kieczka, H. Formic Acid. In *Ullmann's Encyclopedia of Industrial Chemistry*; 2016; Vol. 1, pp 1–22. <https://doi.org/10.1002/14356007>.
- (119) Eppinger, J.; Huang, K. W. Formic Acid as a Hydrogen Energy Carrier. *ACS Energy Lett.* **2017**, *2* (1), 188–195. <https://doi.org/10.1021/acsenerylett.6b00574>.
- (120) Kawanami, H.; Himeda, Y.; Laurenczy, G. Formic Acid as a Hydrogen Carrier for Fuel Cells Toward a Sustainable Energy System. *Adv. Inorg. Chem.* **2017**, *70*, 395–427. <https://doi.org/10.1016/bs.adioch.2017.04.002>.
- (121) Sarathy, S. M.; Brequigny, P.; Katogh, A.; Elbaz, A. M.; Roberts, W. L.; Dibble, R. W.; Foucher, F. Laminar Burning Velocities and Kinetic Modeling of a Renewable E-Fuel: Formic Acid and Its Mixtures with H₂ and CO₂. *Energy and Fuels* **2020**, *34* (6), 7564–7572. <https://doi.org/10.1021/acs.energyfuels.0c00944>.
- (122) Maharjan, S.; Elbaz, A. M.; Roberts, W. L. Investigation on the Formic Acid Evaporation and Ignition of Formic Acid/Octanol Blend at Elevated Temperature and Pressure. *Fuel* **2022**, *313* (July 2021), 122636. <https://doi.org/10.1016/j.fuel.2021.122636>.
- (123) Rees, N. V.; Compton, R. G. Sustainable Energy: A Review of Formic Acid Electrochemical Fuel Cells. *J. Solid State Electrochem.* **2011**, *15* (10), 2095–2100. <https://doi.org/10.1007/s10008-011-1398-4>.
- (124) Coffey, R. S. The Decomposition of Formic Acid Catalysed by Soluble Metal Complexes. *Chem. Commun.* **1967**, No. 18, 923b – 924. <https://doi.org/10.1039/C1967000923b>.
- (125) Wang, Z.; Lu, S. M.; Li, J.; Wang, J.; Li, C. Unprecedentedly High Formic Acid Dehydrogenation Activity on an Iridium Complex with an N,N'-Diimine Ligand in Water. *Chem. - A Eur. J.* **2015**, *21* (36), 12592–12595. <https://doi.org/10.1002/chem.201502086>.

- (126) Hong, D.; Shimoyama, Y.; Ohgomori, Y.; Kanega, R.; Kotani, H.; Ishizuka, T.; Kon, Y.; Himeda, Y.; Kojima, T. Cooperative Effects of Heterodinuclear IrIII–MII Complexes on Catalytic H₂ Evolution from Formic Acid Dehydrogenation in Water. *Inorg. Chem.* **2020**, *59* (17), 11976–11985. <https://doi.org/10.1021/acs.inorgchem.0c00812>.
- (127) Fink, C.; Laurenczy, G. A Precious Catalyst: Rhodium-Catalyzed Formic Acid Dehydrogenation in Water. *Eur. J. Inorg. Chem.* **2019**, No. 18, 2381–2387. <https://doi.org/10.1002/ejic.201900344>.
- (128) Celaje, J. J. A.; Lu, Z.; Kedzie, E. A.; Terrile, N. J.; Lo, J. N.; Williams, T. J. A Prolific Catalyst for Dehydrogenation of Neat Formic Acid. *Nat. Commun.* **2016**, *7* (1), 11308. <https://doi.org/10.1038/ncomms11308>.
- (129) Onishi, N.; Kanega, R.; Fujita, E.; Himeda, Y. Carbon Dioxide Hydrogenation and Formic Acid Dehydrogenation Catalyzed by Iridium Complexes Bearing Pyridyl-Pyrazole Ligands: Effect of an Electron-Donating Substituent on the Pyrazole Ring on the Catalytic Activity and Durability. *Adv. Synth. Catal.* **2019**, *361* (2), 289–296. <https://doi.org/10.1002/adsc.201801323>.
- (130) Filonenko, G. A.; Van Putten, R.; Schulpen, E. N.; Hensen, E. J. M.; Pidko, E. A. Highly Efficient Reversible Hydrogenation of Carbon Dioxide to Formates Using a Ruthenium PNP-Pincer Catalyst. *ChemCatChem* **2014**, *6* (6), 1526–1530. <https://doi.org/10.1002/cctc.201402119>.
- (131) Kar, S.; Rauch, M.; Leitus, G.; Ben-David, Y.; Milstein, D. Highly Efficient Additive-Free Dehydrogenation of Neat Formic Acid. *Nat. Catal.* **2021**, *4* (3), 193–201. <https://doi.org/10.1038/s41929-021-00575-4>.
- (132) Piccirilli, L.; Rabell, B.; Padilla, R.; Riisager, A.; Das, S.; Nielsen, M. Versatile CO₂ Hydrogenation-Dehydrogenation Catalysis with a Ru-PNP/Ionic Liquid System. *J. Am. Chem. Soc.* **2023**, *145* (10), 5655–5663. <https://doi.org/10.1021/jacs.2c10399>.
- (133) Endres, F.; Zein El Abedin, S. Air and Water Stable Ionic Liquids in Physical Chemistry. *Phys. Chem. Chem. Phys.* **2006**, *8* (18), 2101–2116. <https://doi.org/10.1039/b600519p>.
- (134) Huang, K.; Wu, R.; Cao, Y.; Li, H.; Wang, J. Recycling and Reuse of Ionic Liquid in Homogeneous Cellulose Acetylation. *Chinese J. Chem. Eng.* **2013**, *21* (5), 577–584. [https://doi.org/10.1016/S1004-9541\(13\)60524-8](https://doi.org/10.1016/S1004-9541(13)60524-8).
- (135) Huddleston, J. G.; Willauer, H. D.; Swatloski, R. P.; Visser, A. E.; Rogers, R. D. Room Temperature Ionic Liquids as Novel Media for “clean” Liquid-Liquid Extraction. *Chem. Commun.* **1998**, No. 16, 1765–1766. <https://doi.org/10.1039/A803999B>.
- (136) Kröckel, J.; Kragl, U. Nanofiltration for the Separation of Nonvolatile Products from Solutions Containing Ionic Liquids. *Chem. Eng. Technol.* **2003**, *26* (11), 1166–1168. <https://doi.org/10.1002/ceat.200301830>.
- (137) Nasir Shah, S.; Mutalib, M. I. A.; Pilus, R. B. M.; Lethesh, K. C. Extraction of Naphthenic Acid from Highly Acidic Oil Using Hydroxide-Based Ionic Liquids. *Energy & Fuels* **2015**, *29* (1), 106–111. <https://doi.org/10.1021/ef502169q>.
- (138) Benavides-Garcia, M. G.; Monroe, M. Molecular Models and IR Spectra of Asymmetric Tetraalkyl Phosphonium Iodide Ionic Liquids. *Chem. Phys. Lett.* **2009**, *479* (4–6), 238–243. <https://doi.org/10.1016/j.cplett.2009.08.054>.
- (139) Huang, K.; Cai, D.-N.; Chen, Y.-L.; Wu, Y.-T.; Hu, X.-B.; Zhang, Z.-B. Thermodynamic Validation of 1-Alkyl-3-Methylimidazolium Carboxylates as Task-Specific Ionic Liquids for H₂S Absorption. *AIChE J.* **2013**, *59* (6), 2227–2235. <https://doi.org/10.1002/aic>.

- (140) Weaver, K. D.; Kim, H. J.; Sun, J.; MacFarlane, D. R.; Elliott, G. D. Cyto-Toxicity and Biocompatibility of a Family of Choline Phosphate Ionic Liquids Designed for Pharmaceutical Applications. *Green Chem.* **2010**, *12* (3), 507–513. <https://doi.org/10.1039/b918726j>.
- (141) Docherty, K. M.; Kulpa, C. F. Toxicity and Antimicrobial Activity of Imidazolium and Pyridinium Ionic Liquids. *Green Chem.* **2005**, *7* (4), 185–189. <https://doi.org/10.1039/b419172b>.
- (142) Lange, C.; Patil, G.; Rudolph, R. Ionic Liquids as Refolding Additives: N'-Alkyl and N'-(ω -Hydroxyalkyl) N-Methylimidazolium Chlorides. *Protein Sci.* **2005**, *14* (10), 2693–2701. <https://doi.org/10.1110/ps.051596605>.
- (143) Di Noto, V.; Negro, E.; Sanchez, J. Y.; Iojoiu, C. Structure-Relaxation Interplay of a New Nanostructured Membrane Based on Tetraethylammonium Trifluoromethanesulfonate Ionic Liquid and Neutralized Nafion 117 for High-Temperature Fuel Cells. *J. Am. Chem. Soc.* **2010**, *132* (7), 2183–2195. <https://doi.org/10.1021/ja906975z>.
- (144) Blesic, M.; Swadźba-Kwaśny, M.; Holbrey, J. D.; Canongia Lopes, J. N.; Seddon, K. R.; Rebelo, L. P. N. New Catanionic Surfactants Based on 1-Alkyl-3-Methylimidazolium Alkylsulfonates, [C_nH_{2n+1}mim][C_mH_{2m+1}SO₃]: Mesomorphism and Aggregation. *Phys. Chem. Chem. Phys.* **2009**, *11* (21), 4260–4268. <https://doi.org/10.1039/b822341f>.
- (145) García, S.; Larriba, M.; García, J.; Torrecilla, J. S.; Rodríguez, F. Alkylsulfate-Based Ionic Liquids in the Liquid-Liquid Extraction of Aromatic Hydrocarbons. *J. Chem. Thermodyn.* **2012**, *45* (1), 68–74. <https://doi.org/10.1016/j.jct.2011.09.009>.
- (146) Piquet, M.; Poinot, D.; Stutzmann, S.; Tkatchenko, I.; Tommasi, I.; Wasserscheid, P.; Zimmermann, J. Ionic Liquids: Media for Better Molecular Catalysis. *Top. Catal.* **2004**, *29*, 139–143. <https://doi.org/10.1023/B:TOCA.0000029796.11969.ec>.
- (147) Wang, H.; Wang, J.; Zhang, S.; Pei, Y.; Zhuo, K. Ionic Association of the Ionic Liquids [C₄mim][BF₄], [C₄mim][PF₆], and [C_nmim]Br in Molecular Solvents. *ChemPhysChem* **2009**, *10* (14), 2516–2523. <https://doi.org/10.1002/cphc.200900438>.
- (148) Schraml, J.; Capka, M.; Blechta, V. ³¹P and ¹³C NMR Spectra of Cyclohexylphenylphosphines, Tricyclohexylphosphine and Triphenylphosphine. *Magn. Reson. Chem.* **1992**, *30*, 544–547. <https://doi.org/10.1002/mrc.1260300615>.
- (149) Calder, G. V.; Barton, T. J. Actual Effects Controlling the Acidity of Carboxylic Acids. *J. Chem. Educ.* **1971**, *48* (5), 338–340. <https://doi.org/10.1021/ed048p338>.
- (150) Lewandowska, H.; Kalinowska, M.; Brzóska, K.; Wójciuk, K.; Wójciuk, G.; Kruszewski, M. Nitrosyl Iron Complexes - Synthesis, Structure and Biology. *Dalt. Trans.* **2011**, *40*, 8273–8289. <https://doi.org/10.1039/c0dt01244k>.
- (151) Jørgensen, C. K. *Oxidation Numbers and Oxidation States*; Springer Berlin Heidelberg: Heidelberg, 1969.
- (152) Kooistra, T. M.; Hetterscheid, D. G. H.; Schwartz, E.; Knijnenburg, Q.; Budzelaar, P. H. M.; Gal, A. W. Chemical Ligand Non-Innocence in Pyridine Diimine Rh Complexes. *Inorganica Chim. Acta* **2004**, *357* (10), 2945–2952. <https://doi.org/10.1016/j.ica.2004.02.012>.
- (153) Tarrago, M.; Ye, S.; Neese, F. Electronic Structure Analysis of Electrochemical CO₂ Reduction by Iron-Porphyrins Reveals Basic Requirements for Design of Catalysts Bearing Non-Innocent Ligands. *Chem. Sci.* **2022**, *13* (34), 10029–10047. <https://doi.org/10.1039/d2sc01863b>.
- (154) Schaefer, W. P. The Structure of Decaammine-p-Peroxo-Dicobalt Disulfate Tetrahydrate. *Inorg.*

- Chem.* **1968**, 7 (4), 725–731. <https://doi.org/https://doi.org/10.1021/ic50062a022>.
- (155) Olabe, J. A. The Coordination Chemistry of Nitrosyl in Cyanoferrates. An Exhibit of Bioinorganic Relevant Reactions. *Dalt. Trans.* **2008**, No. 28, 3633–3648. <https://doi.org/10.1039/b803153c>.
- (156) Enemark, J. H.; Feltham, R. D. Principles of Structure, Bonding, and Reactivity for Metal Nitrosyl Complexes. *Coord. Chem. Rev.* **1974**, 13 (4), 339–406. [https://doi.org/10.1016/S0010-8545\(00\)80259-3](https://doi.org/10.1016/S0010-8545(00)80259-3).
- (157) Gaviglio, C.; Pellegrino, J.; Milstein, D.; Doctorovich, F. NO Disproportionation by a {RhNO}₃ Pincer-Type Complex. *Dalt. Trans.* **2017**, 46 (48), 16878–16884. <https://doi.org/10.1039/c7dt03944a>.
- (158) Averill, B. A. Dissimilatory Nitrite and Nitric Oxide Reductases. *Chem. Rev.* **1996**, 96 (7), 2951–2964. <https://doi.org/10.1021/cr950056p>.
- (159) Wasser, I. M.; de Vries, S.; Moëne-Loccoz, P.; Schröder, I.; Karlin, K. D. Nitric Oxide in Biological Denitrification: Fe/Cu Metalloenzyme and Metal Complex NO_x Redox Chemistry. *Chem. Rev.* **2002**, 102 (4), 1201–1234. <https://doi.org/10.1021/cr0006627>.
- (160) Conradie, J.; Ghosh, A. Stereochemical Diversity of {MNO}₃ Complexes: Molecular Orbital Analyses of Nickel and Copper Nitrosyls. *Inorg. Chem.* **2014**, 53 (10), 4847–4855. <https://doi.org/10.1021/ic4028157>.
- (161) Mingos, D. M. P.; Sherman, D. J. Transition Metal Nitrosyl Complexes. In *Advances in Inorganic Chemistry*; Sykes, A. G. B. T.-A. in I. C., Ed.; Academic Press, 1989; Vol. 34, pp 293–377. [https://doi.org/10.1016/S0898-8838\(08\)60019-7](https://doi.org/10.1016/S0898-8838(08)60019-7).
- (162) De La Cruz, C.; Sheppard, N. A Structure-Based Analysis of the Vibrational Spectra of Nitrosyl Ligands in Transition-Metal Coordination Complexes and Clusters. *Spectrochim. Acta - Part A Mol. Biomol. Spectrosc.* **2011**, 78 (1), 7–28. <https://doi.org/10.1016/j.saa.2010.08.001>.
- (163) Adeniyi, A. A.; Ajibade, P. A. Exploring the Ruthenium-Ligands Bond and Their Relative Properties at Different Computational Methods. *J. Chem.* **2016**, 2016. <https://doi.org/10.1155/2016/3672062>.
- (164) Yaroshevsky, A. A. Abundances of Chemical Elements in the Earth's Crust. *Geochemistry Int.* **2006**, 44 (1), 48–55. <https://doi.org/10.1134/S001670290601006X>.
- (165) Anderson, N. H.; Boncella, J.; Tondreau, A. M. Manganese-Mediated Formic Acid Dehydrogenation. *Chem. - A Eur. J.* **2019**, 25 (45), 10557–10560. <https://doi.org/10.1002/chem.201901177>.
- (166) Léval, A.; Junge, H.; Beller, M. Manganese(i) K₂-: NN Complex-Catalyzed Formic Acid Dehydrogenation. *Catal. Sci. Technol.* **2020**, 10 (12), 3931–3937. <https://doi.org/10.1039/d0cy00769b>.
- (167) Dutta, I.; Alobaid, N. A.; Menicucci, F. L.; Chakraborty, P.; Guan, C.; Han, D.; Huang, K. W. Dehydrogenation of Formic Acid Mediated by a Phosphorus–Nitrogen PN₃P-Manganese Pincer Complex: Catalytic Performance and Mechanistic Insights. *Int. J. Hydrogen Energy* **2022**. <https://doi.org/10.1016/j.ijhydene.2022.04.220>.
- (168) Wang, Y.; Liu, S.; Yang, H.; Li, H.; Lan, Y.; Liu, Q. Structure, Reactivity and Catalytic Properties of Manganese-Hydride Amidate Complexes. *Nat. Chem.* **2022**, 14 (11), 1233–1241. <https://doi.org/10.1038/s41557-022-01036-6>.

- (169) Yang, L.; Wang, H. Recent Advances in Carbon Dioxide Capture, Fixation, and Activation by Using N-Heterocyclic Carbenes. *ChemSusChem* **2014**, *7* (4), 962–998. <https://doi.org/10.1002/cssc.201301131>.
- (170) Villiers, C.; Dognon, J. P.; Pollet, R.; Thuéry, P.; Ephritikhine, M. An Isolated CO₂ Adduct of a Nitrogen Base: Crystal and Electronic Structures. *Angew. Chemie - Int. Ed.* **2010**, *49* (20), 3465–3468. <https://doi.org/10.1002/anie.201001035>.
- (171) Wei, D.; Junge, H.; Beller, M. An Amino Acid Based System for CO₂ capture and Catalytic Utilization to Produce Formates. *Chem. Sci.* **2021**, *12* (17), 6020–6024. <https://doi.org/10.1039/d1sc00467k>.
- (172) Buß, F.; Mehlmann, P.; Mück-Lichtenfeld, C.; Bergander, K.; Dielmann, F. Reversible Carbon Dioxide Binding by Simple Lewis Base Adducts with Electron-Rich Phosphines. *J. Am. Chem. Soc.* **2016**, *138* (6), 1840–1843. <https://doi.org/10.1021/jacs.5b13116>.
- (173) Buß, F.; Röthel, M. B.; Werra, J. A.; Roterling, P.; Wilm, L. F. B.; Daniliuc, C. G.; Löwe, P.; Dielmann, F. Tris(Tetramethylguanidiny)Phosphine: The Simplest Non-Ionic Phosphorus Superbase and Strongly Donating Phosphine Ligand. *Chem. – A Eur. J.* **2022**, *28* (3), e202104021. <https://doi.org/10.1002/chem.202104021>.
- (174) Tolman, C. A. Electron Donor-Acceptor Properties of Phosphorus Ligands. Substituent Additivity. *J. Am. Chem. Soc.* **1970**, *92* (10), 2953–2956. <https://doi.org/10.1021/ja00713a006>.
- (175) Coll, D. S.; Vidal, A. B.; Rodríguez, J. A.; Ocando-Mavárez, E.; Añez, R.; Sierraalta, A. A Simple Method for the Determination of the Tolman Electronic Parameter of Different Phosphorus Containing Ligands, by Means of the Average Local Ionization Energy. *Inorganica Chim. Acta* **2015**, *436*, 163–168. <https://doi.org/10.1016/j.ica.2015.08.003>.
- (176) Chen, L.; Ren, P.; Carrow, B. P. Tri(1-Adamantyl)Phosphine: Expanding the Boundary of Electron-Releasing Character Available to Organophosphorus Compounds. *J. Am. Chem. Soc.* **2016**, *138* (20), 6392–6395. <https://doi.org/10.1021/jacs.6b03215>.
- (177) Serron, S.; Huang, J.; Nolan, S. P. Solution Thermochemical Study of Tertiary Phosphine Ligand Substitution Reactions in the Rh(Acac)(CO)(PR₃) System. *Organometallics* **1998**, *17* (4), 534–539. <https://doi.org/10.1021/om970766g>.
- (178) Wünsche, M. A.; Mehlmann, P.; Witteler, T.; Buß, F.; Rathmann, P.; Dielmann, F. Imidazolin-2-Ylidenaminophosphines as Highly Electron-Rich Ligands for Transition-Metal Catalysts. *Angew. Chemie Int. Ed.* **2015**, *54* (40), 11857–11860. <https://doi.org/10.1002/anie.201504993>.
- (179) Courtemanche, M. A.; Légaré, M. A.; Rochette, É.; Fontaine, F. G. Phosphazenes: Efficient Organocatalysts for the Catalytic Hydrosilylation of Carbon Dioxide. *Chem. Commun.* **2015**, *51* (31), 6858–6861. <https://doi.org/10.1039/c5cc01282a>.
- (180) Wittig, G.; Schöllkopf, U. Über Triphenyl-Phosphin-Methylene Als Olefinbildende Reagenzien (I. Mitteil.). *Chem. Ber.* **1954**, *87* (9), 1318–1330. <https://doi.org/10.1002/cber.19540870919>.
- (181) Álvarez, A.; Borges, M.; Corral-Pérez, J. J.; Olcina, J. G.; Hu, L.; Cornu, D.; Huang, R.; Stoian, D.; Urakawa, A. CO₂ Activation over Catalytic Surfaces. *ChemPhysChem* **2017**, *18* (22), 3135–3141. <https://doi.org/10.1002/cphc.201700782>.
- (182) Yang, Z.; Ng, D.; Garcia-Garibay, M. A. Engineering Reactions in Crystalline Solids: Photochemical Generation of Secondary and Tertiary Enol Radical Pairs from Crystalline Ketodiester. *J. Org. Chem.* **2001**, *66* (13), 4468–4475. <https://doi.org/10.1021/jo005747m>.

-
- (183) Tewari, A.; Hein, M.; Zapf, A.; Beller, M. General Synthesis and Catalytic Applications of Di(1-Adamantyl) Alkylphosphines and Their Phosphonium Salts. *Synthesis (Stuttg)*. **2004**, No. 6, 935–941. <https://doi.org/10.1055/s-2004-822313>.
- (184) Gottlieb, H. E.; Kotlyar, V.; Nudelman, A. NMR Chemicals Shifts of Common Laboratory Solvents as Traces Impurities. *J. org. Chem* **1997**, 62 (21), 7512–7515. <https://doi.org/10.1021/jo971176v>.
- (185) Riisager, A.; Fehrmann, R.; Haumann, M.; Wasserscheid, P. Supported Ionic Liquid Phase (SILP) Catalysis: An Innovative Concept for Homogeneous Catalysis in Continuous Fixed-Bed Reactors. *Eur. J. Inorg. Chem.* **2006**, No. 4, 695–706. <https://doi.org/10.1002/ejic.200500872>.
- (186) Van Doorslaer, C.; Wahlen, J.; Mertens, P.; Binnemans, K.; De Vos, D. Immobilization of Molecular Catalysts in Supported Ionic Liquid Phases. *Dalt. Trans.* **2010**, 39 (36), 8377–8390. <https://doi.org/10.1039/C001285H>.
- (187) Fulmer, G. R.; Miller, A. J. M.; Sherden, N. H.; Gottlieb, H. E.; Nudelman, A.; Stoltz, B. M.; Bercaw, J. E.; Goldberg, K. I. NMR Chemical Shifts of Trace Impurities: Common Laboratory Solvents, Organics, and Gases in Deuterated Solvents Relevant to the Organometallic Chemist. *Organometallics* **2010**, 29 (9), 2176–2179. <https://doi.org/10.1021/om100106e>.
- (188) Dolomanov, O. V.; Bourhis, L. J.; Gildea, R. J.; Howard, J. A. K.; Puschmann, H. OLEX2: A Complete Structure Solution, Refinement and Analysis Program. *J. Appl. Crystallogr.* **2009**, 42 (2), 339–341. <https://doi.org/10.1107/S0021889808042726>.
- (189) Sheldrick, G. M. SHELXT - Integrated Space-Group and Crystal-Structure Determination. *Acta Crystallogr. Sect. A Found. Crystallogr.* **2015**, 71 (1), 3–8. <https://doi.org/10.1107/S2053273314026370>.
- (190) Spek, A. L. PLATON SQUEEZE: A Tool for the Calculation of the Disordered Solvent Contribution to the Calculated Structure Factors. *Acta Crystallogr. Sect. C Struct. Chem.* **2015**, 71, 9–18. <https://doi.org/10.1107/S2053229614024929>.
- (191) Karschin, N.; Krenek, S.; Heyer, D.; Griesinger, C. Extension and Improvement of the Methanol-D4 NMR Thermometer Calibration. *Magn. Reson. Chem.* **2022**, 60 (2), 203–209. <https://doi.org/10.1002/mrc.5216>.

9. Appendices

The following appendices will contain notes about general instrumentation and synthetic procedures as well as the entirety of the scientific data gathered in this work. This is then followed by preliminary versions of the scientific publications based on this work as well as scientific dissemination activities.

Appendix A. General instrumentation

Nuclear Magnetic Resonance spectroscopy (NMR)

NMR spectra were obtained using a Bruker Ascend 400, 600 or 800 MHz spectrometer equipped with BBFO and TCI CryoProbe probes. Chemical shifts are expressed in ppm relative to tetramethylsilane (TMS) for ^1H and ^{13}C spectra using residual solvent signal peaks or TMS as internal reference. For ^{31}P spectra, values are expressed in ppm relative to H_3PO_4 . Residual solvent chemical shifts are explained according to literature.¹⁸⁷ Coupling constants, if available, are given in Hz as absolute values. Multiplicities are given as singlets (s), doublets (d), triplets (t), quartets (q) and multiplets (m). Literature-known compounds were analyzed only using ^1H -NMR spectroscopy to confirm purity. NMR spectra were analysed using MestReNova software. Two-dimensional and variable temperature experiments taken at DTU were obtained by KASPER ENEMARK RASMUSSEN. All spectra taken at LIKAT were obtained by WOLFGANG BAUMANN or the analytical laboratory technicians.

Single-Crystal X-ray diffraction (SC-XRD)

All crystals were submerged in polybutene oil (Sigma, > 90%) as protection against oxidation and hydrolysis by air. Suitable crystals were identified using light microscopy and harvested with a MiTeGen cryo loop. They were mounted on a 5-axis goniometer attached to a Rigaku SuperNova dual source CCD-diffractometer. The measurements were conducted at 120 K using either Mo $K\alpha$ or Cu $K\alpha$ radiation. Structures were solved using Olex2¹⁸⁸ equipped with SHELXT software¹⁸⁹ using intrinsic phasing and refined to completion using SHELXL employing least square minimizations against F^2 . Structure factors regarding to solvent molecules were filtered out in cases of high disorder using Platon squeeze.¹⁹⁰ In all depictions, co-crystallized solvents are omitted for clarity. Thermal ellipsoids are printed at 50% probability throughout this thesis. All depictions follow the same colour code: Hydrogen white, boron yellow, carbon grey, nitrogen light blue, oxygen red, fluorine bright green, phosphorous purple, chlorine dark green, bromine dark red, metals dark blue.

Elemental Analysis (EA)

Elemental Analysis (EA, CHNS analysis) was performed at the Department of Chemistry at the University of Copenhagen (KU) on a Thermo Fischer FlashEA 112 analyzer. Reported values are given as the average of two measurements. All handling of samples was conducted under ambient conditions without exclusion of air.

Infrared Spectroscopy (ATR-IR)

Attenuated total reflectance infrared spectroscopy (ATR-IR) was performed on a Bruker Optics VERTEX 80 vacuum Fourier-transform spectrometer equipped with a Germanium on KBr beam splitter, a LN₂-cooled HgCdTe detector. A global radiation source was used. The solid samples were pressed against a single-reflection Germanium crystal or a diamond ATR surface. Signals of water vapour and baseline drift were corrected by subtraction of a blank run and ATR corrections were applied to compensate for wavelength-dependent penetration depth of the IR beam into the sample. All ATR-IR measurements were taken by Associate Professor RENÉ WUGT LARSEN.

Gas chromatography (GC)

GC-FID measurements were taken on an Agilent Technologies 6890N network gas chromatograph equipped with a 7683B series injector. The injection volume of each sample was set to 1.0 μ L.

GCMS measurements were taken on an Agilent Technologies 7890A network gas chromatograph equipped with a mass spectrometer with a 5975C VL MSD with a triple-axis detector. The injection volume of each sample was set to 1.0 μ L.

Appendix B. General synthesis protocols

All reactions, unless otherwise stated, were carried out under anaerobic and anhydrous conditions using an *Inert* (at the facilities of DTU) or *M. Braun* (at the facilities of LIKAT) glovebox or standard Schlenk techniques. All glassware was dried in an oven at 140 °C for 18 hours before use and introduced into the glovebox while hot. All plasticware was dried in a vacuum desiccator for 18 hours before use. Refluxing under Schlenk conditions was performed after cycling the hot reflux condenser between vacuum and inert gas three times. Commercially obtained solid chemicals were, unless otherwise stated, used without further purification and introduced into the glovebox when delivered under inert gas atmosphere. Commercially obtained liquid chemicals were introduced into the glovebox without further purification when delivered under inert atmosphere. Air sensitive compounds were weighed and handled in an oxygen-free glovebox under argon atmosphere (typically <0.1 ppm O₂, <0.5 ppm H₂O) and stored at reduced temperature when necessary. Technical solvents for workup and chromatography were purified by rotary evaporation under aerobic conditions unless otherwise stated. Solvents for handling under inert conditions were degassed by argon bubbling for one hour and passed through a solvent purification system (SPS) equipped with alumina columns to remove traces of water. Water content measurements were performed in regular intervals using Karl Fischer titration methods. Pentane and hexane were either dried and deoxygenated via SPS use or alternatively distilled from sodium/benzophenone. In the latter case, they were refluxed under inert conditions for at least two hours until the formation of the purple ketyl radical, and then distilled to a STRAUS flask containing 3 Å molecular sieves.

For reactions requiring high-pressure reactors, two different high-pressure reactor types were utilized:

- Type A: Stainless steel, inner diameter 25.0 mm, reactor capacity 20.8 mL (including gas volume above teflon cup), teflon cup volume 13.0 mL. This reactor type was produced in house. The pressure was recorded using an analog manometer of the range – bar, and subject to error. Operational range up to 130 °C and 40 bar. The reactors were heated inside specially made aluminum heat blocks to ensure good contact and heated on standard laboratory heating plates. The temperature was controlled externally via a standard laboratory thermometer embedded into the aluminum block.
- Type B: Stainless steel (alloy 600), 2550 flat gasket micro reactor, capacity 16 mL (including gas volume above teflon cup), teflon cup volume 6.0 mL. These reactors were connected to a *Parr Microbatch* reactor setup with digital temperature control using an internal thermometer and an integrated pressure sensor with automatic data recording.

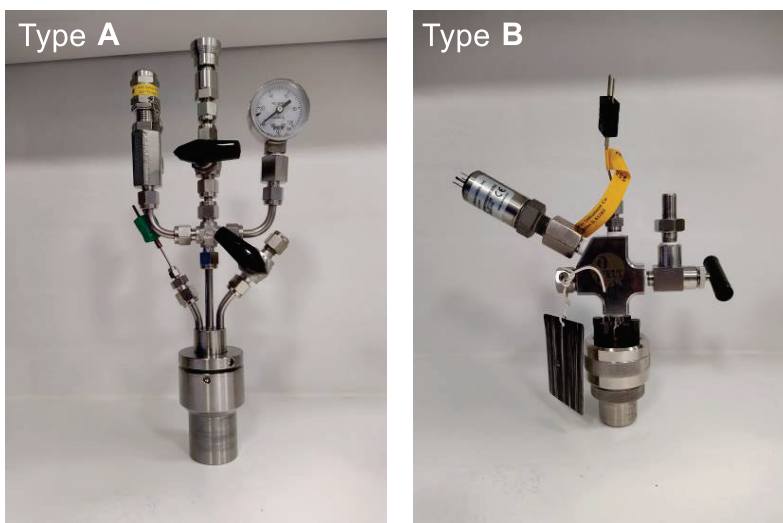


Figure 9.1: Autoclave reactor types used in this work.

Appendix C. Chapter 2

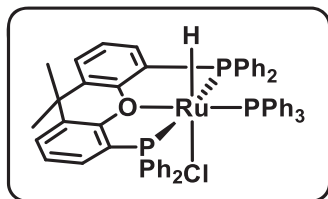
C1 Synthesis of precursors and ligands

The precursor $[\text{Ru}(\text{PPh}_3)_3\text{HCl}] \cdot \text{toluene}$ was synthesized according to a literature protocol by WILKINSON.⁵³ While commercially available (Sigma-Aldrich), it was found that the physical and chemical properties of the commercial product did not agree with those in published literature, pointing to severe degradation of the precursor during transport. The complex was stored in an inert gas glovebox at -30 °C under the exclusion of light to prevent any form of degradation.

Ligands **L1**, **L2**, **L3**, **L4**, **L9**, **L10**, and **L11** were commercially achieved. Ligands **L5**, **L6**, **L7**, **L8**, and **L12** were synthesized according to literature.^{17,18,29,30} Their spectroscopic properties agreed with those in published procedures.

C2 Synthesis of $[\text{RuHCl}(\text{POP})(\text{PPh}_3)]$

Complexes **Ru-1a**, **Ru-2a**, and **Ru-3a** were synthesized according to literature.⁴⁰ Their spectroscopic properties corresponded to those in published procedures.

[RuHCl(xantphos)(PPh₃)] **Ru-1a**

In a 50 mL Schlenk tube, xantphos **L1** (98 mg, 169 μ mol, 1.05 eq.) and [RuHCl(PPh₃)₃] toluene adduct (164 mg, 161 μ mol, 1.0 eq.) were dissolved in dry THF (10 mL) and refluxed for 3 hours while vigorously stirred. A colour change to orange was observed. The mixture was allowed to cool down to room temperature and the solvent was removed in vacuo. The crude product was washed in hexane (2 times 10 mL), dried in vacuo and obtained as a yellow powder in quantitative yield.

Selected ¹H NMR (400 MHz, Tol, 298 K) δ -16.29 (dt, J = 27.4, 23.9 Hz, 1H).

³¹P {¹H} NMR (162 MHz, Tol, 298 K) δ 75.00 (td, J = 32.6, 4.4 Hz), 42.05 (dd, J = 32.6, 4.2 Hz).

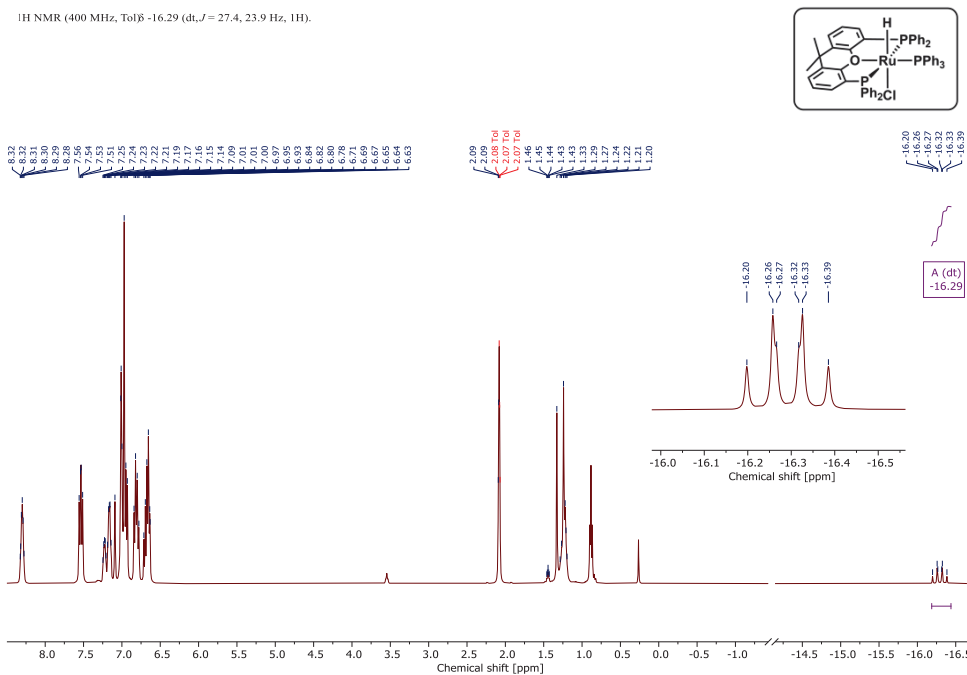
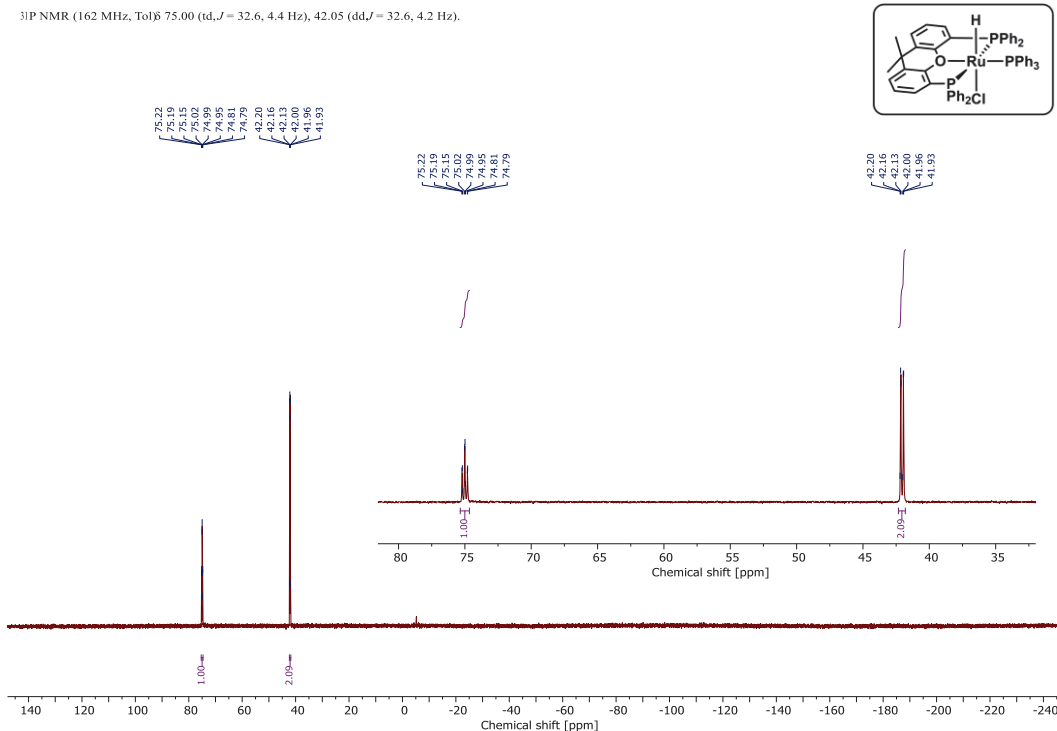
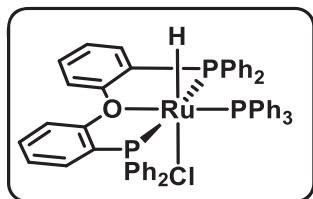


Figure 9.2: 400 MHz ¹H NMR spectrum of **Ru-1a** in toluene-d₈ at 25 °C.

Figure 9.3: 162 MHz $^3\text{P}\{^1\text{H}\}$ NMR spectrum of **Ru-1a** in toluene- d_8 at 25 °C.**[RuHCl(DPEphos)(PPh₃)] Ru-2a**

In a 50 mL Schlenk tube, DPEphos **L2** (45.7 mg, 85 μmol , 1.05 eq.) and $[\text{RuHCl}(\text{PPh}_3)_3]$ toluene adduct (82.5 mg, 81 μmol , 1.0 eq.) were dissolved in dry toluene (12 mL) and refluxed for 40 min while vigorously stirred. A colour change to orange was observed. The mixture was allowed to cool down to room temperature and the solvent was removed in vacuo. The crude product was washed in hexane and diethyl ether (2 times 10 mL each), dried in vacuo and obtained as a yellow powder in quantitative yield.

Selected ^1H NMR (400 MHz, C_6D_6 , 298 K) δ -15.50 (dt, $J = 27.2, 24.2$ Hz, 1H).

$^3\text{P}\{^1\text{H}\}$ NMR (162 MHz, C_6D_6 , 298 K) δ 76.65 (d, $J = 31.4$ Hz), 36 (extremely broad).

^1H NMR (400 MHz, CDCl_3) δ -15.50 (dt, J = 27.2, 24.2 Hz, 1H).

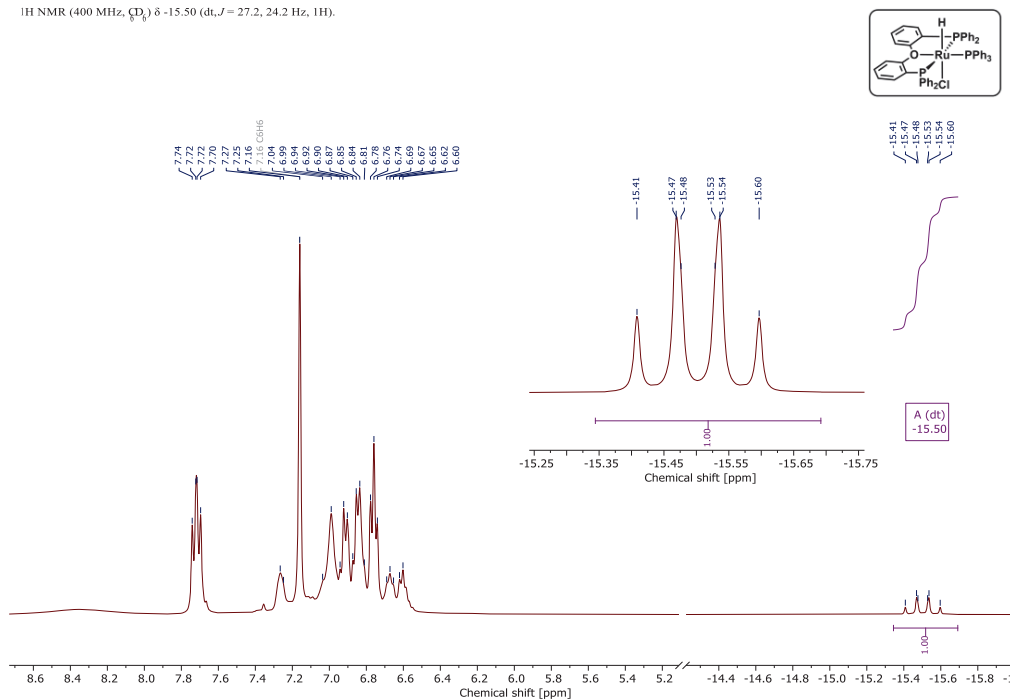


Figure 9.4: 400 MHz ^1H NMR spectrum of **Ru-2a** in C_6D_6 at 25 °C.

^{31}P NMR (162 MHz, CDCl_3) δ 76.65 (d, J = 31.4 Hz), 36 (broad).

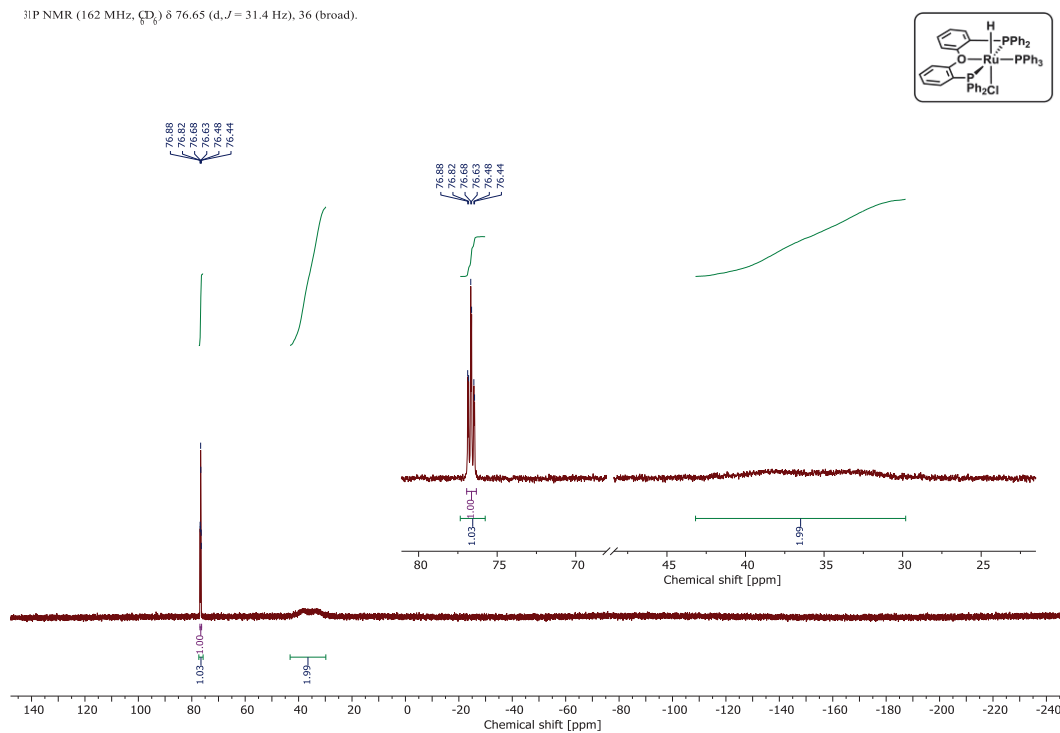
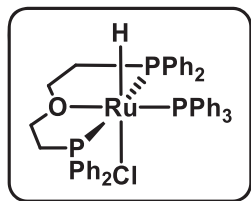


Figure 9.5: 162 MHz $^{31}\text{P}\{^1\text{H}\}$ NMR spectrum of **Ru-2a** in C_6D_6 at 25 °C.

[RuHCl(DPPEE)(PPh₃)] **Ru-3a**

In a 50 mL Schlenk tube, DPPEE **L3** (45.7 mg, 85 μ mol, 1.05 eq.) and [RuHCl(PPh₃)₃] toluene adduct (82.5 mg, 81 μ mol, 1.0 eq.) were dissolved in dry toluene (12 mL) and refluxed for 40 min while vigorously stirred. A colour change to orange was observed. The mixture was allowed to cool down to room temperature and the solvent was removed in vacuo. The crude product was washed in hexane and diethyl ether (2 times 10 mL each), dried in vacuo and obtained as a yellow powder in quantitative yield.

Selected ¹H NMR (400 MHz, C₆D₆, 298 K) δ -17.37 (dt, J = 28.5, 21.6 Hz, 1H).

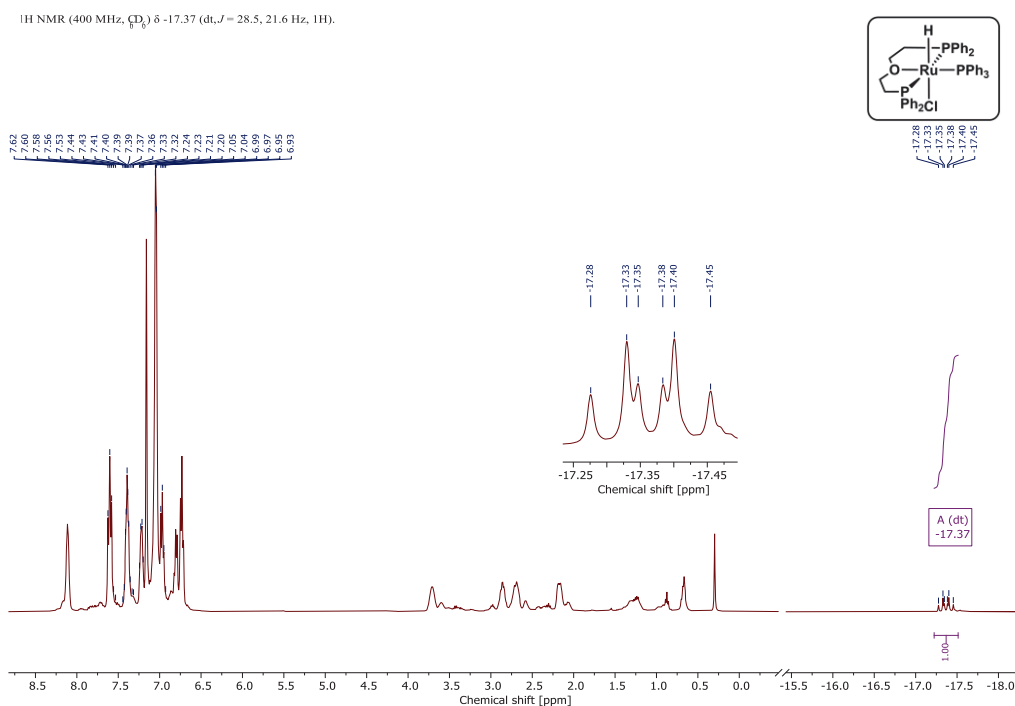
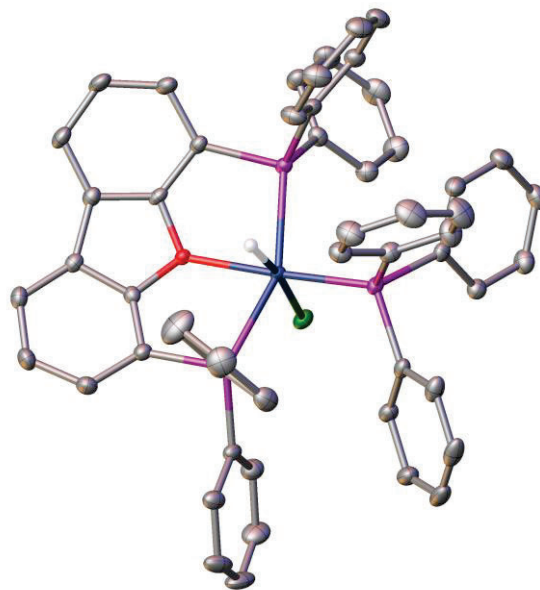
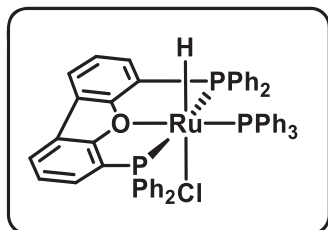


Figure 9.6: 400 MHz ¹H NMR spectrum of **Ru-3a** in C₆D₆ at 25 °C.

[RuHCl(DBFphos)(PPh₃)] **Ru-4a**

In a 50 mL Schlenk tube, DBFphos **L4** (45.7 mg, 85 μmol , 1.05 eq.) and [RuHCl(PPh₃)₃] toluene adduct (82.5 mg, 81 μmol , 1.0 eq.) were dissolved in dry toluene (12 mL) and refluxed for 40 min while vigorously stirred. A colour change to orange was observed. The mixture was allowed to cool down to room temperature and the solvent was removed in vacuo. The crude product was washed in hexane and diethyl ether (2 times 10 mL each), dried in vacuo and obtained as a yellow powder in quantitative yield.

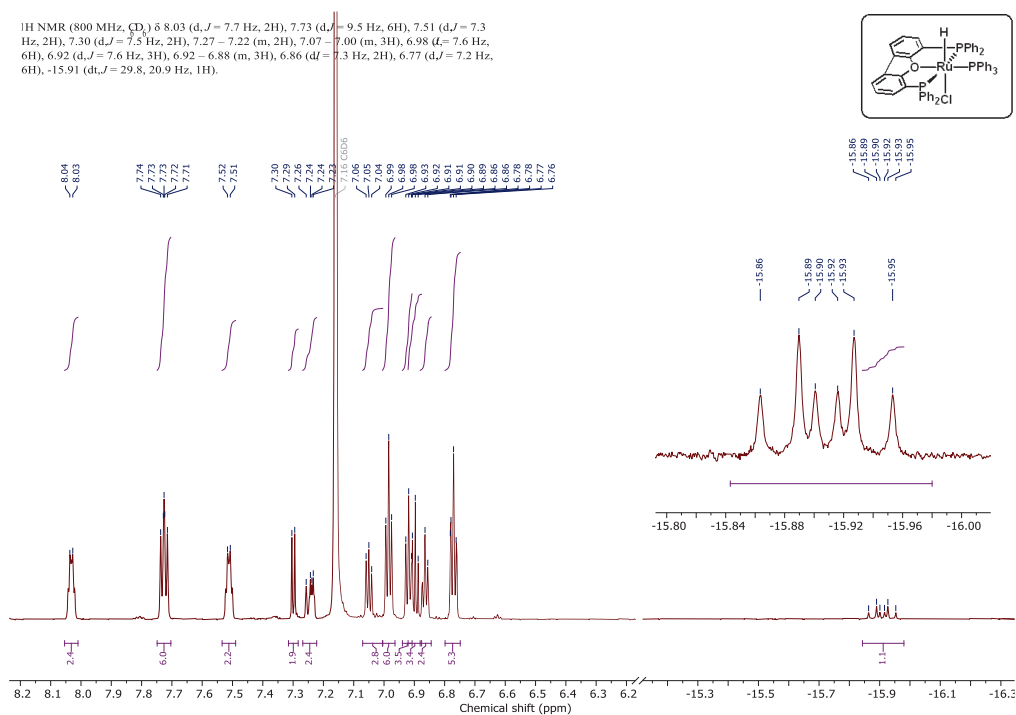
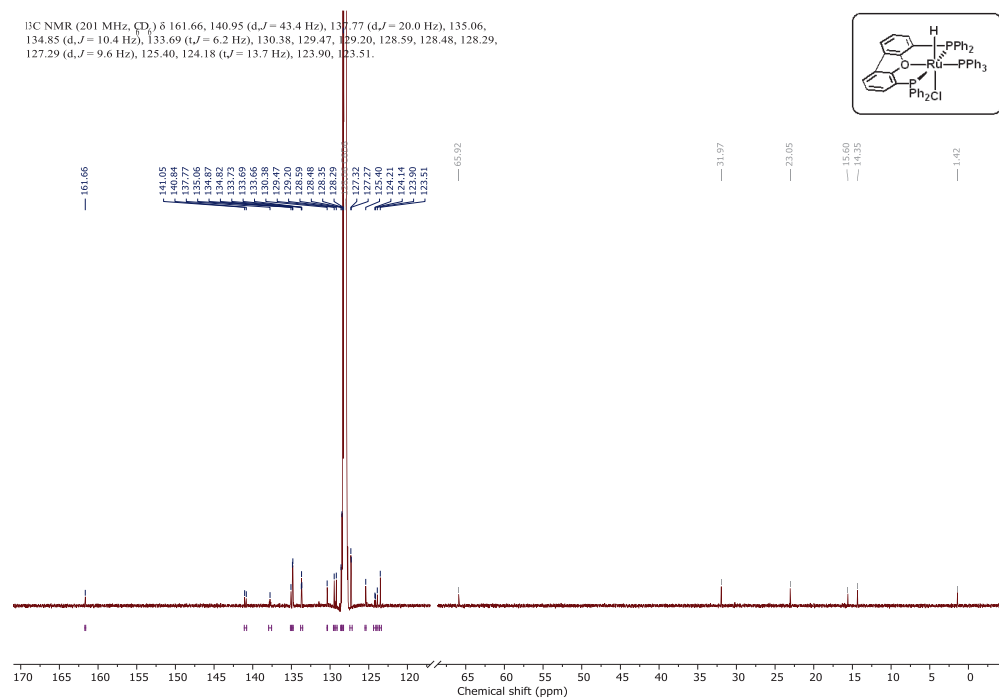
The crude product can be crystallized by dissolving in THF, followed by filtration and layering under hexane in an NMR tube at room temperature, causing the product to crystallize as yellow cuboids.

¹H NMR (800 MHz, C₆D₆, 298 K) δ 8.03 (d, J = 7.7 Hz, 2H), 7.73 (d, J = 9.5 Hz, 6H), 7.51 (d, J = 7.3 Hz, 2H), 7.30 (d, J = 7.5 Hz, 2H), 7.27 – 7.22 (m, 2H), 7.07 – 7.00 (m, 3H), 6.98 (t, J = 7.6 Hz, 6H), 6.92 (d, J = 7.6 Hz, 3H), 6.92 – 6.88 (m, 3H), 6.86 (d, J = 7.3 Hz, 2H), 6.77 (d, J = 7.2 Hz, 6H), -15.91 (dt, J = 29.8, 20.9 Hz, 1H, RuH).

¹³C NMR (201 MHz, C₆D₆, 298 K) δ 161.66, 140.95 (d, J = 43.4 Hz), 137.77 (d, J = 20.0 Hz), 135.06, 134.85 (d, J = 10.4 Hz), 133.69 (t, J = 6.2 Hz), 130.38, 129.47, 129.20, 128.59, 128.48, 128.29, 127.29 (d, J = 9.6 Hz), 125.40, 124.18 (t, J = 13.7 Hz), 123.90, 123.51.

³¹P {¹H} NMR (162 MHz, C₆D₆, 298 K) δ 70.66 (t, J = 30.4 Hz), 41.74 (d, J = 29.5 Hz).

EA: Calcd. (%) for C₅₄H₄₂ClOP₃Ru (936.37) C 69.27, H 4.52, found C 68.90, H 4.96.


 Figure 9.7: 800 MHz ^1H NMR spectrum of **Ru-4a** in C_6D_6 at 25 °C.

 Figure 9.8: 201 MHz ^{13}C NMR spectrum of **Ru-4a** in C_6D_6 at 25 °C.

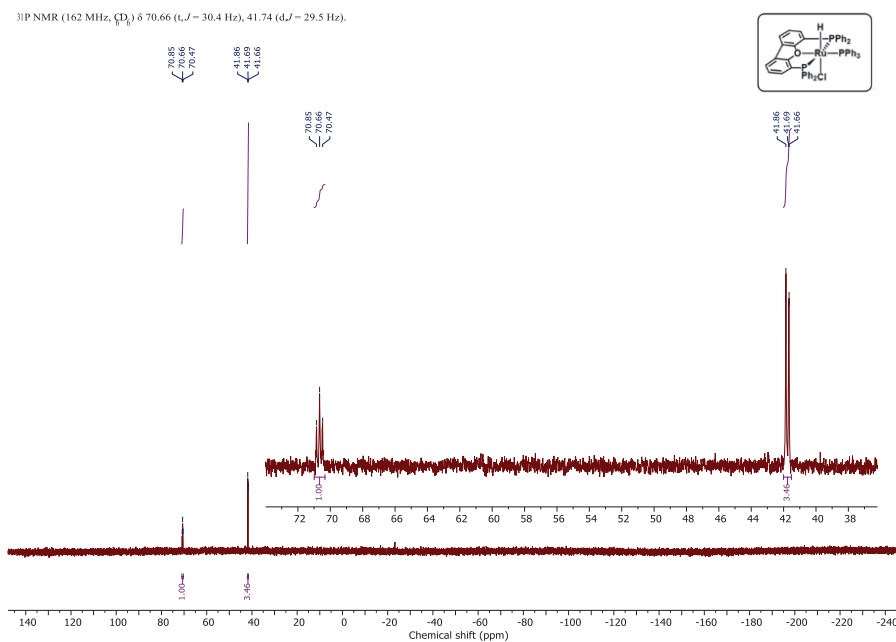


Figure 9.9: 162 MHz $^{31}\text{P}\{^1\text{H}\}$ NMR spectrum of **Ru-4a** in C_6D_6 at 25 °C.

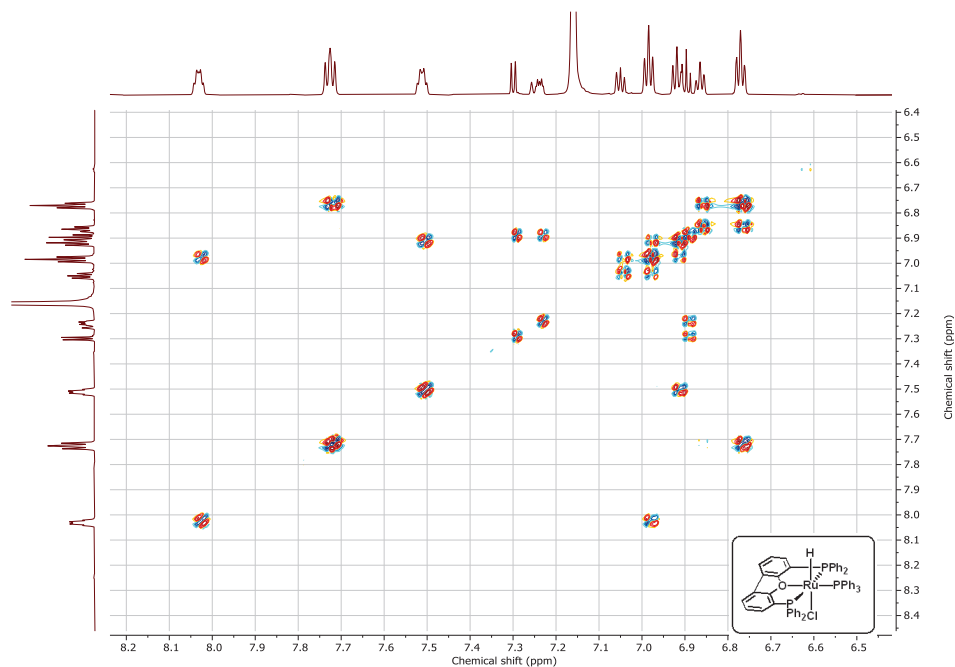


Figure 9.10: 800 MHz COSY spectrum of **Ru-4a** in C_6D_6 at 25 °C.

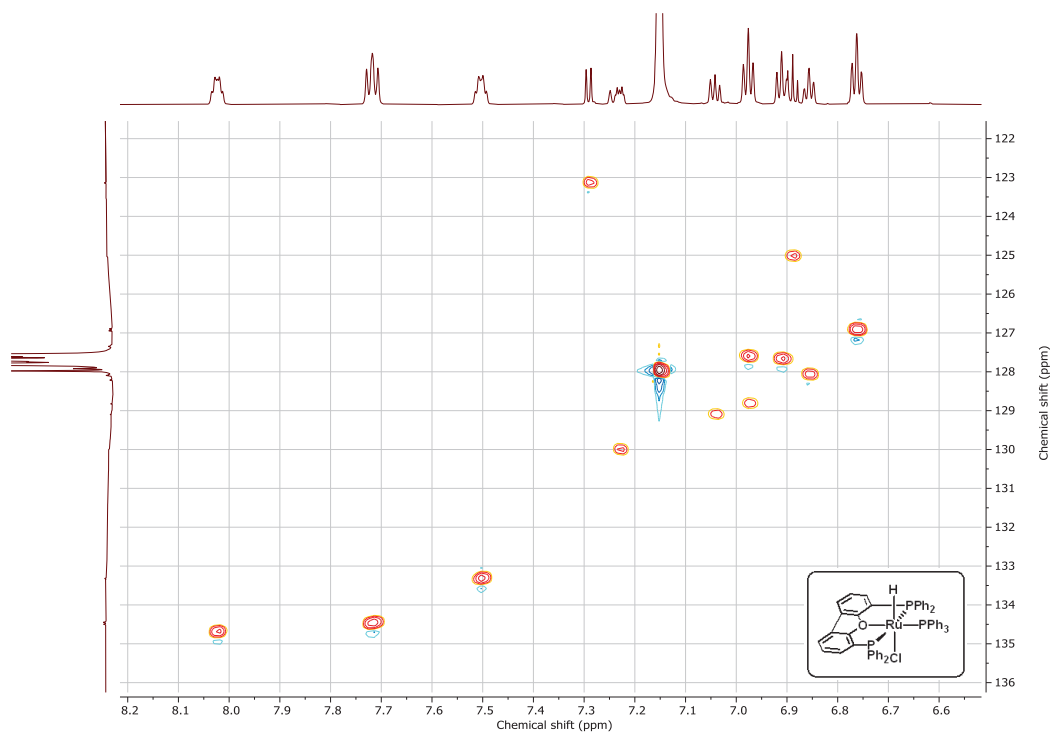
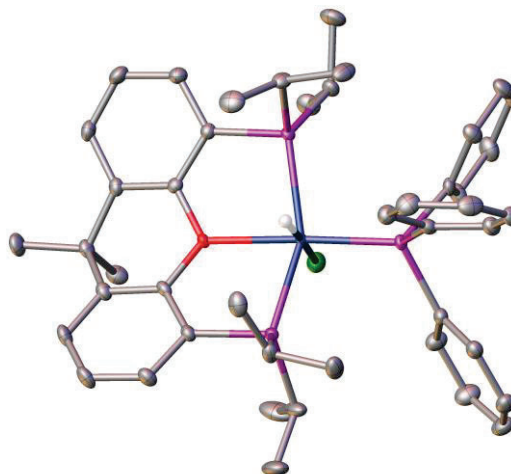
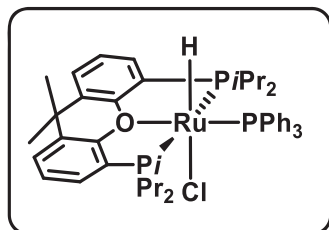


Figure 9.11: 800 MHz HSQC spectrum of **Ru-4a** in C_6D_6 at 25 °C.

[RuHCl(*i*Pr-xantphos)(PPh₃)] **Ru-5a**

In a 50 mL Schlenk flask, *i*Pr-Xantphos **L5** (111 mg, 0.257 mmol, 1.6 eq.) and [RuHCl(PPh₃)₃] toluene adduct (163 mg, 0.161 mmol, 1.0 eq.) were dissolved in dry toluene (10 mL) and refluxed for 75 min while vigorously stirred. A colour change to orange was observed. The mixture was allowed to cool to room temperature and the solvent was removed in vacuo. The crude product was powderized by stirring in hexane, washed in hexane (3x20 mL) and dried in vacuo overnight (118 mg, 87%). This product can be alternatively synthesized by stirring at 50 °C for 96 h.

The crude product can be crystallized by dissolving in a mixture of benzene and hexane, followed by filtration and cooling to – 20 °C in which the product crystallizes as orange needles.

¹H NMR (400 MHz, C₆D₆, 298 K) δ 8.52 (dd, *J* = 9.7, 7.5 Hz, 6H, *o*-PPh₃), 7.39 – 7.32 (m, 2H), 7.19 – 7.13 (m, 6H), 7.12 – 7.08 (m, 2H), 7.08 – 7.02 (m, 3H), 6.91 (t, *J* = 7.6 Hz, 2H), 2.34 – 2.22 (m, 2H), 1.43 (s, 6H), 1.40 (s, 3H), 1.30 (s, 3H), 1.17 (q, *J* = 7.0 Hz, 6H), 1.01 – 0.92 (m, 8H), 0.87 (q, *J* = 7.5 Hz, 6H), -16.66 (dt, *J* = 27.3, 24.3 Hz, 1H, RuH).

¹³C NMR (201 MHz, C₆D₆) δ 156.62 (t, *J* = 7.1 Hz), 136.29, 132.13, 129.65, 129.11, 128.35, 128.29, 127.00 (d, *J* = 8.7 Hz), 126.32, 124.06, 35.85, 34.29, 28.49 (t, *J* = 14.2 Hz), 26.88 (d, *J* = 5.6 Hz), 25.48, 21.76, 19.70, 19.14, 18.95 (d, *J* = 4.4 Hz).

³¹P{¹H} NMR (162 MHz, C₆D₆, 298 K) δ 76.81 (td, *J* = 31.8, 10.5 Hz), 52.33 (dd, *J* = 31.4, 8.0 Hz).

EA: Calcd. (%) for C₄₅H₅₆ClOP₃Ru (842.38) C 64.16, H 6.70, found C 64.66, H 7.00.

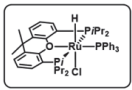


Figure 9.12: 400 MHz ^1H NMR spectrum of **Ru-5a** in C_6D_6 at 25 $^\circ\text{C}$.

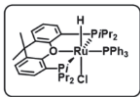


Figure 9.13: 400 MHz ^{13}C NMR spectrum of **Ru-5a** in C_6D_6 at 25 $^\circ\text{C}$.

^{31}P NMR (162 MHz, CDCl_3) δ 76.81 (td, $J = 31.8, 10.5$ Hz), 52.33 (dd, $J = 31.4, 8.0$ Hz).

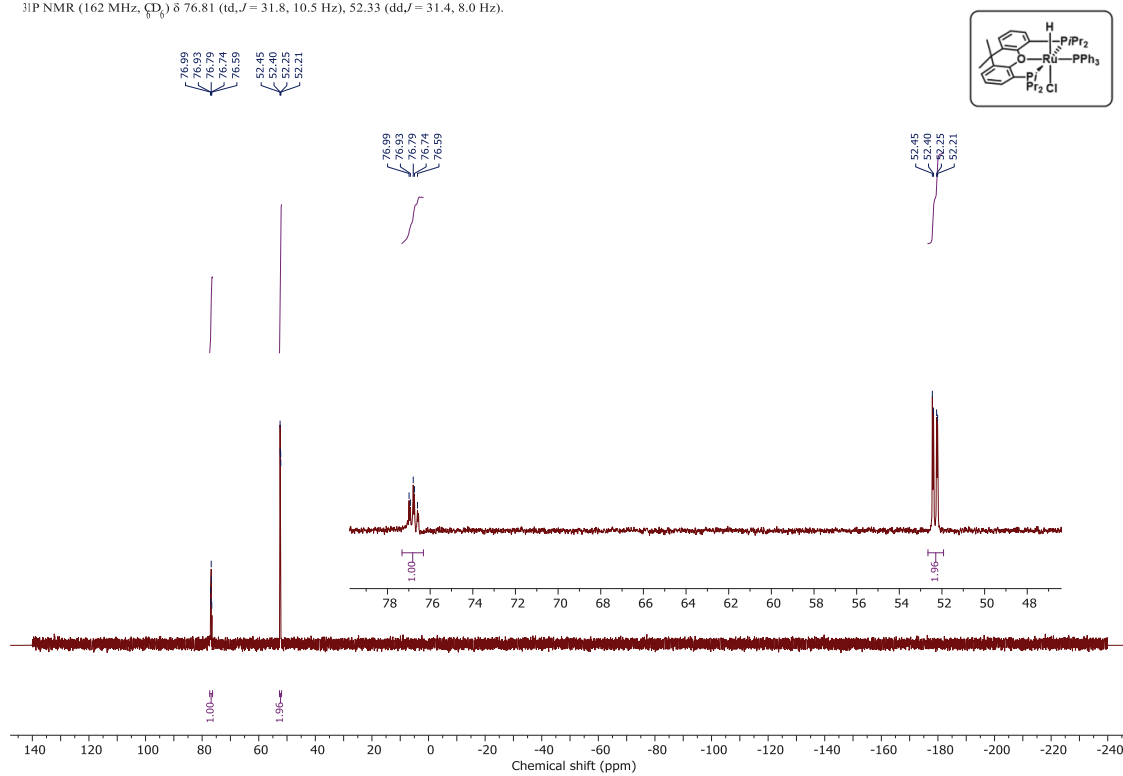
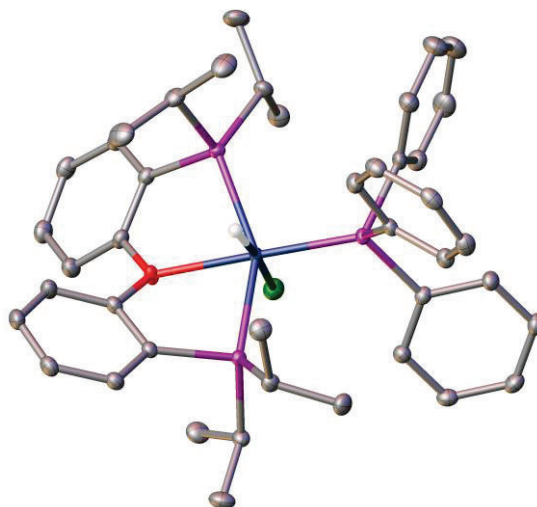
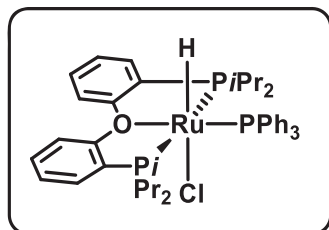


Figure 9.14: 162 MHz $^{31}\text{P}\{^1\text{H}\}$ NMR spectrum of **Ru-5a** in C_6D_6 at 25 °C.

[RuHCl(*i*Pr-DPEphos)(PPh₃)] Ru-6a

In a 50 mL Schlenk flask, *i*Pr-DPEphos **L6** (51.0 mg, 0.127 mmol, 1.1 eq.) and [RuHCl(PPh₃)₃] toluene adduct (117.2 mg, 0.115 mmol, 1.0 eq.) were dissolved in dry toluene (15 mL) and refluxed for 5 hours while vigorously stirred. A colour change to orange was observed. The mixture was allowed to cool to room temperature and the solvent was removed in vacuo. The crude product was freeze-dried from benzene and obtained as an orange powder. It was washed with hexane (2 times 10 mL) and pentane (2 times 10 mL), dried in vacuo overnight and obtained in quantitative yield.

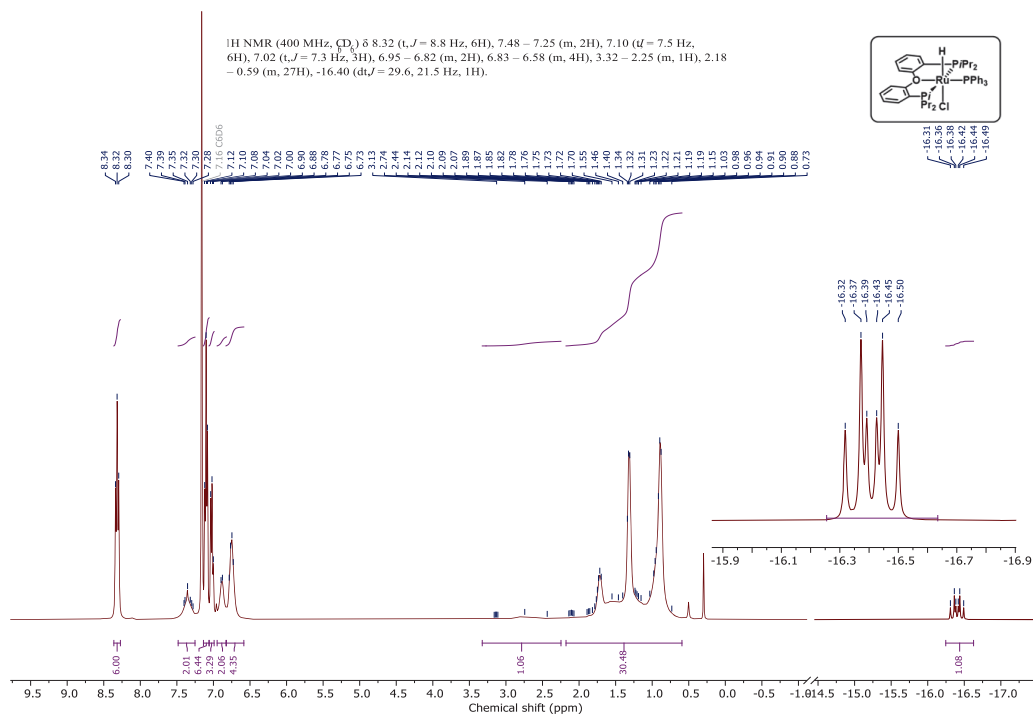
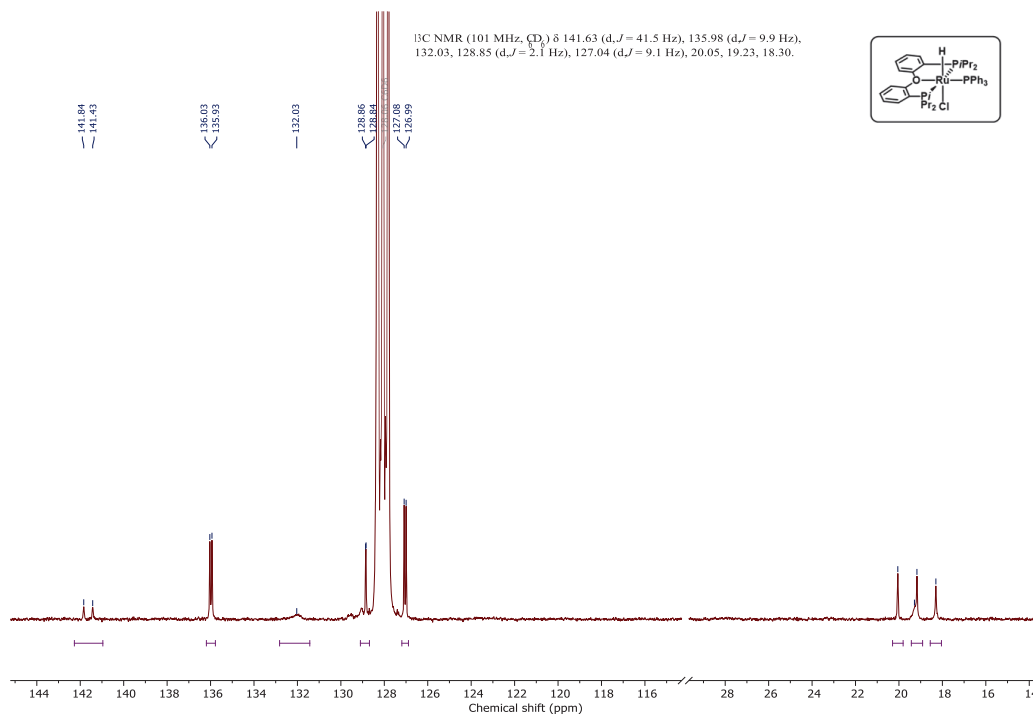
Crystals of sufficient quality for XRD can be grown by crystallization from toluene/hexane using the gas diffusion method at -30 °C.

¹H NMR (400 MHz, C₆D₆, 25 °C) δ 8.32 (t, *J* = 8.8 Hz, 6H), 7.48 – 7.25 (m, 2H), 7.10 (t, *J* = 7.5 Hz, 6H), 7.02 (t, *J* = 7.3 Hz, 3H), 6.95 – 6.82 (m, 2H), 6.83 – 6.58 (m, 4H), 3.32 – 2.25 (m, 1H), 2.18 – 0.59 (m, 27H), -16.40 (dt, *J* = 29.6, 21.5 Hz, 1H).

¹³C NMR (101 MHz, C₆D₆, 25 °C) δ 141.63 (d, *J* = 41.5 Hz), 135.98 (d, *J* = 9.9 Hz), 132.03, 128.85 (d, *J* = 2.1 Hz), 127.04 (d, *J* = 9.1 Hz), 20.05, 19.23, 18.30.

³¹P {¹H} NMR (162 MHz, C₆D₆, 25 °C) δ 75.70 (t, *J* = 30.4 Hz), 48.90 – 47.84 (m).

EA: Calcd. (%) for C₄₂H₅₂ClOP₃Ru (802.32) C 62.88, H 6.53, found C 63.28, H 6.64.


 Figure 9.15 400 MHz ^1H NMR spectrum of **Ru-6a** in C_6D_6 at 25 °C.

 Figure 9.16: 101 MHz ^{13}C NMR spectrum of **Ru-6a** in C_6D_6 at 25 °C.

^{31}P NMR (162 MHz, CDCl_3) δ 75.70 (t, $J = 30.4$ Hz), 48.90 – 47.84 (m).

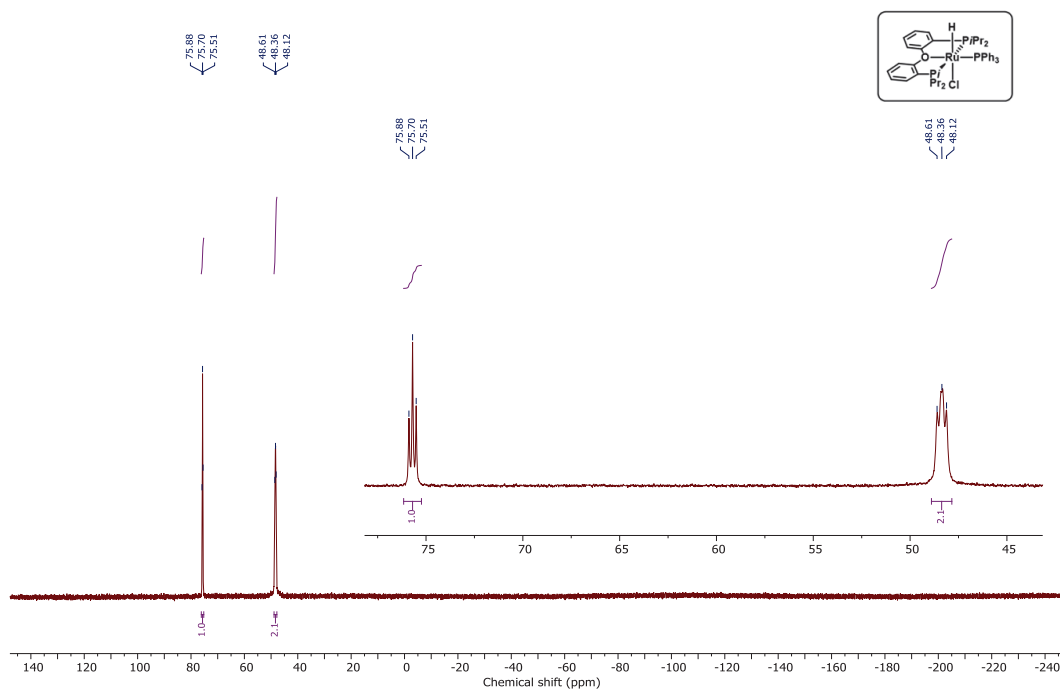
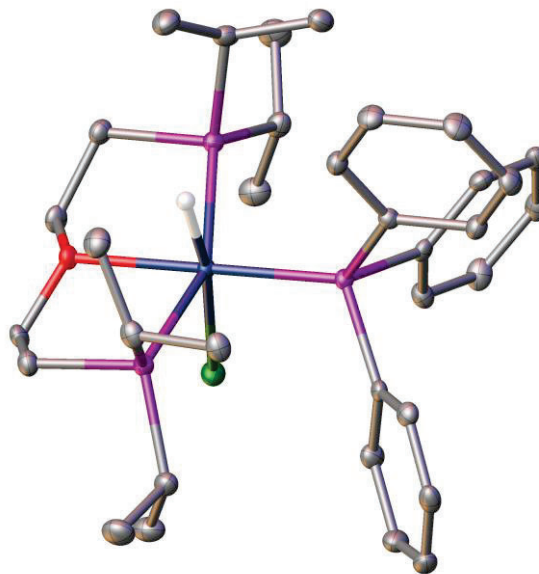
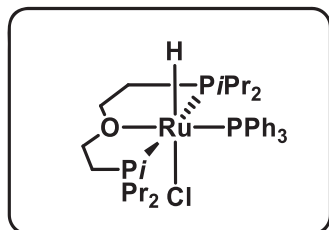


Figure 9.17: 162 MHz $^{31}\text{P}\{^1\text{H}\}$ spectrum of **Ru-6a** in C_6D_6 at 25 °C.

[RuHCl(DiPrPEE)(PPh₃)] Ru-7a

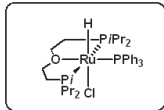
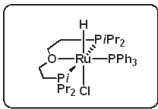
In a 50 mL Schlenk flask, DiPrPEE **L7** (32.2 mg, 0.105 mmol, 1.1 eq.) and [RuHCl(PPh₃)₃] toluene adduct (100.0 mg, 0.096 mmol, 1.0 eq.) were dissolved in dry THF (15 mL) while vigorously stirred. The solution was stirred for 3 h, and a colour change from purple to orange was observed. The solvent was removed in vacuo and the crude product was dried overnight. The crude product was washed in hexane (3 times 10 mL) and dried in vacuo overnight to be obtained as a yellow powder in quantitative yield.

Crystals of sufficient quality for XRD can be grown by crystallization from toluene/hexane using the gas diffusion method at -30 °C.

¹H NMR (400 MHz, C₆D₆, 298 K) δ 8.36 (t, J = 8.7 Hz, 6H, *o*-PPh₃), 7.15 – 7.11 (m, 6H, *m*-PPh₃), 7.04 (t, J = 7.3 Hz, 3H, *p*-PPh₃), 4.37 – 4.26 (m, 2H, O-CH₂-CH₂), 3.09 – 2.94 (m, 2H, O-CH₂-CH₂), 1.59 – 1.46 (m, 10H, CH(CH₃)₂+ O-CH₂-CH₂), 1.36 – 1.27 (m, 6H, CH(CH₃)₂), 1.27 – 1.19 (m, 2H, CH(CH₃)₂), 0.97 (hept, J = 7.0 Hz, 2H, CH(CH₃)₂), 0.74 – 0.64 (m, 12H, CH(CH₃)₂), -17.62 (dt, J = 27.6, 23.5 Hz, 1H, RuH).

¹³C-NMR (101 MHz, 298 K): δ 141.97 (d, J = 39.6 Hz), 135.88 (d, J = 9.6 Hz), 128.71 (d, J = 2.1 Hz), 126.93 (d, J = 8.9 Hz), 71.76, 27.26 (t, J = 13.8 Hz), 25.78 (t, J = 5.8 Hz), 22.28 (t, J = 6.8 Hz), 20.88, 19.28, 18.63 (t, J = 3.0 Hz), 17.74 (d, J = 2.4 Hz) ppm.

³¹P{¹H} NMR (162 MHz, C₆D₆, 298 K) δ 74.61 (td, J = 29.8, 5.7 Hz, Ru-PPh₃), 52.57 (dd, J = 29.9, 5.0 Hz, Ru-P(*i*Pr)₂), -5.36 (s, PPh₃).



^{31}P NMR (162 MHz, CDCl_3) δ 74.61 (td, $J = 29.8, 5.7$ Hz), 52.57 (dd, $J = 29.9, 5.0$ Hz), -5.36.

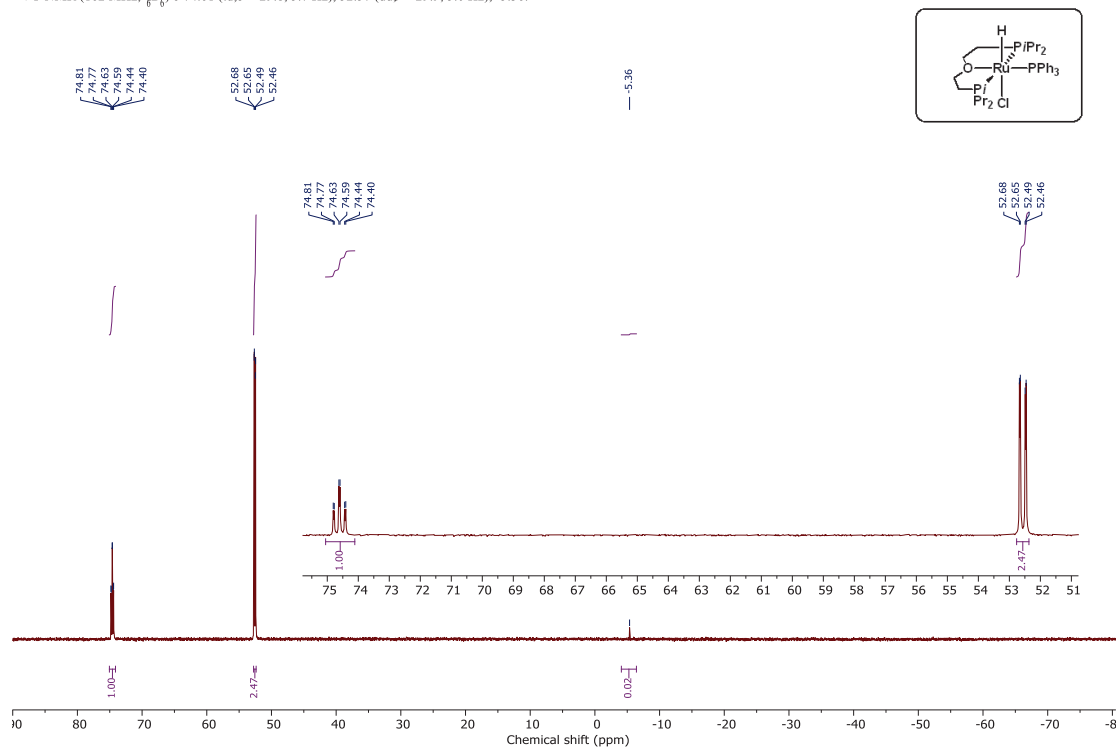
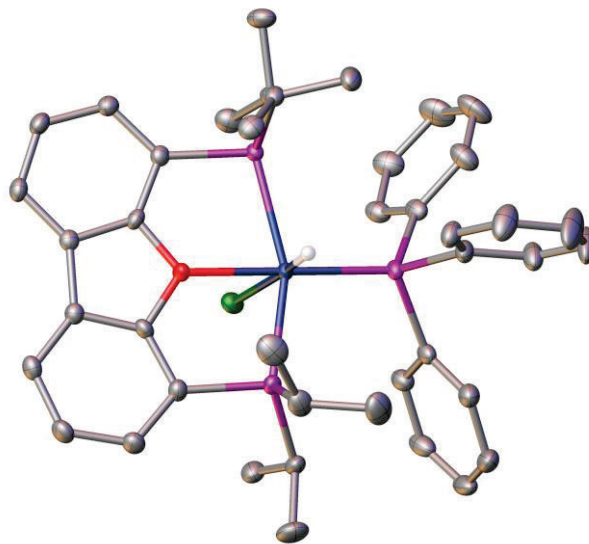
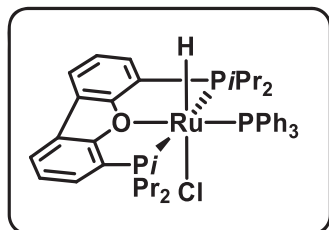


Figure 9.20: 162 MHz $^{31}\text{P}\{^1\text{H}\}$ NMR spectrum of **Ru-7a** in C_6D_6 at 25 °C.

[RuHCl(*i*Pr-DBFphos)(PPh₃)] Ru-8a

In a 50 mL Schlenk flask, *i*Pr-DBFphos **L8** (46.2 mg, 0.115 mmol, 1.1 eq.) and [RuHCl(PPh₃)₃] toluene adduct (106.4 mg, 0.105 mmol, 1.0 eq.) were dissolved in dry THF (15 mL) and stirred at room temperature for 30 hours. A colour change to orange was observed. The mixture was allowed to cool to room temperature and the solvent was removed in vacuo. The crude product was freeze-dried from benzene and obtained as an orange powder. It was washed with hexane (3 times 12 mL), dried in vacuo overnight and obtained as a yellow solid in quantitative yield.

Crystals of sufficient quality for XRD can be grown by crystallization from THF/diethyl ether, toluene/diethyl ether or toluene/hexane using the gas diffusion method at -30 °C.

¹H NMR (400 MHz, C₆D₆, 298 K) δ 8.49 (t, *J* = 9.7 Hz, 6H), 7.47 (d, *J* = 7.6 Hz, 2H), 7.40 (d, *J* = 7.5 Hz, 2H), 7.20 (d, *J* = 7.6 Hz, 6H), 7.07 (t, *J* = 7.4 Hz, 3H), 7.01 (t, *J* = 7.6 Hz, 2H), 2.04 – 1.93 (m, 2H), 1.64 – 1.54 (m, 6H), 1.16 – 1.09 (m, 8H), 0.95 – 0.81 (m, 12H), -16.80 (dt, *J* = 28.6, 22.0 Hz, 1H, RuH).

¹³C NMR (101 MHz, C₆D₆, 298 K) δ 161.20, 141.71 (d, *J* = 39.9 Hz), 135.80 (d, *J* = 9.5 Hz), 129.11, 128.89, 127.20 (d, *J* = 8.9 Hz), 124.59, 123.32, 123.08 (t, *J* = 3.0 Hz), 120.78 (t, *J* = 7.5 Hz), 28.41 (t, *J* = 12.1 Hz), 26.06 (t, *J* = 6.4 Hz), 22.01, 19.79 (t, *J* = 2.5 Hz), 19.30, 19.03 (t, *J* = 4.4 Hz).

³¹P{¹H}-NMR (162 MHz, C₆D₆, 298 K): δ 73.22 (t, ²*J*_{PP} = 27.8 Hz, 1P, PPh₃), 58.97 (d, ²*J*_{PP} = 27.4 Hz, 2P, *i*Pr-DBFphos) ppm.

^1H NMR (400 MHz, CDCl_3) δ 8.49 (t, $J = 9.7$ Hz, 6H), 7.47 (d, $J = 7.6$ Hz, 2H), 7.40 (d, $J = 7.5$ Hz, 2H), 7.20 (d, $J = 7.6$ Hz, 6H), 7.07 (t, $J = 7.4$ Hz, 3H), 7.01 (t, $J = 7.6$ Hz, 2H), 2.04 – 1.93 (m, 2H), 1.64 – 1.54 (m, 6H), 1.16 – 1.09 (m, 8H), 0.95 – 0.81 (m, 12H), -16.80 (dq, $\text{Ru} = 28.6$, 22.0 Hz, 1H).

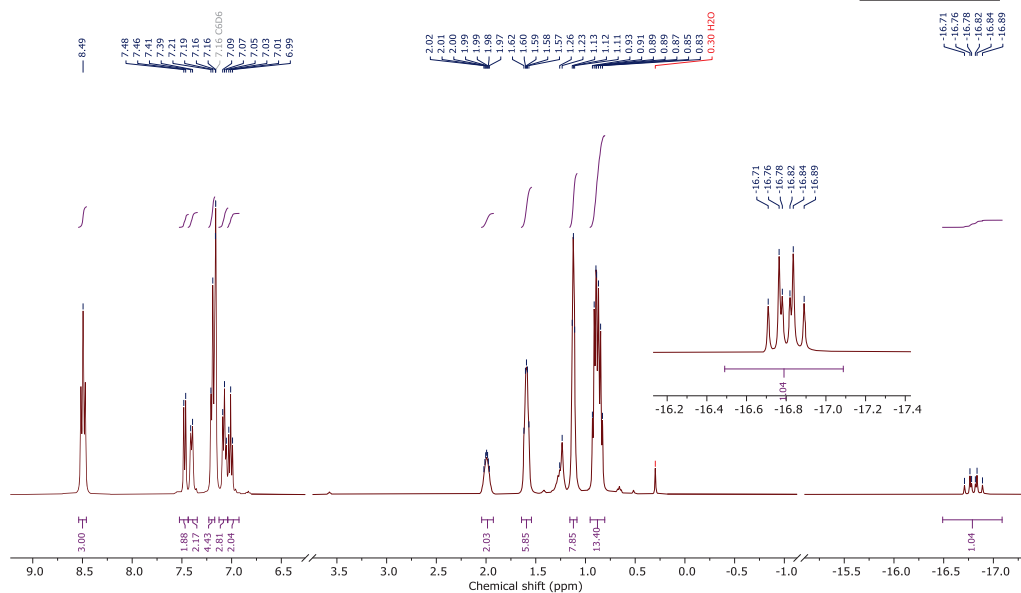
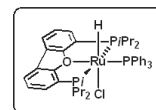


Figure 9.21: 400 MHz ^1H NMR spectrum of **Ru-8a** in C_6D_6 at 25 °C.

^{13}C NMR (101 MHz, CDCl_3) δ 161.20, 141.71 (d, $J = 39.9$ Hz), 135.80 (d, $J = 9.5$ Hz), 129.11, 128.89, 127.20 (d, $J = 8.9$ Hz), 124.59, 123.32, 123.08 (t, $J = 3.0$ Hz), 120.18 (t, $J = 7.5$ Hz), 28.41 (t, $J = 12.1$ Hz), 26.06 (t, $J = 6.4$ Hz), 22.01, 19.79 (t, $J = 2.5$ Hz), 19.30, 19.03 (t, $J = 4.4$ Hz).

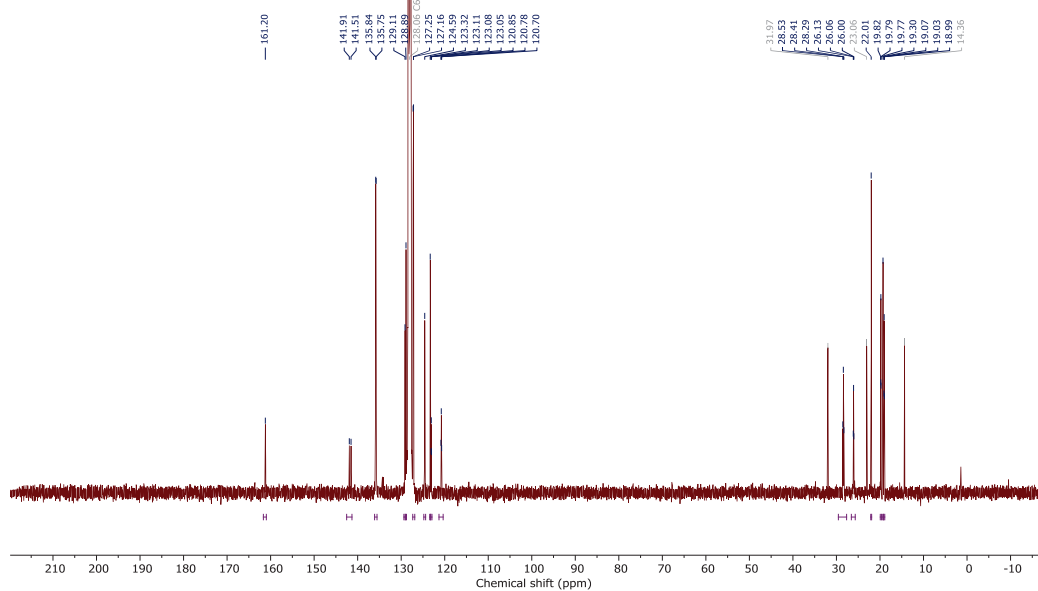
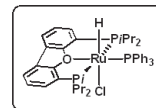


Figure 9.22: 101 MHz ^{13}C NMR spectrum of **Ru-8a** in C_6D_6 at 25 °C.

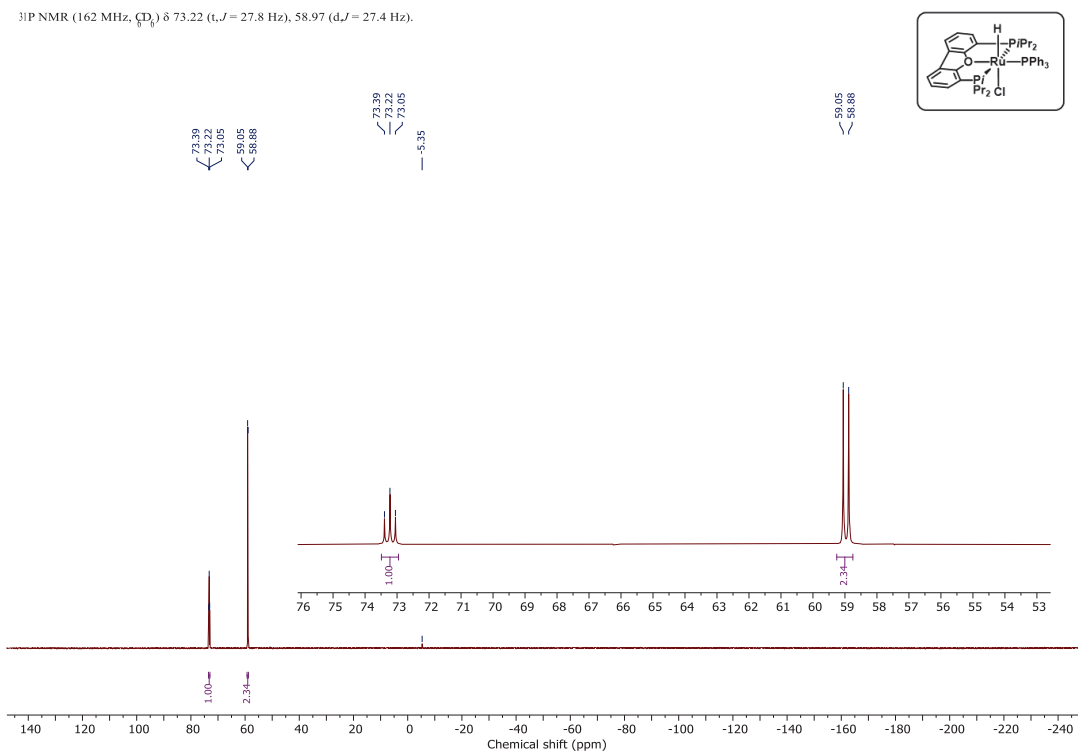
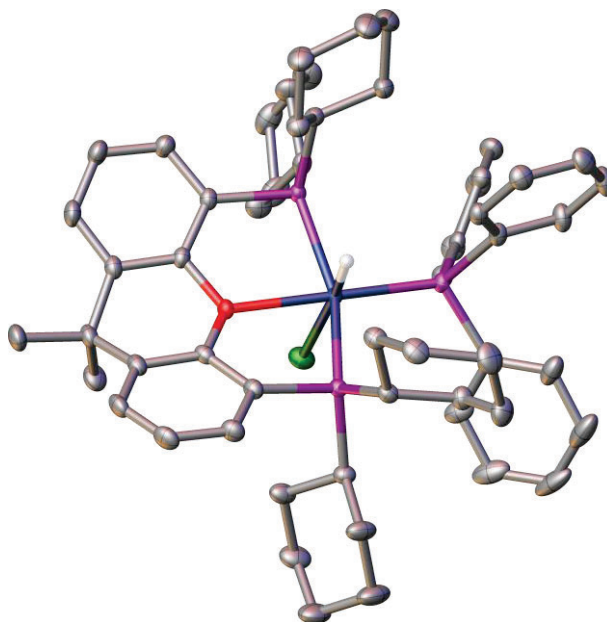
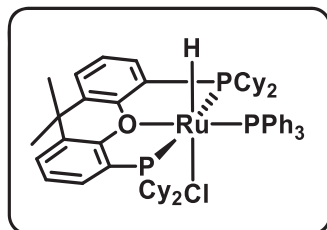


Figure 9.23: 162 MHz $^{31}\text{P}\{^1\text{H}\}$ NMR spectrum of **Ru-8a** in C_6D_6 at 25 °C.

[RuHCl(Cy-xantphos)(PPh₃)] **Ru-9a**

In a 25 mL Schlenk flask, Cy-Xantphos **L9** (82.1 mg, 0.136 mmol, 1.2 eq.) and [RuHCl(PPh₃)₃] toluene adduct (115.4 mg, 0.113 mmol, 1.0 eq.) were dissolved in dry THF (10 mL) and refluxed for 24 hours. A colour change to orange was observed. The mixture was allowed to cool to room temperature and the solvent was removed in vacuo. The crude product was washed with hexane (4x20 mL) and dried in vacuo, yielding the product as yellow powder (107 mg, 94 %).

The product can be crystallized in sufficient quality for XRD measurements by adding polybutene crystallization oil to a concentrated toluene solution of the product and prolonged standing.

¹H NMR (400 MHz, C₆D₆, 298 K) δ 8.57 (t, J = 8.5 Hz, 6H), 7.53 (d, J = 7.4 Hz, 2H), 7.23 (t, J = 7.5 Hz, 6H), 7.12 (t, J = 6.8 Hz, 5H), 6.99 (t, J = 7.5 Hz, 2H), 3.59 (d, J = 12.9 Hz, 2H), 2.34 – 2.21 (m, 4H), 1.63 (tt, J = 26.8, 11.0 Hz, 16H), 1.45 (s, 3H), 1.32 (s, 3H), 1.28 – 1.10 (m, 16H), 1.09 – 0.93 (m, 2H), 0.89 (t, J = 6.7 Hz, 4H), 0.52 (q, J = 14.4, 13.5 Hz, 3H), -16.70 (q, J = 25.0 Hz, 1H).

¹³C NMR (101 MHz, C₆D₆, 298 K) δ 157.96 (t, J = 6.7 Hz), 136.62, 132.85 (t, J = 3.0 Hz), 129.71, 129.09, 127.21 (d, J = 9.1 Hz), 126.04 (t, J = 10.3 Hz), 125.43, 124.27, 37.52 (t, J = 13.9 Hz), 36.93 (t, J = 4.6 Hz), 35.33, 34.52, 30.66, 29.31, 28.71 (t, J = 13.8 Hz), 27.55 – 27.25 (m), 27.13 (t), 26.93 (t), 26.77, 23.67.

³¹P NMR (162 MHz, C₆D₆) δ 76.63 – 75.52 (m, Ru-PPh₃), 44.29 (t, J = 28.3 Hz, Ru-PCy₂).

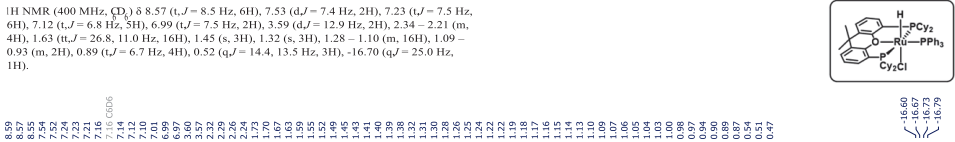


Figure 9.24: 400 MHz ^1H NMR spectrum of **Ru-9a** in C_6D_6 at 25 $^\circ\text{C}$.

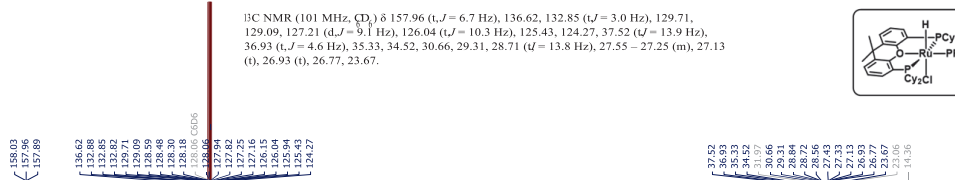


Figure 9.25: 101 MHz ^{13}C NMR spectrum of **Ru-9a** in C_6D_6 at 25 °C.

^{31}P NMR (162 MHz, CDCl_3) δ 76.63 (m), 44.29 (t, $J = 28.3$ Hz).

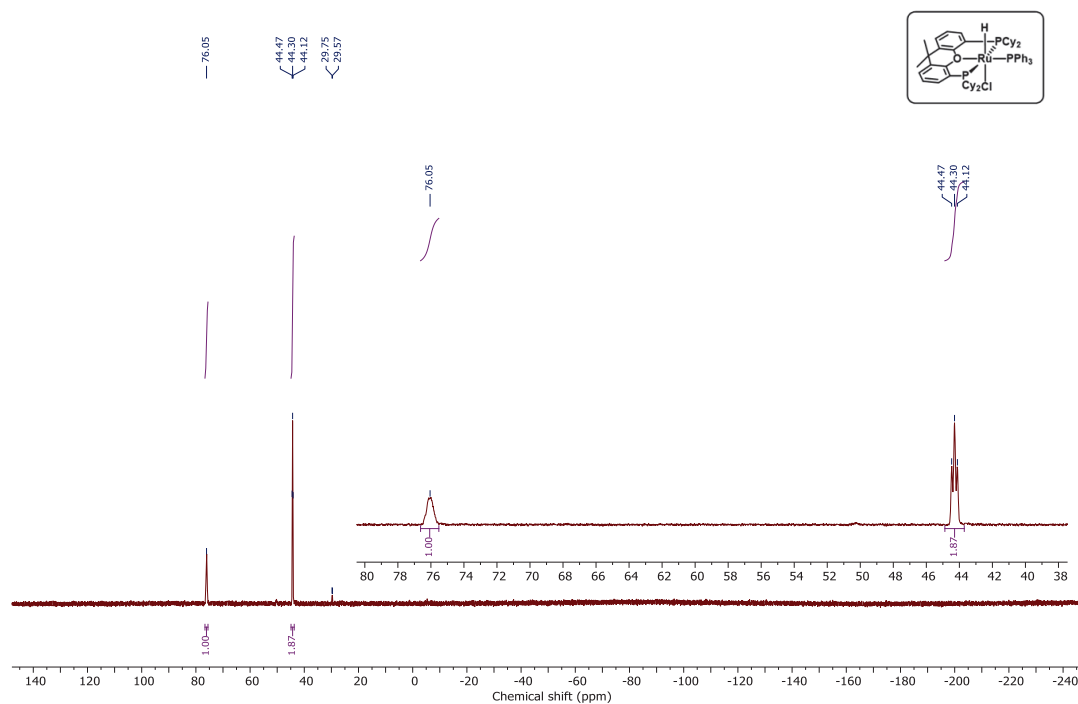
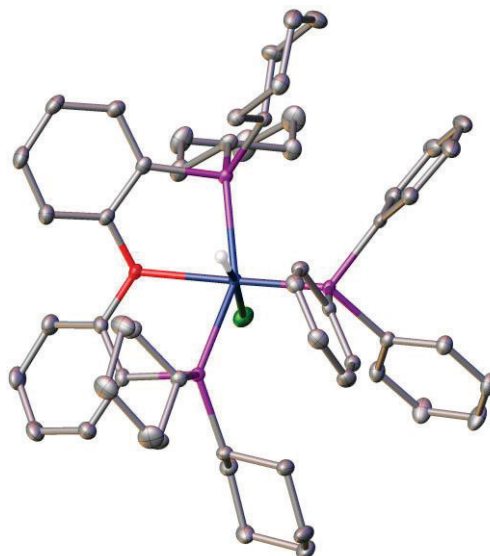
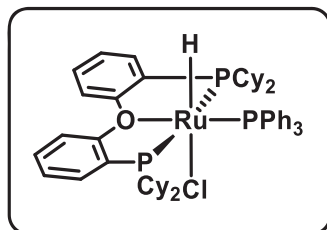


Figure 9.26: 162 MHz $^{31}\text{P}\{^1\text{H}\}$ NMR spectrum of **Ru-9a** in C_6D_6 at 25 °C.

[RuHCl(Cy-DPEphos)(PPh₃)] **Ru-10a**

In a 25 mL Schlenk flask, Cy-DPEphos **L10** (68.0 mg, 0.121 mmol, 1.2 eq.) and [RuHCl(PPh₃)₃] toluene adduct (102.5 mg, 0.101 mmol, 1.0 eq.) were dissolved in dry THF (10 mL) and refluxed for 3 hours. A colour change to orange was observed. The mixture was allowed to cool to room temperature and the solvent was removed in vacuo. The crude product was powderized by freeze-drying from benzene and washed with hexane (4x20 mL) and dried in vacuo, yielding the product as yellow powder (84 mg, 86 %).

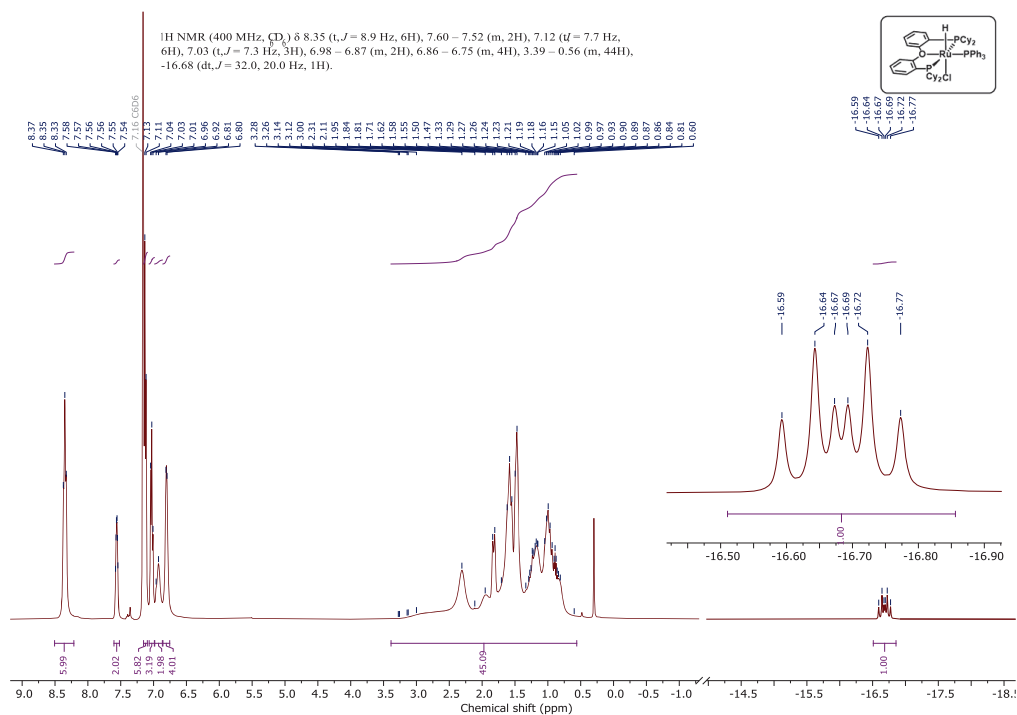
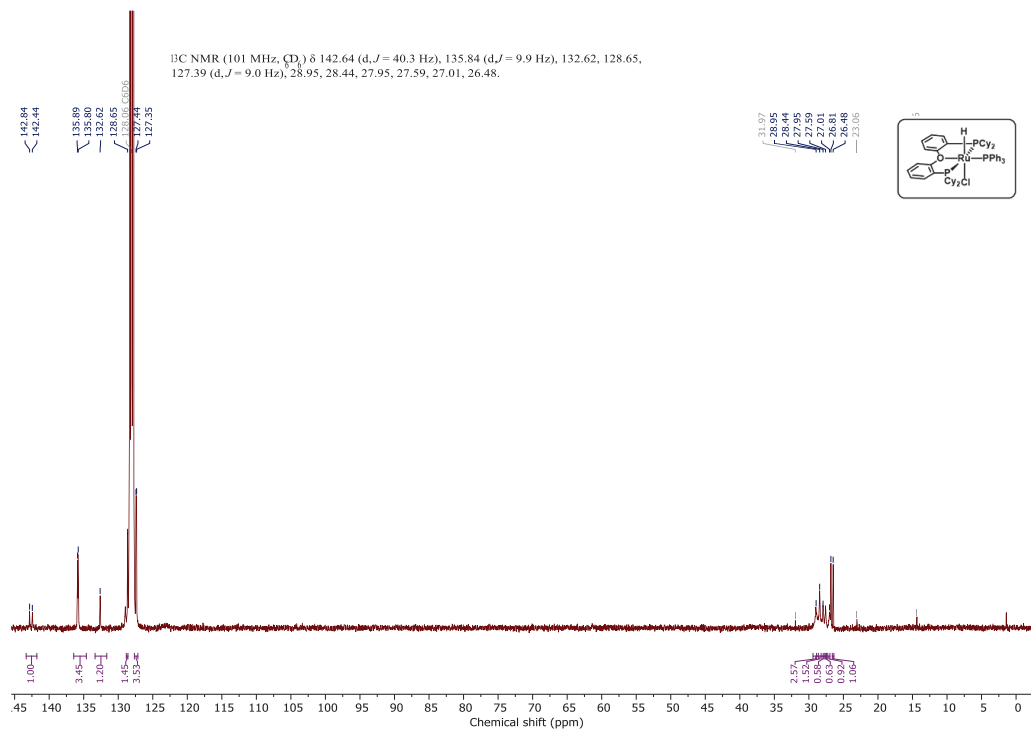
Crystals of sufficient quality for XRD can be grown by crystallization from toluene/hexane using the gas diffusion method at room temperature. The crystals contain one molecule of co-crystallized benzene per unit cell.

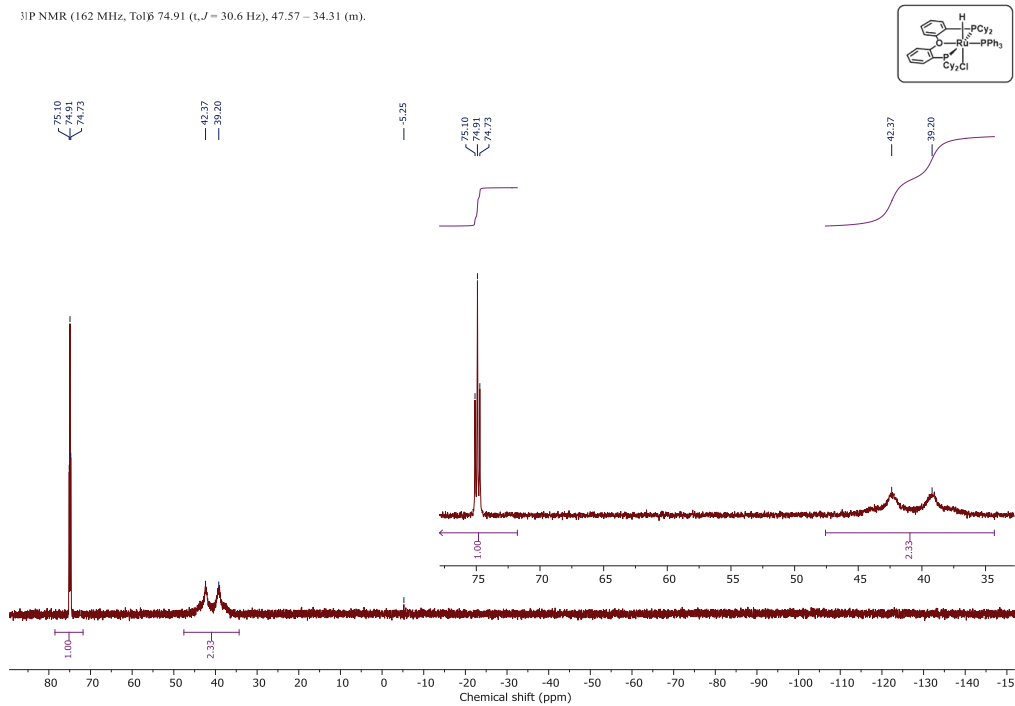
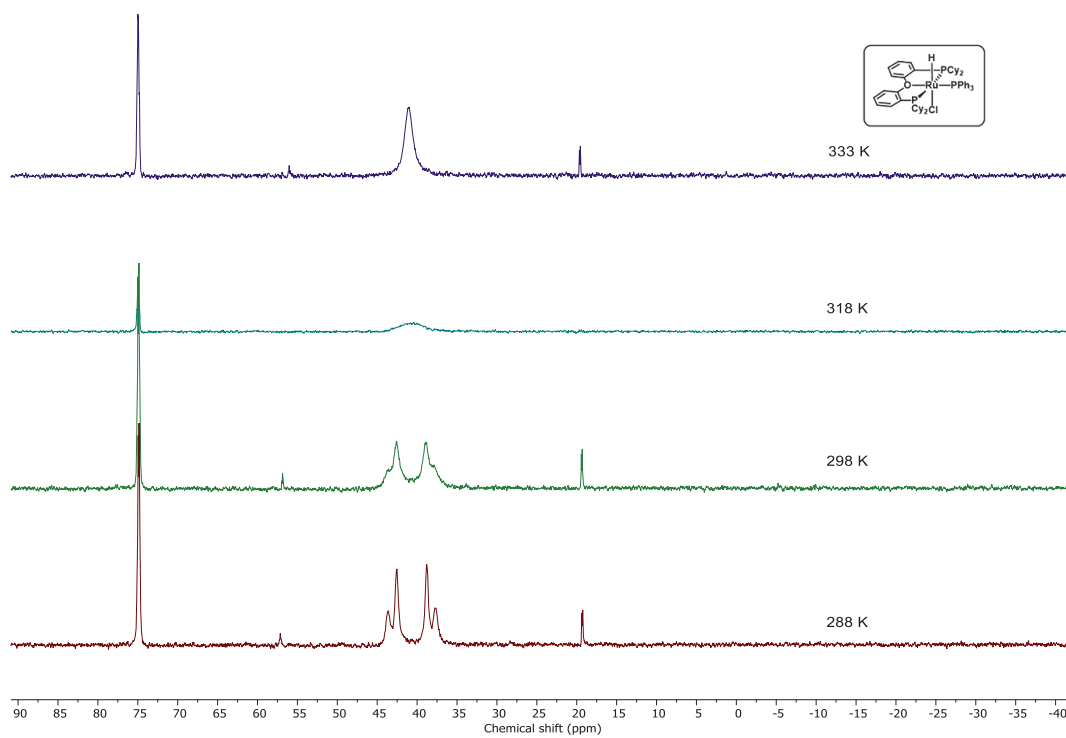
¹H NMR (400 MHz, C₆D₆, 298 K) δ 8.35 (t, J = 8.9 Hz, 6H), 7.60 – 7.52 (m, 2H), 7.12 (t, J = 7.7 Hz, 6H), 7.03 (t, J = 7.3 Hz, 3H), 6.98 – 6.87 (m, 2H), 6.86 – 6.75 (m, 4H), 3.39 – 0.56 (m, 44H, all peaks of P-Cy₂), -16.68 (dt, J = 32.0, 20.0 Hz, 1H).

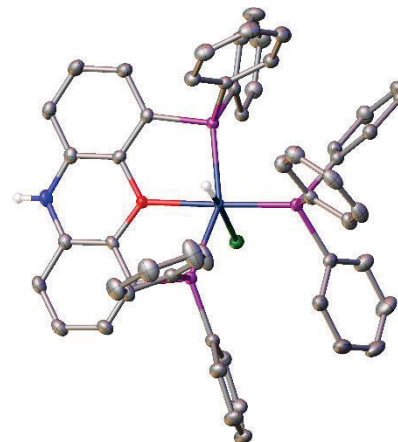
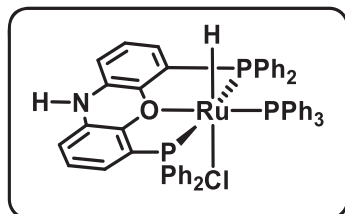
¹³C NMR (101 MHz, C₆D₆) δ 142.64 (d, J = 40.3 Hz), 135.84 (d, J = 9.9 Hz), 132.62, 128.65, 127.39 (d, J = 9.0 Hz), 28.95, 28.44, 27.95, 27.59, 27.01, 26.48.

³¹P {¹H} NMR (162 MHz, Tol, 298 K) δ 74.91 (t, J = 30.6 Hz), 47.57 – 34.31 (m).

EA: Calcd. (%) for C₅₄H₆₈ClOP₃Ru×C₆H₆ (962.58+78.11) C 69.25, H 7.17, found C 68.27, H 7.13.


 Figure 9.27: 400 MHz ¹H NMR spectrum of **Ru-10a** in C₆D₆ at 25 °C.

 Figure 9.28: 101 MHz ¹³C NMR spectrum of **Ru-10a** in C₆D₆ at 25 °C.

Figure 9.29: 162 MHz $^{31}\text{P}\{^1\text{H}\}$ NMR spectrum of **Ru-10a** in toluene- d_8 at 25 °C.Figure 9.30: Variable temperature 243 MHz $^{31}\text{P}\{^1\text{H}\}$ NMR spectrum of **Ru-10a** in toluene- d_8 .

[RuHCl(nixantphos)(PPh₃)] **Ru-11a**

In a 25 mL Schlenk flask, nixantphos **L11** (69.5 mg, 0.126 mmol, 1.2 eq.) and [RuHCl(PPh₃)₃] toluene adduct (106.7 mg, 0.105 mmol, 1.0 eq.) were dissolved in dry THF (12 mL) and refluxed for 3 hours. A colour change to orange was observed and a beige solid precipitated. Reaction completion was signaled by complete colour loss of the solution. The mixture was allowed to cool to room temperature and solvent was carefully removed via syringe. The crude product was washed with hexane (2x5 mL) and dried in vacuo, yielding the product as a beige powder (88 mg, 88 %).

For crystallization: In an inert gas glovebox, [Ru(PPh₃)₃HCl] toluene adduct (2.0 mg, 1.97 μmol, 1.0 eq.) was dissolved in THF (0.5 mL). The solution was injected into an NMR tube via syringe. THF (0.5 mL) was carefully layered on top of the solution via syringe. Nixantphos **L11** (1.8 mg, 3.26 μmol, 1.7 eq.) was dissolved in THF (0.5 mL) and very carefully layered on top via syringe. The solution was left standing for weeks at room temperature in a beaker filled with sand to reduce vibration. The compound formed as orange crystals. Due to the small scale of the reaction, no yield was determined.

Selected ¹H NMR (400 MHz, DMSO-d₆, 298 K) δ -17.47 (dt, J = 28.1, 22.6 Hz, 1H).

³¹P{¹H} NMR (162 MHz, DMSO-d₆, 298 K) δ 72.25 (t, J = 32.3 Hz, Ru-PPh₃), 42.25 (d, J = 31.6 Hz, Ru-POP), 6.90 (s, free PPh₃).

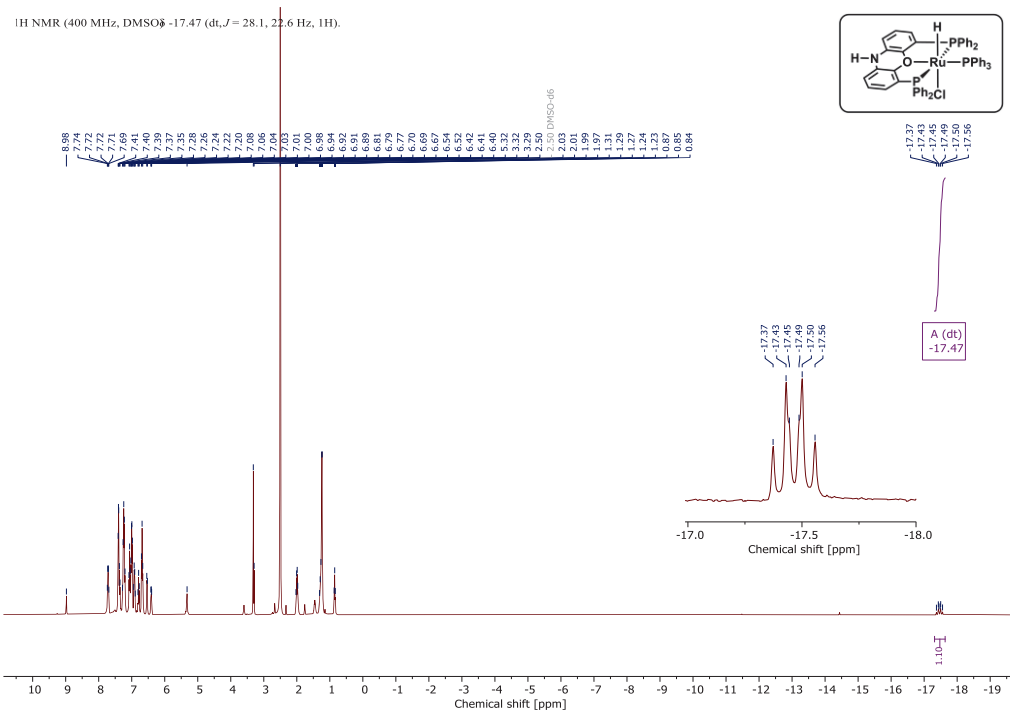


Figure 9.31: 400 MHz ^1H NMR spectrum of crude **Ru-11a** in DMSO- d_6 at 25 $^\circ\text{C}$.

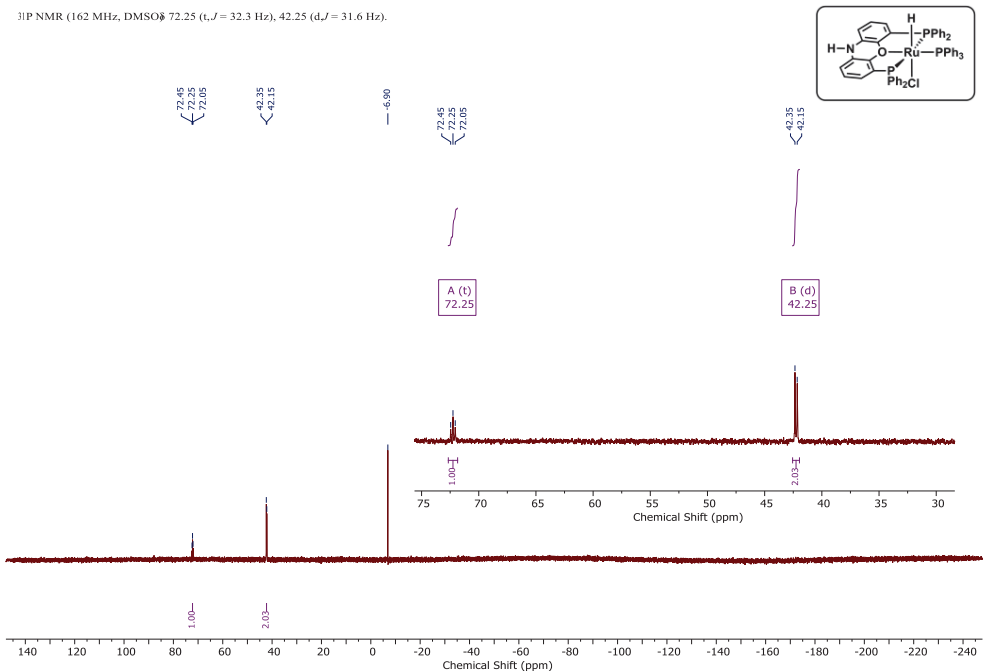
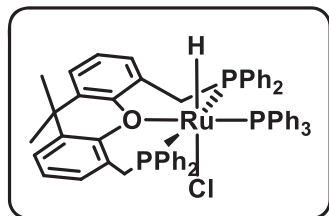


Figure 9.32: 162 MHz $^{31}\text{P}\{^1\text{H}\}$ NMR spectrum of crude **Ru-11a** in DMSO- d_6 at 25 °C.

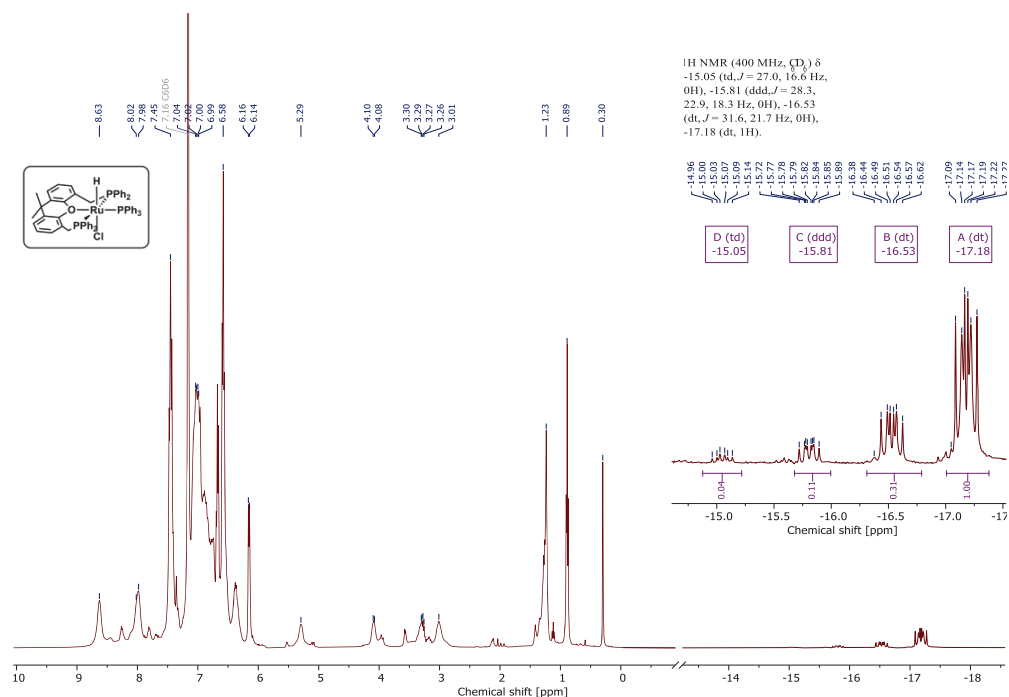
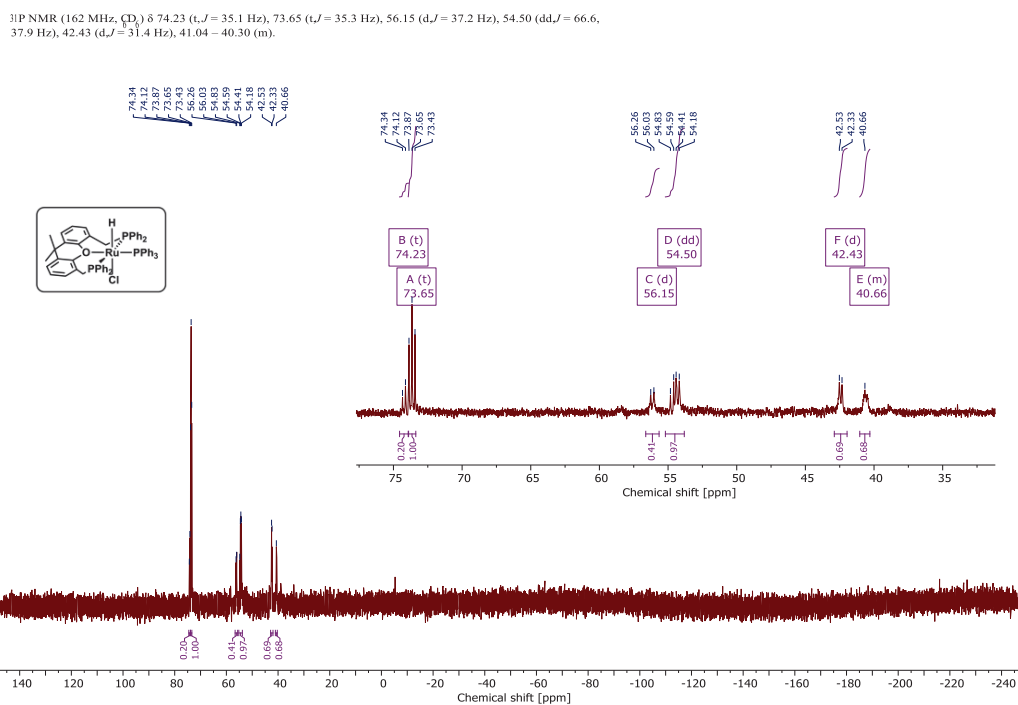
[RuHCl(L12)(PPh₃)] **Ru-12a**

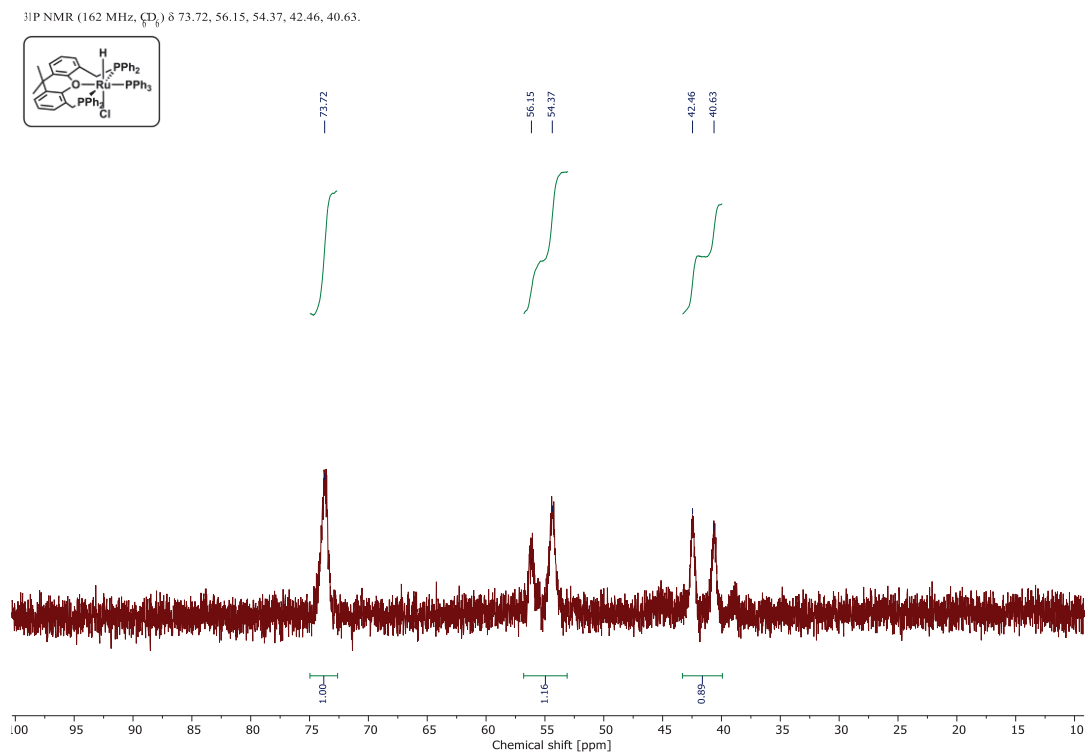
In a 25 mL Schlenk flask, **L12** (69.5 mg, 0.126 mmol, 1.2 eq.) and [RuHCl(PPh₃)₃] toluene adduct (106.7 mg, 0.105 mmol, 1.0 eq.) were dissolved in dry THF (12 mL) and refluxed for 3 hours. A colour change to orange was observed and a beige solid precipitated. Reaction completion was signaled by complete colour loss of the solution. The mixture was allowed to cool to room temperature and solvent was carefully removed via syringe. The crude product was washed with hexane (2x5 mL) and dried in vacuo, yielding product as a beige powder (88 mg, 88 %).

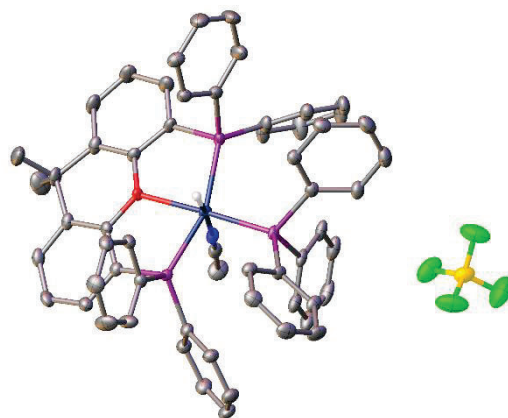
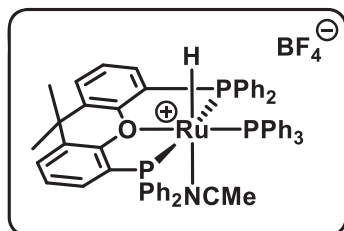
Attempts at recrystallization were performed in DMSO, THF, MeCN, Et₂O, toluene, benzene, hexane, and combinations thereof, however did not yield any crystals of suitable quality for XRD as of the time of writing.

³¹P {¹H} NMR (162 MHz, C₆D₆, 298 K) δ 74.23 (t, J = 35.1 Hz), 73.65 (t, J = 35.3 Hz), 56.15 (d, J = 37.2 Hz), 54.50 (dd, J = 66.6, 37.9 Hz), 42.43 (d, J = 31.4 Hz), 41.04 – 40.30 (m).

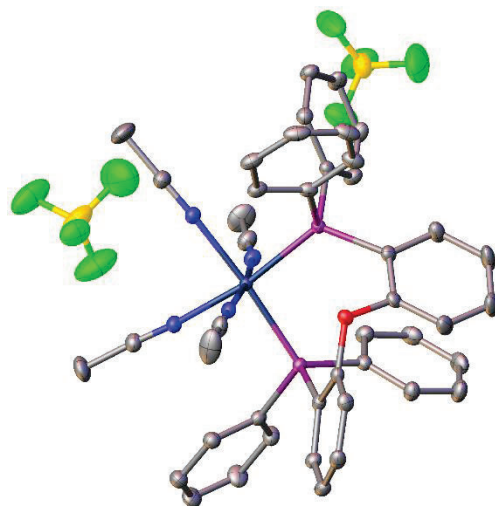
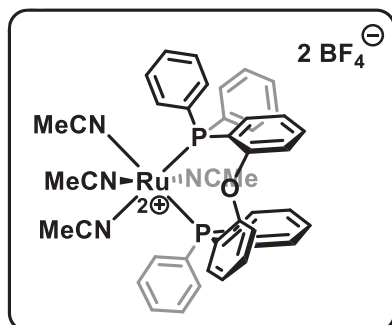
³¹P NMR (162 MHz, C₆D₆, 298 K) δ 73.72, 56.15, 54.37, 42.46, 40.63.


 Figure 9.33: 400 MHz ¹H NMR spectrum of crude **Ru-12a** in C₆D₆ at 25 °C.

 Figure 9.34: 162 MHz ³¹P{¹H} NMR spectrum of crude **Ru-12a** in C₆D₆ at 25 °C.

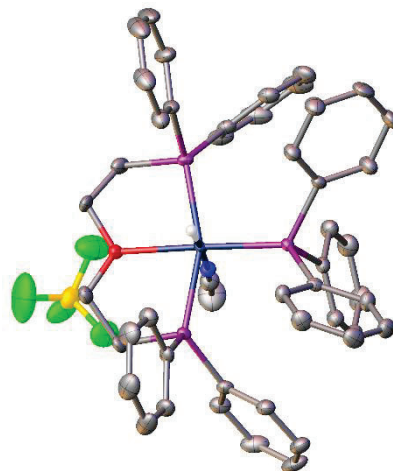
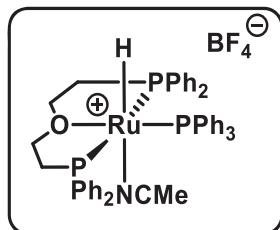


C3 Synthesis of $[\text{RuH}(\text{POP})(\text{PPh}_3)(\text{MeCN})]\text{X}$ $[\text{RuH}(\text{xantphos})(\text{PPh}_3)(\text{MeCN})]\text{BF}_4$ **Ru-1b**

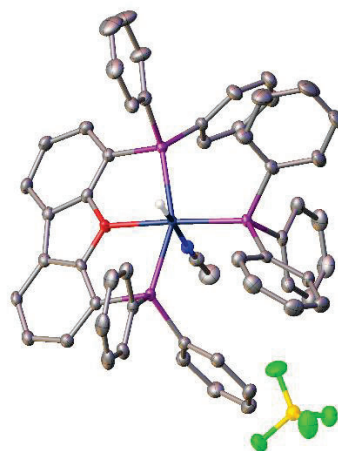
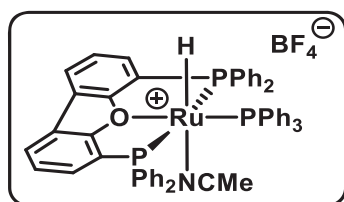
In a 20 mL vial equipped with stir bar, **Ru-1a** (23.8 mg, 24.3 μmol , 1.00 eq.) and NaBF_4 (2.8 mg, 25.5 μmol , 1.05 eq.) were dissolved in 10 mL MeCN and stirred at room temperature overnight. Precipitation of NaCl was observed. Upon completion, the solution was filtered through a GFB filter and dried in vacuo to obtain the product as a yellow crystalline solid. Crystals of sufficient quality for XRD can be grown by crystallization from MeCN/diethyl ether by layering in an NMR tube at room temperature.

 $[\text{Ru}(\text{DPEphos})(\text{MeCN})_4](\text{BF}_4)_2$ **Ru-2b**

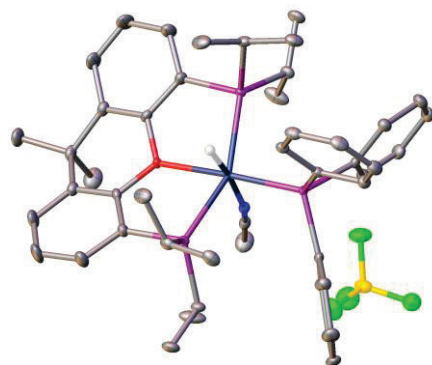
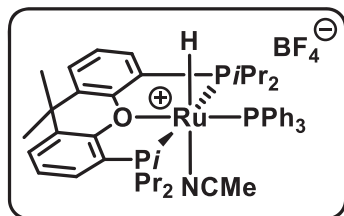
In a 20 mL vial equipped with stir bar, **Ru-2a** (29.3 mg, 31.2 μmol , 1.00 eq.) and NaBF_4 (3.6 mg, 22.7 μmol , 1.05 eq.) were dissolved in 10 mL MeCN and stirred at room temperature overnight. Precipitation of NaCl was observed. Upon completion, the solution was filtered through a GFB filter and dried in vacuo to obtain the product as a white powder. Crystals of sufficient quality for XRD can be grown by crystallization from MeCN/diethyl ether by layering in an NMR tube at room temperature.

[RuH(DPPEE)(PPh₃)(MeCN)]BF₄ **Ru-3b**

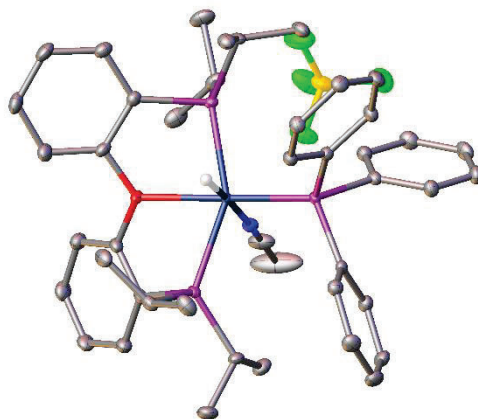
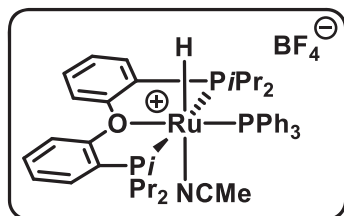
In a 20 mL vial equipped with stir bar, **Ru-3a** (51.7 mg, 61.4 μmol , 1.00 eq.) and NaBF₄ (2.0 mg, 64.6 μmol , 1.05 eq.) were dissolved in 10 mL MeCN and stirred at room temperature overnight. Precipitation of NaCl was observed. Upon completion, the solution was filtered through a GFB filter and dried in vacuo to obtain the product as a yellow crystalline solid (57 mg, 99%). Crystals of sufficient quality for XRD can be grown by crystallization from MeCN/diethyl ether by either layering in an NMR tube at room temperature or slow vapour diffusion with MeCN/diethyl ether at -30 °C.

[RuH(DBFphos)(PPh₃)(MeCN)]BF₄ **Ru-4b**

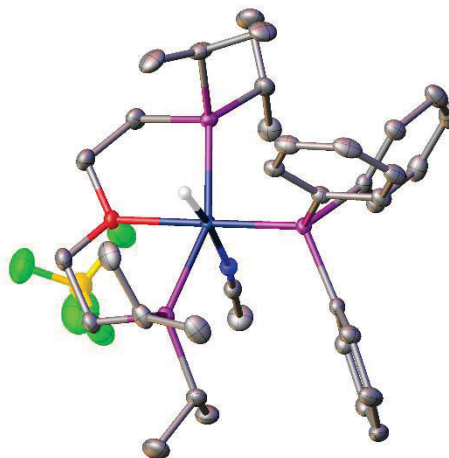
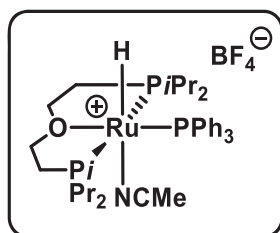
In a 20 mL vial equipped with stir bar, **Ru-4a** (16.2 mg, 17.3 μmol , 1.00 eq.) and NaBF₄ (2.0 mg, 18.2 μmol , 1.05 eq.) were dissolved in 10 mL MeCN and stirred at room temperature overnight. Precipitation of NaCl was observed. Upon completion, the solution was filtered through a GFB filter and dried in vacuo to obtain the product as a yellow crystalline solid (17 mg, 97%). Crystals of sufficient quality for XRD can be grown by crystallization from MeCN/diethyl ether by either layering in an NMR tube at room temperature or slow vapour diffusion with MeCN/diethyl ether at -30 °C.

[RuH(*i*Pr-xantphos)(PPh₃)(MeCN)]BF₄ **Ru-5b**

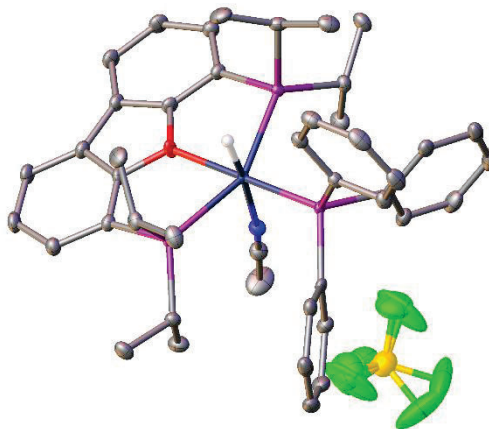
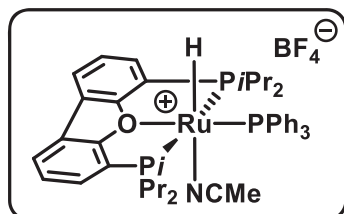
In a 20 mL vial equipped with stir bar, **Ru-5a** (26.3 mg, 31.2 μmol , 1.00 eq.) and NaBF₄ (3.6 mg, 32.8 μmol , 1.05 eq.) were dissolved in 10 mL MeCN and stirred at room temperature overnight. Precipitation of NaCl was observed. Upon completion, the solution was filtered through a GFB filter and dried in vacuo to obtain the product as a yellow crystalline solid in quantitative yield. Crystals of sufficient quality for XRD can be grown by crystallization from dichloromethane/diethyl ether by layering in an NMR tube at room temperature.

[RuH(*i*Pr-DPEphos)(PPh₃)(MeCN)]BF₄ **Ru-6b**

In a 20 mL vial equipped with stir bar, **Ru-6a** (9.1 mg, 11.3 μmol , 1.00 eq.) and NaBF₄ (1.3 mg, 11.8 μmol , 1.05 eq.) were dissolved in 10 mL MeCN and stirred at room temperature overnight. Precipitation of NaCl was observed. Upon completion, the solution was filtered through a GFB filter and dried in vacuo to obtain the product as a yellow crystalline solid (10 mg, 99%). Crystals of sufficient quality for XRD can be grown by crystallization from MeCN/diethyl ether by layering in an NMR tube at room temperature.

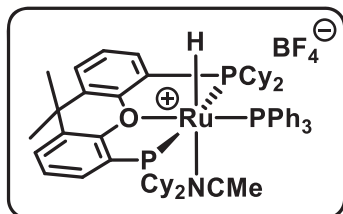
[RuH(DiPrPEE)(PPh₃)(MeCN)]BF₄ **Ru-7b**

In a 20 mL vial equipped with stir bar, **Ru-7a** (20.8 mg, 29.5 μmol , 1.00 eq.) and NaBF₄ (3.4 mg, 31.0 μmol , 1.05 eq.) were dissolved in 10 mL MeCN and stirred at room temperature overnight. Precipitation of NaCl was observed. Upon completion, the solution was filtered through a GFB filter and dried in vacuo to obtain the product as a yellow crystalline solid (24 mg, 99%). Crystals of sufficient quality for XRD can be grown by crystallization from MeCN/diethyl ether by layering in an NMR tube at room temperature.

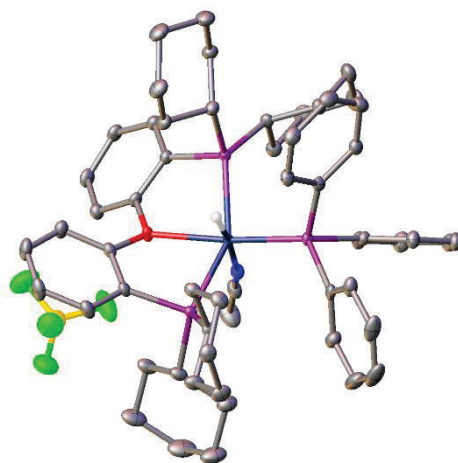
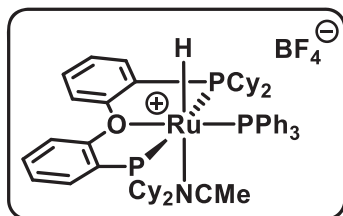
[RuH(*i*Pr-DBFphos)(PPh₃)(MeCN)]BF₄ **Ru-8b**

In a 20 mL vial equipped with stir bar, **Ru-8a** (20.9 mg, 26.1 μmol , 1.00 eq.) and NaBF₄ (3.1 mg, 28.2 μmol , 1.08 eq.) were dissolved in 10 mL MeCN and stirred at room temperature overnight. Precipitation of NaCl was observed. Upon completion, the solution was filtered through a GFB filter and dried in vacuo to obtain the product as a yellow crystalline solid (23 mg, 99%).

Crystals of sufficient quality for XRD can be grown by crystallization from MeCN/diethyl ether by layering in an NMR tube at room temperature.

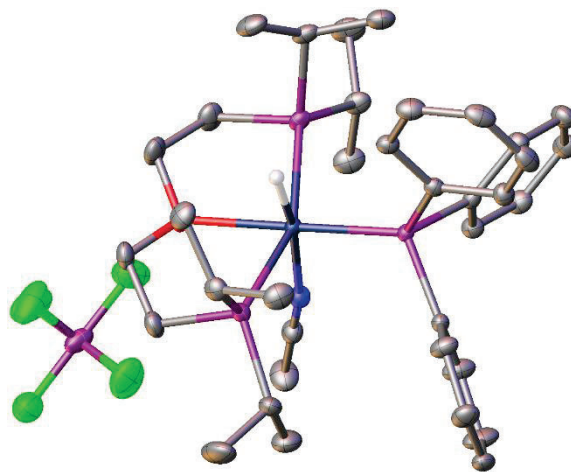
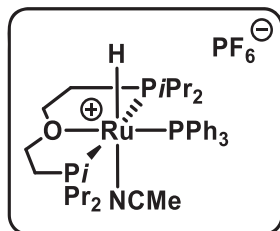
[RuH(Cy-xantphos)(PPh₃)(MeCN)]BF₄ **Ru-9b**

In a 20 mL vial equipped with stir bar, **Ru-9a** (1.00 eq.) and NaBF₄ (1.05 eq.) were dissolved in 10 mL MeCN and stirred at room temperature overnight. Precipitation of NaCl was observed. Upon completion, the solution was filtered through a GFB filter and dried in vacuo to obtain the product as a yellow crystalline solid. No crystals could as of yet be obtained.

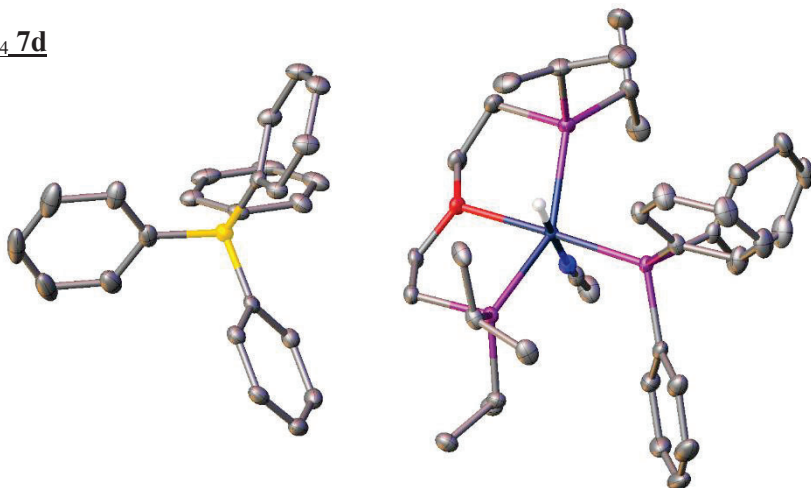
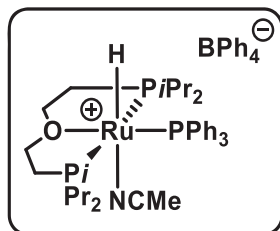
[RuH(Cy-DPEphos)(PPh₃)(MeCN)]BF₄ **Ru-10b**

In a 20 mL vial equipped with stir bar, **3j** (20.3 mg, 21.1 μmol, 1.00 eq.) and NaBF₄ (2.4 mg, 21.8 μmol, 1.08 eq.) were dissolved in 10 mL MeCN and stirred at room temperature overnight. Precipitation of NaCl was observed. Upon completion, the solution was filtered through a GFB filter and dried in vacuo to obtain the product as a yellow crystalline solid (24 mg, 99%).

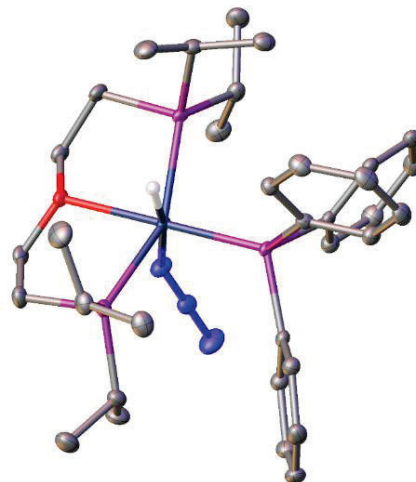
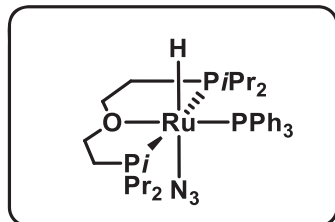
Crystals of sufficient quality for XRD can be grown by crystallization from MeCN/diethyl ether by layering in an NMR tube at room temperature.

[RuH(DiPrPEE)(PPh₃)(MeCN)]PF₆ **Ru-7c**

In a 20 mL vial equipped with stir bar, **Ru-7a** (24.8 mg, 35.1 μmol , 1.00 eq.) and KPF₆ (6.8 mg, 36.9 μmol , 1.05 eq.) were dissolved in 10 mL MeCN and stirred at room temperature overnight. Precipitation of NaCl was observed. Upon completion, the solution was filtered through a GFB filter and dried in vacuo to obtain the product as a yellow crystalline solid (33 mg, 99%). Crystals of sufficient quality for XRD can be grown by crystallization from MeCN/diethyl ether or DCM/diethyl ether by layering in an NMR tube at room temperature.

[Ru(DiPrPEE)(PPh₃)(MeCN)H]PPh₄ **7d**

In a 20 mL vial equipped with stir bar, **Ru-7a** (24.0 mg, 34.0 μmol , 1.00 eq.) and NaBPh₄ (12.2 mg, 35.7 μmol , 1.05 eq.) were dissolved in 10 mL MeCN and stirred at room temperature overnight. Precipitation of NaCl was observed. Upon completion, the solution was filtered through a GFB filter and dried in vacuo to obtain the product as a yellow crystalline solid (34 mg, 97%). Crystals of sufficient quality for XRD can be grown by crystallization from MeCN/diethyl ether by layering in an NMR tube at room temperature.

C4 Synthesis of $[\text{RuH}(\text{N}_3)(\text{POP})(\text{PPh}_3)]$ $[\text{RuH}(\text{N}_3)(\text{DiPrPEE})(\text{PPh}_3)]$ **Ru-7e**

In an inert gas glovebox, a 20 mL vial was charged with $[\text{RuHCl}(\text{DiPrPEE})(\text{PPh}_3)]$ **Ru-7a** (40.6 mg, 57 μmol , 1.0 eq.) and NaN_3 (4.0 mg, 60 μmol , 1.05 eq.). Benzene (6.0 mL) was added and the solution was stirred at room temperature for 96 hours. Shorter reaction times led to incomplete conversions. Precipitation of white solid (NaCl) was observed. The mixture was filtrated through a GFB filter, and the solvent was removed in vacuo. The crude product was obtained as an amorphous orange solid and was powdered by stirring in hexane (15 mL) overnight, dried in vacuo and obtained as a yellow powder in high yield (36 mg, 51 μmol , 88%). Crystals of sufficient quality for SC-XRD can be obtained by dissolving in benzene in high concentration and layering with hexane in an NMR tube.

^1H NMR (400 MHz, C_6D_6 , 298 K) δ 8.09 (t, J = 8.2 Hz, 6H, *o*- PPh_3), 7.08 (t, J = 7.5 Hz, 6H, *m*- PPh_3), 7.01 (t, J = 7.2 Hz, 3H, *p*- PPh_3), 3.86 – 3.62 (m, 2H, $\text{O}-\text{CH}_2-\text{CH}_2-$), 3.09 – 2.87 (m, 2H, $\text{O}-\text{CH}_2-\text{CH}_2-$), 2.03 – 1.92 (m, 2H, $\text{O}-\text{CH}_2-\text{CH}_2-$), 1.52 – 1.26 (m, 6H, $-\text{CH}(\text{CH}_3)_2$), 1.25 – 1.19 (m, 2H, $\text{O}-\text{CH}_2-\text{CH}_2-$), 1.19 – 1.12 (m, 8H, $-\text{CH}(\text{CH}_3)_2$ + , $-\text{CH}(\text{CH}_3)_2$), 0.84 – 0.78 (m, 2H, $-\text{CH}(\text{CH}_3)_2$), 0.78 – 0.71 (m, 6H, $-\text{CH}(\text{CH}_3)_2$), 0.70 – 0.52 (m, 6H, $-\text{CH}(\text{CH}_3)_2$), -17.49 (dt, J = 28.1, 21.6 Hz, 1H, RuH).

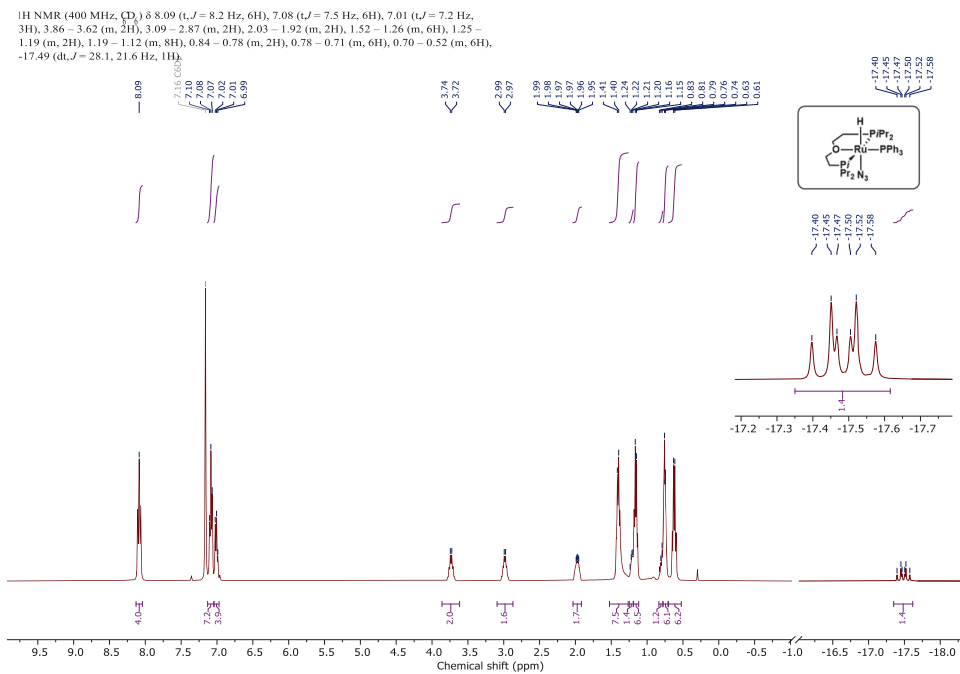
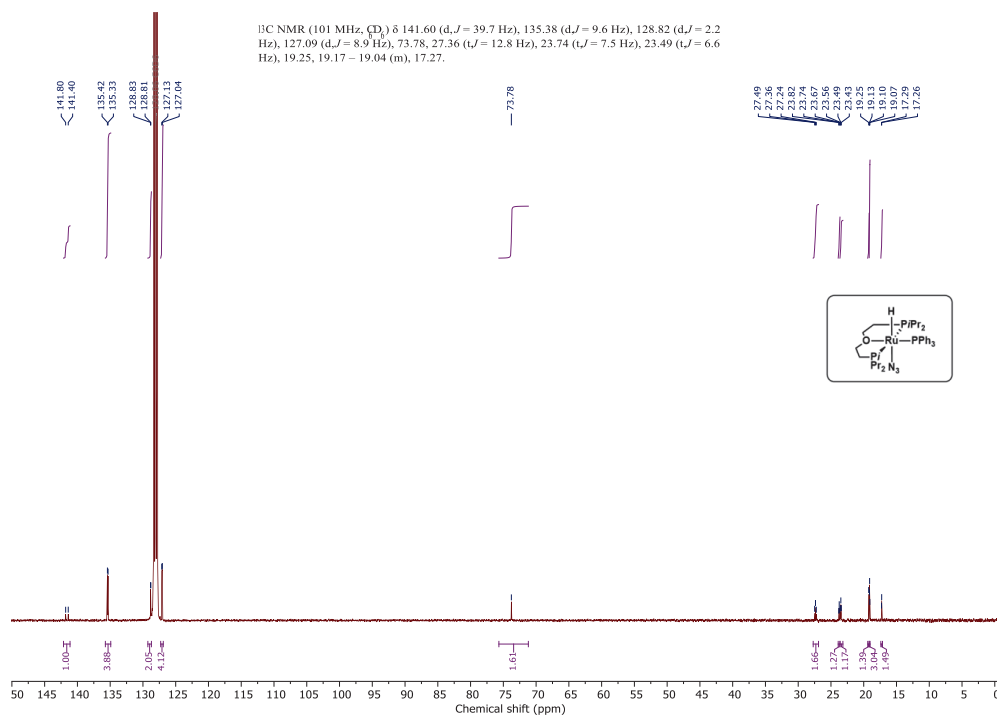
^{13}C NMR (101 MHz, C_6D_6 , 298 K) δ 141.60 (d, J = 39.7 Hz), 135.38 (d, J = 9.6 Hz), 128.82 (d, J = 2.2 Hz), 127.09 (d, J = 8.9 Hz), 73.78, 27.36 (t, J = 12.8 Hz), 23.74 (t, J = 7.5 Hz), 23.49 (t, J = 6.6 Hz), 19.25, 19.17 – 19.04 (m), 17.27.

^{31}P $\{^1\text{H}\}$ NMR (162 MHz, C_6D_6 , 298 K) δ 73.42 (td, J = 31.1, 30.5, 4.8 Hz), 56.40 (dd, J = 30.5, 3.9 Hz).

^{15}N - ^1H HMBC NMR (81 MHz, C_6D_6 , 298 K) δ 50.04 (α -N), 249.89 (β -N).

IR(ATR, Germanium): 2980, 2958, 2923, 2881, 2870, 2043 (N_3), 1453, 1435, 1429, 1244, 1062, 946 cm^{-1} .

EA: Calcd. (%) for $\text{C}_{34}\text{H}_{52}\text{OP}_3\text{N}_3\text{Ru}$ (712.80) C 57.29, H 7.35, N 5.90 found C 58.95, H 7.41, N 5.50.


 Figure 9.36: 400 MHz ^1H NMR spectrum of **Ru-7e** in C_6D_6 at 25 $^\circ\text{C}$.

 Figure 9.37: 101 MHz ^{13}C NMR spectrum of **Ru-7e** in C_6D_6 at 25 $^\circ\text{C}$.

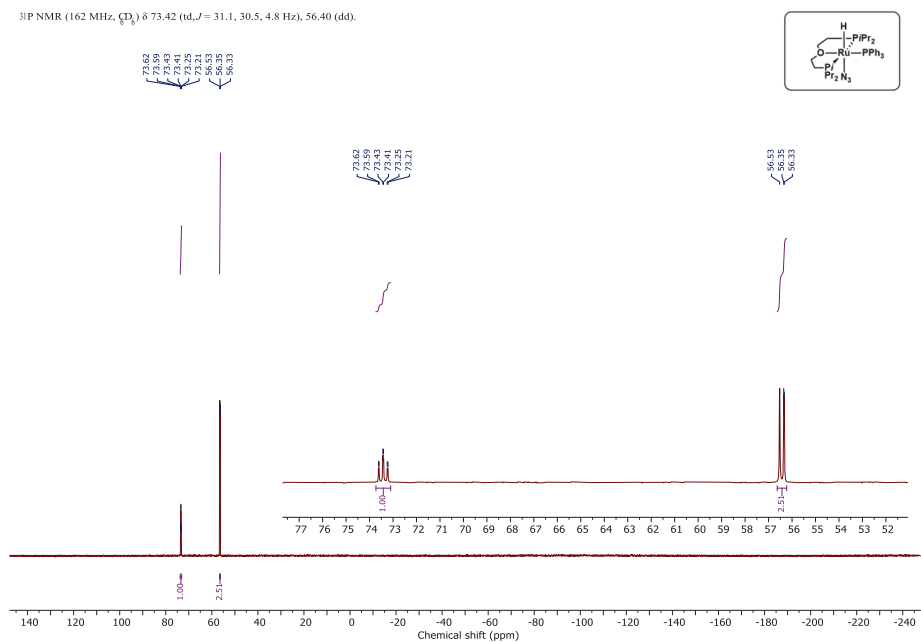


Figure 9.38: 162 MHz $^3\text{P}\{^1\text{H}\}$ NMR spectrum of **Ru-7e** in C_6D_6 at 25 °C.

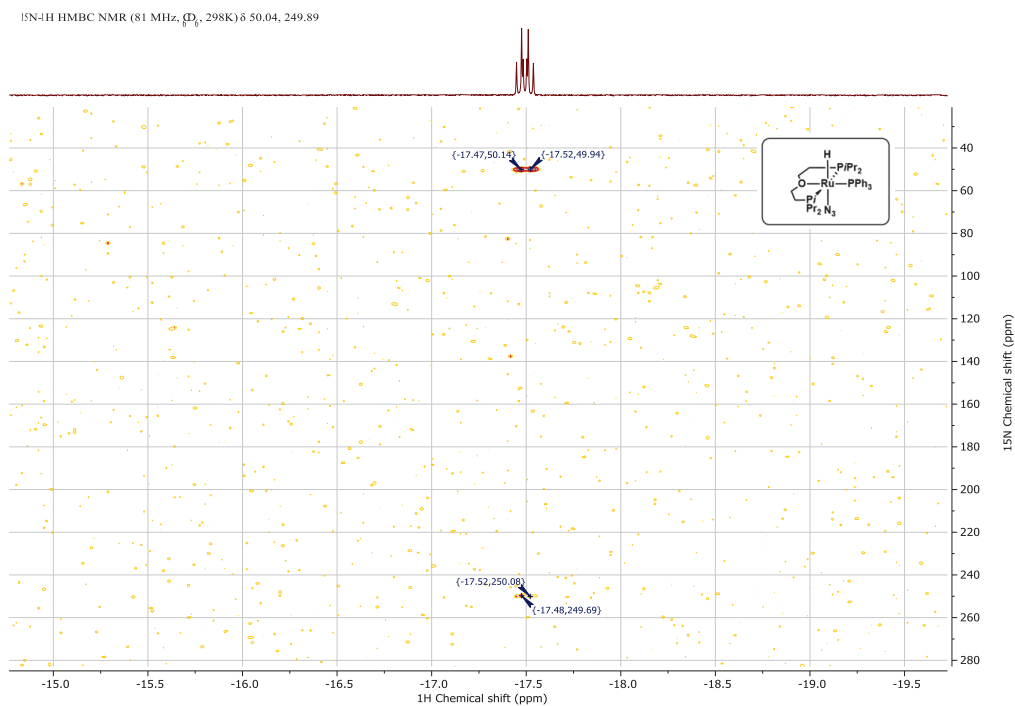


Figure 9.39: 81 MHz $^1\text{H}/^{15}\text{N}$ HMBC NMR spectrum of **Ru-7e** in C_6D_6 at 25 °C.

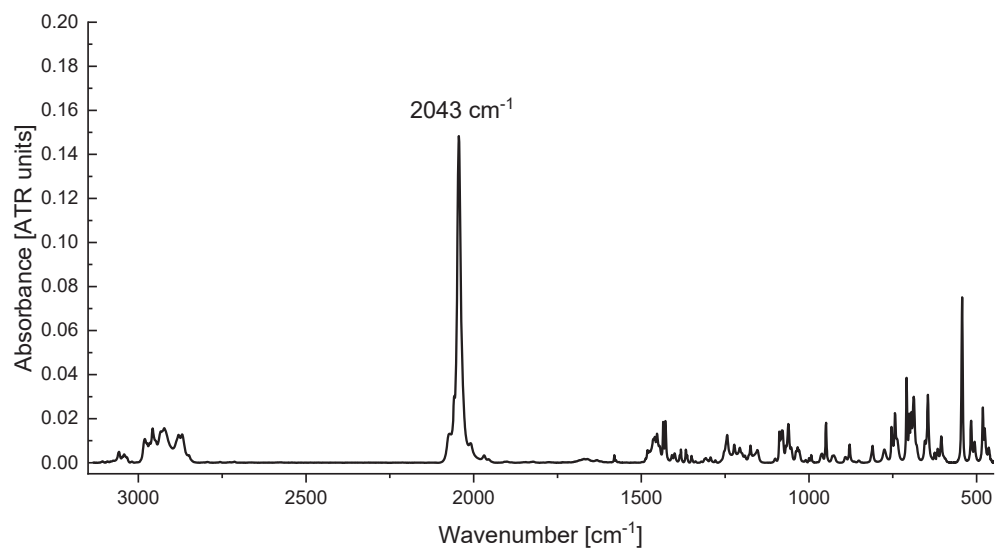


Figure 9.40: ATR-IR spectrum of **Ru-7e**.

C5 Crystallographic data

	[RuHCl(DBFphos)(PPh ₃)]*2 THF Ru-4a	[RuHCl(<i>i</i> Pr-xantphos)(PPh ₃)] Ru-5a
Empirical formula	C _{11.26} H _{10.26} Cl _{0.18} O _{0.55} P _{0.55} Ru _{0.18}	C ₃₆ H _{44.8} Cl _{0.8} O _{0.8} P _{2.4} Ru _{0.8}
Formula weight	196.060	842.32
Temperature/K	120.00(19)	119.97(12)
Crystal system	monoclinic	monoclinic
Space group	P2 ₁ /c	P2 ₁ /n
a/Å	13.1123(1)	12.06910(10)
b/Å	12.2105(1)	16.65290(10)
c/Å	31.9482(2)	20.62330(10)
α /°	90	90
β /°	97.533(1)	94.1590(10)
γ /°	90	90
Volume/Å ³	5071.01(7)	4134.07(5)
Z	22	5
$\rho_{\text{calc}}/\text{cm}^3$	1.412	1.692
μ/mm^{-1}	4.252	6.261
F(000)	2243.8	2200.0
Crystal size/mm ³	? × ? × ?	? × ? × ?
Radiation	Cu K α (λ = 1.54184)	Cu K α (λ = 1.54184)
2 θ range for data collection/°	7.76 to 153.3	6.83 to 153.222
Index ranges	-16 ≤ h ≤ 11, -15 ≤ k ≤ 15, -39 ≤ l ≤ 40	-15 ≤ h ≤ 14, -20 ≤ k ≤ 20, -26 ≤ l ≤ 25
Reflections collected	58870	62493
Independent reflections	10611 [R _{int} = 0.0314, R _{sigma} = 0.0222]	8655 [R _{int} = 0.0305, R _{sigma} = 0.0192]
Data/restraints/parameters	10611/149/700	8655/0/474
Goodness-of-fit on F ²	1.044	1.039
Final R indexes [I ≥ 2 σ (I)]	R ₁ = 0.0306, wR ₂ = 0.0786	R ₁ = 0.0209, wR ₂ = 0.0512
Final R indexes [all data]	R ₁ = 0.0337, wR ₂ = 0.0806	R ₁ = 0.0226, wR ₂ = 0.0521
Largest diff. peak/hole / e Å ⁻³	1.27/-0.79	0.64/-0.45

	[RuHCl(<i>i</i> Pr-DPEphos)(PPh ₃)] Ru-6a	[RuHCl(D <i>i</i> PrPEE)(PPh ₃)] Ru-7a
Empirical formula	C _{33.6} H _{41.6} Cl _{0.8} O _{0.8} P _{2.4} Ru _{0.8}	C ₃₄ H ₅₂ ClOP ₃ Ru
Formula weight	802.26	705
Temperature/K	119.99(11)	128(12)
Crystal system	monoclinic	orthorhombic
Space group	P2 ₁ /n	Pnma
<i>a</i> /Å	11.18020(10)	18.3802(7)
<i>b</i> /Å	16.9933(2)	19.8204(9)
<i>c</i> /Å	20.3787(2)	9.2406(5)
α /°	90	90
β /°	94.7780(10)	90
γ /°	90	90
Volume/Å ³	3858.26(7)	3366.4(3)
<i>Z</i>	5	5
$\rho_{\text{calc}}/\text{cm}^3$	1.726	1.393
μ/mm^{-1}	0.790	0.713
F(000)	2090.0	1480
Crystal size/mm ³	? × ? × ?	? × ? × ?
Radiation	Mo K α (λ = 0.71073)	Mo K α (λ = 0.71073)
2 Θ range for data collection/°	6.45 to 59.426	7.484 to 59.358
Index ranges	-15 ≤ <i>h</i> ≤ 15, -23 ≤ <i>k</i> ≤ 23, -28 ≤ <i>l</i> ≤ 28	-17 ≤ <i>h</i> ≤ 25, -24 ≤ <i>k</i> ≤ 27, -8 ≤ <i>l</i> ≤ 11
Reflections collected	169350	13182
Independent reflections	10619 [<i>R</i> _{int} = 0.0808, <i>R</i> _{sigma} = 0.0294]	4135 [<i>R</i> _{int} = 0.0365, <i>R</i> _{sigma} = 0.0412]
Data/restraints/parameters	10619/0/445	4135/0/203
Goodness-of-fit on <i>F</i> ²	1.071	1.072
Final <i>R</i> indexes [<i>I</i> ≥ 2 σ (<i>I</i>)]	<i>R</i> ₁ = 0.0291, <i>wR</i> ₂ = 0.0665	<i>R</i> ₁ = 0.0306, <i>wR</i> ₂ = 0.0623
Final <i>R</i> indexes [all data]	<i>R</i> ₁ = 0.0348, <i>wR</i> ₂ = 0.0706	<i>R</i> ₁ = 0.0431, <i>wR</i> ₂ = 0.0668
Largest diff. peak/hole / e Å ⁻³	1.36/-0.91	0.53/-0.57

	[RuHCl(<i>i</i> Pr-DBFphos)(PPh ₃)] Ru-8a	[RuHCl(Cy-xantphos)(PPh ₃)]*hexane Ru-9a
Empirical formula	C _{33.6} H ₄₀ Cl _{0.8} O _{0.8} P _{2.4} Ru _{0.8}	C _{50.4} H _{68.8} Cl _{0.8} O 0.8P _{2.4} Ru _{0.8}
Formula weight	640.20	870.99
Temperature/K	120.00(10)	119.9(9)
Crystal system	triclinic	orthorhombic
Space group	P-1	Pbca
<i>a</i> /Å	16.8690(2)	23.93720(10)
<i>b</i> /Å	18.0550(2)	19.19120(10)
<i>c</i> /Å	18.7890(2)	24.91140(10)
α /°	66.3100(10)	90
β /°	64.9560(10)	90
γ /°	87.3680(10)	90
Volume/Å ³	4694.19(10)	11443.89(9)
<i>Z</i>	5	10
ρ_{calc} /cm ³	1.132	1.264
μ /mm ⁻¹	4.388	3.733
F(000)	1664.0	4624.0
Crystal size/mm ³	? × ? × ?	? × ? × ?
Radiation	Cu K α (λ = 1.54184)	Cu K α (λ = 1.54184)
2 Θ range for data collection/°	7.064 to 153.234	6.888 to 153.232
Index ranges	-21 ≤ <i>h</i> ≤ 21, -22 ≤ <i>k</i> ≤ 22, -23 ≤ <i>l</i> ≤ 23	-30 ≤ <i>h</i> ≤ 28, -24 ≤ <i>k</i> ≤ 23, -31 ≤ <i>l</i> ≤ 31
Reflections collected	14014	133963
Independent reflections	19555 [<i>R</i> _{int} = 0.0326, <i>R</i> _{sigma} = 0.0192]	12009 [<i>R</i> _{int} = 0.0355, <i>R</i> _{sigma} = 0.0152]
Data/restraints/parameters	19555/0/889	12009/0/630
Goodness-of-fit on <i>F</i> ²	1.071	1.032
Final <i>R</i> indexes [<i>I</i> ≥ 2 σ (<i>I</i>)]	<i>R</i> ₁ = 0.0242, <i>wR</i> ₂ = 0.0582	<i>R</i> ₁ = 0.0264, <i>wR</i> ₂ = 0.0691
Final <i>R</i> indexes [all data]	<i>R</i> ₁ = 0.0262, <i>wR</i> ₂ = 0.0592	<i>R</i> ₁ = 0.0294, <i>wR</i> ₂ = 0.0717
Largest diff. peak/hole / e Å ⁻³	0.41/-0.50	0.80/-0.47

	[RuHCl(Cy-DPEphos)(PPh ₃)] Ru-10a	[RuHCl(nixantphos)(PPh ₃)]*2 THF Ru-11a
Empirical formula	C _{48.03} H _{59.23} Cl _{0.8} O _{0.8} P _{2.4} Ru _{0.8}	C _{49.6} H _{47.2} Cl _{0.8} N _{0.8} O _{2.4} P _{2.4} Ru _{0.8}
Formula weight	832.946	876.482
Temperature/K	120.00(10)	120.00(10)
Crystal system	Monoclinic	monoclinic
Space group	I2/a	P2 ₁ /c
a/Å	18.4084(1)	12.5252(1)
b/Å	14.0010(1)	24.2139(2)
c/Å	41.1217(2)	17.0055(1)
α /°	90	90
β /°	90.957(1)	97.768(1)
γ /°	90	90
Volume/Å ³	10520.51(11)	5110.17(7)
Z	10	5
ρ_{calc} /cm ³	1.315	1.424
μ /mm ⁻¹	4.041	4.233
F(000)	44407.8	2283.6
Crystal size/mm ³	? × ? × ?	? × ? × ?
Radiation	Cu K α (λ = 1.54184)	Cu K α (λ = 1.54184)
2 Θ range for data collection/°	7.96 to 153.5	7.12 to 153.44
Index ranges	-20 ≤ h ≤ 23, -17 ≤ k ≤ 17, -51 ≤ l ≤ 51	-12 ≤ h ≤ 15, -30 ≤ k ≤ 29, -21 ≤ l ≤ 21
Reflections collected	106054	104626
Independent reflections	11031 [R _{int} = 0.0574, R _{sigma} = 0.0210]	10711 [R _{int} = 0.0468, R _{sigma} = 0.0215]
Data/restraints/parameters	11031/0/625	10711/0/669
Goodness-of-fit on F ²	1.038	1.055
Final R indexes [I ≥ 2 σ (I)]	R ₁ = 0.0261, wR ₂ = 0.0690	R ₁ = 0.0274, wR ₂ = 0.0663
Final R indexes [all data]	R ₁ = 0.0271, wR ₂ = 0.0700	R ₁ = 0.0329, wR ₂ = 0.0711
Largest diff. peak/hole / e Å ⁻³	0.94/-0.49	0.65/-0.38

Compound name	[RuH(xantphos)(PPh ₃)]BF ₄ *1.5 MeCN Ru-1b	[Ru(dpephos)(MeCN) ₄](BF ₄) ₂ Ru-2b
Empirical formula	C ₆₂ H _{55.5} BF ₄ N _{2.5} OP ₃ Ru	C _{25.14} H _{22.86} B _{1.14} F _{4.57} N _{2.29} O _{0.57} P _{1.14} Ru _{0.57}
Formula weight	1132.452	558.53
Temperature/K	119.97(12)	119.99(10)
Crystal system	triclinic	monoclinic
Space group	P-1	P2 ₁ /n
a/Å	10.0238(1)	15.51250(10)
b/Å	22.5348(3)	14.39670(10)
c/Å	24.1427(3)	20.53350(10)
α/°	86.375(1)	90
β/°	89.022 (1)	111.6040(10)
γ/°	79.247(1)	90
Volume/Å ³	5346.90(11)	4263.58(5)
Z	4	7
ρ _{calc} /g/cm ³	1.407	1.523
μ/mm ⁻¹	3.705	4.344
F(000)	2343.0	1984.0
Crystal size/mm ³	? × ? × ?	? × ? × ?
Radiation	Cu Kα (λ = 1.54184)	Cu Kα (λ = 1.54184)
2Θ range for data collection/°	7.34 to 153.74	7.692 to 153.342
Index ranges	-12 ≤ h ≤ 12, -26 ≤ k ≤ 28, -30 ≤ l ≤ 30	-19 ≤ h ≤ 19, -18 ≤ k ≤ 18, -25 ≤ l ≤ 2586494
Reflections collected	110118	86494
Independent reflections	22281 [R _{int} = 0.0380, R _{sigma} = 0.0256]	8947 [R _{int} = 0.0379, R _{sigma} = 0.0161]
Data/restraints/parameters	22281/6/1429	8947/0/563
Goodness-of-fit on F ²	1.042	1.030
Final R indexes [I ≥ 2σ (I)]	R ₁ = 0.0451, wR ₂ = 0.1102	R ₁ = 0.0328, wR ₂ = 0.0873
Final R indexes [all data]	R ₁ = 0.0493, wR ₂ = 0.1129	R ₁ = 0.0344, wR ₂ = 0.0887
Largest diff. peak/hole / e Å ⁻³	1.83/-0.83	1.89/-0.74

Compound name	[RuH(DPPEE)(PPh ₃)(MeCN)]BF ₄ Ru-3b	3[RuH(dbfphos)(PPh ₃)(MeCN)]BF ₄ * Ru-4b*
Empirical formula	C ₄₈ H ₄₆ BNOF ₄ P ₃ Ru	C _{354.24} H _{297.73} B ₄ F ₁₆ N ₁₅ O ₆ P ₁₈ Ru ₆
Formula weight	933.710	6371.79
Temperature/K	120.00(11)	123(5)
Crystal system	triclinic	triclinic
Space group	P1	P-1
a/Å	9.9675(3)	16.7760(2)
b/Å	10.4945(4)	21.5573(2)
c/Å	12.5965(4)	24.6408(2)
α/°	65.800(3)	79.2500(10)
β/°	67.119(3)	71.3000(10)
γ/°	89.567(3)	74.9370(10)
Volume/Å ³	1089.06(8)	8098.74(15)
Z	2	1
ρ _{calc} /cm ³	2.847	1.306
μ/mm ⁻¹	8.815	3.599
F(000)	962.9	3274.0
Crystal size/mm ³	? × ? × ?	? × ? × ?
Radiation	Cu Kα (λ = 1.54184)	Cu Kα (λ = 1.54184)
2θ range for data collection/°	8.5 to 152.88	7.624 to 153.364
Index ranges	-12 ≤ h ≤ 12, -13 ≤ k ≤ 8, -15 ≤ l ≤ 15	-21 ≤ h ≤ 21, -27 ≤ k ≤ 26, -26 ≤ l ≤ 31
Reflections collected	10658	165874
Independent reflections	5585 [R _{int} = 0.0359, R _{sigma} = 0.0677]	33746 [R _{int} = 0.0394, R _{sigma} = 0.0271]
Data/restraints/parameters	5585/3/562	33746/51/1938
Goodness-of-fit on F ²	0.929	1.013
Final R indexes [I ≥ 2σ (I)]	R ₁ = 0.0247, wR ₂ = 0.0536	R ₁ = 0.0586, wR ₂ = 0.1923
Final R indexes [all data]	R ₁ = 0.0256, wR ₂ = 0.0543	R ₁ = 0.0641, wR ₂ = 0.2000
Largest diff. peak/hole / e Å ⁻³	0.30/-0.31	4.79/-0.80

* The crystal structure of this complex showed extreme disorder in the BF₄ counterions, as well as in co-crystallized MeCN and Et₂O solvent molecules, which could not be resolved to this date. Fitting the structure factors relating to these crystallographic voids using Platon squeeze proved unsuccessful. Three complexes per unit cell.

Compound name	[RuH(<i>i</i> Pr-xantphos)(PPh ₃)(MeCN)]BF ₄ *DCM Ru-5b	[RuH(<i>i</i> Pr-dpephos)(PPh ₃)(MeCN)]BF ₄ Ru-6b
Empirical formula	C ₄₈ H ₆₀ BCl ₂ F ₄ NOP ₃ Ru	C ₄₄ H ₅₅ BF ₄ NOP ₃ Ru
Formula weight	1018.66	894.68
Temperature/K	120.00(10)	134(20)
Crystal system	monoclinic	monoclinic
Space group	P2 ₁ /m	P2 ₁ /n
a/Å	12.61151(5)	11.74500(10)
b/Å	13.99152(6)	14.57510(10)
c/Å	13.72829(6)	24.7582(2)
α/°	90	90
β/°	103.9289(4)	90.9780(10)
γ/°	90	90
Volume/Å ³	2351.183(18)	4237.60(6)
Z	2	4
ρ _{calc} /cm ³	1.439	1.402
μ/mm ⁻¹	5.145	4.497
F(000)	1054.0	1856.0
Crystal size/mm ³	? × ? × ?	? × ? × ?
Radiation	Cu Kα (λ = 1.54184)	Cu Kα (λ = 1.54184)
2θ range for data collection/°	7.222 to 153.084	7.038 to 153.408
Index ranges	-15 ≤ h ≤ 15, -17 ≤ k ≤ 17, -17 ≤ l ≤ 17	-14 ≤ h ≤ 14, -18 ≤ k ≤ 18, -31 ≤ l ≤ 30
Reflections collected	48328	85773
Independent reflections	5135 [R _{int} = 0.0363, R _{sigma} = 0.0132]	8894 [R _{int} = 0.0367, R _{sigma} = 0.0156]
Data/restraints/parameters	5135/0/323	8894/0/509
Goodness-of-fit on F ²	1.064	1.036
Final R indexes [I >= 2σ (I)]	R ₁ = 0.0224, wR ₂ = 0.0574	R ₁ = 0.0230, wR ₂ = 0.0583
Final R indexes [all data]	R ₁ = 0.0225, wR ₂ = 0.0574	R ₁ = 0.0242, wR ₂ = 0.0592
Largest diff. peak/hole / e Å ⁻³	0.38/-0.75	1.01/-0.50

Appendix C. Chapter 2

Compound name	[RuH(DiPrPEE)(PPh ₃)(MeCN)]BF ₄ Ru-7b	[RuH(<i>i</i> Pr-dbfphos)(PPh ₃)(MeCN)]BF ₄ *MeCN Ru-8b
Empirical formula	C _{28.8} H ₄₄ B _{0.8} F _{3.2} N _{0.8} O _{0.8} P _{2.4} Ru _{0.8}	C ₄₆ H ₅₆ BF ₄ N ₂ OP ₃ Ru
Formula weight	798.60	933.71
Temperature/K	119.99(11)	120.00(10)
Crystal system	orthorhombic	triclinic
Space group	Pnma	P-1
a/Å	19.47470(9)	12.19600(10)
b/Å	14.11540(7)	14.06460(10)
c/Å	13.80786(7)	13.71270(10)
α/°	90	90
β/°	90	102.2940(10)
γ/°	90	90
Volume/Å ³	3795.69(3)	2298.22(3)
Z	5	2
ρ _{calc} /cm ³	1.747	1.349
μ/mm ⁻¹	6.181	4.177
F(000)	2080.0	968.0
Crystal size/mm ³	? × ? × ?	? × ? × ?
Radiation	Cu Kα (λ = 1.54184)	Cu Kα (λ = 1.54184)
2Θ range for data collection/°	7.848 to 164.456	7.418 to 153.182
Index ranges	-16 ≤ h ≤ 24, -17 ≤ k ≤ 17, -17 ≤ l ≤ 17	-15 ≤ h ≤ 15, -17 ≤ k ≤ 15, -17 ≤ l ≤ 17
Reflections collected	75562	46819
Independent reflections	4163 [R _{int} = 0.0579, R _{sigma} = 0.0162]	9543 [R _{int} = 0.0504, R _{sigma} = 0.0224]
Data/restraints/parameters	4163/0/243	9543/0/574
Goodness-of-fit on F ²	1.050	1.044
Final R indexes [I ≥ 2σ (I)]	R ₁ = 0.0274, wR ₂ = 0.0737	R ₁ = 0.0242, wR ₂ = 0.0624
Final R indexes [all data]	R ₁ = 0.0283, wR ₂ = 0.0747	R ₁ = 0.0244, wR ₂ = 0.0625
Largest diff. peak/hole / e Å ⁻³	0.68/-0.87	0.73/-0.72

Compound name	[RuH(Cy-dpephos)(PPh ₃)(MeCN)]BF ₄ *MeCN*Et ₂ O Ru-10b
Empirical formula	C _{49.6} H _{67.2} B _{0.8} F _{3.2} N _{1.6} O _{1.6} P _{2.4} Ru _{0.8}
Formula weight	936.08
Temperature/K	119.99(10)
Crystal system	monoclinic
Space group	P2 ₁ /c
a/Å	18.58992(7)
b/Å	13.61359(6)
c/Å	24.27175(11)
α /°	90
β /°	96.4328(4)
γ /°	90
Volume/Å ³	6103.91(4)
Z	5
$\rho_{\text{calc}}/\text{cm}^3$	1.273
μ/mm^{-1}	3.261
F(000)	2464.0
Crystal size/mm ³	? × ? × ?
Radiation	Cu K α (λ = 1.54184)
2 Θ range for data collection/°	7.33 to 153.468
Index ranges	-21 ≤ h ≤ 23, -17 ≤ k ≤ 16, -30 ≤ l ≤ 30
Reflections collected	123392
Independent reflections	12811 [R _{int} = 0.0419, R _{sigma} = 0.0180]
Data/restraints/parameters	12811/21/713
Goodness-of-fit on F ²	1.096
Final R indexes [I ≥ 2 σ (I)]	R ₁ = 0.0307, wR ₂ = 0.0835
Final R indexes [all data]	R ₁ = 0.0322, wR ₂ = 0.0845
Largest diff. peak/hole / e Å ⁻³	0.83/-0.41

Compound name	[RuH(DiPrPEE) PPh ₃)(MeCN)]PF ₆ *0.5DCM Ru-7c	[RuH(DiPrPEE) (PPh ₃)(MeCN)]PPh ₄ Ru-7d
Empirical formula	C _{32.44} H _{49.78} Cl _{0.89} F _{5.33} N _{0.89} O _{0.89} P _{3.56} Ru _{0.89}	C ₆₀ H ₇₅ BNOP ₃ Ru
Formula weight	799.31	1031.00
Temperature/K	119.99(10)	120.00(10)
Crystal system	monoclinic	triclinic
Space group	P2 ₁ /n	P-1
a/Å	20.30049(7)	12.0789(2)
b/Å	18.64291(6)	14.1431(2)
c/Å	22.00302(8)	15.8041(3)
α /°	90	84.409(2)
β /°	97.9564(3)	87.916(2)
γ /°	90	87.8810(10)
Volume/Å ³	8247.11(5)	2683.73(8)
Z	9	2
ρ_{calc} /cm ³	1.448	1.276
μ /mm ⁻¹	5.630	3.510
F(000)	3720.0	1088.0
Crystal size/mm ³	? × ? × ?	? × ? × ?
Radiation	Cu K α (λ = 1.54184)	Cu K α (λ = 1.54184)
2 Θ range for data collection/°	7.304 to 153.402	7.328 to 153.202
Index ranges	-25 ≤ h ≤ 25, -23 ≤ k ≤ 22, -27 ≤ l ≤ 27	-15 ≤ h ≤ 15, -17 ≤ k ≤ 13, -19 ≤ l ≤ 19
Reflections collected	168814	55397
Independent reflections	17337 [R _{int} = 0.0421, R _{sigma} = 0.0179]	11173 [R _{int} = 0.0412, R _{sigma} = 0.0274]
Data/restraints/parameters	17337/2/955	11173/0/617
Goodness-of-fit on F ²	1.010	1.022
Final R indexes [I > 2 σ (I)]	R ₁ = 0.0238, wR ₂ = 0.0597	R ₁ = 0.0242, wR ₂ = 0.0583
Final R indexes [all data]	R ₁ = 0.0273, wR ₂ = 0.0625	R ₁ = 0.0277, wR ₂ = 0.0603
Largest diff. peak/hole / e Å ⁻³	0.55/-0.41	0.57/-0.59

Compound name	[RuH(N ₃)(DiPrPEE)(PPh ₃)] Ru-7e
Empirical formula	C _{27.2} H _{41.6} N _{2.4} O _{0.8} P _{2.4} Ru _{0.8}
Formula weight	712.798
Temperature/K	120.00(10)
Crystal system	monoclinic
Space group	P2 ₁ /c
a/Å	9.5934(1)
b/Å	15.9163(1)
c/Å	22.6302(2)
α /°	90
β /°	99.861(1)
γ /°	90
Volume/Å ³	3404.39(5)
Z	5
$\rho_{\text{calc}}/\text{cm}^3$	1.738
μ/mm^{-1}	6.618
F(000)	1879.6
Crystal size/mm ³	? × ? × ?
Radiation	Cu K α (λ = 1.54184)
2 Θ range for data collection/°	6.82 to 153.4
Index ranges	-12 ≤ h ≤ 12, -17 ≤ k ≤ 20, -28 ≤ l ≤ 28
Reflections collected	69677
Independent reflections	7148 [R _{int} = 0.0462, R _{sigma} = 0.0200]
Data/restraints/parameters	7148/0/416
Goodness-of-fit on F ²	1.039
Final R indexes [I ≥ 2 σ (I)]	R ₁ = 0.0212, wR ₂ = 0.0543
Final R indexes [all data]	R ₁ = 0.0229, wR ₂ = 0.0556
Largest diff. peak/hole / e Å ⁻³	0.46/-0.36

Appendix D. Chapter 3

D1 Product identification and calibration curves

D1.1 GC and GC-MS spectra of reaction products

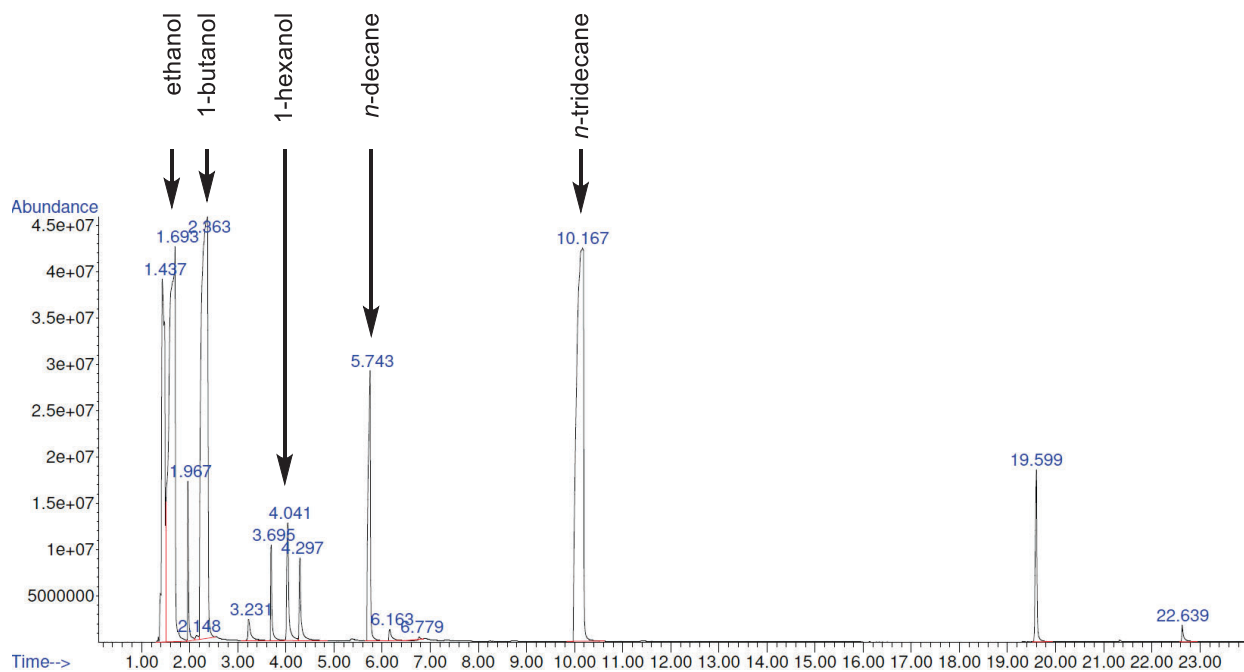


Figure 9.41: Example of a gas chromatography spectrum of a reaction mixture.

x-Axis in minutes, abundance in arbitrary units.

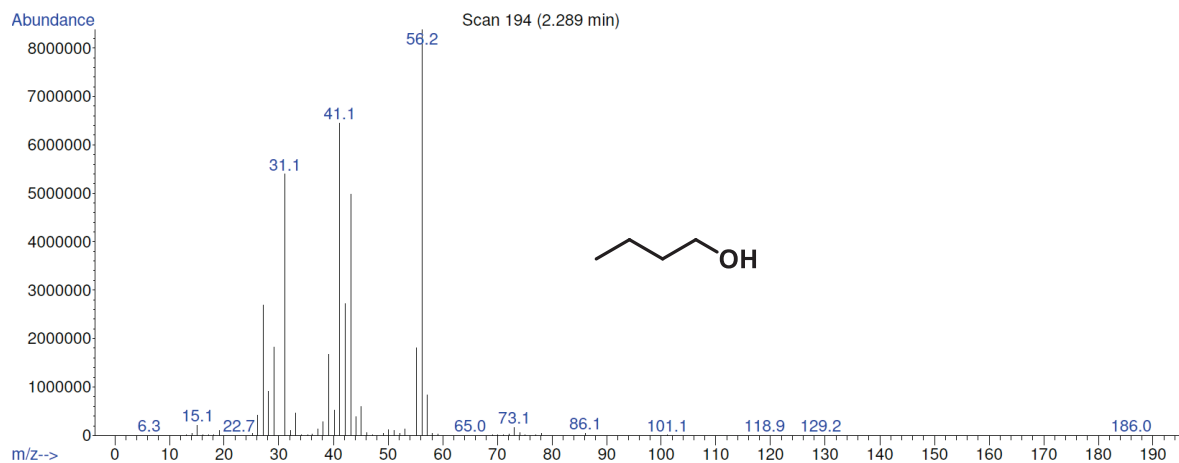


Figure 9.42: Mass spectrum of 1-butanol.

Typical retention time 2.3 minutes.

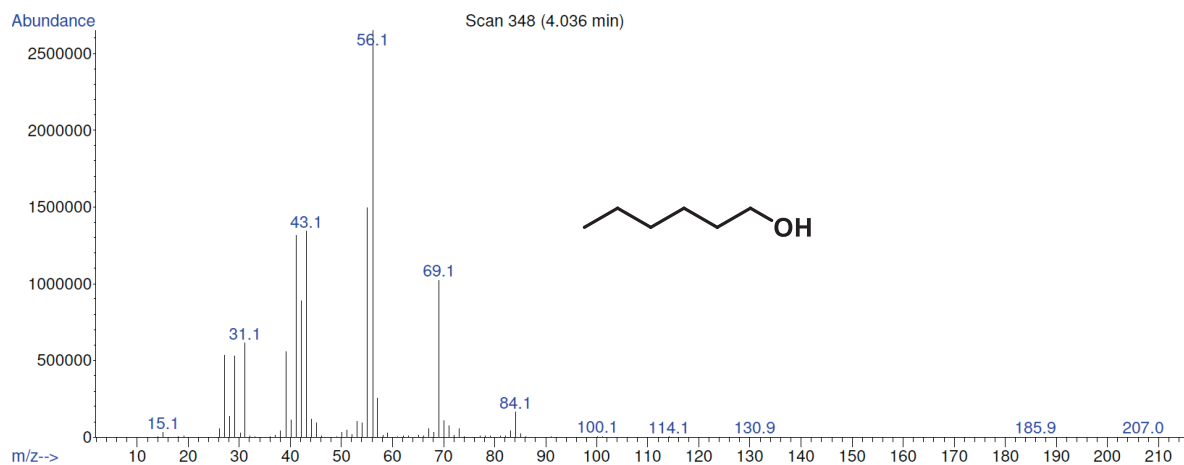


Figure 9.43: Mass spectrum of 1-hexanol.

Typical retention time 4.0 minutes

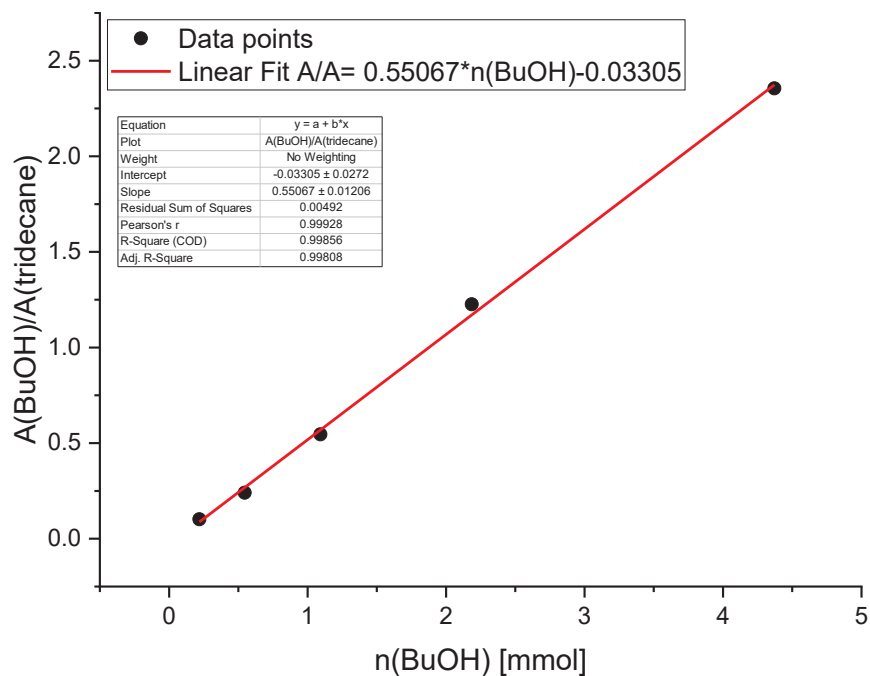
D1.2 Calibration curves

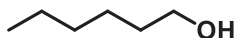
1-Butanol

 $d = 0.81 \text{ g/mL}$ $M = 74.12 \text{ g/mol}$

V(BuOH)[μL]	m(BuOH) [mg]	n (BuOH) [mmol]	A (BuOH) [a.u.]	A (tridecane) [a.u.]	A / A
20	16.2	0.21856449	737.731	7242.859	0.101856325
50	40.5	0.546411225	1750.521	7284.738	0.240299788
100	81.0	1.09282245	3430.488	6287.339	0.545618425
200	162	2.1856449	7747.831	6321.005	1.225728682
400	324	4.3712898	15502.005	6582.651	2.35497902

$$\frac{A_{\text{BuOH}}}{A_{\text{tridecane}}} = 0.55067 \times n_{\text{BuOH}} - 0.03305$$



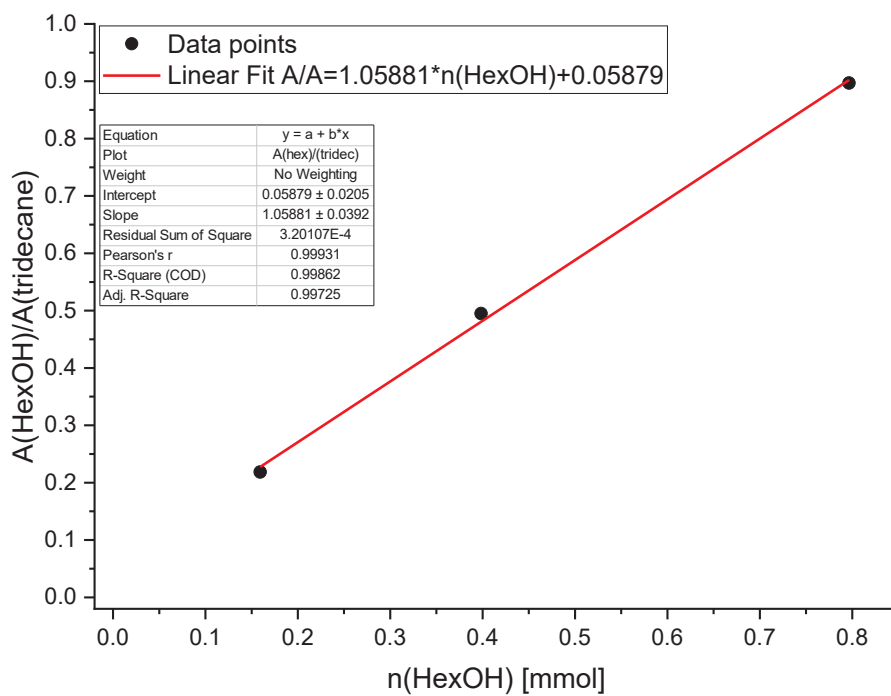
1-Hexanol

$d = 0.814 \text{ g/mL}$

$M = 102.18 \text{ g/mol}$

V(HexOH) [μL]	m(HexOH) [mg]	n (HexOH) [mmol]	A (HexOH) [a.u.]	A (tridecane) [a.u.]	A / A
20	16.28	0.159326678	1593.3	7293.6	0.218451793
50	40.7	0.398316696	3657.4	7338.8	0.494992421
100	81.4	0.796633392	6406.5	7143.3	0.896854395

$$\frac{A_{\text{HexOH}}}{A_{\text{tridecane}}} = 1.0588 \times n_{\text{HexOH}} + 0.05879$$



D2 General procedure for ethanol upgrading reactions

In an inert gas glovebox, the reactors, equipped with a matching teflon cup, and stir bar, were charged with the reactants (catalyst, base). The bottom reactor half was sealed (glass cap and secured with self-vulcanizing tape for reactor type A; sealed plastic zip-lock bag for reactor type B). It was transferred to an inert gas glove bag (*Aldrich, AtmosBag*) attached to a Schlenk line and equipped with a Straus flask containing degassed and water-free ethanol, a high precision syringe and the top reactor half. The glove bag was sealed, evacuated, and inflated with argon. This was repeated three times. The reactor was unsealed, and the ethanol was injected via syringe. The top reactor half was screwed on and secured.

After the desired reaction time, the autoclave reactions were allowed to room temperature. Any gas overpressures were slowly and carefully released into the atmosphere. The reactors were unsealed. Dichloromethane (15 mL) was added for dilution purposes. *n*-Tridecane (100 μ L) and *n*-decane (20 μ L) were injected via precision pipette as internal standards. The solutions were passed through a syringe filter and analyzed via GC-FID and GC-MS. The amounts of 1-butanol and 1-hexanol were calculated according to the calibration curves discussed previously.

The yields were calculated the following way:

$$Yield_{BuOH} = \frac{n_{BuOH}}{n_{EtOH}} \times 2$$

$$Yield_{HexOH} = \frac{n_{HexOH}}{n_{EtOH}} \times 3$$

For the TONs, it was assumed that the catalyst would perform 4 catalytic cycles per molecule of 1-butanol, and 6 cycles per molecule of 1-hexanol. In cases where only traces of 1-hexanol were found, it was not included in the TON ($n_{HexOH}=0$), as the calibration curve proved too imprecise for very low amounts of product.

$$TON = \frac{n_{BuOH}}{n_{catalyst}} \times 4 + \frac{n_{HexOH}}{n_{catalyst}} \times 6$$

$$TOF = \frac{TON}{t}$$

D3 Ethanol upgrading experiments

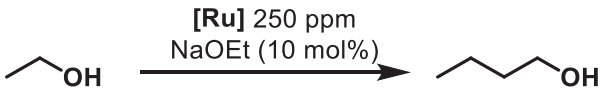
Table 9.1: Catalyst screening

$ \text{CH}_3\text{CH}_2\text{OH} \xrightarrow[\text{120 } ^\circ\text{C, 48 h}]{\text{[Ru] 250 ppm, NaOEt (10 mol\%)}} \text{CH}_3\text{CH}_2\text{CH}_2\text{CH}_2\text{OH} $				
Catalyst	Yields [%]		TON	TOF (h ⁻¹)
	1-BuOH	1-HexOH		
No catalyst	not found	not found	---	---
Ru-1a	2.33	0.42	156	3.2
Ru-2a	15.1	0.22	1224	25.5
Ru-3a	12.1	0.57	1014	21.1
Ru-4a	8.91	traces	713	14.8
Ru-5a	4.28	traces	343	7.1
Ru-6a	7.65	not found	612	12.7
Ru-7a	11.6	not found	927	19.3
Ru-8a	4.89	traces	391	8.1
Ru-9a	3.98	traces	318	6.6

Conditions: 2.50 mL (42.8 mmol) EtOH, 291 mg (4.28 mmol) NaOEt, 10.7 μmol (250 ppm) catalyst, 120 $^\circ\text{C}$ 48 h, reactor type A, 600 rpm.

Appendix D. Chapter 3

Table 9.2: Temperature and time screenings.

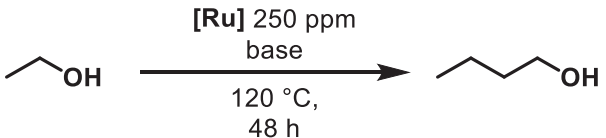
<div>  </div>						
Catalyst	Temperature [°C]	Time [h]	Yields [%]		TON	TOF (h ⁻¹)
			1-BuOH	1-HexOH		
Ru-1a	90	48	0.70	traces	100	2.1
Ru-1a	120	48	2.33	0.42	156	3.2
Ru-1a	150	48	8.79	0.16	717	14.9
Ru-2a	90	48	0.52	not found	68	0.5
Ru-2a	90	96	1.28	not found	102	1.1
Ru-2a	120	24	10.7	0.44	893	37.2
Ru-2a	120	48	15.1	0.22	1224	25.5
Ru-2a	120	96	13.7	0.35	1124	11.7
Ru-2a	150	48	4.73	traces	378	7.9
Ru-3a	120	48	12.1	0.57	1014	21.1
Ru-3a	120	96	10.6	0.31	870	9.1
Ru-4a	120	48	8.91	traces	713	14.8
Ru-4a	120	96	20.0	1.53	1720	17.9
Ru-4a	150	48	13.5	traces	1080	22.5
Ru-7a	120	48	11.6	not found	927	19.3
Ru-7a	150	48	9.86	traces	789	16.4
Ru-9a	120	48	3.98	traces	318	6.6
Ru-9a	150	48	4.59	traces	368	7.7

Conditions:

90 and 120 °C: 2.50 mL (42.8 mmol) EtOH, 291 mg (4.28 mmol) NaOEt, 10.7 μmol (250 ppm) catalyst, reactor type A, 600 rpm.

150 °C: 1.25 mL (21.4 mmol) EtOH, 146 mg (21.4 mmol) NaOEt, 5.35 μmol (250 ppm) catalyst, reactor type B, 600 rpm.

Table 9.3: Base screenings at 120 °C.

<div style="text-align: center;">  </div>						
Catalyst	Base	Base equivalent (%)	Yields [%]		TON	TOF (h ⁻¹)
			1- BuOH	1-HexOH		
Ru-1a	LiOEt	10%	3.74	not found	299	6.2
Ru-1a	NaOEt	10%	2.33	0.42	156	3.2
Ru-2a	No base	---	traces	not found	---	---
Ru-2a	LiOEt	10%	9.32	0.15	758	15.8
Ru-2a	NaOEt	10%	15.1	0.22	1224	25.5
Ru-2a	NaOEt	20%	13.0	0.67	1095	22.8
Ru-2a	NaOtBu	10%	8.47	traces	682	14.2
Ru-2a	KOtBu	10%	28.2	1.56	2382	49.6
Ru-3a	LiOEt	10%	11.0	0.10	889	18.5
Ru-3a	NaOEt	10%	12.1	0.57	1014	21.1
Ru-3a	NaOtBu	10%	7.90	0.11	640	13.3
Ru-3a	KOtBu	10%	8.70	0.90	768	16.0

Conditions: 2.50 mL (42.8 mmol) EtOH, 10.7 μmol (250 ppm) catalyst, 120 °C 48 h, reactor type A, 600 rpm.

D4 Stoichiometric NMR experiments

Reaction of **Ru-2a** with NaOEt in ethanol- d_6

In an inert gas glovebox, **Ru-2a** (1.0 eq.) and NaOEt (10 eq.) were suspended in ethanol- d_6 and injected into a J-Young NMR tube. ^1H , $^{31}\text{P}\{^1\text{H}\}$ and ^2H experiments were run at 25 °C and 60 °C on a 400 MHz NMR magnet.

Attempts at recrystallization from the reaction mixture are as of yet unsuccessful.

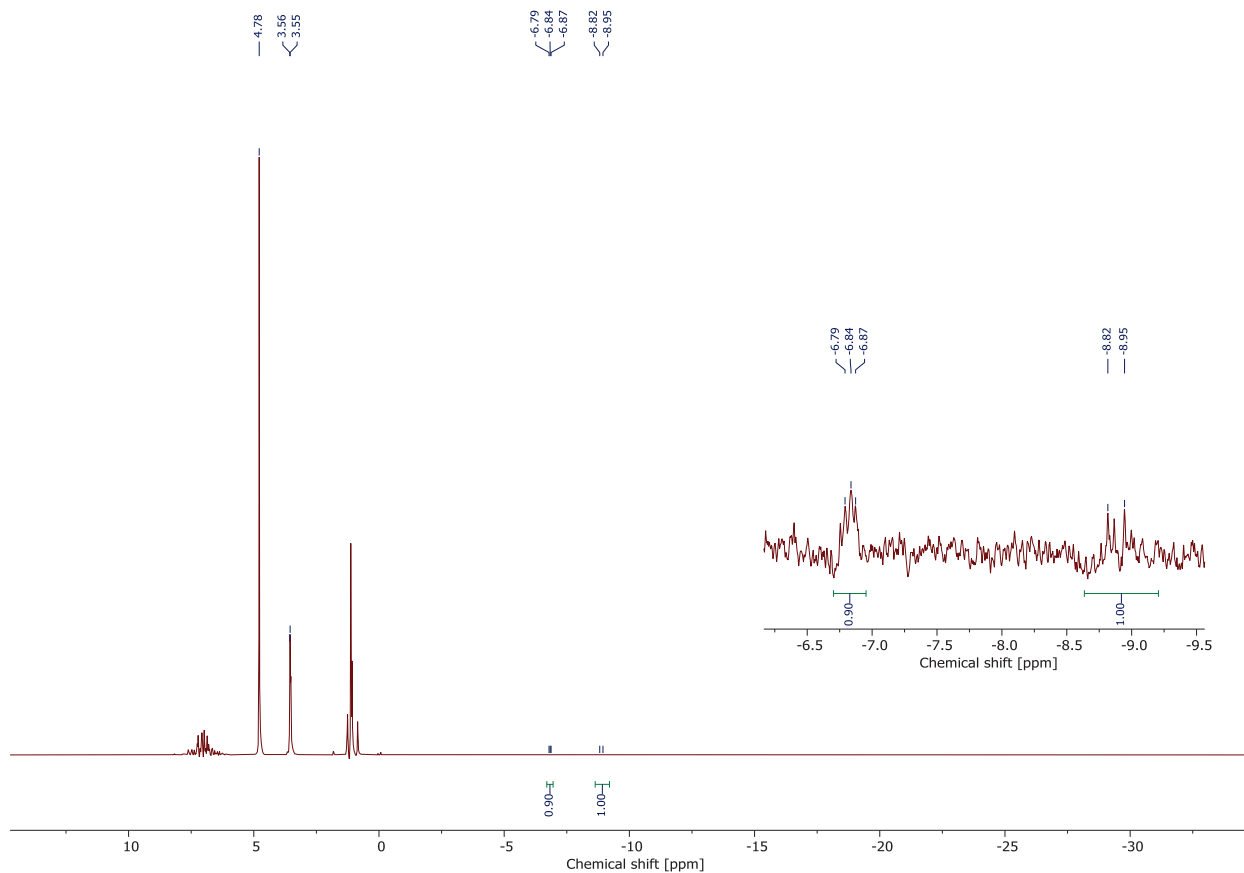


Figure 9.44: 400 MHz ^1H NMR spectrum of the reaction of **Ru-2a** with NaOEt in ethanol- d_6 at 333 K (60 °C).

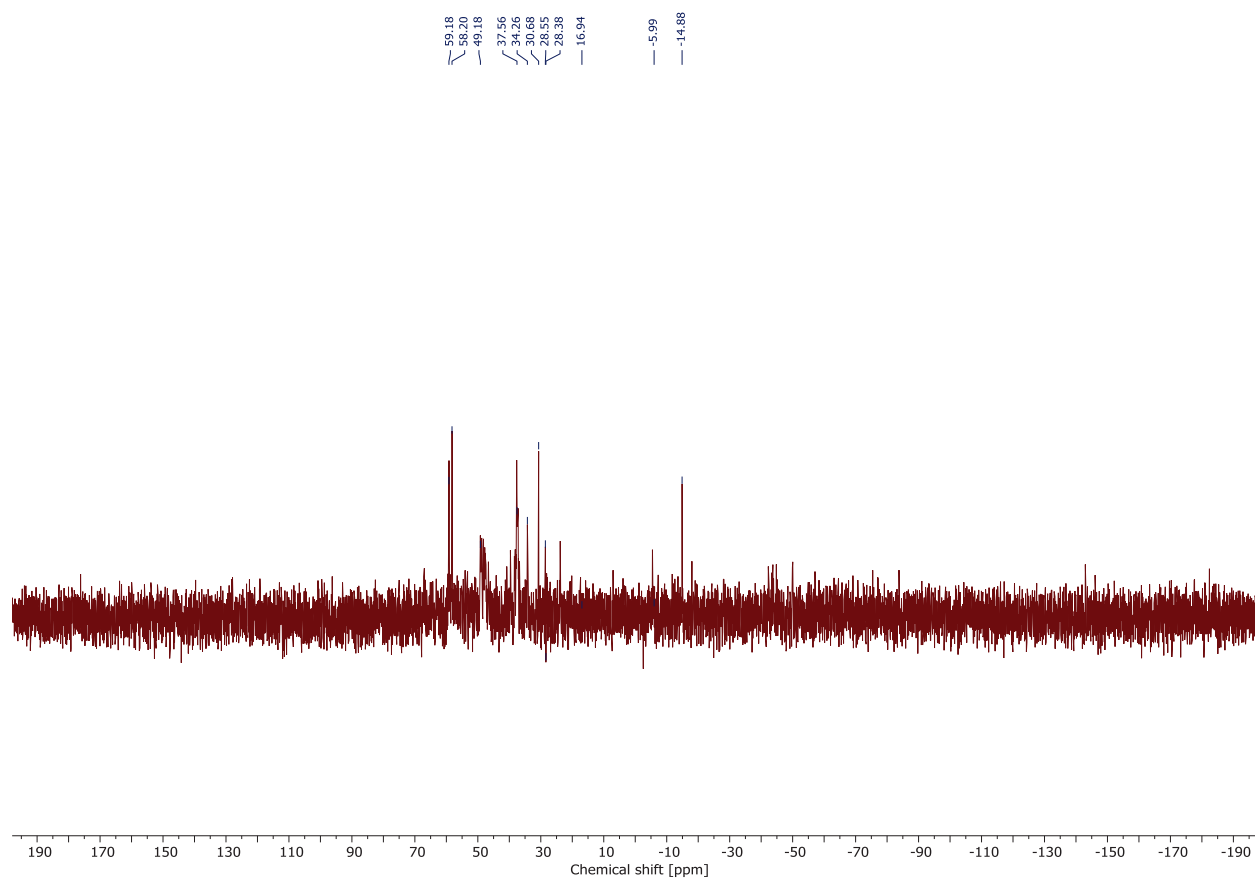


Figure 9.45: 162 MHz $^{31}\text{P}\{^1\text{H}\}$ NMR spectrum of the reaction of **Ru-2a** with NaOEt in ethanol- d_6 at 333 K (60 °C).

Reaction of **Ru-2a** with NaOEt in THF

In an inert gas glovebox, a 20 mL vial was charged with **Ru-2a** (13.0 mg, 13.8 μmol , 1.00 eq.), NaOEt (1.0 mg, 14.5 μmol , 1.05 eq) and THF- d_8 (1.0 mL). The mixture was stirred at room temperature overnight, filtered through a GFB syringe filter and sealed in a J-Young NMR tube.

Attempts at recrystallization from the reaction mixture are as of yet unsuccessful.

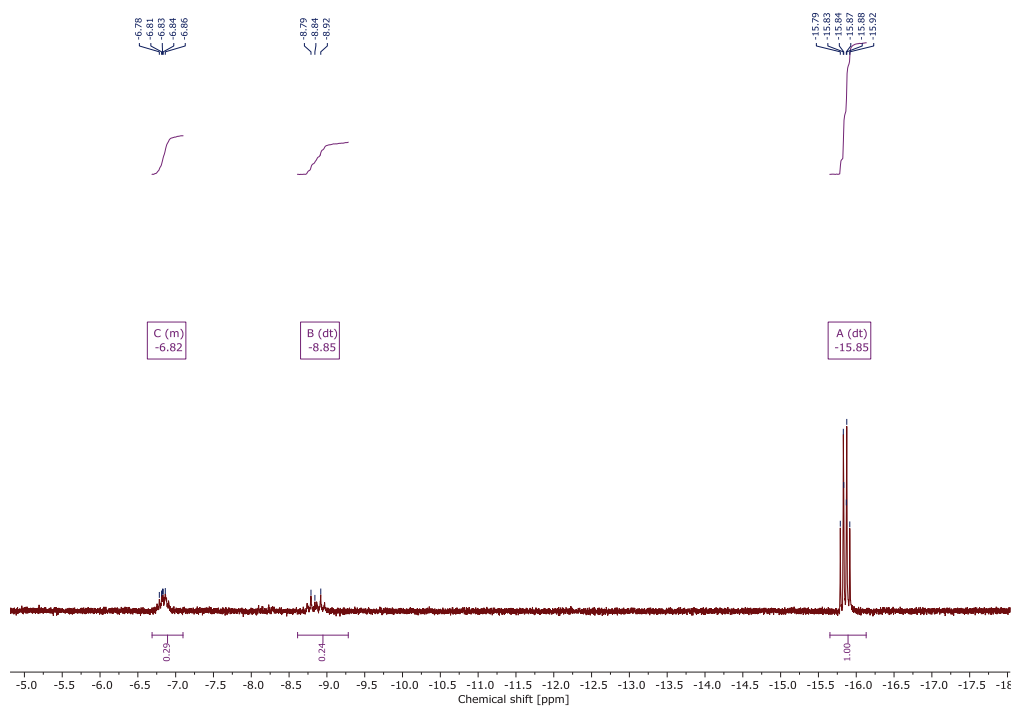


Figure 9.46: 600 MHz ^1H NMR spectrum of a reaction of Ru-2a with EtOAc in THF- d_8 .

Appendix E. Chapter 4

E1 General procedure for formic acid dehydrogenation in ionic liquid

In an inert gas glovebox, a 50 mL two-neck flask equipped with a stir bar was charged with the catalyst, sealed with two rubber septa and brought outside. It was attached under constant gas flow to a small straight reflux condenser. The ionic liquid (1.0 mL) was injected through the second septum. Slight constant argon flow was kept throughout the entire experiment. The ionic liquid was swirled around until all catalyst powder was in contact with it, and the setup was slowly warmed in an oil bath to the desired temperature under constant stirring. Stirring was continued until complete solution of the catalyst was observed, but at least for 10 minutes at which point formic acid (0.5 mL) was injected via syringe through the septum. At given intervals, small samples of the solution were taken using a syringe and dissolved in MeCN- d_3 for NMR analysis. In the case of recycling experiments, new formic acid was injected via syringe and the reaction was repeated.

To calculate conversions, the ^1H NMR signal of the methyl group on the BMIM cation (peak e in Figure 9.47) was integrated to three times the molar amount of BMIM. Then, the formate signal was integrated, and divided by the injected amount of formic acid. An example of this can be found below.

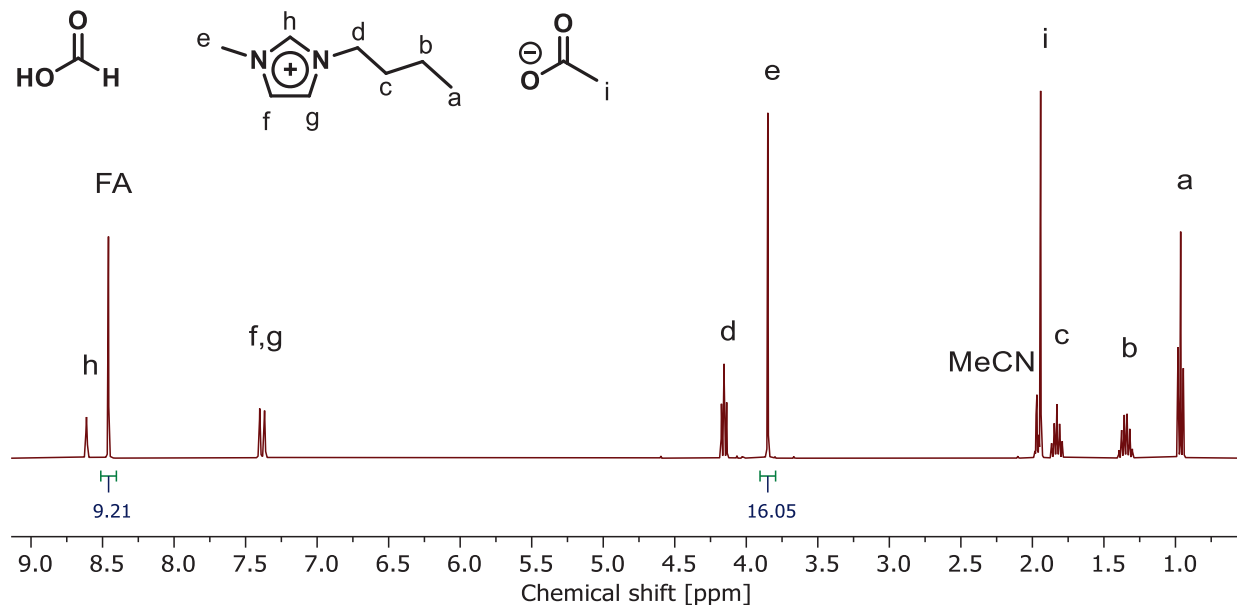


Figure 9.47: ^1H NMR of FA, BMIM-OAc and catalyst in MeCN- d_3 .

Relevant integrals of FA and N- CH_3 group of BMIM (peak e) in mmol.

E2 Formic acid dehydrogenation experiments

The turnover frequencies were calculated using the following formula:

$$TOF = \frac{n (FA)}{n (catalyst)} \times conversion \times \frac{1}{t [h]}$$

For the time of TOF_{max} , the timeframe was chosen in which the conversion per unit time was highest (i.e. where the graph between two datapoints was the steepest). Conversions and times were then taken as the differences between those two datapoints.

ARRHENIUS activation energies were calculated using the following equations according to the protocol used by BELLER:⁴⁷

$$k = A \times e^{\frac{-E_A}{RT}}$$

$$\ln(k) = -\frac{E_A}{RT} + \ln(A)$$

$$E_A = -R \times slope$$

$$R = 8.314 \frac{J}{mol K}$$

Table 9.4: Temperature screening of $[RuHCl(PPh_3)_3]$ toluene adduct.

$ \begin{array}{c} \text{O} \\ \parallel \\ \text{H}-\text{C}-\text{OH} \end{array} \xrightarrow[\text{BMIM-OAc, 60-90 } ^\circ\text{C, 3 h}]{[RuHCl(PPh_3)_3] \cdot \text{toluene}} \text{H}_2 + \text{CO}_2 $						
T [$^\circ\text{C}$]	Conversion [%]					TOF_{max} [h^{-1}] (t [min])
	10 min	30 min	60 min	120 min	180 min	
90	56	78	87	94	97	3424 (10)
80	24	51	72	84	91	1467 (10)
70	18	43	65	81	88	1101 (10)
60	6	29	40	59	65	703 (30-10)*

Conditions: 0.5 mL (13.25 mmol) formic acid, 1.0 mL (5.35 mmol) BMIM-OAc, (13.0 μmol) catalyst.

*TOF calculated in the timeframe between two data points with the steepest conversion slope.

Table 9.5: ARRHENIUS plot data of FA dehydrogenation using $[\text{RuHCl}(\text{PPh}_3)_3]^+\text{toluene}$.

T [°C]	1/T [K ⁻¹]	TOF [h ⁻¹]	ln (TOF)
90	0.00275	3424	8.13856
80	0.00283	1467	7.29097
70	0.00291	1101	7.00397
60	0.003	703	6.55536

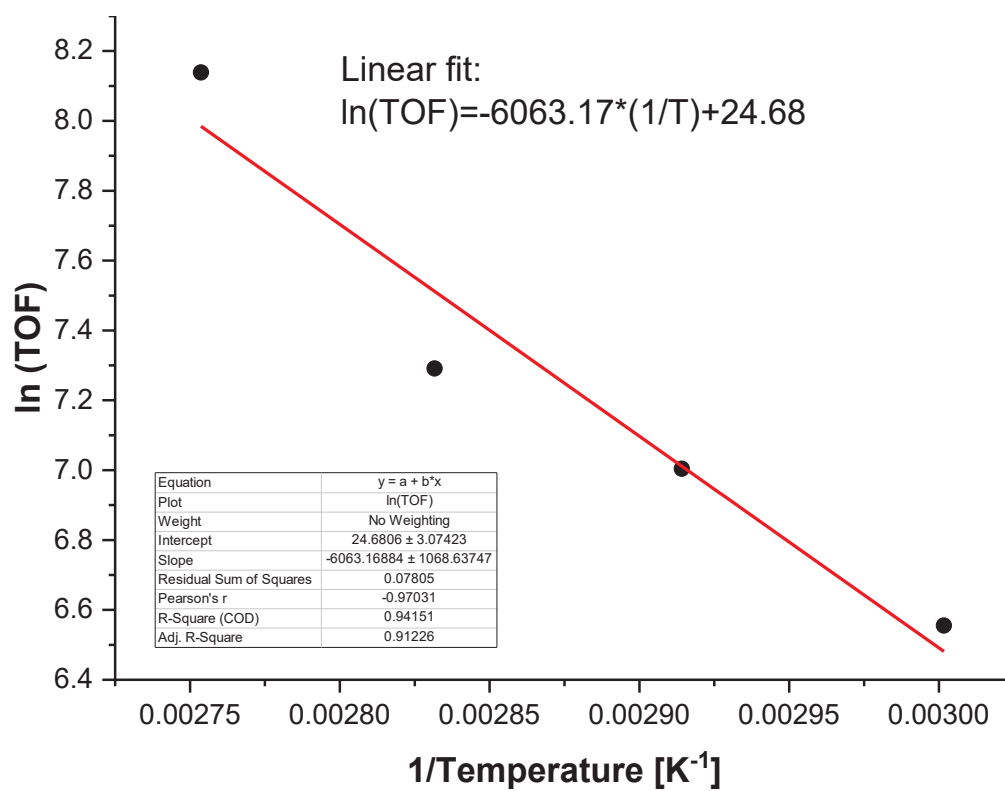


Figure 9.48: ARRHENIUS plot of FA dehydrogenation using $[\text{RuHCl}(\text{PPh}_3)_3]^+\text{toluene}$.

$$\text{Slope} = -6063.17$$

$$E_A = 50.4 \text{ kJ/mol}$$

Table 9.6: Screening of ruthenium catalysts for FA dehydrogenation.

$\text{H}-\text{C}(=\text{O})-\text{OH} \xrightarrow[\text{BMIM-OAc, 90 } ^\circ\text{C, 3 h}]{[\text{Ru}]} \text{H}_2 + \text{CO}_2$						
Complex	Conversion [%]					TOF _{max} [h ⁻¹] (t [min])
	10 min	30 min	60 min	120 min	180 min	
Precursor	56	78	87	94	97	3424 (10)
Ru-1a	74	90	93	96	98	4525 (10)
Ru-2a	27	43	71	80	84	1651 (10)
Ru-3a	15	83	92	96	97	1692 (10)
Ru-4a	---	88	94	98	---	1794 (30)
Ru-5a	25	87	93	94	95	1896 (30-10)*
Ru-6a	20	77	89	97	98	1570 (10)
Ru-7a	0	29	87	91	93	1182 (60-30)*
Ru-8a	60	89	99	---	---	3669 (10)
Ru-9a	18	25	50	84	92	1101 (10)
Ru-10a	11	66	77	93	95	1345 (10)

Conditions: 0.5 mL (13.25 mmol) formic acid, 1.0 mL (5.35 mmol) BMIM-OAc, 90 °C, 13.0 μmol catalyst.

*TOF calculated in the timeframe between two data points with the steepest conversion slope.

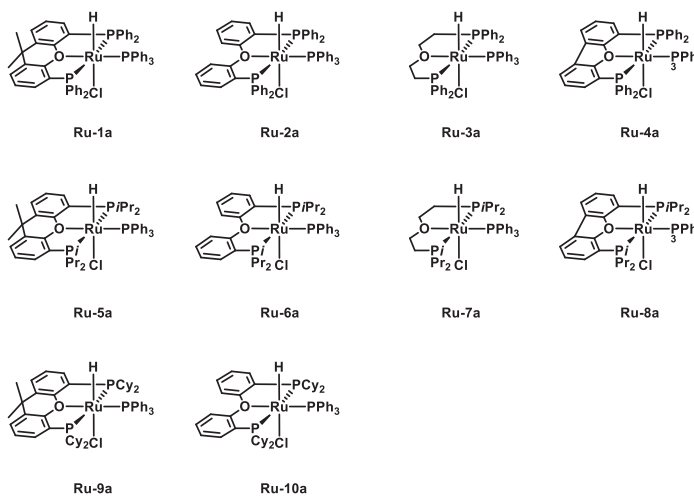


Table 9.7: Temperature screening of **Ru-1a**.

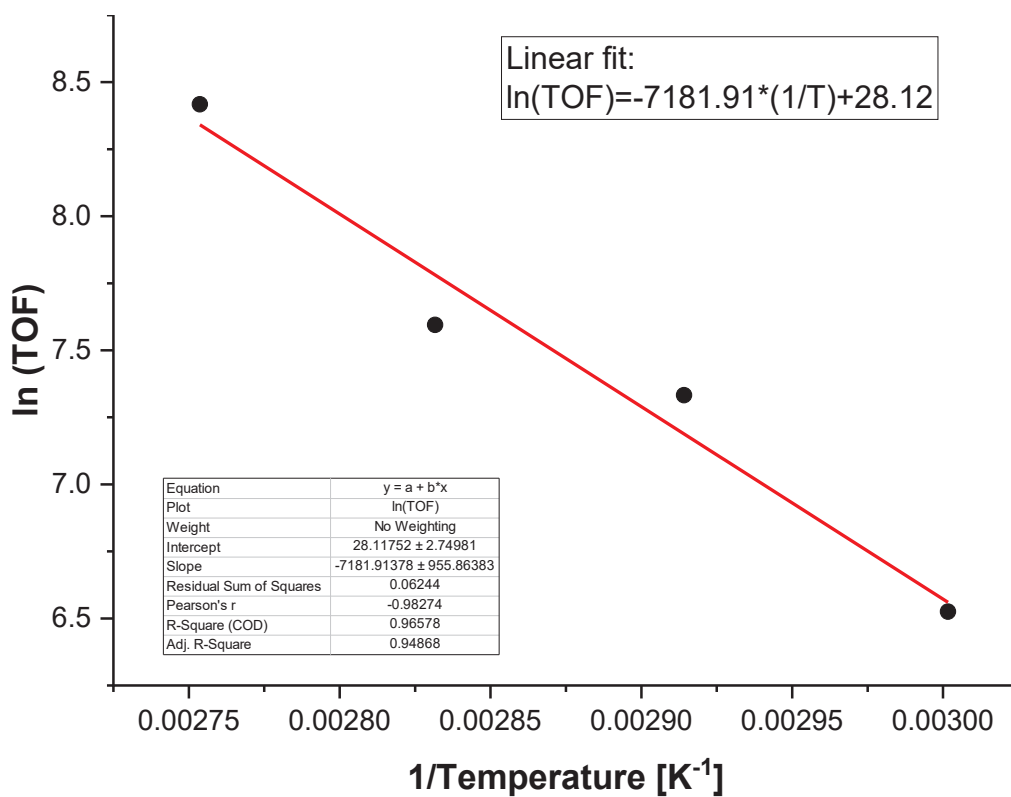
<div style="display: flex; align-items: center; justify-content: space-around;"> <div style="text-align: center;"> </div> <div style="text-align: center;"> </div> <div style="text-align: center;"> Ru-1a </div> </div>						
T [°C]	Conversion [%]					TOF _{max} [h ⁻¹] (t [min])
	10 min	30 min	60 min	120 min	180 min	
90	74	90	93	96	98	4525 (10)
80	14	79	87	92	96	1988 (30-10)*
70	23	73	85	90	---	1529 (30-10)*
60	0	0	12	79	83	682 (120-60)*

Conditions: 0.5 mL (13.25 mmol) formic acid, 1.0 mL (5.35 mmol) BMIM-OAc, 13.0 μmol catalyst.

*TOF calculated in the timeframe between two data points with the steepest conversion slope.

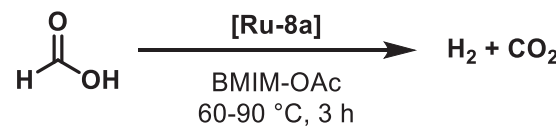
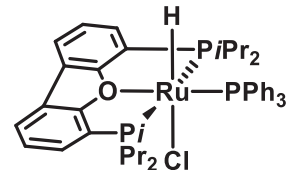
Table 9.8: ARRHENIUS plot data of FA dehydrogenation using **Ru-1a**.

T [°C]	1/T [K ⁻¹]	TOF [h ⁻¹]	ln (TOF)
90	0.00275	4525	8.41737
80	0.00283	1988	7.59488
70	0.00291	1529	7.33237
60	0.003	682	6.52503

Figure 9.49: ARRHENIUS plot of FA dehydrogenation using **Ru-1a**.

$$\text{Slope} = -7181.91$$
$$E_A = 59.7 \text{ kJ/mol}$$

Table 9.9: Temperature screening of **Ru-8a**.

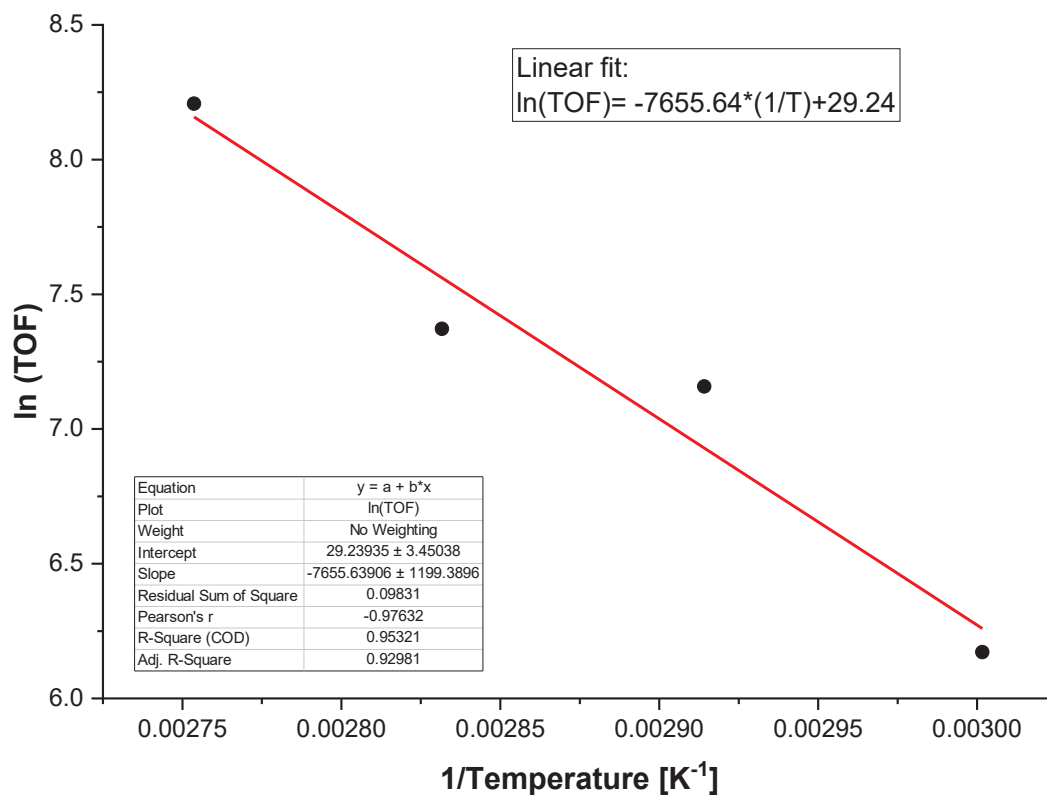
<div style="display: flex; align-items: center; justify-content: space-around;"> <div style="text-align: center;">  </div> <div style="text-align: center;">  </div> <div style="text-align: center;"> Ru-8a </div> </div>						
T [°C]	Conversion [%]					TOF _{max} [h ⁻¹] (t [min])
	10 min	30 min	60 min	120 min	180 min	
90	60	89	99	---	---	3669 (10)
80	24	76	83	92	96	1590 (30-10)*
70	0	42	80	86	86	1284 (30-10)*
60	0	9	31	78	79	479 (120-60)*

Conditions: 0.5 mL (13.25 mmol) formic acid, 1.0 mL (5.35 mmol) BMIM-OAc, 13.0 μmol catalyst.

*TOF calculated in the timeframe between two data points with the steepest conversion slope.

Table 9.10: ARRHENIUS plot of FA dehydrogenation using **Ru-8a**.

T [°C]	1/T [K ⁻¹]	TOF [h ⁻¹]	ln (TOF)
90	0.00275	3669	8.20767
80	0.00283	1590	7.37149
70	0.00291	1284	7.15774
60	0.003	479	6.1717

Figure 9.50: ARRHENIUS plot of FA dehydrogenation using **Ru-8a**.

$$\text{Slope} = -7655.64$$

$$E_A = 63.7 \text{ kJ/mol}$$

Table 9.11: Anion screening of **Ru-8a-c**.

$\text{H}-\text{C}(=\text{O})-\text{OH} \xrightarrow[\text{BMIM-OAc, 70 } ^\circ\text{C, 3 h}]{[\text{Ru-8a-d}]} \text{H}_2 + \text{CO}_2$						
Complex	Conversion [%]					TOF _{max} [1/h] (t [min])
	10 min	30 min	60 min	120 min	180 min	
Ru-8a	0	42	80	86	86	1284 (30-10)*
Ru-8b	2	31	71	81	86	887 (30-10)*
Ru-8c	3	53	74	87	90	1528 (30-10)*

Conditions: 0.5 mL (13.25 mmol) formic acid, 1.0 mL (5.35 mmol) BMIM-OAc, 13.0 μmol complex.

*TOF calculated in the timeframe between two data points with the steepest conversion slope.

E3 Reaction mechanism investigations

Attempted dehydrogenation of neat formic acid

In an inert gas glovebox, a 50 mL two-neck flask equipped with a stir bar was charged with the catalyst, sealed with two rubber septa and brought outside. It was attached under constant gas flow to a small straight reflux condenser. The flask was heated to 90 °C in an oil bath for 15 minutes, at which point formic acid was injected via syringe. The progress of the reaction was observed by following gas formation. No gas formation was detected.

NMR reaction of catalyst with BMIM-OAc

A J-Young NMR tube with a sealed glass inlet containing MeCN-d₃ for the purpose of NMR solvent locking was charged with **Ru-1a** and BMIM-OAc. The reaction mixture was degassed by carefully applying vacuum three times followed by argon. It was then slowly warmed up to 40 °C using an oil bath overnight, during which complete dissolution occurred.

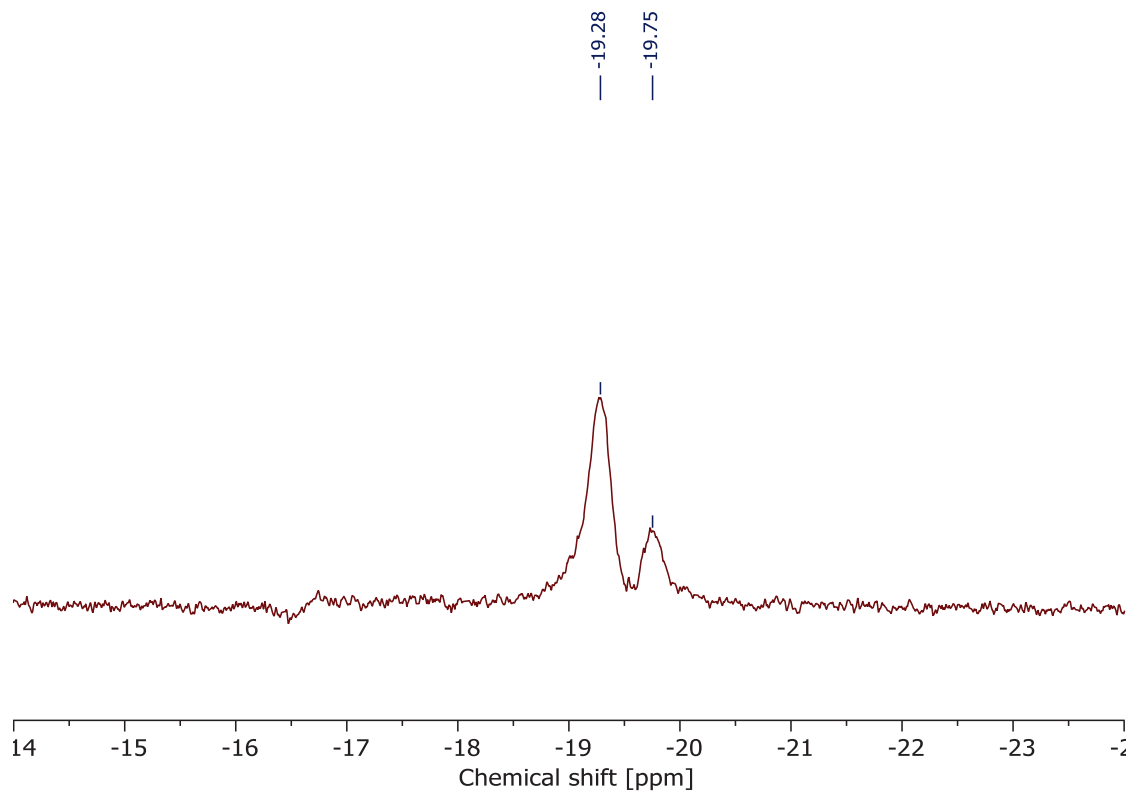


Figure 9.51: 400 MHz ¹H NMR spectrum of **Ru-1a** in BMIM-OAc at 25 °C.

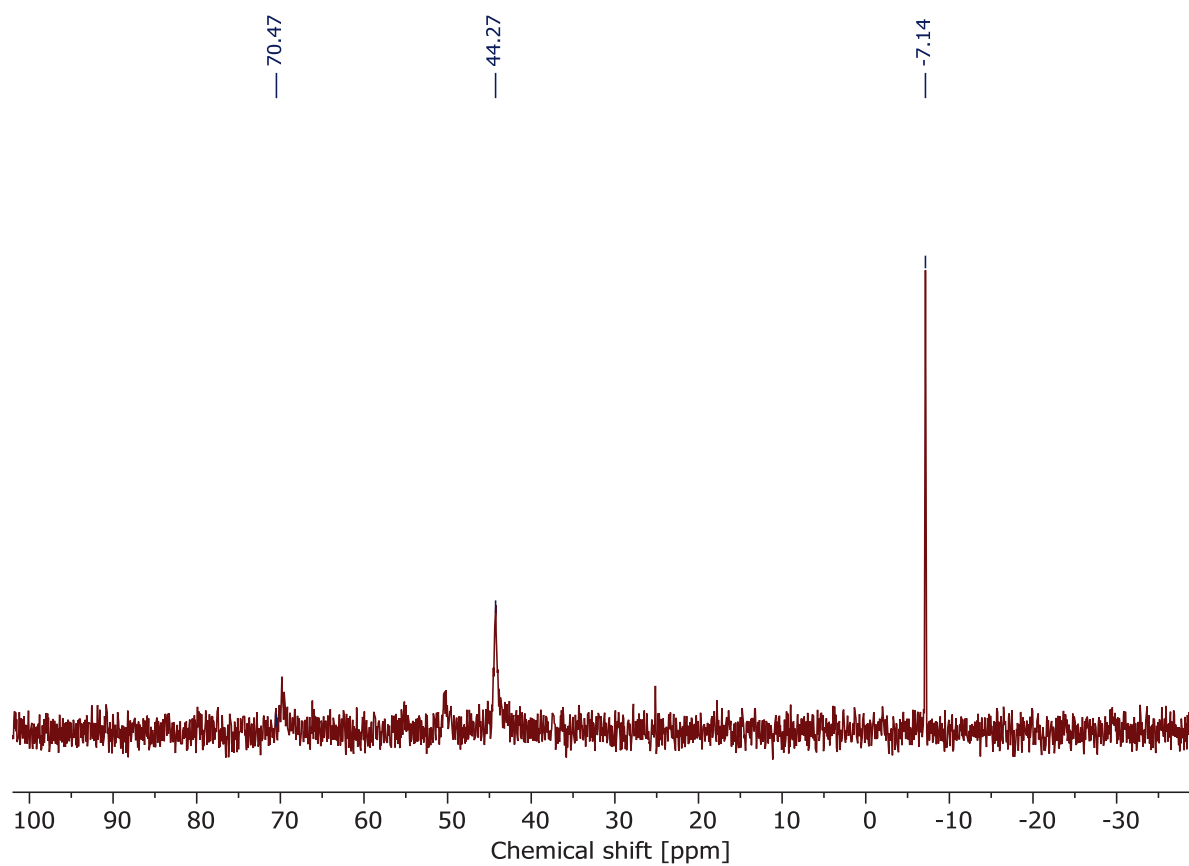
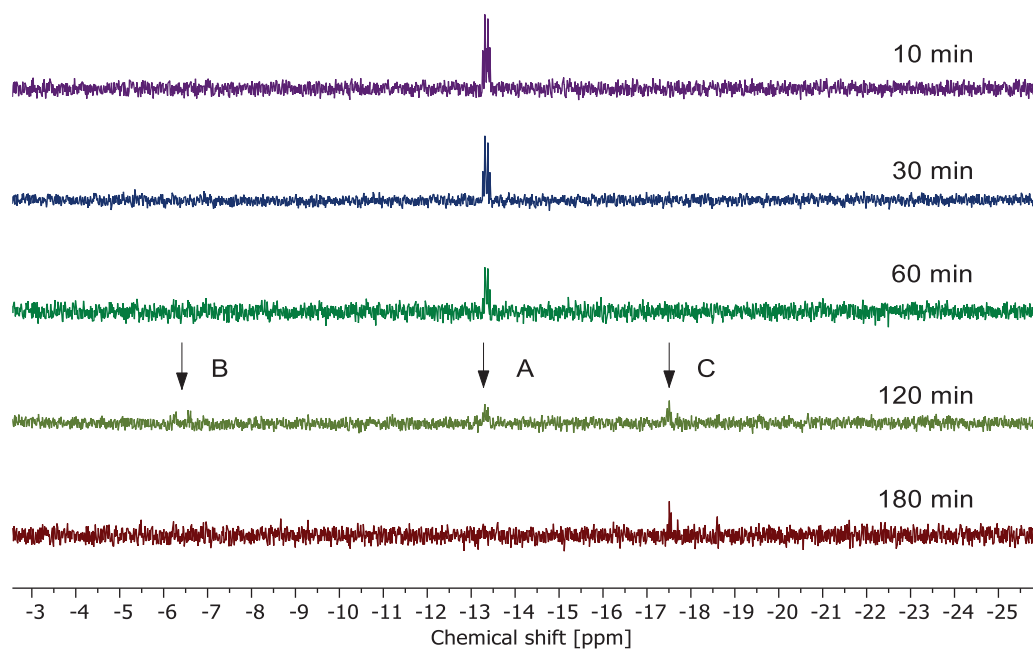
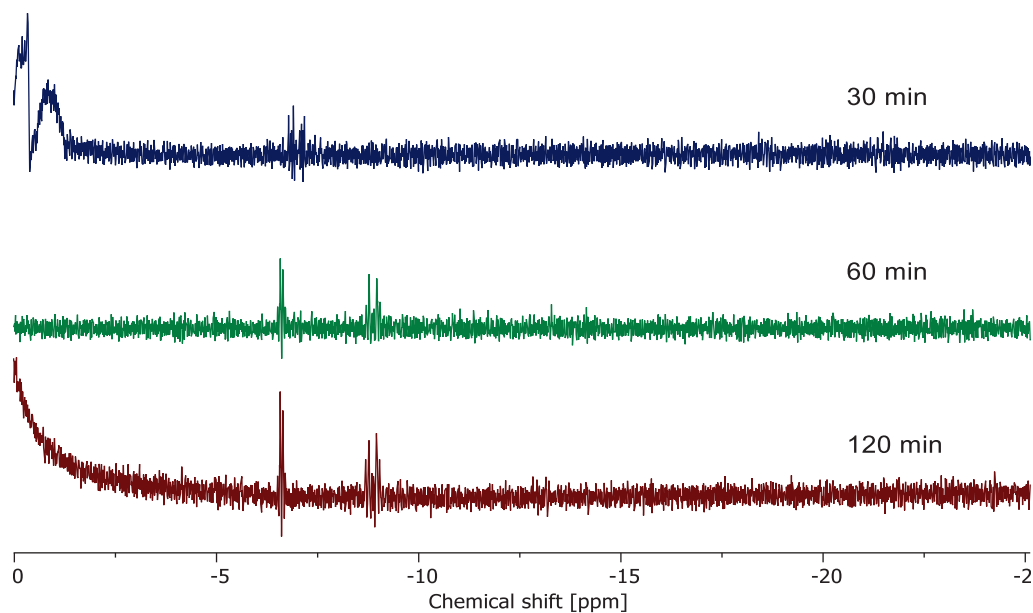
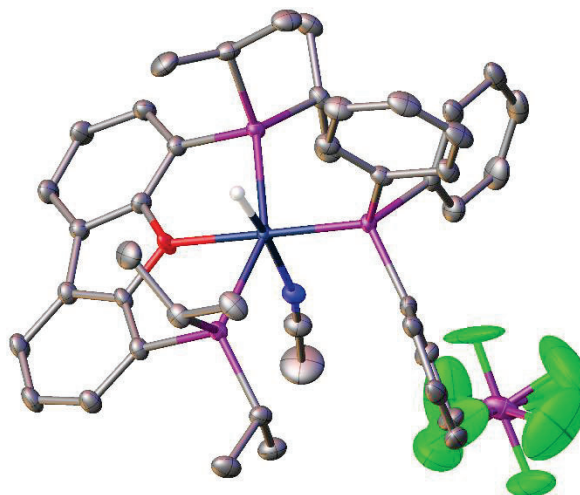
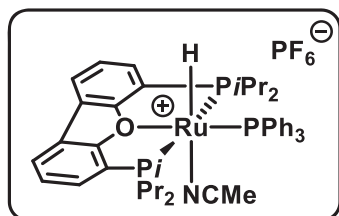
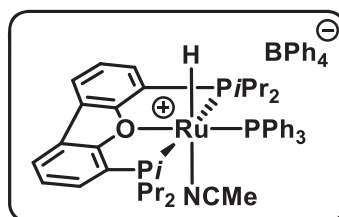


Figure 9.52: 162 MHz ^{31}P NMR spectrum of **Ru-1a** in BMIM-OAc at 25 °C.

Monitoring of hydride region in FA dehydrogenation experimentsFigure 9.53: Hydride region of the ^1H NMR spectrum of FA dehydrogenation using **Ru-1a**.Figure 9.54: Hydride region of the ^1H NMR spectrum of FA dehydrogenation using **Ru-2a**.

E4 Synthesis of $[\text{RuH}(i\text{Pr-DBFphos})(\text{PPh}_3)(\text{MeCN})]\text{X}$ $[\text{RuH}(i\text{Pr-DBFphos})(\text{PPh}_3)(\text{MeCN})]\text{PF}_6$ **Ru-8c**

In a 20 mL vial equipped with stir bar, **Ru-8a** (40 mg, 50.0 μmol , 1.00 eq.) and KPF_6 (9.7 mg, 52.5 μmol , 1.05 eq.) were dissolved in 10 mL MeCN and stirred at room temperature overnight. Precipitation of NaCl was observed. Upon completion, the solution was filtered through a GFB filter and dried in vacuo to obtain the product as a yellow crystalline solid (99%). Crystals of sufficient quality for XRD can be grown by crystallization from MeCN/diethyl ether by layering in an NMR tube at room temperature.

 $[\text{RuH}(i\text{Pr-DBFphos})(\text{PPh}_3)(\text{MeCN})]\text{BPh}_4$ **Ru-8d**

In a 20 mL vial equipped with stir bar, **Ru-8a** (11.1 mg, 13.8 μmol , 1.00 eq.) and NaBPh_4 (5.0 mg, 14.6 μmol , 1.05 eq.) were dissolved in 10 mL MeCN and stirred at room temperature overnight. Precipitation of NaCl was observed. Upon completion, the solution was filtered through a GFB filter and dried in vacuo to obtain the product as a yellow solid (23 mg, 99%). As of yet, no crystals of sufficient quality for XRD could be obtained.

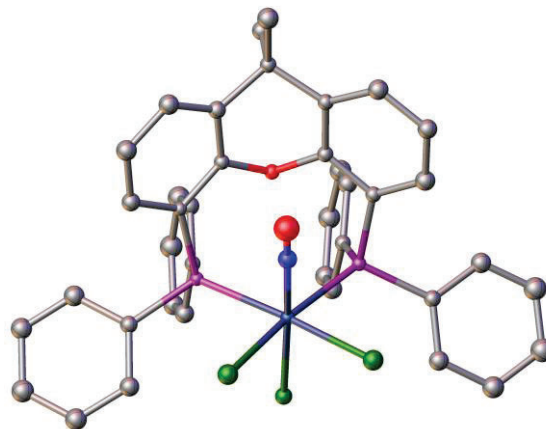
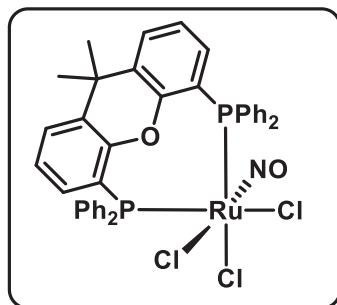
E5 Crystallographic data

Compound name	[RuH(<i>i</i> Pr-dbfphos)(PPh ₃) (MeCN)]PF ₆ *MeCN Ru-8c
Empirical formula	C ₄₆ H ₅₆ F ₆ N ₂ OP ₄ Ru
Formula weight	991.87
Temperature/K	120.00(10)
Crystal system	monoclinic
Space group	P2 ₁ /m
a/Å	12.21500(10)
b/Å	14.50940(10)
c/Å	13.61830(10)
α /°	90
β /°	102.4080(10)
γ /°	90
Volume/Å ³	2357.23(3)
Z	2
$\rho_{\text{calc}}/\text{cm}^3$	1.397
μ/mm^{-1}	4.482
F(000)	1024.0
Crystal size/mm ³	? × ? × ?
Radiation	Cu K α (λ = 1.54184)
2 Θ range for data collection/°	7.41 to 153.29
Index ranges	-15 ≤ h ≤ 15, -18 ≤ k ≤ 18, -16 ≤ l ≤ 1748270
Reflections collected	48270
Independent reflections	5165 [R _{int} = 0.0374, R _{sigma} = 0.0159]
Data/restraints/parameters	5165/0/313
Goodness-of-fit on F ²	1.073
Final R indexes [I >= 2 σ (I)]	R ₁ = 0.0344, wR ₂ = 0.0952
Final R indexes [all data]	R ₁ = 0.0350, wR ₂ = 0.0959
Largest diff. peak/hole / e Å ⁻³	1.22/-0.98

Appendix F. Chapter 5

F1 Synthesis of $[\text{Ru}(\text{POP})(\text{NO})\text{Cl}_3]$

$[\text{Ru}(\text{xantphos})(\text{NO})\text{Cl}_3]$ **Ru-NO-1**



In a 20 mL vial equipped with a stir bar, $[\text{Ru}(\text{NO})\text{Cl}_3] \times \text{H}_2\text{O}$ (175 mg, 0.77 mmol, 1.0 eq.) and xantphos **L1** (493 mg, 0.85 mmol, 1.1 eq.) were dissolved in benzene (15 mL). The solution was stirred at room temperature for 96 hours, during which a beige solid precipitated. The solvent was removed, and the product was washed three times in 5 mL hexane, dried, and was obtained as a beige powder (522 mg, 540 μmol , 83%).

Crystals of sufficient quality for SC-XRD can be obtained by dissolving in DMSO in high concentration and layering with diethyl ether in a 20 mL vial at room temperature.

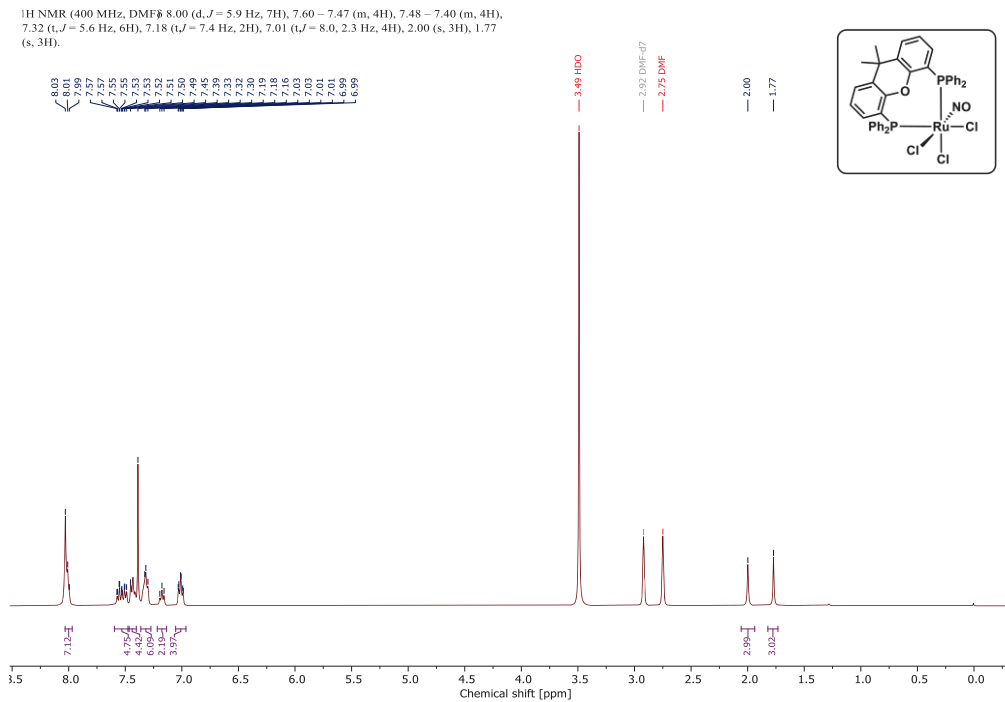
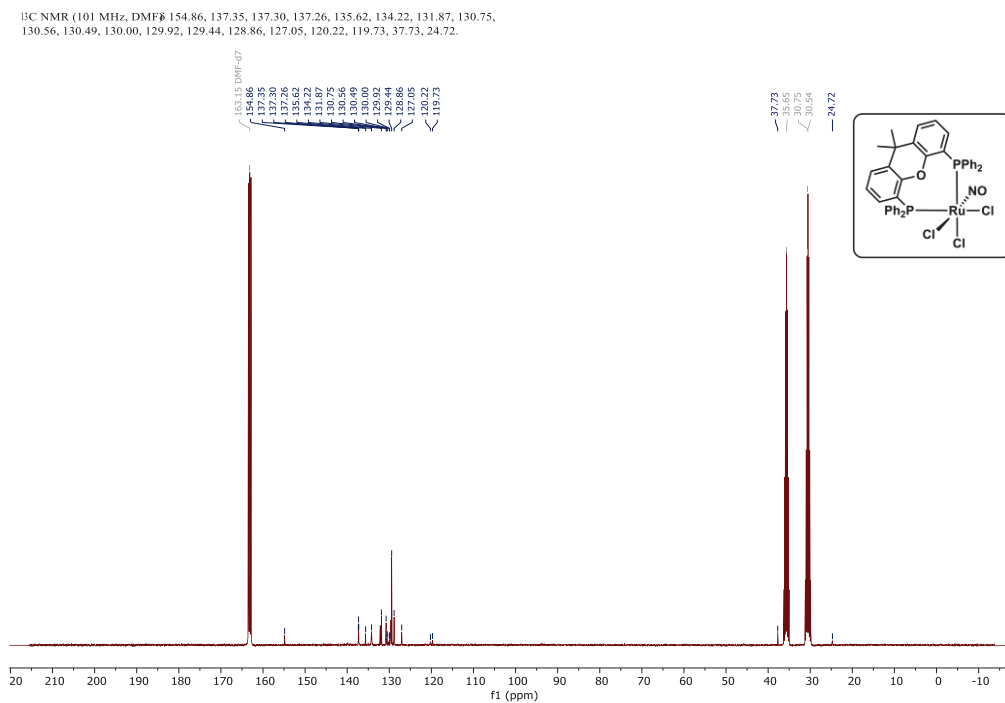
^1H NMR (400 MHz, DMF-d_7 , 25 $^\circ\text{C}$) δ 8.00 (d, $J = 5.9$ Hz, 7H), 7.60 – 7.47 (m, 4H), 7.48 – 7.40 (m, 4H), 7.32 (t, $J = 5.6$ Hz, 6H), 7.18 (t, $J = 7.4$ Hz, 2H), 7.01 (t, $J = 8.0, 2.3$ Hz, 4H), 2.00 (s, 3H), 1.77 (s, 3H).

^{13}C NMR (101 MHz, DMF-d_7 , 25 $^\circ\text{C}$) δ 154.86, 137.35, 137.30, 137.26, 135.62, 134.22, 131.87, 130.75, 130.56, 130.49, 130.00, 129.92, 129.44, 128.86, 127.05, 120.22, 119.73, 37.73, 24.72.

$^{31}\text{P}\{^1\text{H}\}$ NMR (162 MHz, DMF-d_7 , 25 $^\circ\text{C}$) δ 9.39.

ATR-IR (Germanium): 1874, 1478, 1433, 1402, 1213, 745, 739, 685, 511, 504.

EA: Calcd. (%) for $\text{C}_{39}\text{H}_{32}\text{O}_2\text{P}_2\text{N}_1\text{Cl}_3\text{Ru}$ (816.1) C 57.40, H 3.95, N 1.72 found C 57.44, H 4.33, N 0.95.


 Figure 9.55: 400 MHz ^1H NMR spectrum of **Ru-NO-1** in DMF-d_7 at 25 °C.

 Figure 9.56: 101 MHz ^{13}C NMR spectrum of **Ru-NO-1** in DMF-d_7 at 25 °C.

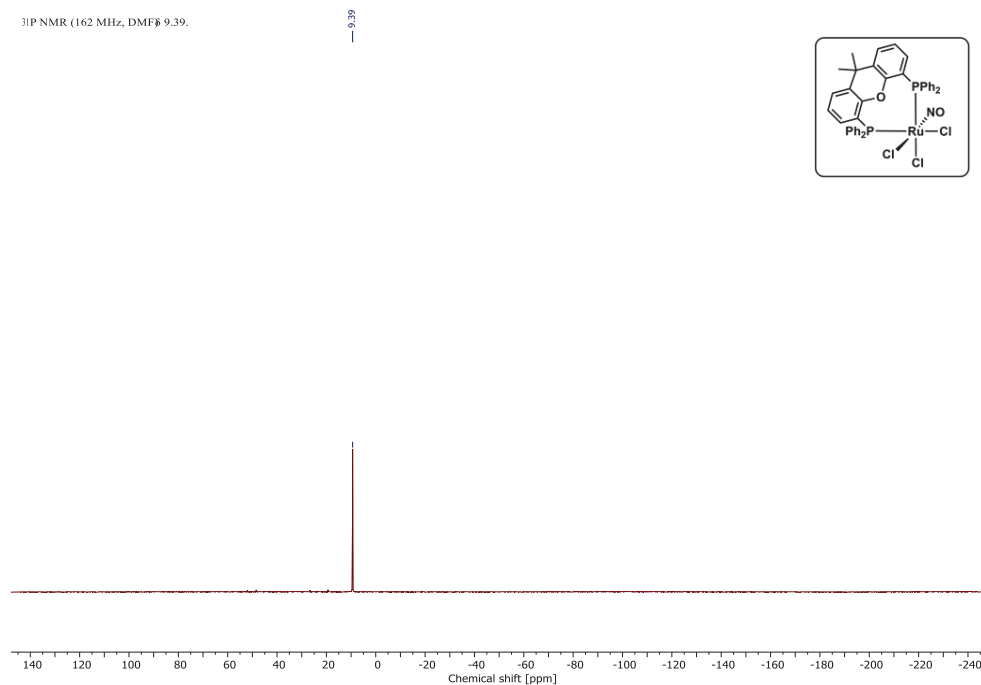


Figure 9.57: 162 MHz $^{31}\text{P}\{^1\text{H}\}$ NMR spectrum of **Ru-NO-1** in DMF-d_7 at 25 °C.

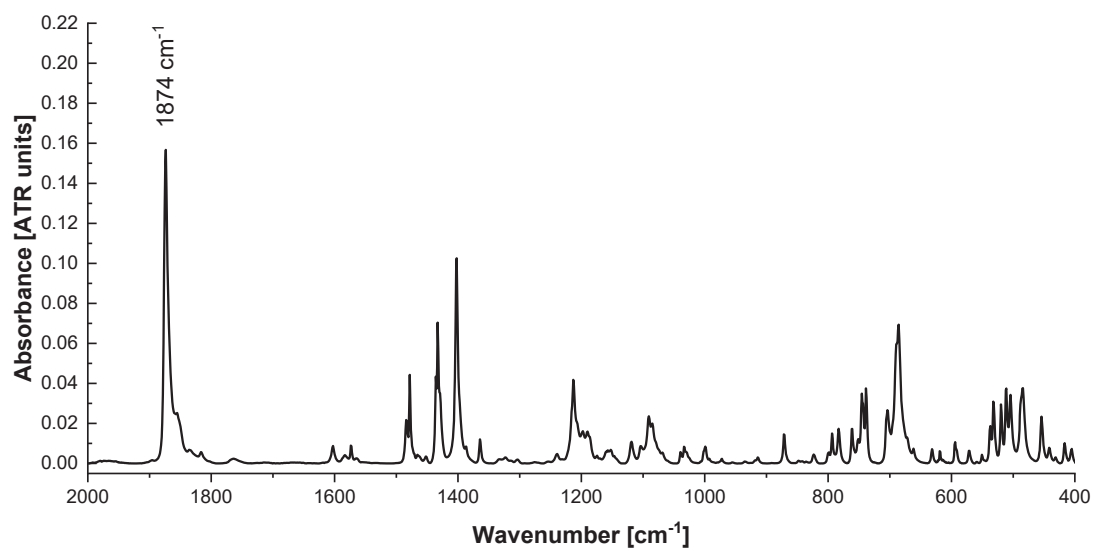
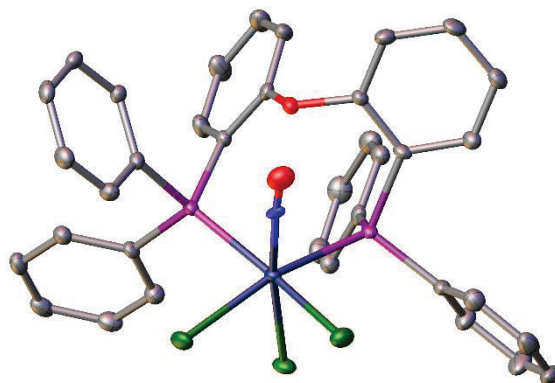
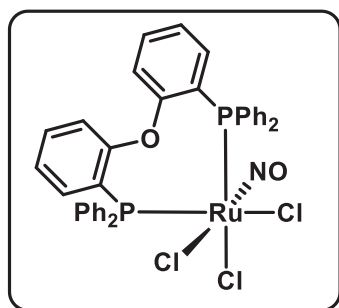


Figure 9.58: ATR-IR spectrum of **Ru-NO-1**.

[Ru(dpephos)(NO)Cl₃] Ru-NO-2

In a 20 mL vial equipped with a stir bar, [Ru(NO)Cl₃] \times H₂O (62.5 mg, 245 μ mol, 1.0 eq.) and **L2** (145 mg, 269 μ mol, 1.1 eq.) were dissolved in MeCN (15 mL). The solution was stirred at room temperature for 96 hours, during which a beige solid precipitated. The solvent was removed, and the product was washed three times in 5 mL hexane, dried, and was obtained as a beige powder (177 mg, 228 μ mol, 93%).

Crystals of sufficient quality for SC-XRD can be obtained by dissolving in DMSO in high concentration and layering with diethyl ether in a 20 mL vial at room temperature.

³¹P{¹H} NMR (162 MHz, DMSO-d₆, 25 °C) δ 13.58, (-17.92, free ligand).

ATR-IR (Germanium): 1868, 1450, 1436, 1259, 1223, 1194, 1120, 765, 754, 747, 744, 740, 722, 693, 544 cm⁻¹.

EA: Calcd. (%) for C₃₆H₂₈O₂P₂N₁Cl₃Ru (776.0) C 55.72, H 3.64, N 1.80 found C 55.62, H 4.43, N 1.59.

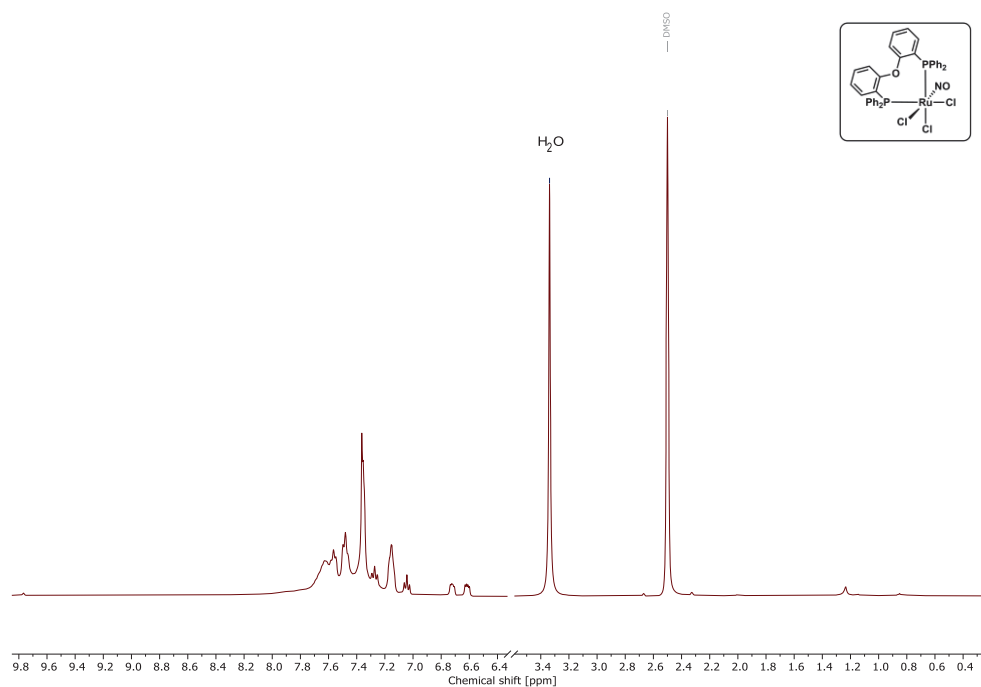


Figure 9.59: 400 MHz ^1H NMR spectrum of **Ru-NO-2** in DMSO- d_6 at 25 $^\circ\text{C}$.

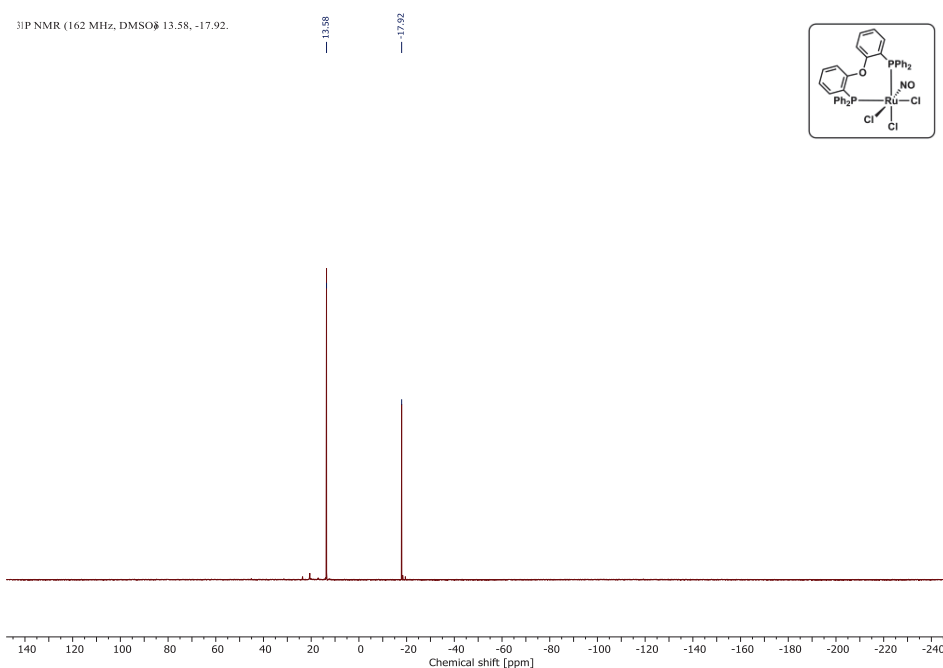
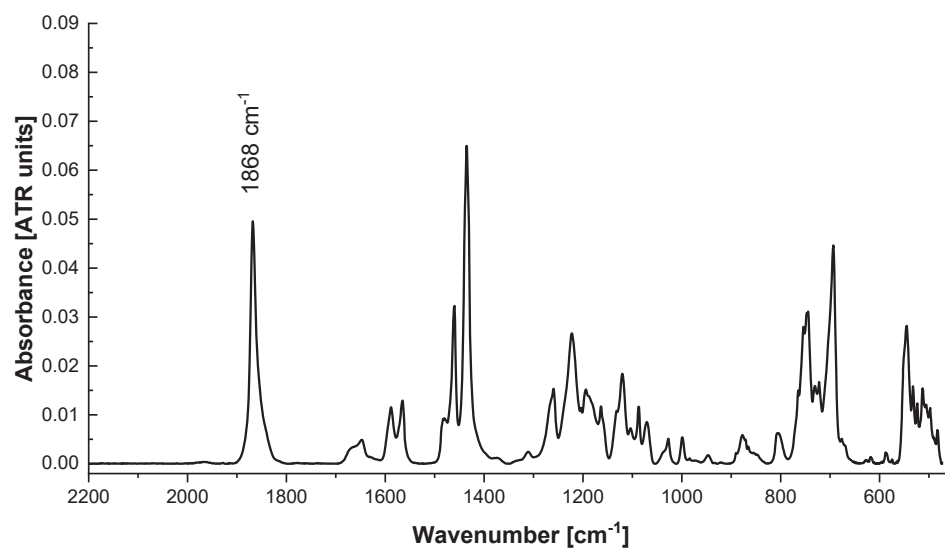
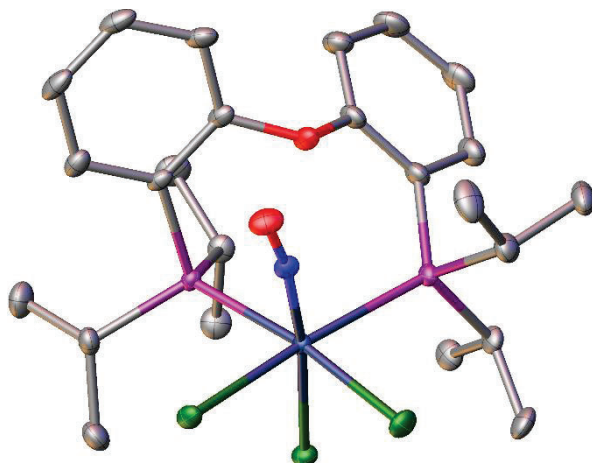
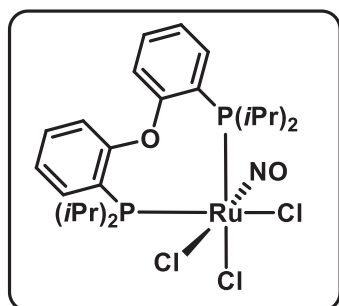


Figure 9.60: 162 MHz $^{31}\text{P}\{^1\text{H}\}$ NMR spectrum of **Ru-NO-2**, revealing free ligand.

Figure 9.61: ATR-IR spectrum of **Ru-NO-2**.

[Ru(*i*Pr-dpephos)(NO)(Cl₃)] Ru-NO-6

In a 20 mL vial equipped with a stir bar, [Ru(NO)(Cl₃)]×H₂O (37.1 mg, 145 μmol, 1.0 eq.) and *i*Pr-DPEphos **L6** (64.3 mg, 160 μmol, 1.1 eq.) were dissolved in THF (8 mL). The solution was stirred at room temperature for 24 hours, during which a brown solid precipitated. The solvent was removed, the product was washed three times in 5 mL pentane, dried, and was obtained as a beige solid in high yield.

Crystals of sufficient quality for SC-XRD can be obtained by dissolving in DMSO in high concentration and layering with diethyl ether in a 20 mL vial at room temperature.

ATR-IR (Germanium): 1863, 1590, 1475, 1460, 1434, 1528, 1064, 761, 535 cm⁻¹.

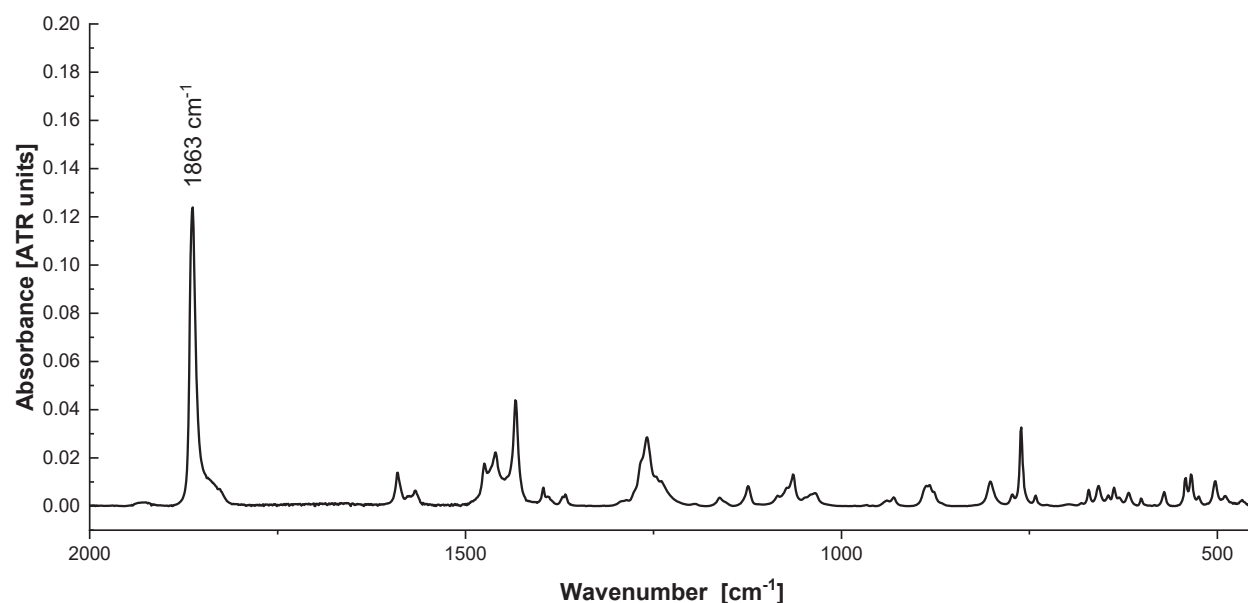
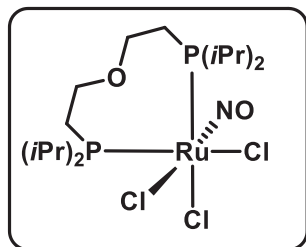


Figure 9.62: ATR-IR spectrum of **Ru-NO-6**

[Ru(DiPrPEE)(NO)(Cl₃)] **Ru-NO-7**

In a 20 mL vial equipped with a stir bar, [Ru(NO)(Cl)₃] \times H₂O (35.3 mg, 138 μ mol, 1.0 eq) and DiPrPEE **L7** (46.6 mg, 152 μ mol, 1.1 eq.) were dissolved in THF (10 mL). The solution was stirred at room temperature for 48 hours, during which a brown solid precipitated. The solvent was removed, the product was washed in ethanol and hexane.

Due to the compound's very low solubility, no NMR spectra could as of yet be obtained.

No crystals of suitable quality for XRD could as of yet be obtained.

ATR-IR (Diamond): 2963, 2933, 2875, 1836, 1462, 1081 cm⁻¹.

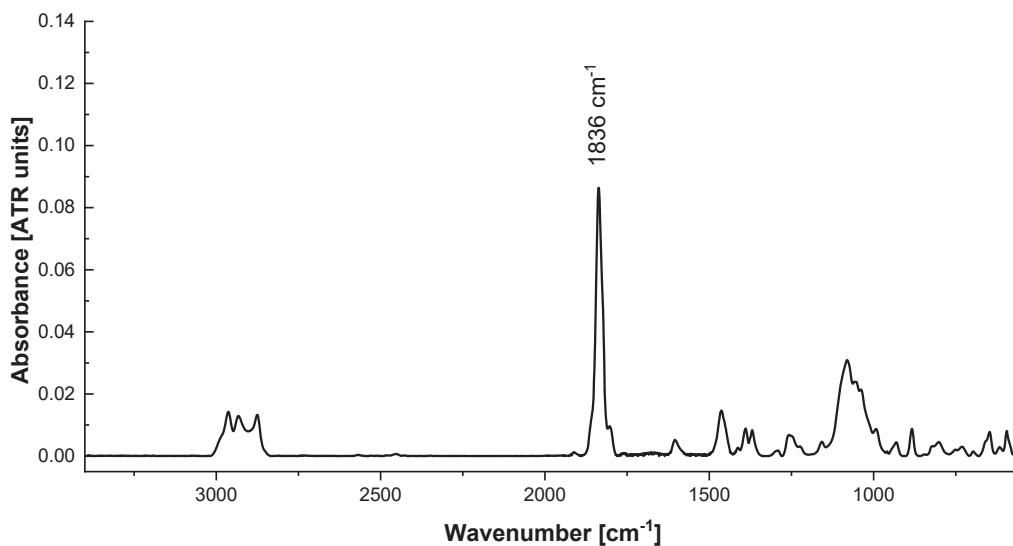


Figure 9.63: ATR-IR spectrum of **Ru-NO-7**.

F2 Crystallographic data

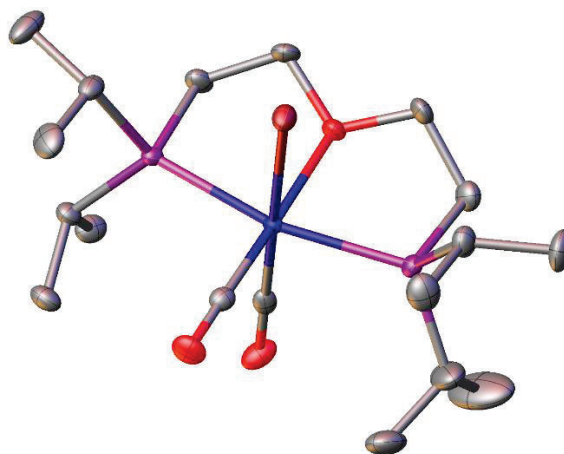
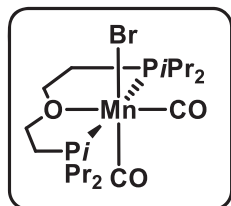
	[Ru(xantphos)(NO)Cl ₃] Ru-NO-1	[Ru(dpephos)(NO)Cl ₃] Ru-NO-2
Empirical formula	C ₃₉ H ₃₂ Cl ₃ NO ₂ P ₂ Ru	C ₃₆ H ₂₈ Cl ₃ NO ₂ P ₂ Ru
Formula weight	816.01	773.94
Temperature/K	120.00(10)	120.00(10)
Crystal system	orthorhombic	triclinic
Space group	Pna2 ₁	P-1
a/Å	17.44436(9)	9.2306(5)
b/Å	21.36110(11)	9.8029(5)
c/Å	9.54837(5)	17.7744(9)
α/°	90	89.066(4)
β/°	90	81.939(4)
γ/°	90	84.186(4)
Volume/Å ³	3558.02(3)	1584.26(14)
Z	4	2
ρ _{calc} /cm ³	1.523	1.622
μ/mm ⁻¹	6.778	0.885
F(000)	1656.0	780.0
Crystal size/mm ³	? × ? × ?	? × ? × ?
Radiation	Cu Kα (λ = 1.54184)	Mo Kα (λ = 0.71073)
2θ range for data collection/°	10.148 to 153.27	6.486 to 59.48
Index ranges	-21 ≤ h ≤ 21, -26 ≤ k ≤ 26, -10 ≤ l ≤ 12	-12 ≤ h ≤ 12, -13 ≤ k ≤ 12, -24 ≤ l ≤ 24
Reflections collected	72971	35555
Independent reflections	6835 [R _{int} = 0.0683, R _{sigma} = 0.0256]	8067 [R _{int} = 0.0480, R _{sigma} = 0.0487]
Data/restraints/parameters	6835/1/435	8067/0/406
Goodness-of-fit on F ²	1.054	1.078
Final R indexes [I ≥ 2σ (I)]	R ₁ = 0.0345, wR ₂ = 0.0972	R ₁ = 0.0382, wR ₂ = 0.0773
Final R indexes [all data]	R ₁ = 0.0346, wR ₂ = 0.0975	R ₁ = 0.0469, wR ₂ = 0.0827
Largest diff. peak/hole / e Å ⁻³	1.14/-1.23	0.94/-1.00

	[Ru(<i>i</i> Pr-dpephos)(NO)Cl ₃] Ru-NO-6
Empirical formula	C ₂₄ H ₃₆ Cl ₃ NO ₂ P ₂ Ru
Formula weight	639.929
Temperature/K	119.8(3)
Crystal system	monoclinic
Space group	P2 ₁ /n
<i>a</i> /Å	9.9066(2)
<i>b</i> /Å	15.0398(3)
<i>c</i> /Å	19.2960(4)
α /°	90
β /°	90
γ /°	90
Volume/Å ³	2874.97(10)
<i>Z</i>	4
$\rho_{\text{calc}}/\text{cm}^3$	1.478
μ/mm^{-1}	8.201
<i>F</i> (000)	1322.2
Crystal size/mm ³	? × ? × ?
Radiation	Cu K α (λ = 1.54184)
2 Θ range for data collection/°	7.46 to 154.04
Index ranges	-12 ≤ <i>h</i> ≤ 12, -18 ≤ <i>k</i> ≤ 18, -24 ≤ <i>l</i> ≤ 24
Reflections collected	58579
Independent reflections	6034 [<i>R</i> _{int} = 0.0438, <i>R</i> _{sigma} = 0.0179]
Data/restraints/parameters	6034/0/331
Goodness-of-fit on <i>F</i> ²	1.036
Final <i>R</i> indexes [<i>I</i> ≥ 2 σ (<i>I</i>)]	<i>R</i> ₁ = 0.0212, <i>wR</i> ₂ = 0.0542
Final <i>R</i> indexes [all data]	<i>R</i> ₁ = 0.0231, <i>wR</i> ₂ = 0.0560
Largest diff. peak/hole / e Å ⁻³	0.48/-0.35

Appendix G. Chapter 6

G1 Synthesis of $[\text{Mn}(\text{POP})(\text{CO})_2\text{Br}]$

$[\text{Mn}(\text{DiPrPEE})(\text{CO})_2\text{Br}]$ **Mn-7**



In a 25 mL Schlenk flask, DiPrPEE **L7** (108.5 mg, 0.352 mmol, 1.4 eq.) and $[\text{Mn}(\text{CO})_5\text{Br}]$ (69.5 mg, 0.252 mmol, 1.0 eq.) were dissolved in dry THF (10 mL). Immediate gas formation was observed. The mixture was refluxed for 24 hours to ensure complete conversion during which a colour change to dark yellow was observed. The mixture was allowed to cool to room temperature and the solvent was removed in vacuo. The crude product was washed with hexane (2x10 mL) and dried in vacuo, yielding the product as yellow powder (88.0 mg, 0.177 mmol, 70%).

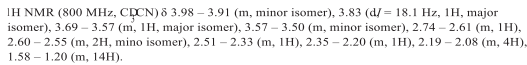
The product can be crystallized in sufficient quality for XRD measurements by layering using acetonitrile and diethyl ether in an NMR tube at room temperature.

^1H NMR (800 MHz, CD_3CN , 298 K) δ 3.98 – 3.91 (m, minor isomer), 3.83 (d, $J = 18.1$ Hz, 1H, major isomer), 3.69 – 3.57 (m, 1H, major isomer), 3.57 – 3.50 (m, minor isomer), 2.74 – 2.61 (m, 1H), 2.60 – 2.55 (m, 2H, minor isomer), 2.51 – 2.33 (m, 1H), 2.35 – 2.20 (m, 1H), 2.19 – 2.08 (m, 4H), 1.58 – 1.20 (m, 14H).

^{13}C NMR (201 MHz, CD_3CN , 298 K) δ 133.05, 75.14, 74.28, 26.59 (dd, $J = 8.4, 6.1$ Hz), 26.31 (t, $J = 9.5$ Hz), 25.75 (dd, $J = 13.1, 11.1$ Hz), 20.43, 20.29, 20.23, 20.21, 19.43, 19.24, 18.76, 18.65. $^{31}\text{P}\{^1\text{H}\}$ NMR (162 MHz, CD_3CN , 25 °C) δ 79.87, 75.87. Peaks of carbonyl groups could not be detected.

$^{31}\text{P}\{^1\text{H}\}$ NMR (162 MHz, CD_3CN , 298 K) δ 79.87, 75.87.

IR (ATR, diamond): 1911, 1828, 1459, 1386, 1053, 954, 823, 697, 663 cm^{-1} .



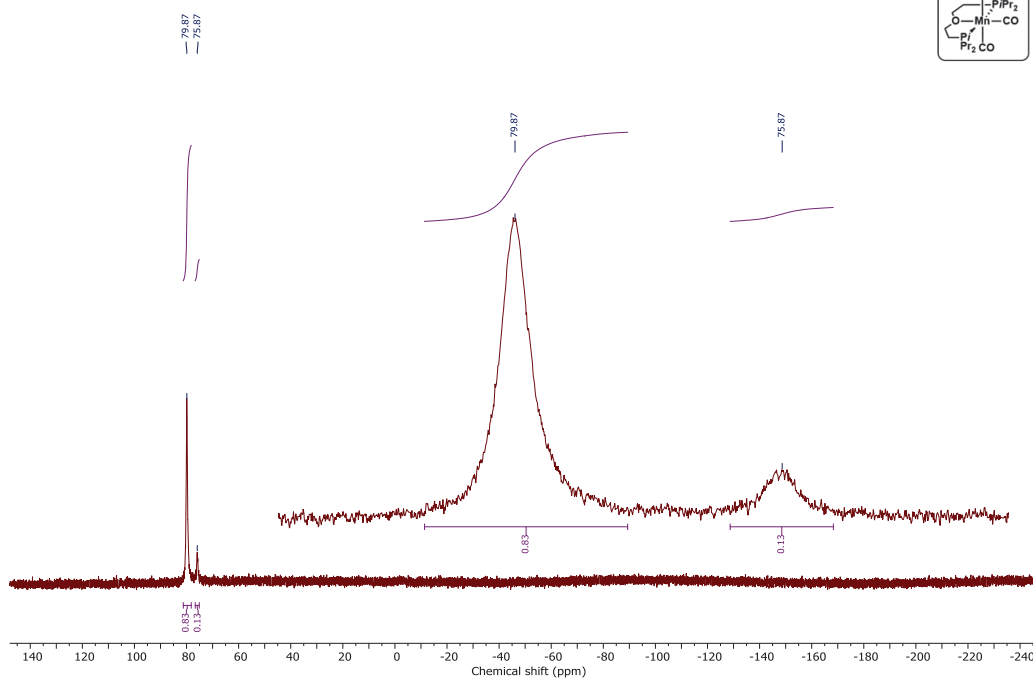


Figure 9.66: 162 MHz $^{31}\text{P}\{^1\text{H}\}$ NMR spectrum of **Mn-7** in CD_3CN at 25 °C.

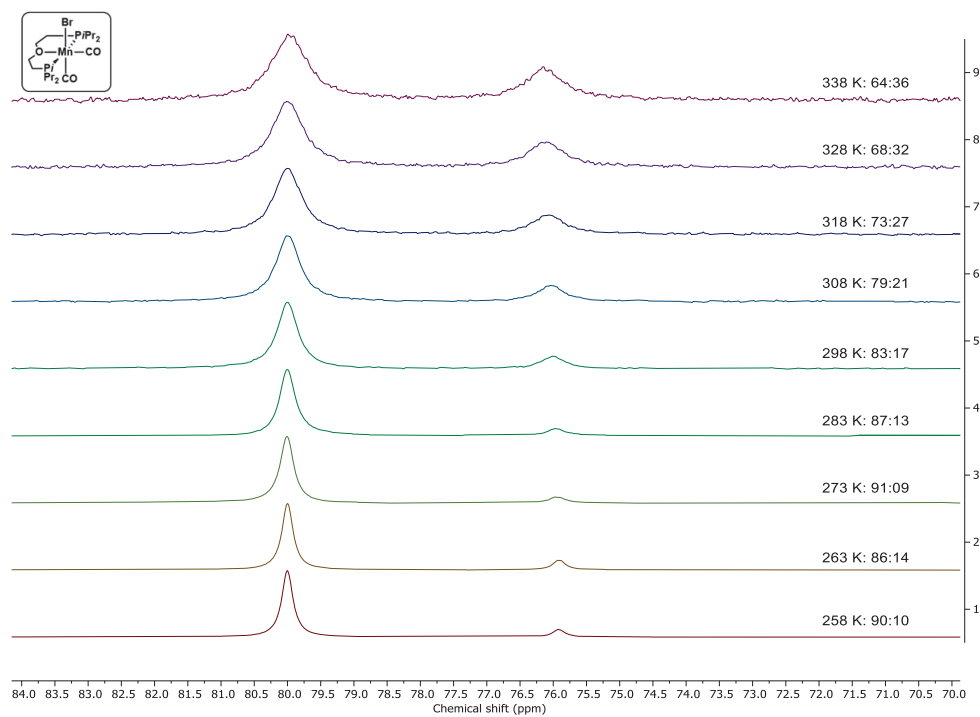


Figure 9.67 162 MHz temperature-dependent $^{31}\text{P}\{^1\text{H}\}$ NMR of **Mn-7** in CD_3CN .

Range 258-338 K.

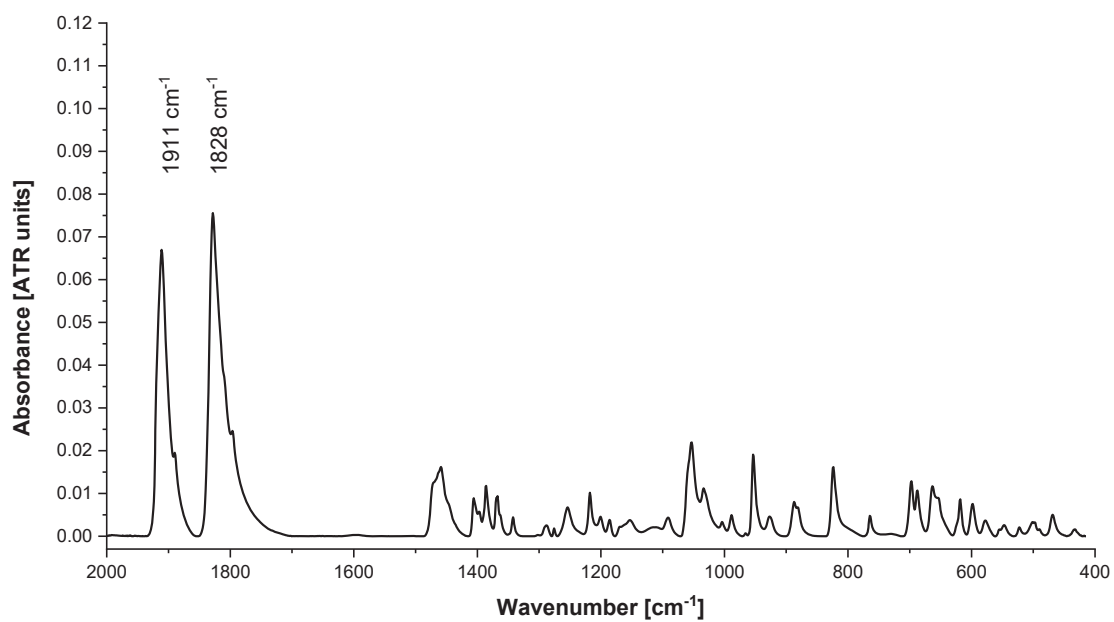
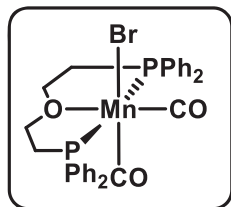


Figure 9.68: ATR-IR spectrum of **Mn-7**.

[Mn(DPPEE)(CO)₂Br] **Mn-3**

In a 25 mL Schlenk flask, DPPEE **L3** (84.0 mg, 190 μmol , 1.2 eq.) and $[\text{Mn}(\text{CO})_5\text{Br}]$ (43.5 mg, 158 μmol , 1.0 eq.) were dissolved in dry THF or toluene (10 mL). Immediate gas formation was observed. The mixture was refluxed for 24 hours to ensure complete conversion during which a colour change to dark yellow was observed. It was allowed to cool to room temperature and the solvent was removed in vacuo. The crude product was washed with hexane (2x10mL) and dried in vacuo, yielding the product as a yellow powder (64 mg, 101 μmol , 64%). Crystals of suitable quality can be obtained by layering acetonitrile and diethyl ether in an NMR tube at room temperature, however show degradation to $[\text{Mn}(\text{DPPEE})(\text{CO})_2\text{Br}][\text{MnBr}_4]$.

^1H -NMR (400 MHz, C_6D_6 , 298 K): Only very broad peaks observed.

$^{31}\text{P}\{^1\text{H}\}$ NMR (162 MHz, C_6D_6 , 298 K) δ 65.76 (s).

IR (ATR, diamond): 1921, 1835, 1483, 1434, 1404, 1220, 1184, 1158, 1097, 1054, 998, 950, 827, 742, 693, 622, 572, 507 cm^{-1} .

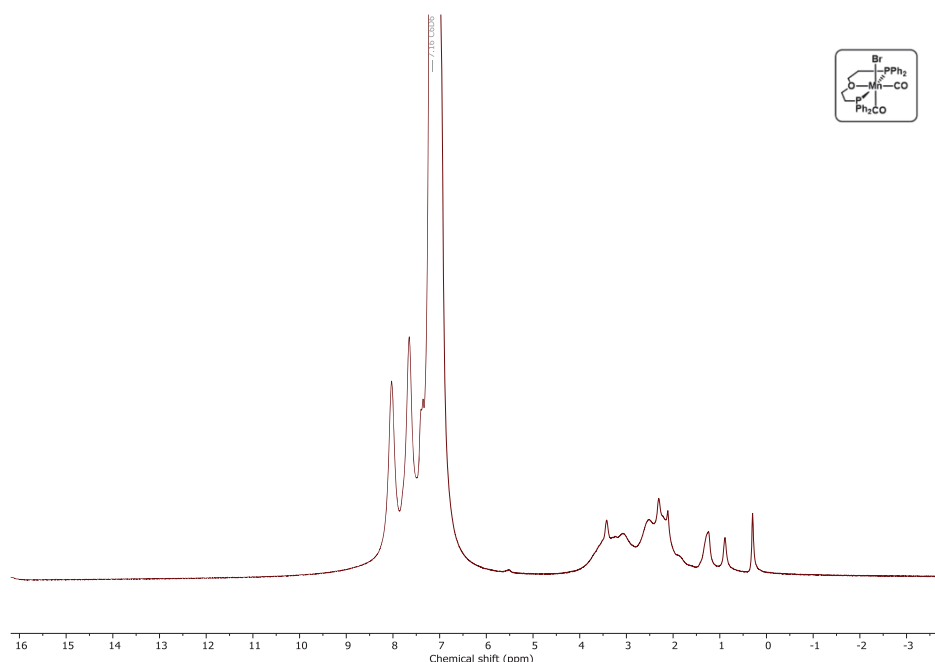


Figure 9.69: ^1H NMR spectrum of **Mn-3** in C_6D_6 at 25 $^\circ\text{C}$.

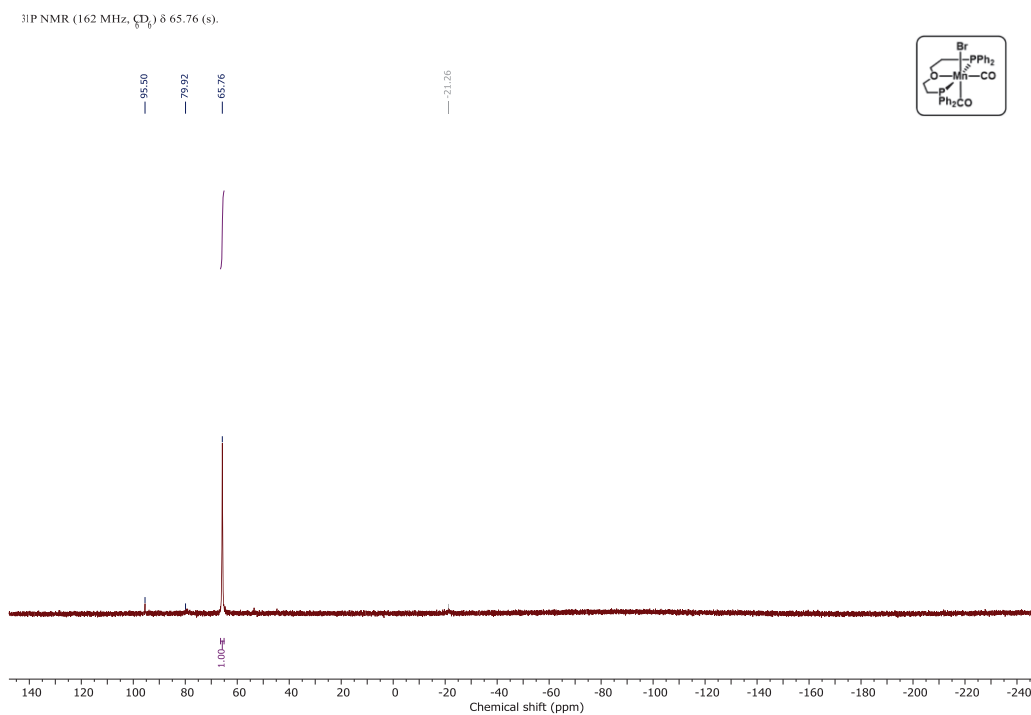


Figure 9.70: 162 MHz $^{31}\text{P}\{^1\text{H}\}$ NMR of **Mn-3** in C_6D_6 at 25 °C.

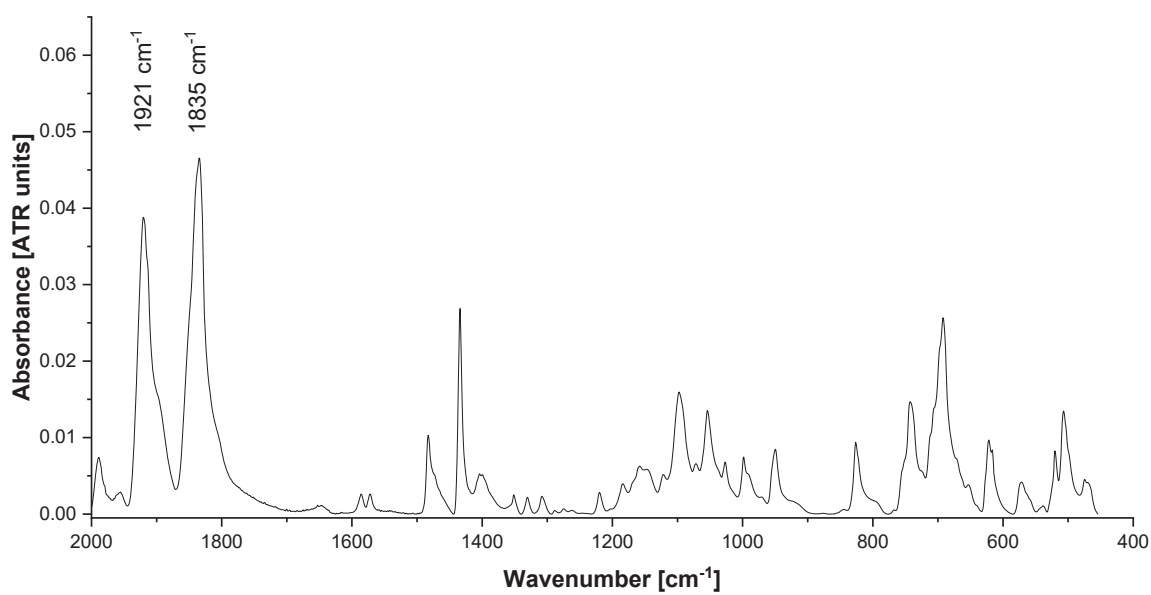
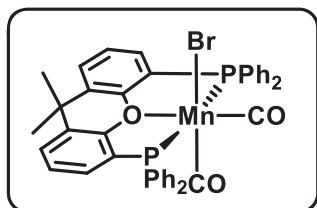


Figure 9.71: ATR-IR spectrum of **Mn-3**.

Attempted synthesis of $[\text{Mn}(\text{xantphos})(\text{CO})_2\text{Br}]$ **Mn-1**

In a 25 mL Schlenk flask, **L1** (182 mg, 315 μmol , 1.05 eq.) and $[\text{Mn}(\text{CO})_5\text{Br}]$ (82.4 mg, 300 μmol , 1.0 eq.) were dissolved in dry THF (10 mL). The mixture was refluxed for 24. It was allowed to cool to room temperature and the solvent was removed in vacuo, yielding a yellow crude mixture.

^1H -NMR (400 MHz, C_6D_6 , 298 K): Only very broad peaks observed.

$^{31}\text{P}\{^1\text{H}\}$ NMR (162 MHz, C_6D_6) δ 84.11, 63.54, 51.48, -17.77 (free ligand).

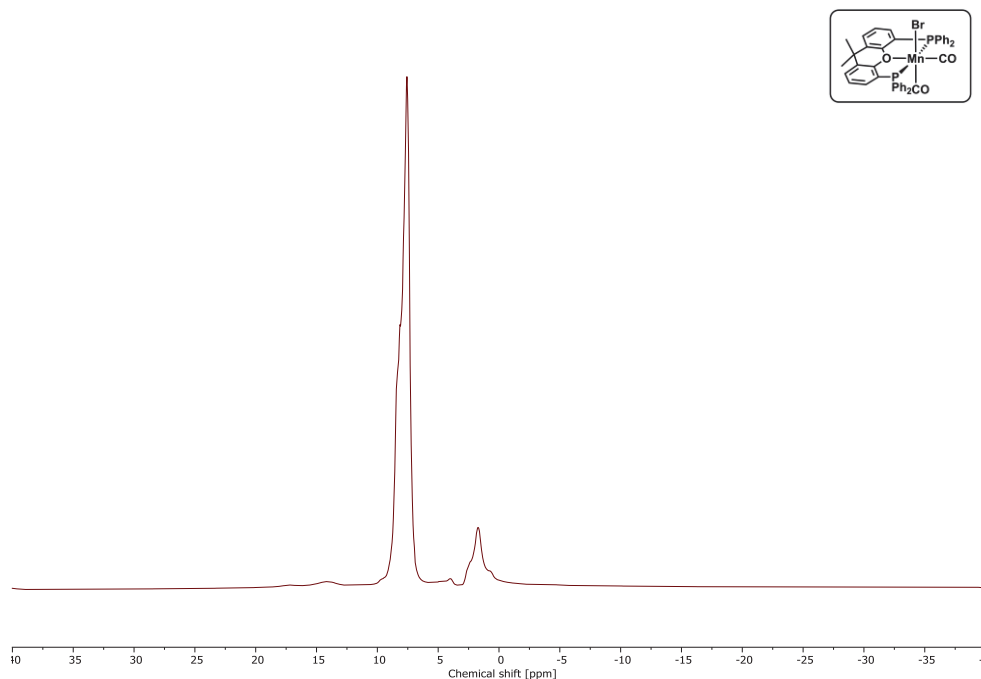
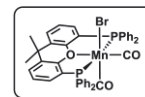
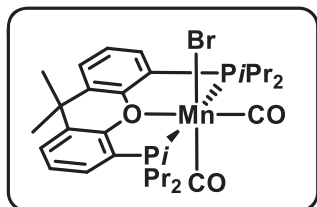


Figure 9.72: 400 MHz ^1H NMR spectrum of the attempted synthesis of **Mn-1** in C_6D_6 at 25 $^\circ\text{C}$.

Chemical shift [ppm]

Chemical Shift [ppm]	Assignment
77.0	CDCl_3 (solvent)
53.8	CH_2Cl_2 (impurity)
51.5	CH_2Cl_2 (impurity)
25.5	$1,2\text{-C}_2\text{H}_4\text{Cl}_2$



[Mn(*i*Pr-xantphos)(CO)₂Br] **Mn-5**

In a 25 mL Schlenk flask, *i*Pr-xantphos **L5** (116.2 mg, 263 μ mol, 1.5 eq.) and [Mn(CO)₅Br] (48.1 mg, 175 μ mol, 1.0 eq.) were dissolved in dry THF (15 mL). Slight gas formation was observed. The mixture was refluxed for 24 hours to ensure complete conversion during which a colour change to dark yellow to green and back to dark yellow was observed. It was allowed to cool to room temperature and the solvent was removed in vacuo, yielding the product as a yellow glassy substance. Hexane was added to force the product to powderize during stirring overnight, and the crude product was washed with hexane (2x10mL) and dried in vacuo, yielding the product as a yellow powder.

¹H NMR (400 MHz, C₆D₆, 298 K) δ 3.37, 2.56, 1.83, 1.50, 1.13. All peaks severely broadened.

³¹P{¹H} NMR (162 MHz, C₆D₆, 298 K) δ 73.21.

IR (ATR, diamond): 1930, 1954, 1845, 1464 1394, 1388, 1186, 1104, 873 745,657, 632 cm⁻¹.

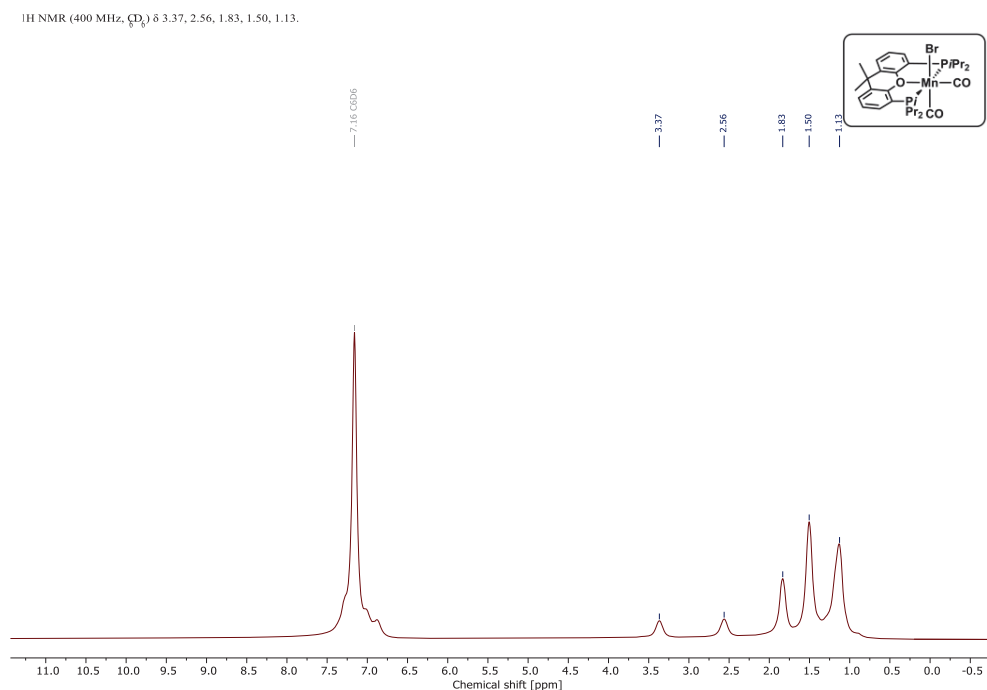


Figure 9.74: 400 MHz ¹H NMR spectrum of **Mn-5** in C₆D₆ at 25 °C.

^3P NMR (162 MHz, CD_6) δ 73.21.

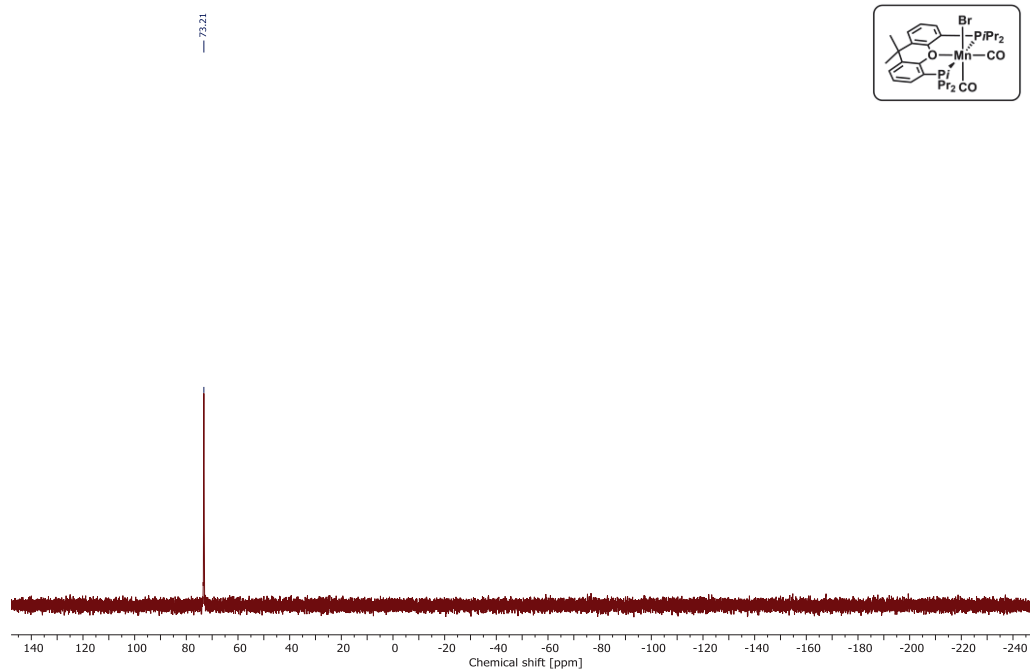


Figure 9.75: $^3\text{P}\{^1\text{H}\}$ NMR spectrum of **Mn-5** in C_6D_6 at 25 °C.

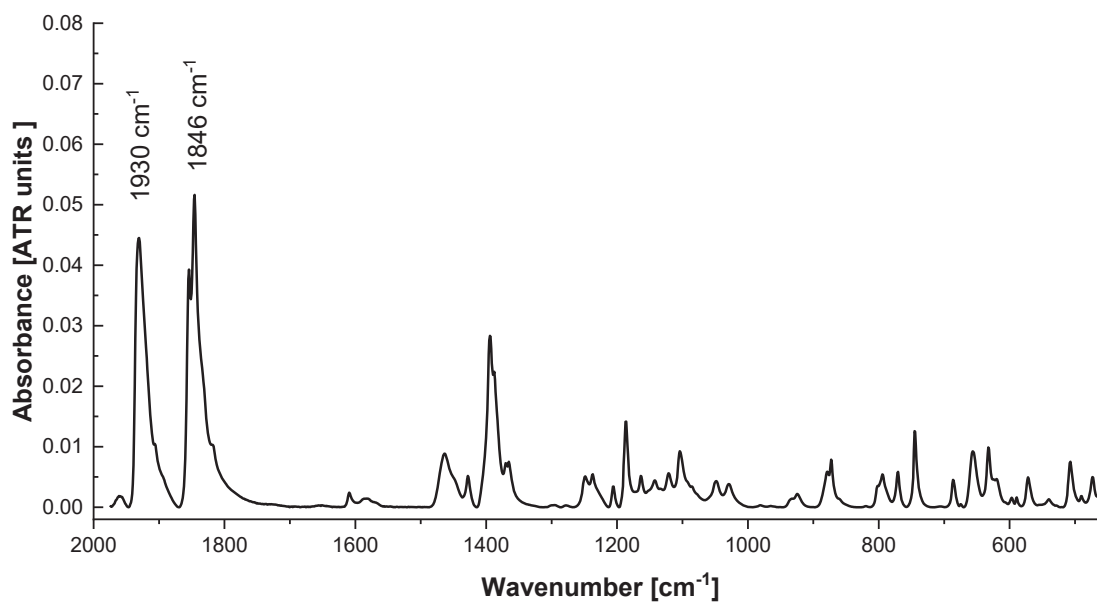


Figure 9.76: ATR-IR spectrum of **Mn-5**.

G2 General procedure for formic acid dehydrogenation in ionic liquid

In an inert gas glovebox, a 50 mL two-neck flask equipped with a stir bar was charged with the catalyst, sealed with two rubber septa and brought outside. It was attached under constant gas flow to a small straight reflux condenser. The ionic liquid (1.0 mL) was injected through the second septum. Slight constant argon flow was kept throughout the entire experiment. The ionic liquid was swirled around until all catalyst powder was in contact with it, and the setup was slowly warmed in an oil bath to the desired temperature under constant stirring. Stirring was continued until complete solution of the catalyst was observed, but at least for 10 minutes at which point formic acid (0.5 mL) was injected via syringe through the septum. At given intervals, small samples of the solution were taken using a syringe and dissolved in DMSO- d_6 for NMR analysis. In the case of recycling experiments, new formic acid was injected via syringe and the reaction was repeated.

To calculate conversions, ^1H NMR was used. An example of this can be found in Figure 9.77. The signal of the methyl group on the BMIM cation (peak e) was integrated to three times the amount of BMIM (3 times 5.35 mmol totaling 16.05 mmol). Then, the formate signal was integrated, and divided by the injected amount of formic acid, giving the conversion.

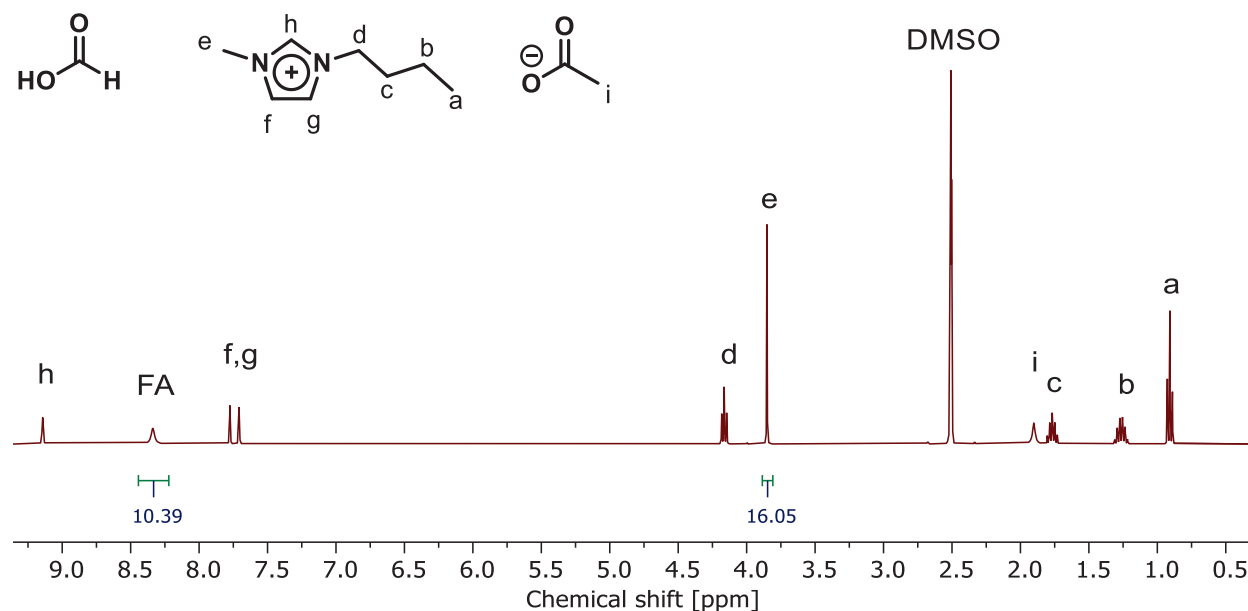


Figure 9.77: NMR of FA, BMIM-OAc and catalyst in DMSO- d_6 .

Relevant integrals of FA and N-CH₃ group of BMIM (peak e) in mmol.

G3 Formic acid dehydrogenation in ionic liquid

The turnover frequencies were calculated using the following formula:

$$TOF = \frac{n(FA)}{n(catalyst)} \times conversion \times \frac{1}{t[h]}$$

For the time of TOF_{max} , the timeframe was chosen in which the conversion per unit time was highest (i.e. where the graph between two datapoints was the steepest). Conversions and times were then taken as the differences between those two datapoints.

Table 9.12: Catalytic screening of manganese complexes.

$ \begin{array}{c} \text{H} \quad \text{O} \\ \diagdown \quad \parallel \\ \text{C} \\ \diagup \quad \text{OH} \end{array} \xrightarrow[\text{BMIM-OAc, 90 }^\circ\text{C, overnight}]{[\text{Mn}]} \text{H}_2 + \text{CO}_2 $								
Complex	n(Complex) [μmol]	Conversion [%]						TOF [h ⁻¹] first hour
		1 h	2 h	3 h	4 h	6 h	Overnight	
Mn-3	13	25	31	35	39	54	58	255
Mn-5	13	21	33	36	42	48	49	214
Mn-5	26	29	40	49	50	54	61	148
Mn-7	13	17	32	46	n.a.	n.a.	72	173
Mn-7	26	22	46	55	63	68	79	112

Conditions: 0.5 mL (13.25 mmol) formic acid, 1.0 mL (5.35 mmol) BMIM-OAc.

G4 Crystallographic data

	[Mn(DiPrPEE)(CO) ₂ Br] Mn-7	[Mn(DPPEE)(CO) ₂ (MeCN)] ₂ [MnBr ₄]*MeCN*0.5 Et ₂ O Degraded Mn-3
Empirical formula	C _{14.4} H _{28.8} Br _{0.8} Mn _{0.8} O _{2.4} P _{1.6}	C ₆₆ H ₆₅ Br ₄ Mn ₃ N ₃ O ₆ P ₄ *
Formula weight	397.80	1604.55
Temperature/K	119.99(10)	119.99(17)
Crystal system	orthorhombic	monoclinic
Space group	P2 ₁ 2 ₁ 2 ₁	P2 ₁ /n
a/Å	10.79520(10)	10.34093(4)
b/Å	14.16690(10)	18.05007(8)
c/Å	14.81550(10)	38.79792(17)
α/°	90	90
β/°	90	94.8878(4)
γ/°	90	90
Volume/Å ³	2265.80(3)	7215.47(5)
Z	5	4
ρ _{calc} /cm ³	1.458	1.477
μ/mm ⁻¹	8.247	8.029
F(000)	1032.0	3220.0
Crystal size/mm ³	? × ? × ?	0.249 × 0.16 × 0.128
Radiation	Cu Kα (λ = 1.54184)	Cu Kα (λ = 1.54184)
2Θ range for data collection/°	8.636 to 153.44	8.432 to 153.404
Index ranges	-13 ≤ h ≤ 13, -17 ≤ k ≤ 17, -16 ≤ l ≤ 18	-13 ≤ h ≤ 12, -22 ≤ k ≤ 22, -48 ≤ l ≤ 48
Reflections collected	46890	146461
Independent reflections	4760 [R _{int} = 0.0490, R _{sigma} = 0.0204]	15123 [R _{int} = 0.0470, R _{sigma} = 0.0201]
Data/restraints/parameters	4760/0/234	15123/0/778
Goodness-of-fit on F ²	1.035	1.051
Final R indexes [I ≥ 2σ (I)]	R ₁ = 0.0245, wR ₂ = 0.0615	R ₁ = 0.0258, wR ₂ = 0.0624
Final R indexes [all data]	R ₁ = 0.0254, wR ₂ = 0.0621	R ₁ = 0.0274, wR ₂ = 0.0634
Largest diff. peak/hole / e Å ⁻³	0.89/-0.60	0.59/-0.33

* One half of a disordered molecule of Et₂O could not be modeled and was removed with Platon Squeeze. It is not included in the sum formula.

Appendix H. Chapter 7

H1 Phosphine synthesis

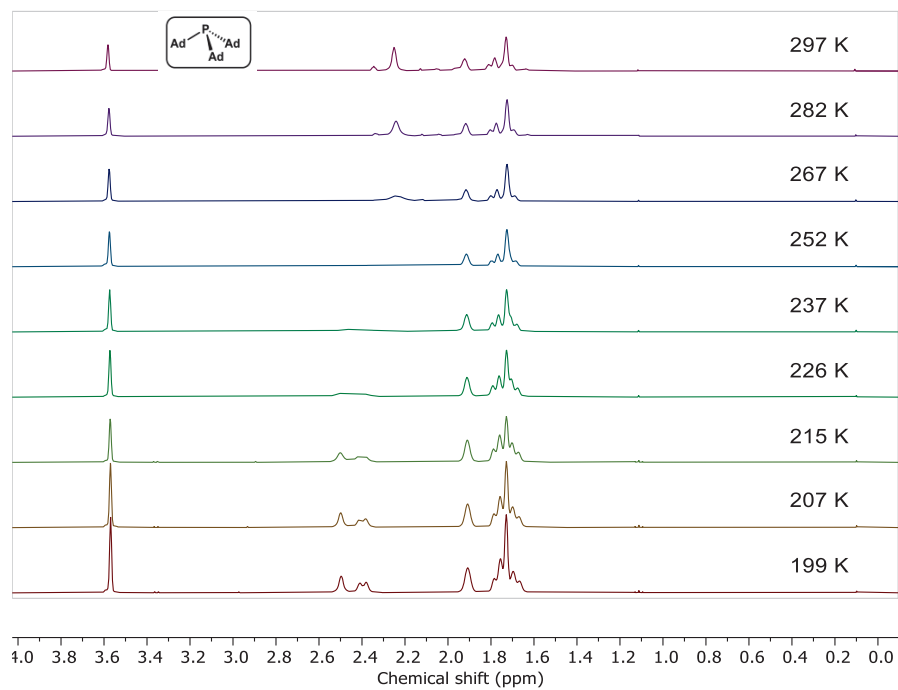
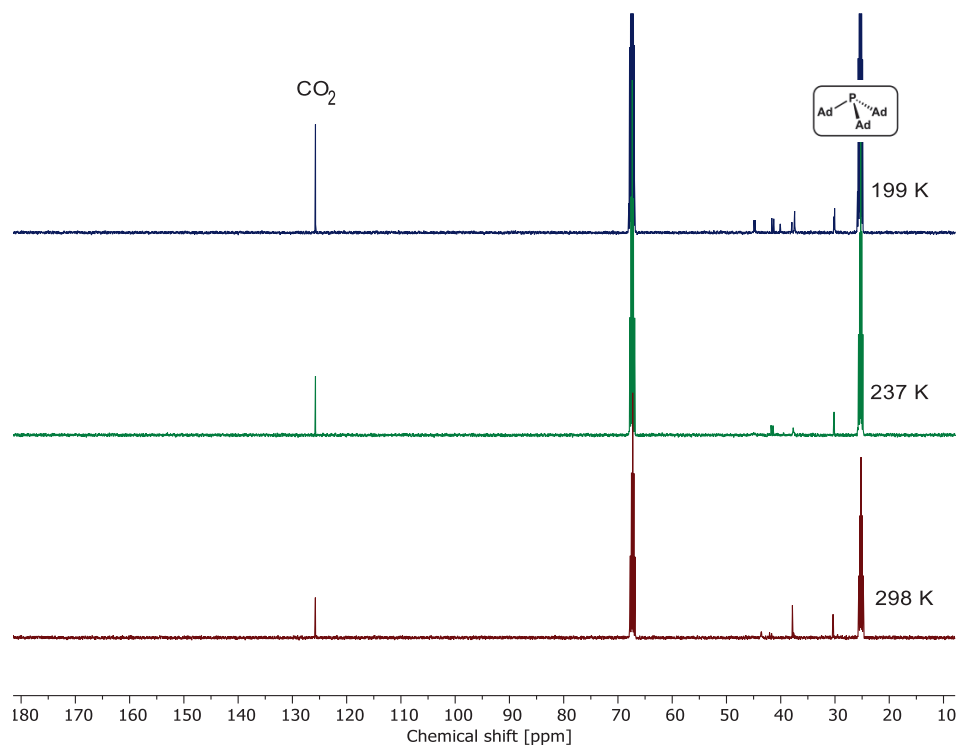
Tri-1-adamantyl phosphine, tris-(tetramethylguanidiny)phosphine $P(\text{tmg})_3$ and tris-(tetramethylguanidiny)phosphine- CO_2 adduct $P(\text{tmg})_3\text{-CO}_2$ were synthesized according to literature.^{182,176,173} Their spectroscopic properties corresponded to those in published procedures.

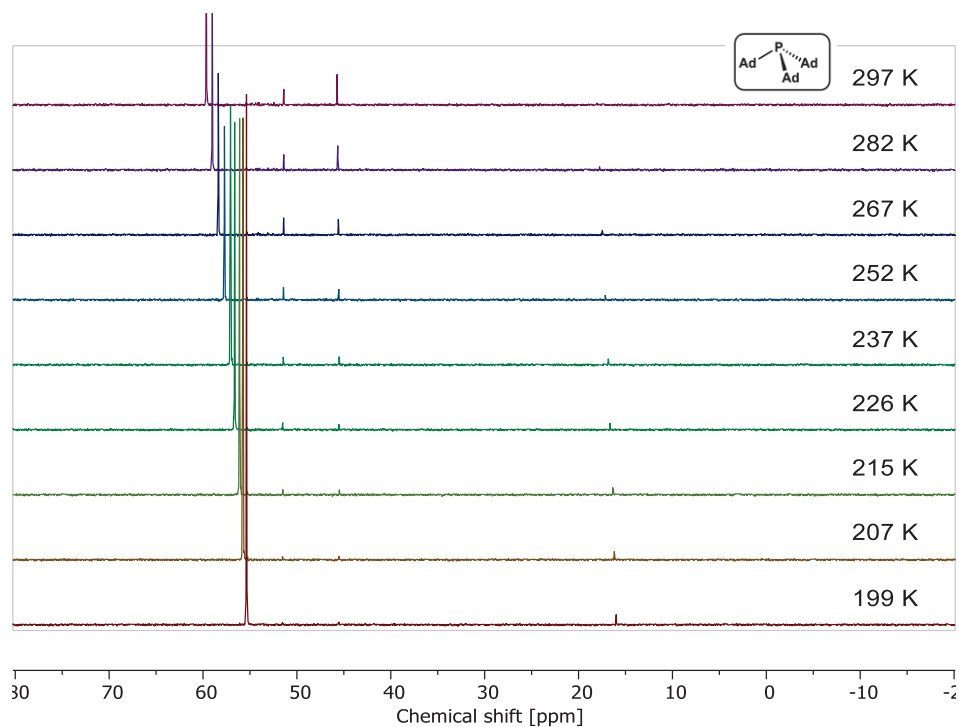
H2 General procedure for temperature-dependent NMR experiments

In an inert gas glovebox, an overpressure-proof J-Young NMR tube was charged with the phosphine ($\sim 10\ \mu\text{mol}$) and THF-d_8 ($550\ \mu\text{L}$) under inert conditions. It was removed from the glovebox and attached to a Schlenk setup via a glass adapter. The solvent was frozen using a liquid nitrogen bath, and the atmosphere in the tube was quickly removed in vacuo. The tube was removed from the liquid nitrogen, and then was pressurized with 2 bar CO_2 (total volume $\sim 1\text{ mL}$, $\sim 90\ \mu\text{mol}$).

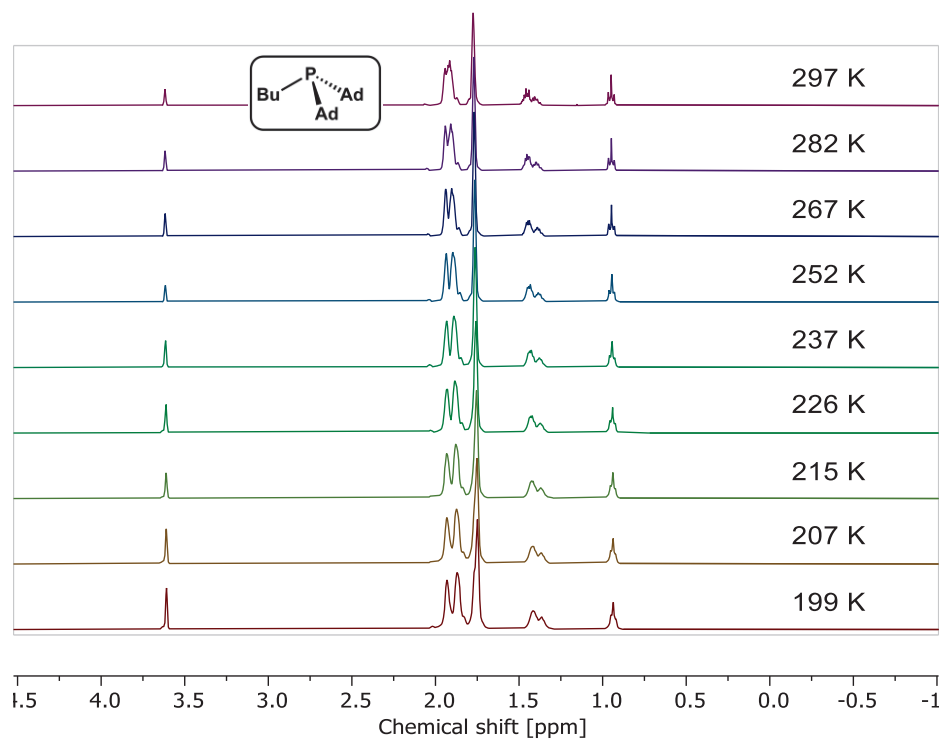
In the NMR spectrometer, the tubes were cooled down to 200 K and slowly warmed again to room temperature, during which time the NMR spectra were measured. Temperatures were calibrated using the methanol- d_4 NMR thermometer method.¹⁹¹

H3 Temperature-dependent NMR experiments

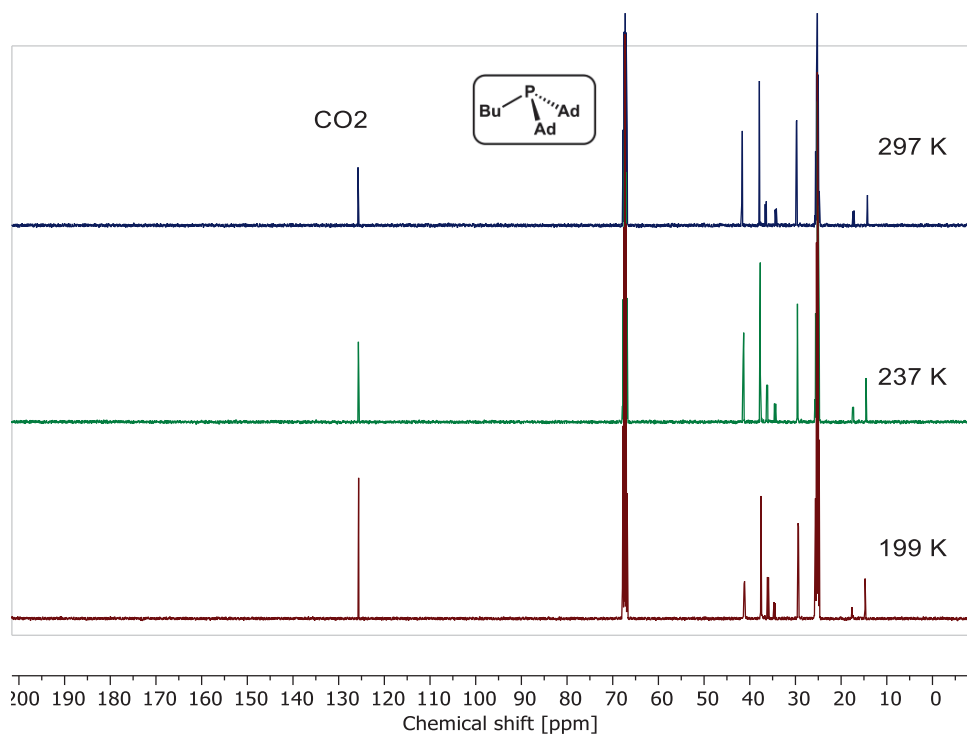
Figure 9.78: Variable temperature ^1H NMR spectrum of $\text{P}(\text{1-Ad})_3$ in THF-d_8 .Figure 9.79: Variable temperature ^{13}C NMR spectrum of $\text{P}(\text{1-Ad})_3$ in THF-d_8 .


 Figure 9.80: Variable temperature $^{31}\text{P}\{^1\text{H}\}$ spectrum of $\text{P}(\text{1-Ad})_3$ in THF-d_8 .

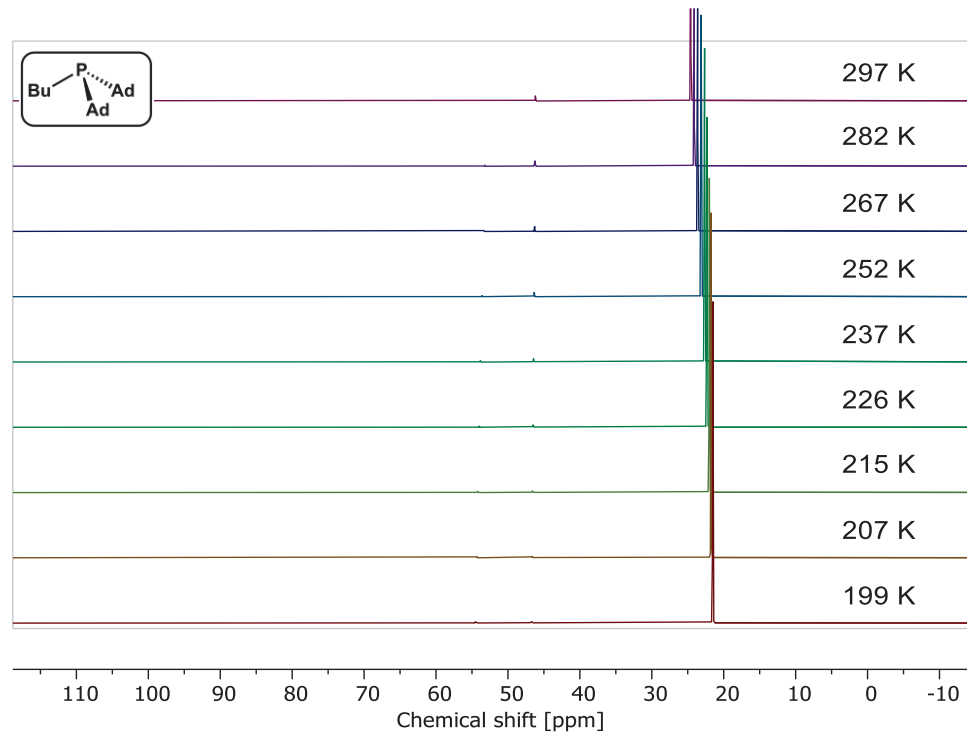
Range 200-300 K.


 Figure 9.81: Variable temperature ^1H spectrum of BuPAD_2 in THF-d_8 .

Range 200-300 K.


 Figure 9.82: Variable temperature ^{13}C spectrum of BuPAD_2 in THF-d_8 .

Range 200-300 K.


 Figure 9.83: Variable temperature $^{31}\text{P}\{^1\text{H}\}$ spectrum of BuPAD_2 in THF-d_8 .

Range 200-300 K.

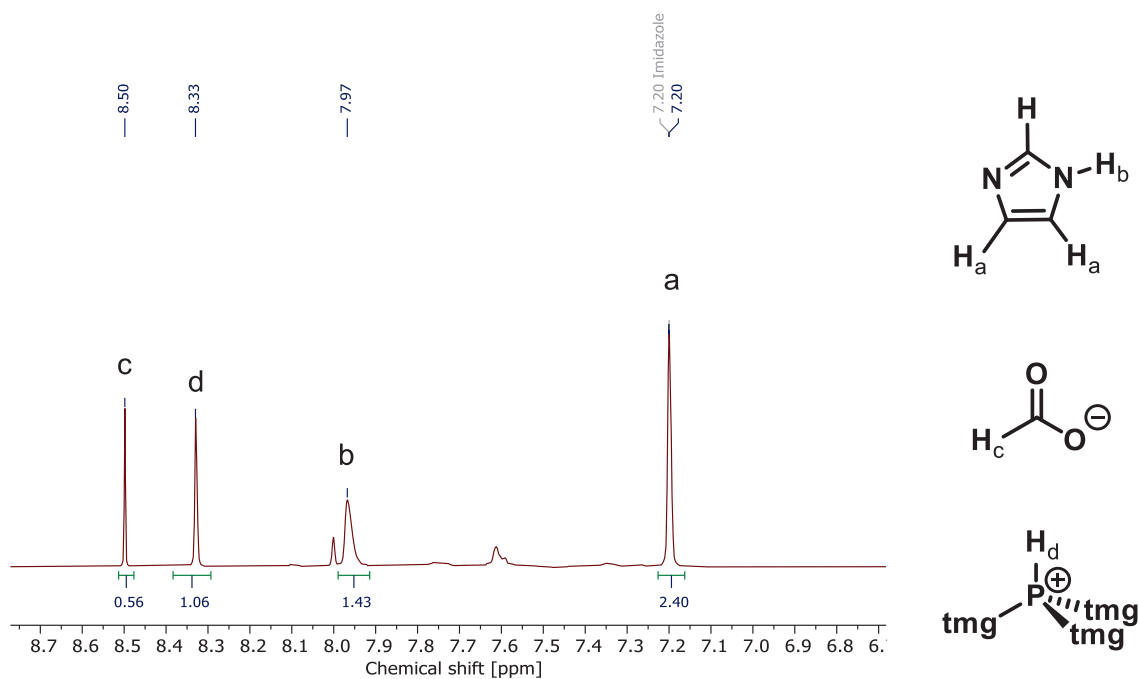
H4 General procedure for CO₂ hydrogenation experiments

In an inert gas glovebox, an autoclave reactor (type B, described earlier in Appendix D) was charged with Ru-MACHO-BH (5.9 mg, 0.01 mmol, 1.0 eq.), additive (0.1 mmol, 10 eq.) and 2.0 mL THF. It was sealed, removed from the glovebox, and pressurized with CO₂ (10 bar) and H₂ (40 bar). It was then for 24 hours at 90 °C. The pressures were monitored using the software of the reactor controller unit. It was allowed to cool to room temperature. For analysis, the solution was diluted with 2.0 mL of D₂O, and imidazole (1.0-1.2 eq., weighed) was added as an internal standard.

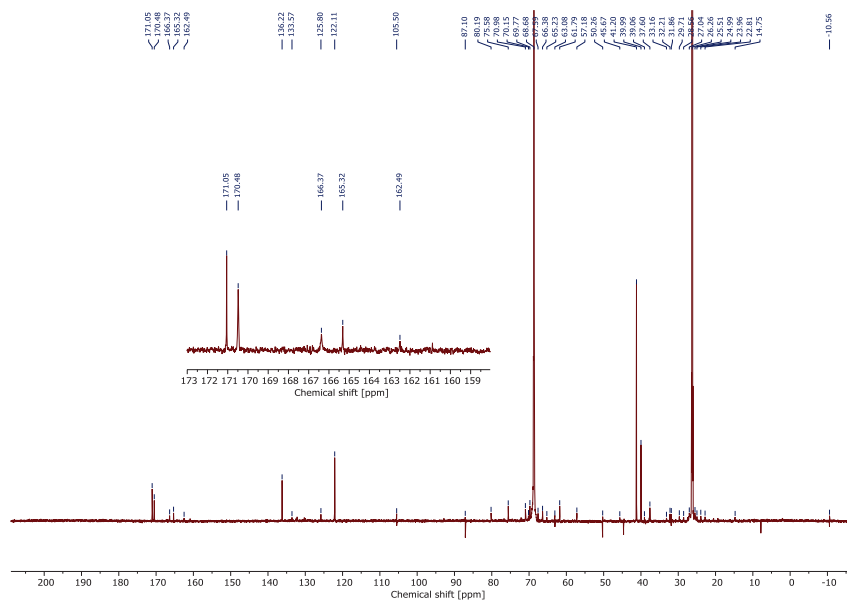
H5 CO₂ hydrogenation experiments using P(tm_g)₃

Table 9.13: Hydrogenation experiments of Ru-MACHO and P(tm_g)₃.

$\text{H}_2 + \text{CO}_2 \xrightarrow[\text{THF (2.0 mL), 90 } ^\circ\text{C 24 h}]{\text{Ru-MACHO-BH (0.01 mmol), Additive (0.1 mmol)}} \text{H}-\text{C}(=\text{O})-\text{OH}$			
Catalyst	Additive	Yield	TON (relative to Ru-MACHO-BH)
Ru-MACHO-BH	---	traces	<1
Ru-MACHO-BH	P(tm _g) ₃ -CO ₂	0.56 eq. relative to P(tm _g) ₃	5.6
Ru-MACHO-BH	P(tm _g) ₃ -CO ₂	0.63 eq. relative to P(tm _g) ₃	6.3

Figure 9.84: Downfield region of ^1H NMR spectrum of hydrogenation reaction.

Conditions: D_2O , THF, 25 °C, 1.2 eq. imidazole as internal reference, suspected assignments on the right.

Figure 9.85: 101 MHz ^{13}C NMR of hydrogenation reaction.

Conditions: D_2O /THF, 25 °C

Reaction conditions found in table above.

Appendix I. Planned publications

1. Alexander Tobias Nikol, Rosa Maria Padilla Paz and Martin Nielsen. Synthesis and Characterization of a Range of new Ruthenium(II) POP Pincer Complexes, *in preparation*.
2. Alexander Tobias Nikol, Rosa Maria Padilla Paz and Martin Nielsen. Non-Noyori-Type Ruthenium-POP Pincer Complexes for Ethanol Upgrading, *in preparation*.
3. Alexander Tobias Nikol, Brenda Rabell Montiel, Anders Riisager, Shoubhik Das, and Martin Nielsen. Formic Acid Dehydrogenation using Ruthenium-POP Pincer Complexes in Ionic Liquids, *in preparation*.

Appendix J. Conferences and scientific exchanges

1. Alexander Tobias Nikol and Martin Nielsen. Ethanol upgrading using Ruthenium-POP pincer complexes. *Inorganic Graduate Student Seminar (IGSS)*, University of Southern Denmark, Odense, Denmark, 15. October 2021 (Poster).
2. Alexander Tobias Nikol and Martin Nielsen. Ethanol upgrading using Ruthenium-POP pincer complexes. *DTU's annual PhD symposium 2021*, Helsingør, Denmark, 04. November 2021 (Poster).
3. Alexander Tobias Nikol and Martin Nielsen. Ethanol upgrading using Ruthenium-POP pincer complexes. *DTU's annual PhD symposium 2022*, Helsingør, Denmark, 03. November 2022 (Presentation).
4. Alexander Tobias Nikol. POP pincer complexes for small molecule transformations. *Scientific exchange with Felipe Rocha workgroup*, Universidade Federal de São Carlos, São Carlos, Brazil, 07. June 2023 (Presentation).